DAMAGE ZONE PREDICTION FOR ROCK BLASTING

by

Changshou Sun

A dissertation submitted to the faculty of
The University of Utah
in partial fulfillment of the requirements for the degree of

Doctor of Philosophy

Department of Mining Engineering

The University of Utah

December 2013

The University of Utah Graduate School

STATEMENT OF DISSERTATION APPROVAL

The dissertation of **Changshou Sun**

has been approved by the following supervisory committee members:

Michael K. McCarter	, Chair	**7/19/2013** Date Approved
Michael G. Nelson	, Member	**12/10/2009** Date Approved
Dal Sun Kim	, Member	**7/19/2013** Date Approved
Aurelian C. Trandafir	, Member	**12/10/2009** Date Approved
Steven F. Bartlett	, Member	**12/10/2009** Date Approved

and by **Michael G. Nelson** , Chair of the Department of **Mining Engineering**

and by David B. Kieda, Dean of The Graduate School.

ABSTRACT

Modern mining systems frequently use drill and blast techniques for rock excavation. Rock blasting not only fragments rock but also creates overbreak in the rock surrounding the excavation. The unwanted damage often results in higher mining costs and severe safety concerns.

To reduce unwanted damage, the ability to predict damage caused by rock blasting is essential. A shock wave based, engineer-friendly technique is developed in this dissertation. The design procedure is based on charts, graphs, and a computer program. The dissertation deals with three major aspects of developing a damage prediction model, namely, theoretical development, experimental research, and validation of the model using laboratory and field results. The theoretical development includes calculation of stress and response of rock for fully-coupled and decoupled blasting using the theory of shock wave transfer. This new procedure will be referred to as SWT. The objective is to use the properties of explosives and the properties of rock materials to develop a reasonable algorithm for predicting the extent of the damage zone caused by rock blasting.

To validate the SWT model, three approaches are presented: (1) currently available experimental data in the literature; (2) large-scale laboratory experiments; and results of a field application in an underground mine. Based on Esen's (2003) laboratory

experiments and large-scale laboratory experiments conducted as part of this dissertation, the SWT model successfully estimates the extent of the crush zone. Based on the work presented by Olsson (Olsson 1993) SWT provides reasonable estimates for the crack zone. Based on the comparison with other approaches, the SWT model is close to the Modified Ash (Energy-based), Modified Ash (Pressure-based), Holmberg Explosive Factor, and Sher Quasi-Static models. However, the crack zone did not conform to that observed in large scale laboratory models. The likely reason for this is the relatively small size of the laboratory models and lack of complete confinement. Application of this new method under field conditions, however, confirms the usefulness of SWT for practical blast design. Several new insights and useful information developed as a result of this research are valuable for the caution blast design at surface and underground mining.

TABLE OF CONTENTS

ACKNOWLEDGMENTS

This project would not have been possible without the support of many people. Many thanks to my adviser, Michael K. McCarter, who helped me set up and conduct laboratory experiments and who read numerous revisions of my dissertation. I am most grateful to my former adviser, committee member, William A. Hustrulid, who helped me select this study project and who provided continuous guidance and support for my study. Also my thanks go to my committee members, Michael G. Nelson, Aurelian C. Trandafir, Dal Sun Kim and Steven F. Bartlett, who offered guidance and support. I gratefully acknowledge the Browning scholarship fund for providing financial assistance. Sincerest appreciation goes to Jeffrey C. Johnson and Robert W. Byrnes who helped me conduct laboratory experiments.

Finally, I really appreciate my wife, Dongmei, my son, Chenxi, who endured this long process with me, always offering support and love.

1. INTRODUCTION

Modern mining systems frequently use drill and blast techniques for rock excavation. For production, the primary objective is fragmentation. From a fragmentation viewpoint, the objective is to create the largest possible damage zone. On the other hand, at the perimeter of the excavation, there must be a protected zone in which the objective is just the opposite. Here, the optimum result is to create minimum damage from the explosives. This principle applies, for example, to the walls of drifts and other openings underground and the slopes of surface mines. Damage to the walls and slopes is termed unwanted damage or overbreak. The unwanted damage often results in higher mining costs and severe safety concerns.

Based on the studies of Holmberg (1993) and Persson et al. (1997), the phenomenon of damage results from induced strain ε for a one-dimensional wave, which for an elastic medium is given by the equation:

$$\varepsilon = \frac{\sigma}{E} \geq \frac{V_{\max}}{V_p} \tag{1.1}$$

where ε is induced strain.

σ is stress generated,

E is Young's modulus,

$V_{\max}$ is peak particle velocity, and

V_p is P-wave propagation velocity of the rock.

The studies conducted by the Swedish Detonic Foundation (Holmberg and Persson 1978) resulted in a damage model, wherein deformation is produced by the bending or stretching caused by vibration resulting from detonation. Holmberg (1993) concluded that rock mass damage is caused by:

- Near hole crushing due to high shock wave amplitudes
- Generation of radial cracks due to high-pressure in the drill hole
- Opening of existing joints caused by high-pressure gases produced from the detonation of explosives
- Fracturing by spalling
- Reduction of shear strength due to blast induced rock movement, and
- Vibration induced displacement affecting slope stability or tunnel perimeter integrity

Unwanted blast-induced damage assessment has a direct impact on safety, productivity, cost, and functioning of both surface and underground workings. Minimizing blast-induced damage results in the following benefits:

- Improved safety
- Reduction in support, scaling, and secondary blasting
- Prevention of damage to nearby structures by controlling ground vibrations
- Improved roof and wall stability
- Improved excavation rates
- Reduced overbreak, scaling, and costs related to removal of extra material

- Smooth walls help in reducing the frictional resistance to the flow of air thus improving mine ventilation
- Lower construction costs and
- Reduction in the amount of maintenance

Therefore, the reduction of unwanted damage is a major objective of rock blasting operations. To reduce unwanted damage, the ability to predict damage caused by rock blasting is essential. If a shock wave based technique can be developed and verified by comparison to laboratory or field results, it would provide a new approach to protect the integrity of rock surrounding mine openings. Unlike many of the existing blast design methods, the shock wave based approach includes the dynamic properties of the rock surrounding the borehole. The design procedure may be implemented through the use of charts, graphs, and/or a simple computer program. This is the main goal of this dissertation. The dissertation deals with three major aspects of developing a damage prediction model namely: theoretical research, experimental research, and validation of the model using laboratory and field results. The theoretical research includes calculation of stress and response of rock for fully-coupled and decoupled detonations using the theory of Shock Wave Transfer. This new procedure will be referred to as SWT. The SWT approach is based on shock wave mechanics (Cooper 1996; Henrych 1979). It is applied to estimate the detonation interactions between explosives and other materials, such as rock, air, concrete, steel, etc. The objective is to use the properties of explosives and rock materials to develop a reasonable prediction algorithm for estimating the extent of the damage zone caused by rock blasting. The experimental research includes determining the properties and detonation characteristics of explosives and the static and

dynamic properties of grout used to simulate rock materials. Validation of the model involves SWT estimates for the extent of damage compared to those found in the literature, determined by laboratory experiment, and observed in field tests.

Rigorous methods for predicting the damage radius presented in the literature require calculation of pressure exerted on the borehole wall. One method is presented by Hustrulid and Johnson (2008). It relies on modified gas laws and explosive properties only. The SWT method is an alternative approach which evaluates borehole pressure by considering both explosive properties and dynamic rock properties estimated from their static values. However, if the dynamic properties of the rock are available, the dynamic properties can be directly used in the program instead of using the static properties and the dynamic factors. As will be shown, damage predictions using the SWT method are in close agreement with Modified Ash Pressure-based, Modified Ash Energy-based, Holmberg Explosive Factor, and Sher Quasi-Static methods for rock properties similar to monzonite. After comparing SWT damage limits with other prediction procedures, laboratory measurements and field results, the conclusion is that SWT provides the basis for practical blast design which can account for the effect of dynamic rock properties on pressure developed within the borehole.

2. LITERATURE REVIEW

A review of published studies dealing with dynamic strength, models for predicting damage extent, and parameters used to indirectly measure damage will be presented in this chapter. Dynamic strength includes both compressive and tensile behavior. Various methods are then presented for predicting the extent of damage. These methods include empirical, numerical and experimental approaches. Finally, parameters used to indirectly assess damage will be summarized.

2.1 Dynamic Strength of Rock

As will be shown, rock exhibits different behaviors under different loading conditions. In other words dynamic rock properties are likely to be different than those determined under static loading conditions. The static properties of rock include the density (ρ_r), Young's modulus (E_s), Poisson's ratio (v_s), compressive strength (σ_c), and the tensile strength (σ_T). The dynamic properties of rock are Young's modulus (E_d), Poisson's ratio (v_d), compressive strength (σ_{cd}), tensile strength (σ_{Td}), P-wave velocity (V_p), and S-wave velocity (V_s). The dynamic rock Poisson's ratio and Young's modulus can be calculated using P-wave velocity and S-wave velocity under low stress:

$$v_d = \frac{V_p^{\,2} - 2V_s^{\,2}}{2(V_p^{\,2} - V_s^{\,2})} \tag{2.1}$$

$$E_d = \frac{V_p^{\,2}\rho_r(1+\nu_d)(1-2\nu_d)}{1-\nu_d} = 2V_s^{\,2}\rho_r(1+\nu_d) \qquad (2.2)$$

Starzec (1999) compared the static and dynamic Young's modulus for 300 samples of five types of rock based on Equation 2.2 and indicated that the dynamic Young's modulus is larger than the static modulus for rock materials. The experiments conducted by Starzec were performed at low stress levels (<0.1MPa).

2.1.1 Dynamic Compressive Strength of Rock

Under dynamic loading, the strength of rock is reported to vary with the rate of loading or strain rate. Generally, the dynamic strength of rock increases as the strain rate increases. Lankford (1981) presented the following relationship between the compressive dynamic strength (σ_{cd}) and strain rate by studying ceramics and rocks:

$$\sigma_{cd} \propto \varepsilon'^{\frac{1}{n+1}} \qquad (2.3)$$

where: ε' is the strain rate (shown as ε' in Figure 2.1), and n is a constant, dependent on the material.

There is a critical value for the strain rate ε'^{*}, at which the dynamic strength of rock appears to increase dramatically. The critical strain rate is usually on the order of $10^2 - 10^3$ /sec. When $\varepsilon' < \varepsilon'^{*}$, n will be a large value; n is 144 for the Soenhofen Limestone. When $\varepsilon' > \varepsilon'^{*}$, n will be a small value, n is 2.2 for the Soenhofen Limestone. The dependence of compressive strength on strain rate is shown in Figure 2.1 for Solenhofen limestone as an example. Blanton (1981) compiled data from many researchers, shown in Figure 2.2. The shape of the curves strongly suggests two different

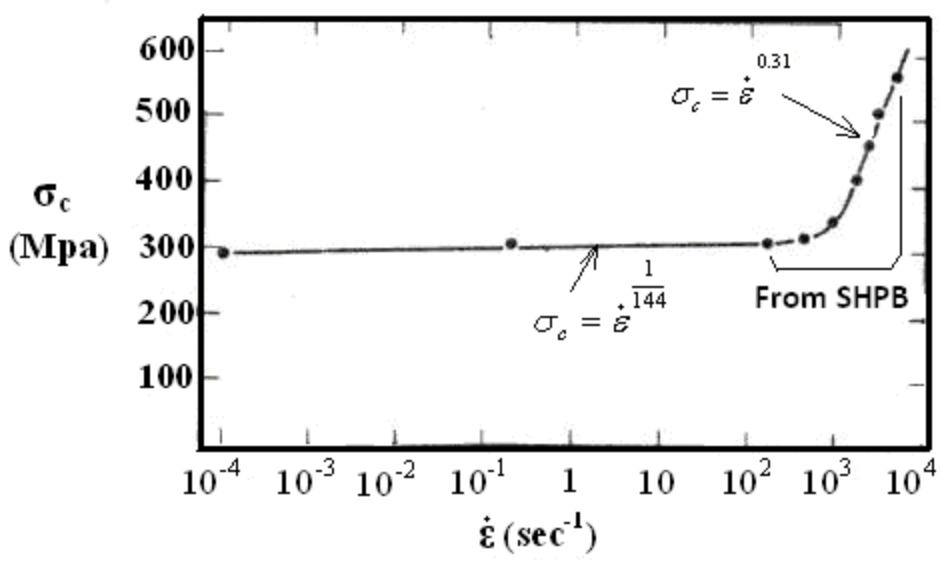

Figure 2.1. Compressive strength with strain rate
for Solenhofen limestone, modified from Lankford (1981)

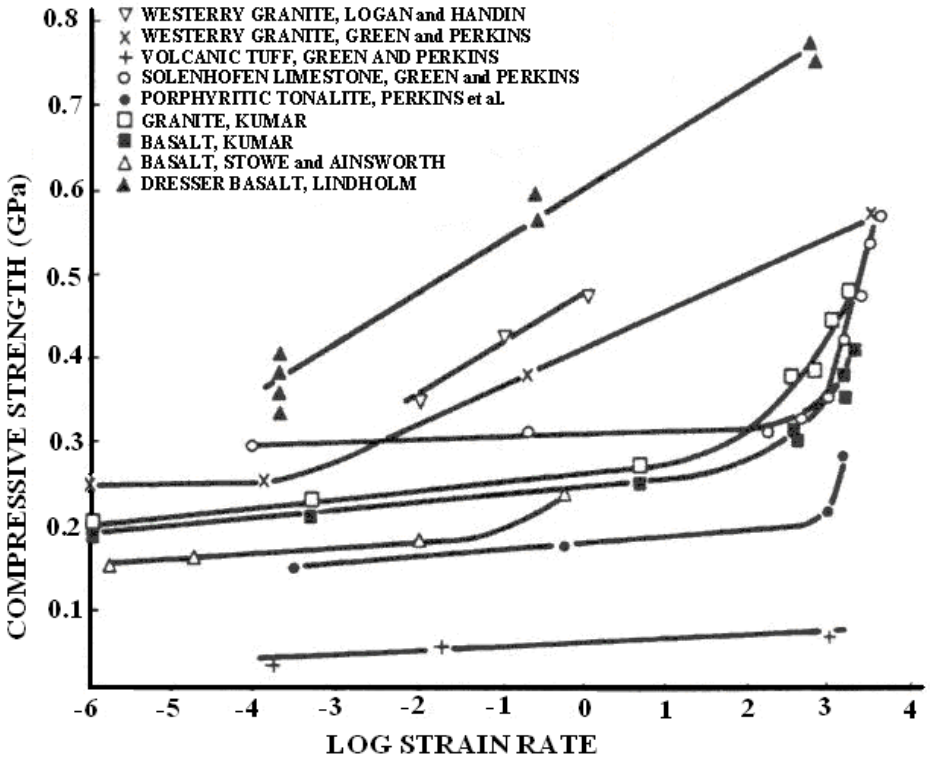

Figure 2.2.The relationships between compressive strength and strain rate from early researchers, Blanton (1981), reprinted by permission of Elsevier

behaviors. The data suggest little or no change in strength as the strain rate increases to the critical value (from 10^{-4} to 10^{2}/s). Thereafter, there is an abrupt increase in strength as the strain rate increases (10^{2}/s and higher). In investigating the testing methods, it is apparent that the two characteristics correspond to the testing method. The low and medium strain rates were obtained using a screw-driven, gas ram, or hydraulic ram testing machine. The high strain rates were obtained using a Split Hopkinson Pressure Bar (SHPB). Assuming that the increase in strength for the strain rate > 10^{2}/s is not an artifact of the testing method, Figure 2.2 indicates the dynamic compressive strength of rocks is on the order of 1.5-2.5 times the static compressive strength when the strain rates are in the range of 10^{2}-10^{4}/sec. Prasad (2000) presented the damage classification based on the strain rate, shown in Table 2.1.

The examples are static damage (low strain rate) in tension or compression, medium strain rate dynamic damage in crushing or grinding, and high strain rate dynamic damage in blasting, respectively. For rock blasting operations, the strain rate around the borehole is about 10^{2}-10^{4}/sec. The data obtained by Prasad (2000) represents the dynamic and static compressive strengths for 12 types of rock. The dynamic compressive strength was tested using SHPB. The diameter of test specimen for the dynamic compressive tests was 8-9 mm. For comparison, the static compressive strength was also measured in the same rock types with samples of identical dimensions as those employed in the dynamic measurements. A minimum of 8 to 12 samples were tested in each case. The strain rate during the dynamic tests was on the order of ~10^{3} /sec. The average value for static and dynamic compressive strengths, their standard deviations, and the ratio of dynamic strength over the static values measured in the laboratory are shown in Table 2.2. The dynamic strength was found to be

Table 2.1. Loading strain rate for different damage processes, modified from Prasad (2000)

Property	Low strain rate	Medium strain rate	High strain rate
Strain rate (Sec^{-1})	$< 10^{-6} – 10^{-4}$	$10^{-4} – 10$	$< 10 – 10^{4}$
Type of stress	Static load	Mechanical load	Impact or explosion
Example	Static standard test	Crushing &grinding	Blasting

Table2.2. Comparison of dynamic and statie compressive strengths with their standard deviation, modified from Prasad (2000)

Rock type	Static compressive strength (MPa)	Dynamic compressive strength (MPa)	The dynamic factor
Stanstead granite	48±13	160±27	3.3
Altered marble	185±42	459±50	2.5
Kingston limestone	83±27	316±65	3.8
Gneiss	40±20	122±25	3.1
Vineland limestone 1	77±31	272±59	3.5
Marble	32±9	128±14	4
Gneissic marble	34±13	153±32	4.5
Laurentian granite	67±17	245±36	3.7
Quartz	67±17	281±65	4.2
Granite	61±16	241±21	4
Gneissic granite	52±13	238±27	4.6
Vineland limestone 2	49±8	147±20	3

significantly higher than its static value. For the dynamic strain rate employed (~10^{3}/sec), the dynamic factor, the ratio of the dynamic to static value, ranged between 2.5 to 4.6.

2.1.2 Dynamic Tensile Strength of Rock

The magnitudes of dynamic tensile strengths of rocks increase as the strain rates increase. Figures 2.3 and 2.4 present the dynamic tensile strength of rocks as a function of the strain rates (Cho et al. 2003). As can be seen, the curves are similar to those for dynamic compressive strength. However, beyond the critical strain rate, the rate of increase in dynamic tensile strength of rock is greater than that for dynamic compressive strength. In Figures 2.3 and 2.4, the flat lines were obtained by the static Brazilian

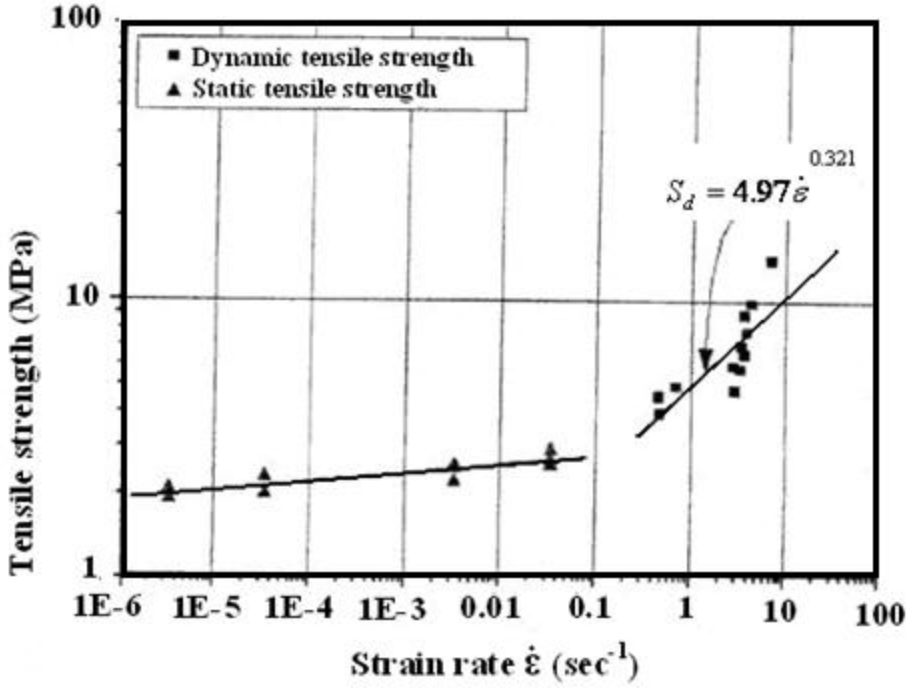

Figure 2.3. Dynamic tensile strength as the function of the strain rates for Inada granite, Cho et al. (2003), reprinted by permission of Elsevier

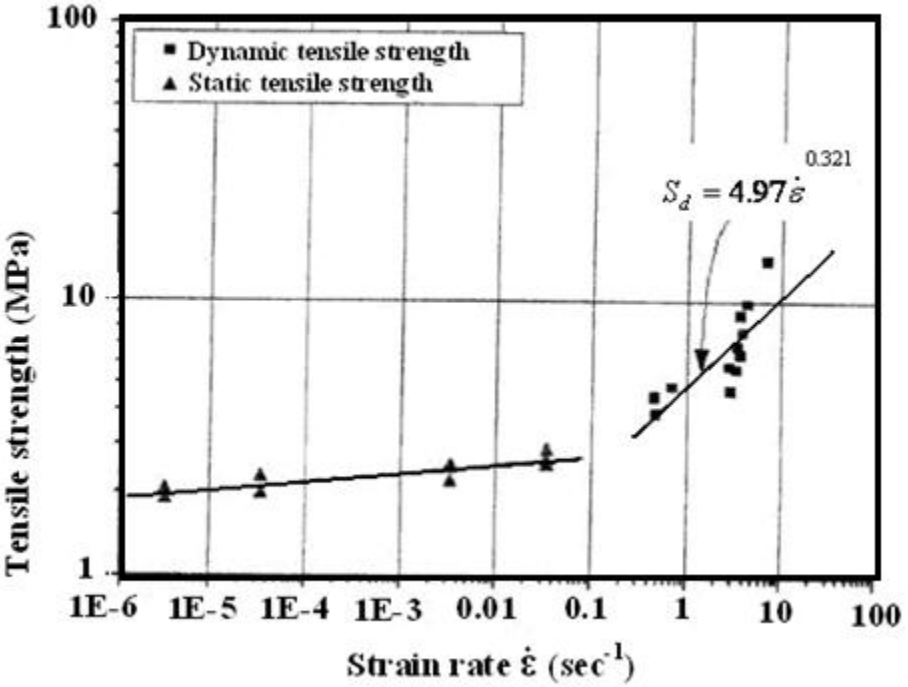

Figure 2.4. Dynamic tensile strength as the function of the strain rates for Tage tuff, Cho et al. (2003), reprinted by permission of Elsevier

method and the steep lines were obtained by using a SHPB. Available data obtained by Rinehart (1965), Bacon (1962) and Cho et al. (2003) for eight kinds of rock are shown in Table 2.3. Rinehart determined the dynamic tensile strengths of rocks using the Rinehart pellet technique (Rinehart 1965). This method involves generation of a dynamic pulse from an explosive cap placed on one side of a thin plate of rock and measurement of the velocity of the pellet ejected on the opposite side of the thin plate. Bacon determined the dynamic tensile strengths of rocks using a pendulum impact technique. Cho et al. used the SHPB method for measuring the dynamic tensile strengths of rocks. Based on their results, the dynamic tensile strengths are 2.1-13 times the static tensile strengths.

2.2 Borehole Pressure

Borehole pressure (P_h) is the starting point for many blast design calculations. For the fully-coupled condition, Hino (1956) presents the following equation to determine the pressure (P) at any point (r) distance from the center of a borehole:

$$P = P_h(\frac{a}{r})^n \tag{2.4}$$

where: n is the pressure decay constant,

Table 2.3. Comparison data of dynamic and static tensile strength of rocks

Rock	Dynamic tensile strength (MPa)	Static tensile strength (MPa)	The dynamic factor	Reference
Bedford limestone	26.8	4.1	6.5	Rinehart 1965
Yule Marble	48.2	6.2	7.8	Rinehart 1965
Granite	39.3	6.9	5.7	Rinehart 1965
Taconite	91	4.8-7	13	Rinehart 1965
Basalt	20	9.6	2.1	Bacon 1962
Freda sandstone	9.3	4.5	2.1	Bacon 1962
Inada granite	35	5	7	Cho et.al. 2003
Tage tuff	10	2	5	Cho et.al. 2003

a is the radius of the spherical charge,

r is distance, and

P_h is borehole pressure (assumed equal to detonation pressure).

Many researchers used Equation 2.4 or similar equations to predict the pressure in the medium around boreholes. However, the value of P directly depends on the assumed value of P_h. Several ways to estimate borehole pressure with fully-coupled condition may be found in the literature, and they are summarized below:

1) Using detonation pressure as the borehole pressure, Hino (1956) defines the borehole pressure for a spherical charge as:

$$P_h = P_{CJ} = \frac{1}{1+\gamma}\rho_0 D^2 \tag{2.5}$$

where: D is velocity of detonation (VOD),

P_{CJ} is the detonation pressure,

ρ_o is the density of the explosive, and

γ is the isentropic exponent.

2) Cook (1958) estimates the borehole pressure for a cylindrical charge as one half of the detonation pressure:

$$P_h = \frac{1}{2}P_{CJ} \tag{2.6}$$

This definition is also referred to as the "explosion pressure" (Hustrulid 1999). Subsequent references to explosion pressure in this dissertation will follow this definition.

3) Based on stress wave propagation, Dai (2002) describes the borehole pressure for both spherical and cylindrical charges by the following equation:

$$P_h = \frac{2}{1+n_z} P_{CJ} \tag{2.7}$$

where: n_z is ratio of impedance of explosive to rock.

$$n_z = \frac{\rho_0 D}{\rho_r V_p} \tag{2.8}$$

4) Based on the hydrodynamic method and regression analysis of modeling results, Liu (1991, 2002) provides a means for calculating the borehole pressure for a cylindrical charge:

$$P_h = 1.62(\rho_o D^2)(\frac{\rho_r V_p}{\rho_o D})^{\frac{1}{4}} \tag{2.9}$$

where: ρ_r is density of the rock.

Equation 2.9 is presented in the publication but numerical results presented indicate the constant 1.62 in Equation 2.9 should be 0.162.

5) Based on adiabatic transfer of shock wave from borehole to rock, Borovikov and Vanyagin (1995) estimate the borehole pressure for both spherical and cylindrical charges when $\rho_r V_p > \rho_o D$ by the following equations:

$$\left\{\frac{P_h}{\rho_r}\left[1-\frac{1}{\left(A\frac{P_h}{\rho_r V_p{}^2+1}\right)^{1/m}}\right]\right\}^{1/2} = V_{CJ} - \frac{(P_h - P_{CJ})\sqrt{2\gamma}}{\sqrt{\rho_o(\gamma-1)[(\gamma+1)P_h+(\gamma-1)P_{CJ}]}} \quad (2.10)$$

where: A and m are coefficients for the shock wave adiabatic process,

A=5.5,

m=5, when $0.1<P_h/(\rho_r C_r^2)<35$, and

V_{CJ} is the particle velocity in the detonation wave.

Summarizing all five methods for borehole pressure estimation, the first method uses detonation pressure, the second assumes borehole pressure is one half of the detonation pressure and is the most popular assumption in rock blasting. However, the effect of the shock wave is not involved in these two methods. The value of borehole pressure only depends on the properties of the explosive. The third method is based on the stress wave propagation but also neglects the effect of the shock wave. The fourth method and the fifth method are based on the shock wave transfer. All shock wave parameters, such as shock wave pressure, shock wave velocity, and peak particle velocity can be estimated with these two methods. In these cases, the value of borehole pressure depends on the properties of the explosive and the properties of surrounding rock.

2.3 Damage Extent Models

To predict the extent of damage for rock blasting, several approaches are currently available. They are described in the following sections.

2.3.1 Holmberg-Persson Approach

Holmberg and Persson (1978) used the following general equation:

$$V = K\frac{W^{\alpha}}{R^{\beta}} \tag{2.11}$$

where: K,α,β are empirical constants,

V is peak particle velocity (PPV),

W is charge weight units, and

R is distance units from charge.

Equation 2.11 was originally derived and tested at long distances from the charge by the U.S. Bureau of Mines as a scaled-distance equation to predict the damage on residences caused by blasting (Devine et al. 1965; Devine et al. 1966; Duvall and Fogelson 1962; and Duvall et al. 1963). Because R is generally very large, the charge dimensions can be ignored. The charge is usually assumed to be of spherical shape. However, at locations close to the charge, the charge dimensions must be taken into account. Most borehole charges in mining and construction are cylindrical. To solve this problem, Holmberg and Persson (1978) assumed that the entire charge length detonates instantaneously. They divided the overall cylindrical charge into a series of small pieces each having a length of dx and linear charge concentration of q (kg/m) in the direction of the borehole. The PPV at any point, for example, (r_o, x_o) shown in Figure 2.5, can be expressed as Equation 2.12:

$$V = K\left[q\int_{T}^{H+J}\frac{dx}{\left[r_o^{\,2}+(x-x_o)^2\right]^{\beta/2\alpha}}\right]^{\alpha} \tag{2.12}$$

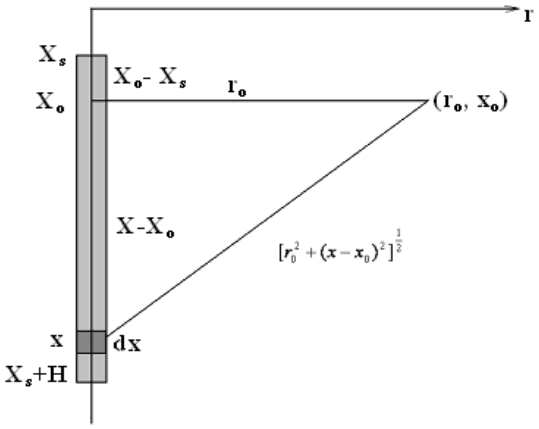

Figure 2.5. Integration over charge length to calculate the PPV at an arbitrary point. Modified from Persson et al. (1993)

where: *T* is stemming depth (m),

H is charge length (m), and

J is subdrill (m).

The exponent α, was then assumed to be:

$$\alpha = \frac{\beta}{2} \tag{2.13}$$

After integrating, the PPV can be expressed as:

$$V = K\left\{\frac{q}{r_o}\left[\tan^{-1}\left(\frac{H + J - x_o}{r_o}\right) - \tan^{-1}\left(\frac{T - x_o}{r_o}\right)\right]\right\}^{\alpha} \tag{2.14}$$

The values *K, α, β* are given the values of 700, 0.7 and 1.4 respectively for hard rock masses. Design charts are presented for both underground tunnel blasting, (Figure 2.6) and surface bench blasting, (Figure 2.7). The critical PPV of rock damage is 700-1000 mm/s, based on Table 2.3. In Figures 2.6 and 2.7, curves represent the loading density in

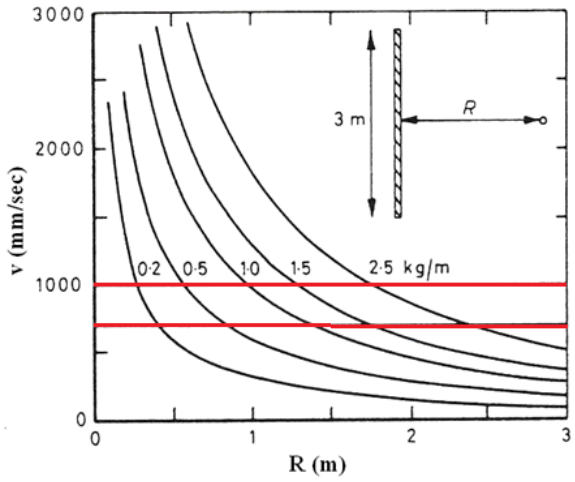

Figure 2.6. Estimated PPV as a function of distance for different linear charge densities in underground tunnel blasting, Persson et al. (1993), modified Rock Blasting & Engineering

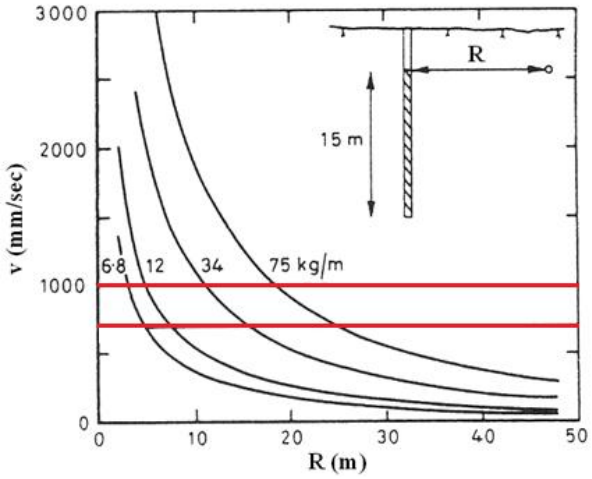

Figure 2.7. Estimated PPV as a function of distance for different linear charge densities in surface bench blasting, Persson et al. (1993), modified from Rock Blasting & Engineering

the borehole. PPV is represented by *v*, and *R* is the distance from the charge. When given the loading density in the borehole, PPV created by a blast in rock can be determined by Figure 2.6 or 2.7. Finally, a damage zone can be determined assuming damage occurs where the PPV exceeds the critical value listed on Table 2.4. This is a convenient approach for design application. However, there are some issues in the calculation.

- Hustrulid and Lu (2002) identified a mistake in Equation 2.12. It should be:

$$V = Kq^{\alpha} \int_{T}^{H+J} \left[\frac{dx}{\left[r_o^{\,2} + (x - x_o)^2 \right]^{\beta/2\alpha}} \right]^{\alpha} \tag{2.15}$$

  Obviously Equation 2.15 cannot be analytically integrated.

- Using a similarity analysis, a cylindrical charge can be treated as a two-dimensional problem assuming a cylindrical charge of unit length. With these assumptions, the weight of the explosive is

$$W = \pi R_o^{\,2} \rho_o \tag{2.16}$$

  where: R_o is radius of the borehole and ρ_o is density of the explosive.

  So, Equation 2.11 can be expressed as:

$$V = K(\pi \rho_o)^{\alpha} \frac{R_o^{\,2\alpha}}{R^{\beta}} \tag{2.17}$$

Table 2.4. PPV with damage and fragmentation effects in hard Scandinavian bedrock*, modified from Persson (1997)

PPV (m/s)	Tensile stress (MPa)	Strain energy (J/kg)	Typical effect in hard Scandinavian bedrock
0.7	8.7	0.25	Incipient swelling
1	12.5	0.5	Incipient damage
2.5	31.2	3.1	Fragmentation
5	62.4	12.5	Good fragmentation
15	187	112.5	Crushing

*For hard Scandinavian bedrock, density ρ_r=2600 kg/m^3, V_p=4800 m/s, E=60 GPa

for,

$$\alpha = \frac{\beta}{2},$$

Equation 2.17 becomes:

$$V = K_o(\frac{R_o}{R})^{\beta} \tag{2.18}$$

where: K_o is the particle velocity on the borehole wall which is constant.

$$K_o = K(\pi\rho_o)^{\frac{\beta}{2}}$$

Because the problem is two-dimensional (the length in the axial direction of the charge is infinite). Therefore, it is not necessary to integrate along the entire length.

A spherical charge can be treated as a three dimensional problem. The weight of the charge is:

$$W = \frac{4}{3}\pi R_o^{\ 3}\rho_o \tag{2.19}$$

Equation 2.11 can now be written as:

$$V = K(\frac{4}{3}\pi\rho_o)^{\alpha}\frac{R_o^{3\alpha}}{R^{\beta}} \tag{2.20}$$

If,

$$\alpha = \frac{\beta}{3},$$

Then Equation 2.20 becomes:

$$V = K_o(\frac{R_o}{R})^{\beta} \tag{2.21}$$

where: R_o is the radius of the spherical cavity and

K_o is constant, namely the particle velocity on the cavity wall,

$$K_o = K(\frac{4}{3}\pi\rho_o)^{\frac{\beta}{3}}$$

Because the problem is a three-dimensional one, it is reasonable to integrate along the axial direction of the entire charge. However, the relationship of α and β is different.

- The derivation of Equation 2.12 does not take into account that the PPV is a vector.
- The assumption of the entire charge length detonating instantaneously is not true.
- Using only the weight of the explosive is not enough to represent the properties of the explosive.

- A number of field tests must be run to determine the parameters, K, α and β.
- Evaluation of these constants is based on experimental data regression. There is no logical basis for their derivation based on explosive and rock properties.

2.3.2 SveBeFo Approach

SveBeFo, Swedish Rock Engineering Research Organization, has conducted research for many years on crack generation in rock surrounding a blasted excavation. In contour blasting of tunnels, Järnvägs (1996), offered the following:

- Gentle contour blasting limits damage to a depth allowed by the design.
- Fracturing from stoping and helper holes which are located inside the contour holes must not extend farther into the remaining rock than that produced by the charges in the contour row.
- Microcracks produced by blasting may extend beyond the allowed damage zone.

In the SveBeFo approach, the damage zone is defined as the crack zone. In rock blasting operations, a few or many cracks are driven from the borehole into the rock. The most common theory of crack generation includes two stages. First, the shock wave causes radial cracks to form around the borehole. Second, the gases from blasting penetrate into the cracks to widen and make them longer (Langefors and Kihlstrom 1973). Brinkmann (1987, 1990), suggests that damage produced by blasting is primarily controlled by shock, and that gas penetration is the mechanism controlling breakout of the burden. His conclusions are:

- Gas penetration is the dominant mechanism controlling fragment velocities
- Breakout is controlled by gas penetration, and fragment size is governed by shock

To predict the damage zone, Ouchterlony (1997) gives an equation for the radial crack length:

$$2\frac{R_{co}}{d_h} = \left(\frac{P_h}{P_{h,crack}}\right)^{2/(3(\frac{D}{c})^{0.25}-1)} \tag{2.22}$$

where: $P_{h,crack}$ is the experimental value of borehole critical pressure or

$$P_{h,crack} = 3.30\frac{K_{IC}}{\sqrt{d_h}}, \tag{2.23}$$

Ouchterlony (1997) also defines the borehole pressure P_h as:

$$P_h = \frac{\gamma^{\gamma}\rho_o}{(\gamma+1)^{\gamma+1}} D^2 \left(\frac{d_e}{d_h}\right)^{2.2}, \tag{2.24}$$

d_e is diameter of explosive,

d_h is diameter of borehole,

γ is isentropic exponent for a given explosives, 1.254-2.145,

R_{co} is the uncorrected radius of the crack zone,

c is speed of sound in the rock,

K_{IC} is fracture toughness of the rock, and

D is velocity of detonation (VOD).

In Equation 2.24, the decoupling exponent (2.2) was empirically determined. Later Ouchterlony et al. (2002) refined the process by applying adjustment factors:

$$R_c = R_{co}F_hF_tF_rF_b \tag{2.25}$$

where: R_c is the corrected damage zone radius,

F_h is correction for hole spacing,

F_t is correction for time spread in initiation,

F_r is correction for wet holes, and

F_b is correction for fracturing.

The derivation is based on fracture mechanics and is difficult for design engineers to follow. The parameter, K_{IC}, fracture toughness of the rock, is difficult to determine, particularly for weak rocks, and multiple "correction" coefficients may actually make predictions more complicated.

2.3.3 CSM Approach

The following approach was developed at the Colorado School of Mines (CSM). It is based on the particle velocity arising from the detonation of a spherical charge in an infinite, isotropic and homogeneous medium as presented by Favreau (1969):

$$V = e^{\frac{-\alpha^2 \tau}{\rho_r V_p r_h}} \left[\frac{P\, r_h{}^2 V_p}{\alpha \beta R^2} - \frac{\alpha P\, r_h}{\beta \rho_r V_p R} \sin \frac{\alpha \beta t}{\rho_r} + \frac{P\, r_h}{\rho_r V_p R} \cos \frac{\alpha \beta t}{\rho_r V_p r_h} \right] \tag{2.26}$$

where:

$$\alpha = \sqrt{\frac{2(1-2\nu)\rho_r V_p{}^2 + 3(1-\nu)\gamma P}{2(1-\nu)}}, \tag{2.27}$$

$$\beta = \sqrt{\frac{2\rho_r V_p{}^2 - 3(1-\nu)\gamma P}{2(1-\nu)}}, \tag{2.28}$$

V is peak particle velocity,

t is time,

P is explosion pressure,

τ is retarded time, the time to transmit the shock wave from detonation point to the point considered,

$$\tau = t - (R - r_h)/V_p$$

R is distance,

V_p is longitudinal wave speed,

r_h is radius of borehole,

γ is isentropic exponent,

ρ_r is density of rock, and

v is Poisson ratio.

Hustrulid et al. (1992) introduced a simplified equation for determining PPV for a cylindrical charge in an inelastic attenuating rock mass:

$$V = \frac{1.2247P\ r_h e^{-I(R-1.2247r_h)}}{\rho V_p R} \tag{2.29}$$

where: I is the inelasticity coefficient.

This approach considers a cylindrical charge to be divided into a chain of spherical charges with a diameter equal to the equivalent borehole diameter. Hustrulid et al. (1992) assumed that each spherical charge acts independently in producing peak particle velocity at a given point. In this approach, a number of field tests must be

conducted to determine the inelasticity coefficient (I). The explosion pressure (P) is used as the borehole pressure (P_h):

$$P_h = \frac{1}{2} P_{CJ} \tag{2.30}$$

where: P_{CJ} is the detonation pressure.

The explosion pressure is much lower than the shock wave pressure on the borehole.

2.3.4 Hustrulid-Lu Approach

Hustrulid and Lu (2002) presented a new hybrid approach for PPV (V):

$$V = k \frac{\rho_o D^2}{2(\gamma+1)\rho_r V_p} R_r{}^{2\gamma} (\frac{r_h}{R})^{\alpha} \tag{2.31}$$

where: k, α are constants, and R_r is the ratio of the diameter of the explosive to the diameter of the borehole.

When considering the borehole pressure as:

$$P_h = \frac{P_{CJ}}{2} (\frac{d_e}{d_h})^{2\gamma} \tag{2.32}$$

and

$$P_{CJ} = \frac{1}{1+\gamma} \rho_0 D^2 \tag{2.33}$$

then Equation 2.31 can be written as:

$$V = k\frac{P_h}{\rho_r V_p}\left(\frac{r_h}{R}\right)^{\alpha} \tag{2.34}$$

Equation 2.34 is similar to Equation 2.29. The only difference is the attenuation formulations. In addition, the relationship for the decoupling factor expressed in Equation 2.32 has been revised (Hustrulid and Johnson 2008) using an isothermal approach.

2.3.5 Russian Approach

Drukovanyi et al. (1976) theoretically derived the extent of the crush zone (R_{crush}) and fracture zone (R_c) for a specific rock by the following equations:

$$R_{crush} = r_h\left(\frac{P_h}{-\frac{C}{f}+(\sigma_c+\frac{C}{f})L^{\frac{f}{1+f}}}\right)^{\frac{1}{2\gamma}}\sqrt{L} \tag{2.35}$$

where: C is cohesion,

f is coefficient of internal friction, $f = tan\varphi$,

φ is internal friction angle,

σ_c is uniaxial compressive strength,

L is a constant defined by:

$$L = \frac{\mu}{\sigma_c\left(1+\ln\frac{\sigma_c}{\sigma_T}\right)} \tag{2.36}$$

where: σ_T is tensile strength, and

$$\mu = \frac{E}{1+\nu}$$

Then, the fracture zone can be expressed as:

$$R_c = (\frac{\sigma_c}{\sigma_T})R_{crush} \tag{2.37}$$

Drukovanyi reports that the extent of damage predicted using this approach is higher than observed in practice for those rocks whose compressive strength is less 100 MPa.

2.3.6 Modified Ash Approach

Hustrulid (2010) used Ash's (1963) classic approach to develop the extent of damage based on explosive energy

$$\frac{R_d}{r_h} = 25\left(\frac{d_e}{d_h}\right)\sqrt{\frac{\rho_o S_{ANFO}}{\rho_{ANFO}}}\sqrt{\frac{2.65}{\rho_r}} \tag{2.38}$$

where: R_d is the radius of damage zone,

S_{ANFO} is the weight strength of the explosive relative to ANFO, and

ρ_{ANFO} is the density of ANFO, and

ρ_e is the density of the explosive

Hustrulid (2010) also developed the extent of damage based on borehole pressure

$$\frac{R_d}{r_h} = 25\sqrt{\frac{P_h}{1300}}\sqrt{\frac{2.65}{\rho_r}} \tag{2.39}$$

assuming a detonation velocity of 3500 m/sec and a density of 0.85 g/cc.

2.3.7 Rock Constant Approach

Hustrulid (2010) presents the Rock Constant Approach based on Holmberg's (1982) paper on calculating charges for tunneling.

$$\frac{R_d}{r_h} = 14.3\left(\frac{d_e}{d_h}\right)\sqrt{\frac{RBS}{EF_t(f)}} \tag{2.40}$$

where: *RBS* is relative bulk strength (compared to ANFO),

EF_t is explosive factor measured in terms of kilograms of explosive per metric ton of rock, and

f is fixation factor which refers to the degree of hole confinement, 0.6 to 1.45.

2.3.8 Neiman Hydrodynamic Approach

Based on hydrodynamics (Hustrulid 1999), Neiman obtained the following equations for particle velocity in the surrounding rock oriented at right angles to the axis of a cylindrical charge and located at midlength of the explosive charge:

$$V_h = \frac{1}{\rho}\sqrt{\frac{\rho_{qe} q}{8\rho_r}} \tag{2.41}$$

where: ρ_{qe} is equivalent explosive density,

ρ_r is density of rock,

q is explosive energy/unit mass, and

$$\rho = \frac{\frac{R}{d_h}\sqrt{\ln\frac{\frac{L}{d_h}+\sqrt{1+(\frac{L}{d_h})^2}}{-\frac{L}{d_h}+\sqrt{1+(\frac{L}{d_h})^2}}}\sqrt{(\frac{R}{d_h})^2+\frac{(\frac{L}{d_h})^2}{4}}}{\frac{L}{d_h}} \tag{2.42}$$

where: R is radial distance from the charge axis, and L is charge length.

The particle velocity (V_h), where compressive stress equals the compressive strength, defines the conditions at the limit of the damage zone.

$$V_h = V_p \frac{\sigma_c}{E} \tag{2.43}$$

Combining Equations 3.41 through 3.43 allows determination of the radius of the damage zone R.

2.3.9 NIOSH Stress Decay Approach

This approach was developed at the Spokane Research Lab, NIOSH (Johnson 2010). In his approach, five zones are presented. They are the explosive zone, the borehole decoupled zone, the crush zone, the crack zone (also described as transition zone), and the no-damage zone (also described as seismic zone). The extent of the crush zone for a cylindrical charge is described in Equation 2.44:

$$\sigma_{cd} = P_h \sqrt{\frac{r_h}{R_{crush}}} e^{-(R_{crush}-r_h)\lambda} \tag{2.44}$$

where: R_{crush} is the extent of the crush zone, and λ is the crush damage decay constant (determined by laboratory experiment).

The extent of the crack zone is presented in Equation 2.45.

$$\sigma_{trans} = \sigma_{cd}\sqrt{\frac{R_{crush}}{R_{trans}}}e^{-(R_{trans}-R_{crush})\beta} \tag{2.45}$$

where: R_{trans} is the extent of transition zone,

β is the transition damage decay constant, and

σ_{trans} is the dynamic strength of rock in the transition zone.

The ability to calculate the extent of crushing and cracking provides a means to determine how far into the rock mass damage can be expected.

2.3.10 NIOSH Modified Holmberg Persson Model

The difficulty in mathematically integrating Equation 2.15 was simplified by assuming an average distance from an arbitrary point to the center of the charge (Iverson et al. 2008). This average distance, R_{ave}, is determined by Equation 2.46.

$$R_{ave} = \frac{1}{L}\int\left[(x-x_0)^2 + (r-r_0)^2\right]^{1/2}dx \tag{2.46}$$

where: L is charge length x_f-x_i [previously defined as the integration limits (H+J) – T in Equation 2.12] .

Knowing R_{ave} it is thus possible to determine the peak particle velocity, and using the damage criteria established by Holmberg and Persson, the extent of the damage zone surrounding a cylindrical charge can be estimated.

2.3.11 Sher Quasi-Static Approach

Sher and Aleksandrova (1997 and 2007) developed the prediction model for damage zones surrounding a cylindrical charge assuming equilibrium between borehole pressure and stress in the surrounding rock. This dynamic process is approximated by a quasi-static approach. The following equations are used to determine the radius of the damage zone for a cylindrical charge:

$$\left(\frac{Y}{E\alpha}-\frac{q}{E}\right)\left(\frac{R_d}{r}\right)^{\alpha/(1+\alpha)}-\frac{Y}{E\alpha}-\frac{P_h}{E}=0 \tag{2.47}$$

$$\frac{q}{E}=-\frac{\frac{\sigma_c}{E}+2\left(\frac{\sigma}{E}(\frac{\sigma_c}{\sigma_T})\right)}{1+\left(\frac{\sigma_c}{\sigma_T}\right)} \tag{2.48}$$

$$\frac{u_b}{r_h}=-(1+\nu)\frac{R_d}{r_h}\frac{\left[q+2\sigma(1-\nu)\right]}{E} \tag{2.49}$$

$$\left(\frac{r}{r_h}\right)^2-1=\left(\frac{R_d}{r_h}\right)^2-\left(\frac{R_d}{r_h}-\frac{u_b}{r_h}\right)^2 \tag{2.50}$$

$$\frac{P_h}{E}=\frac{P_{CJ}}{E}\left(\frac{r}{r_h}\right)^{-2\gamma_1}, \quad r\leq r^* \tag{2.51}$$

$$\frac{P_h}{E}=\frac{P_{CJ}}{E}\left(\frac{r^*}{r_h}\right)^{-2\gamma_1}\left(\frac{r^*}{r_h}\right)^{-2\gamma_2}, \quad r\geq r^* \tag{2.52}$$

where: $\alpha=\dfrac{2\sin\varphi}{1-\sin\varphi}$,

$$Y = \frac{2c\cos\varphi}{1-\sin\varphi},$$

c is cohesion,

φ is angle of internal friction,

r_h is initial hole radius,

r is final hole radius,

u_b is elastic deformation of rock,

$\frac{r}{r_h}$ is radius ratio of final radius and initial radius of hole.

r^* is radius at which the adiabatic constant changes,

γ_1 is initial adiabatic expansion constant, 3, and

γ_2 is final adiabatic expansion constant, 1.27.

Hustrulid (2010) summarizes the following calculation procedure to obtain the radius of the damage zone.

1. Calculate $\frac{q}{E}$ with Equation 2.48.
2. Make a guess of $\frac{R_d}{r_h}$.
3. Calculate $\frac{u_b}{r_h}$ by substituting $\frac{q}{E}$ and $\frac{R_d}{r_h}$ into Equation 2.49.
4. Calculate $\frac{r}{r_h}$ by substituting $\frac{u_b}{r_h}$ into Equation 2.50.
5. Compare $\frac{r}{r_h}$ with $\frac{r^*}{r_h} = 1.89$ and choose Equation 2.51 or 2.52 to calculate $\frac{P_h}{E}$ 6.

6. Substitute $\frac{P_h}{E}$ into Equation 2.47 and examine whether the equality is achieved.

   If the equality is achieved, $\frac{R_d}{r_h}$ is the final result. If not, repeat from step 2 to 6 until the final result is obtained.

2.3.12 Hustrulid Approach

Hustrulid (1999) analyzes the energy and work done by detonating a borehole charge.

1. The radial stresses can be high enough in comparison to the rock compressive strength and produce compaction or compressive failure of the borehole wall.
2. Due to the applied radial pressure, the circumference of the borehole is stretched to the point that radial cracks develop in tension.
3. A combination of 1 and 2.

He gives a prediction of the number of cracks as:

$$T_o n = \frac{P_h(1+\nu)}{E}\left(\frac{r_h}{R_c}\right)^2 \tag{2.53}$$

where: T_o is critical strain,

n is number of cracks,

P_h is borehole pressure,

E is Young's modulus,

ν is Poisons ratio,

r_h is borehole radius, and

R_c is Maximum crack length.

The maximum velocity of crack extension is:

$$V_{crac} = 0.38 c_R \tag{2.54}$$

where: c_R is speed of sound in rock.

2.3.13 McHugh Approach

McHugh (1983) points out that the effect of internal gas pressurization predominates over the effect of tensile stresses in extending cracks into the surrounding rock. He gives the following equation for estimating the crack length for a cylindrical charge:

$$R_c^{(2-1/2\gamma)} + (\frac{2V_b}{n\pi w}) R_c^{-(1/2\gamma)} - (\frac{2V_b}{n\pi w})(\frac{2P_h}{\sqrt{\pi} K_{IC}})^{1/\gamma} = 0 \tag{2.55}$$

where: R_c is crack length,

V_b is borehole volume,

P_h is borehole pressure,

$$P_h = \frac{P_{CJ}}{2} (\frac{d_e}{d_b})^{2\gamma}, \tag{2.56}$$

P_{CJ} is pressure on the CJ front,

d_e is diameter of explosive,

d_b is diameter of borehole,

γ is the ratio of specific heats of the gas, γ=1.3,

n is number of cracks of width w,

K_{IC} is fracture toughness of the rock, and

w is crack width.

This approach is based on fracture mechanics in metals. For rock, the parameters, $K_{IC,}$ n, and w, are hard to obtain, especially for weak rocks.

2.3.14 Mosinets Approach

Mosinets et al. (1972) give the following relationship for calculating the radius of the crack zone R_c and the radius of the crush R_{crush} zone for a spherical charge:

$$R_c = \sqrt{\frac{V_p}{V_s}}\sqrt[3]{q} \tag{2.57}$$

$$R_{crush} = \sqrt{\frac{V_s}{V_p}}\sqrt[3]{q} \tag{2.58}$$

where: V_p is longitudinal wave velocity,

V_s is transverse wave velocity, and

q is weight of explosive.

2.3.15 Senuk Approach

Senuk (1979) predicts the radius of the crack zone for a cylindrical charge using the following relationship:

$$R_c = kr_h\sqrt{\frac{P_h}{\sigma_T}} \tag{2.59}$$

where: k is a factor allowing for stress concentration in sharp cracks or joints

(usually k =1.12),

P_h is the borehole pressure, the explosion pressure previously defined, and

σ_T is tensile strength of rock.

2.3.16 Kanchibotla Approach

Kanchibotla et al. (1999) estimate the radius of the crush zone for a cylindrical charge with the following equation:

$$R_{crush} = r_h \sqrt{\frac{P_h}{\sigma_c}} \tag{2.60}$$

where: σ_c is compressive strength of rock,

P_h is the borehole pressure, the explosion pressure as previously defined.

2.3.17 Numerical Approach

Numerical simulation methods applied to rock fragmentation by blasting, blast vibration, and related topics include the Dynamic Finite Element Method (DFEM) (Blair and Minchinton 1997), Finite Difference Method (FDM), AUTODYN (Ansys 2000), and some hybrid methods such as the combination of FEM and BEM (Boundary Element Method) (Jaroslav 2002). Numerical simulation has the advantages of being able to take into account the propagation of the detonation wave in the explosive column, propagation of the stress wave in the rock mass, attenuation of the stress wave in the rock, and the influence of existing free surfaces. However, the main disadvantage of numerical simulation is that it is not always accessible to engineers because of the complicated theoretical basis and programming requirements.

2.3.18 Experimental Approach

Experimental determination of the extent of the crack zone and the crush zone are expensive and present safety concerns from vibration and potential of flying rock. Not many data are available from experimental work. The most complete sets of data for crack and crush zone extents have been published (Esen et al. 2003; Olsson and Bergqvist 1993; Olsson and Bergqvist 1996; Olsson et al. 2002; Liu 1991; Vovk et al 1973). They are discussed in the following paragraphs.

An extensive group of experiments for crack zone measurement was conducted by Esen et al. (2003). In this study, two explosives were used, gelatin dynamite and Elbar 1 dynamite. Ninety-two concrete samples were tested. The sample dimensions were 1.5 m in length, 1.0 m in width and 1.1 m in height. All samples were divided into three groups according to strength. The physical and mechanical properties of the concrete samples are shown in Table 2.5. The properties of explosives used are shown in Table 2.6. Experiments using fully-coupled and decoupled loading conditions were conducted as defined in Table 2.7. In Table 2.7, d_h and d_e are the diameter of borehole and charge, respectively. Figure 2.8 shows the relationship of the extent of the crush zone and crush zone index found by experiment for cylindrical charges. The radius of borehole and the radius of the crush zone are r_o and r_c, respectively. These researchers have documented a very complete data base that will be used to verify the new SWT procedure to be developed subsequently.

Table 2.5. Physical and mechanical properties of concrete samples, modified from Esen et al. (2003)

Sample	UCS (MPa)	Tensile strength (MPa)	Density (g/cc)	V-wave velocity (m/s)	S-wave velocity (m/s)	Young's modulus (GPa)	Poisson's ratio
Low strength (-)	6.7	0.3	2.26	3372	1871	20.2	0.278
Low strength (+)	10.5	0.8	2.27	3752	2064	24.8	0.283
Medium strength (-)	16.3	1.2	2.29	3935	2157	27.3	0.285
Medium strength (+)	24.6	2.9	2.38	4553	2471	37.5	0.291

High strength (-)	42.1	2.2	2.34	4341	2363	33.7	0.29
High strength (+)	56.5	4.3	2.46	4891	2642	44.4	0.294

Table 2.6. Properties of explosives, modified from Esen et al. (2003)

Property	Gelatin dynamite	Elbar 1 dynamite	Remarks
Density (g/cc)	1.5	1.0	
Velocity of detonation (m/s)	1278	1081	Based on unconfined charge with 16 mm diameter
Energy (KJ/kg)	4700	3760	

Table 2.7. Experimental parameters, modified from Esen et al. (2003)

Parameter	Fully-coupled tests	Decoupled tests (d_h/d_e)
Decoupled ratio	1	1.25, 1.5, 1.75, 2.0
Borehole diameter (mm)	16 -20	20, 24, 28, 32
Burden (cm)	22.7-46.2	18.2-31.3
Hole depth (cm)	40.4-45.4	39.8-45.0
Specific charge (kg/m^3)	0.11-0.25	0.15-0.175
Explosive amount (g)	8.0-22.8	7.8-16.1
Stemming material	1.18-3 mm aggregate	1.18-3 mm aggregate
Stemming length (cm)	26.5-40.3	20.0-39.6

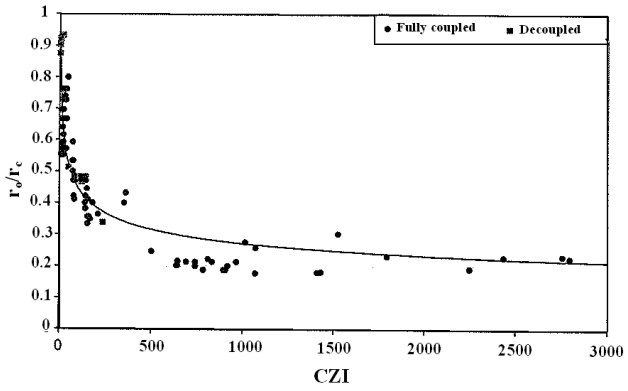

Figure 2.8. Crush Zone r_o/r_c versus Crush Zone Index (CZI). Reprinted from *Int. J. Rock Mech., Min. Sci. & Geomech*. Esen, Sedat, Modeling the Size of the Crushed Zone around the Blasthole. Abstract, pp 485-495, 2003, with permission from Elsevier.

Olsson and Bergqvist (1993) conducted a series of crack zone experiments for cylindrical charges in which six kinds of explosives were used. Parameters for these explosives are shown in Table 2.8.

The rock used by Olsson and Bergqvist is identified as fine-grained granite. The

compressive strength and tensile strength for this material are 200 MPa and 10-15 MPa, respectively. The results of the experiments are shown in Table 2.9. The reported crack length is the longest crack measured in the crack zone.

Table 2.8. The parameters of explosives, modified from Olsson and Bergqvist 1993)

Explosive	Density (g/cc)	Diameter of explosive (mm)	VOD (m/s)
Gurit	1	17	2200
Kimulux	1.15	22	4800
Emulet 20	0.25	Bulk	1850
Emulet 50	0.5	Bulk	2650
Detonex 40	1.05	8.3*	7000
Detonex 80	1.05	10.6*	7000

*Based on the manufactures specifications, the equivalent explosive core diameters should be 7.0 mm and 10.0 mm for Detonex 40 and Detonex 80, respectively.

Table 2.9. Crack length comparison of measurement and calculation, modified from Olsson and Bergqvist 1993)

Hole # and explosive	Density (g/cc)	Diameter of explosive (mm)	VOD (m/s)	Diameter of hole (mm)	Crack Length (cm)
#1 Gurit	1	17	2200	38	44
#2 Gurit	1	17	2200	51	28
#3 Gurit	1	17	2200	64	20
#4 Kimulux	1.15	22	4800	38	45
#5 Kimulux	1.15	22	4800	51	35
#6 Emulet 20	0.25	Bulk	1850	38	40
#7 Emulet 50	0.5	Bulk	2650	38	80
#8 Detonex 40	1.05	8.3*	7000	38	22
#9 Detonex 80	1.05	10.6*	7000	38	30

Liu (1991) presents a crush zone test for measuring the dust created by blasting using cylindrical charges. The goal of his study was to control the dust created by rock blasting underground.

Vovk et al. (1973) conducted crush zone and crack zone tests with different rocks. The method for emplacing the explosive employed by these researchers approximated a spherical charge. The results are shown in Table 2.10.

2.4 Parameters Used for Estimating the Extent of the Damage Zone

To successfully predict the extent of the damage zone in rock blasting, it is very important to choose a critical parameter for the prediction model. As presented above (Section 2.3.1), peak particle velocity is used to estimate the damage radius. In Sections 2.3.2 through 2.3.16 the borehole pressure or explosion pressure is used for this purpose.

2.4.1 PPV

Holmberg and Persson (1980) and Hustrulid et al. (1992) used peak particle velocity (PPV) as a critical parameter for damage zone assessment because PPV is easily measured. PPV failure criteria are generally used to protect structures on the surface, which are typically located far away from a blast pattern. These same criteria are not appropriate for estimating damage close to boreholes because far field effects are generally the result of surface waves, whereas near field effects may be the result of directly transmitted compressive, tensile and/or shear waves. Not much information is available for PPV measurements in close proximity to boreholes. Near field PPV-based

Table 2.10. Crush zone and crack zone, modified from Vovk et al. (1973)

Rock	Explosive	Radius of charge (cm)	Crush zone (r/r_h)	Crack zone (r/r_h)
Concrete	TNT	2.62	10-12.8	51.6
Granite	TNT	2.62	11-14	53.5-68.5
Limestone	TNT	3.10	8	38.7-48.4
Limestone	TNT	2.98	9-12	45.0

Limestone	TNT	2.98	8-10	36.2-62.8

blasting damage criteria for surface and underground structures are shown in Tables 2.11 and 2.12.

2.4.2 Pressure

Liu et al. (2002) and Drukovanyi et al. (1976) used applied pressure or stress as the critical parameter defining damage. This is consistent with traditional rock mechanics. For example, when the compressive pressure (P_r, radial pressure) exceeds the dynamic confined compressive strength of rock (σ_c), the rock fails and forms a crush zone surrounding the borehole:

$$P_r \geq \sigma_c \tag{2.61}$$

When the tensile stress ($P_{\theta,}$ tangential stress) exceeds the tensile strength of the rock (σ_T), rock failure is in the form of a crack zone surrounding the borehole:

Table 2.11. PPV Criterion for blast induced damage in rock, modified from Bauer and Calder (1978)

PPV (mm/s)	Effects of damage
<250	No fracturing of intact rock
250-635	Minor tensile, slabbing will occur
635-2540	Strong tensile and some radial cracking
>2540	Complete break-up of rock mass

Table 2.12. PPV Criterion for blast induced damage in rock, modified from Mojitabai and Beattie (1996).

Rock Type	Uniaxial Strength (MPa)	RQD (%)	Minor damage PPV (mm/s)	Medium damage PPV (mm/s)	Heavy damage PPV (mm/s)
Soft schist	14-30	20	130-155	155-355	>355

Hard Schist	49	50	230-350	305-600	>600
Shultze granite	30-55	40	310-470	470-1700	>1700
Granite Porphyry	30-80	40	440-775	775-1240	>1240

$$P_\theta \geq \sigma_T \tag{2.62}$$

However, the pressure parameter is not easy to measure, particularly for the regions close to the borehole. Another problem is the dynamic strength. The dynamic strength of the rock could be larger than the static strength. This difference varies depending on the rock type and rate of loading.

2.5 Conclusions

Rock blasting is a dynamic process. The results of experiments show that the value of dynamic strength of rock may be several times greater than the static strength. It may not be appropriate to use the static properties of rock in predicting a dynamic process.

According to Hino (1956), borehole pressure is the same as detonation pressure. An estimate for the borehole pressure can be computed by dividing the detonation pressure by 2 (Cook 1958). This estimate is also identified by Hustrulid (1999) as the explosion pressure. Liu (2002), Dai (2002), and Borovikov and Vanyagin (1995) present methods for calculating borehole pressure using properties of rock and explosives. The explosion pressure is frequently used as the borehole pressure. The explosion pressure, also called adiabatic pressure, is defined as the hypothetical pressure that would be generated at a constant volume without heat loss to the surroundings. This is an appropriate estimate for the gas pressure within the borehole, but the dynamic stress on

the walls of the borehole may be greater than or less than the explosion pressure at the instant of the shock wave arrival at the borehole wall. For example, the shock wave pressure on a borehole wall in strong rock will be much different than the pressure exerted by the shock wave on a borehole wall in weak rock.

Many damage zone prediction models have been reviewed. Some of them are regularly used in practice, such as the PPV model proposed by Holmberg and Persson (1978). Most models estimate the shock properties only using the properties of explosives and ignore the properties of rock. The Shock Wave Transfer approach developed in subsequent sections includes both the properties of explosive and rock. Verification of this technique will be accomplished by comparing the SWT predictions with the data presented by Essen et al. (2003). These researchers have documented a very complete data base which includes the properties of explosives and properties of blasted materials.

3. THEORETICAL DAMAGE ZONE PREDICTION MODEL

The damage zone prediction model described in this chapter provides a shock wave-based technique for perimeter control blast design in surface and underground mining applications. The unique aspect of this model is that it includes the dynamic properties of the rock as well as the properties of the explosive. Rigorous solution of this combination can be very complicated, so convenient equations and charts will be developed to make the approach useable and more engineer-friendly.

3.1 Perimeter Blast Design Principles

Olsson et al. (2002) conducted crack generation tests with granite blocks. He found that:

- The shock wave is primarily responsible for cracks in the borehole walls in rock blasting
- Gases are responsible for moving the rock
- Gases from nitroglycerin (NG) sensitized explosives seem to affect crack generation more than gases from emulsions
- A low VOD explosive works more gently on the rock, while a high VOD explosive will subject the rock to high impact pulses
- Crack length is reduced when decoupling ratio is increased. The decoupling ratio is the ratio of the diameter of charge to the diameter of the borehole

- Instantaneous firing of holes in a blast pattern reduces the extent of cracking
- High VOD explosives create a high number of fine cracks in the vicinity of the borehole
- The crack length increases when the spacing between holes in a pattern increases
- There is no significant influence of burden on crack length for reasonable blast patterns

In rock blasting, cracks are mainly induced by the shock wave, and gases can help to widen and make them longer. However, due to the different properties of explosives and rocks, there are different fragmentation patterns. For hard rocks, the shock wave predominates in fragmentation, and gases contribute little to the fragmentation process. For soft rocks, both the shock wave and gases contribute to fragmentation. In general, the shock wave fractures the rock, and gases are responsible for moving fragments toward the free surface. Secondary fragmentation may also result from collisions of fragments propelled by gas pressure. The focus of this study is on the fragmentation resulting from the shock wave.

Drill and blast design for underground excavation should follow the principles illustrated in Figure 3.1 and described by Persson et al. (1993). Gentle contour blasting requires that the damage generated by the stoping and helper holes must not extend farther into the rock surrounding the opening than the damage produced by the contour (perimeter) holes. Damage zones due to the perimeter holes, helper holes, and production holes are described as a, b, and c, respectively. The acceptable extent of damage into the surrounding rock by perimeter holes (red) is defined by A. The burden on the perimeter holes is B and the burden for the helper holes is C. To protect the integrity of the rock

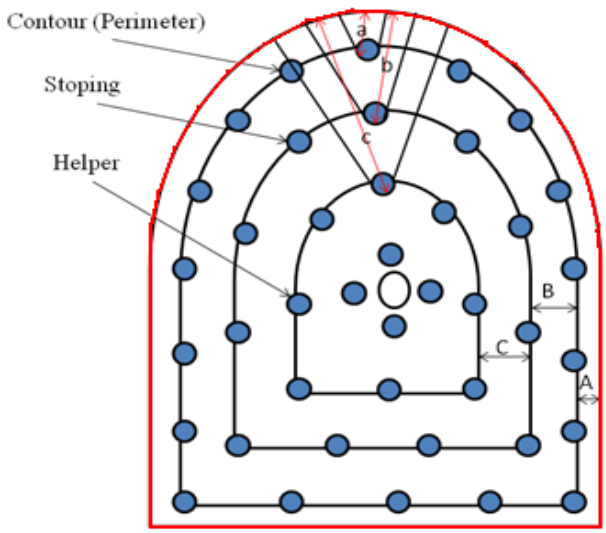

Figure 3.1. Gentle contour blasting design principle in the underground drift, modified from Persson et al. (1993)

surrounding the perimeter holes, the extent of damage by stoping and helper holes should not extend beyond the damage line produced by perimeter holes, as shown in Equations 3.1, 3.2 and 3.3. In surface mine blast design, the same principle should be followed. This is shown in Figure 3.2. Based on those principles, NIOSH developed a detail design procedure for perimeter control blasting, Hustrulid and Johnson (2008).

$$a \leq A \tag{3.1}$$

$$b \leq A + B \tag{3.2}$$

$$c \leq A + B + C \tag{3.3}$$

3.2 Damage Zone Prediction

The theoretic analysis for damage zone prediction is based on the assumption that the charges are spherical in shape. To extend the spherical charge analysis for the

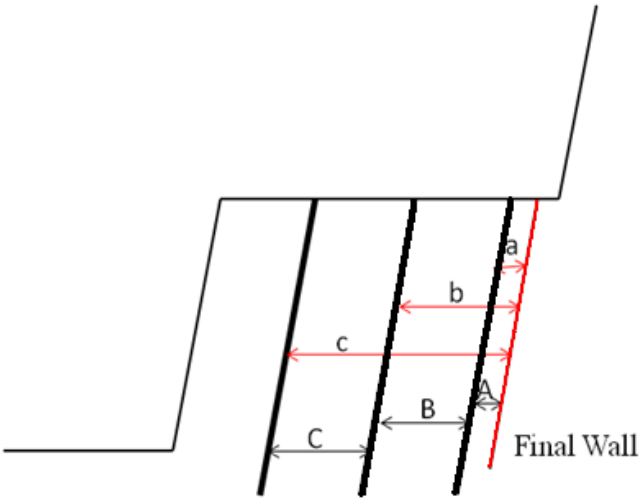

Figure 3.2. Gentle contour blasting design principle in surface mining based on Equations 3.1, 3.2 and 3.3

cylindrical charge, the cylindrical charge is approximated by a linear array of just-touching spherical charges.

To predict blast damage zones, the damage mechanism must be identified. The most common theory of rock breakage by blasting consists of two stages: In the first stage, the shock wave causes crushing and radial cracks to form around the borehole. In the second stage, gases penetrate into the cracks, widen them, and make them longer (Langefors and Kihlstone 1973). Brinkmann (1987, 1990) describes that the "back damage" (overbreak) is primarily controlled by shock and that the gas penetration is the mechanism controlling breakout of the burden. For practical design, the most common method used is the Holmberg-Persson method. In the Holmberg-Persson design system, only shock effects are taken into account. The relationship among particle velocity (V), strain (ε) and stress (σ) in an idealized case (when a plane shock wave passes through an infinite elastic medium) can be expressed as:

$$\sigma = \varepsilon E \tag{3.4}$$

$$\varepsilon = \frac{V}{V_p} \tag{3.5}$$

where: E, V_p, ρ_r and ν are material properties, Young's modulus, P-wave velocity, density and Poisson's ratio, respectively. Knowing the rock density ρ_r, they are related by the following equation:

$$V_p = \sqrt{\frac{E(1-\nu)}{\rho_r(1-2\nu)(1+\nu)}} \tag{3.6}$$

In blasting, three zones exist surrounding the borehole. They are the crush zone, the crack zone, and finally, the elastic zone. These are shown in Figure 3.3.

To predict the extent of the crush and crack zones, the borehole pressure, P_h, should be estimated first. The shock wave transfer (SWT) method is used to estimate the borehole pressure in this dissertation. The detail calculations of borehole pressure and other shock wave properties for both fully-coupled and decoupled conditions are presented in Chapters 4 and 5.

In the crush zone, the extent of crushing for a spherical charge or cylindrical charge is:

$$R_{crush} \le r(\sigma = \sigma_{cd}) \tag{3.7}$$

where: σ_{cd} is the dynamic compressive strength of the rock.

In the crush zone, the pressure of the shock wave on the wall of the borehole propagates outward in the radial direction. It is expressed by the following equation

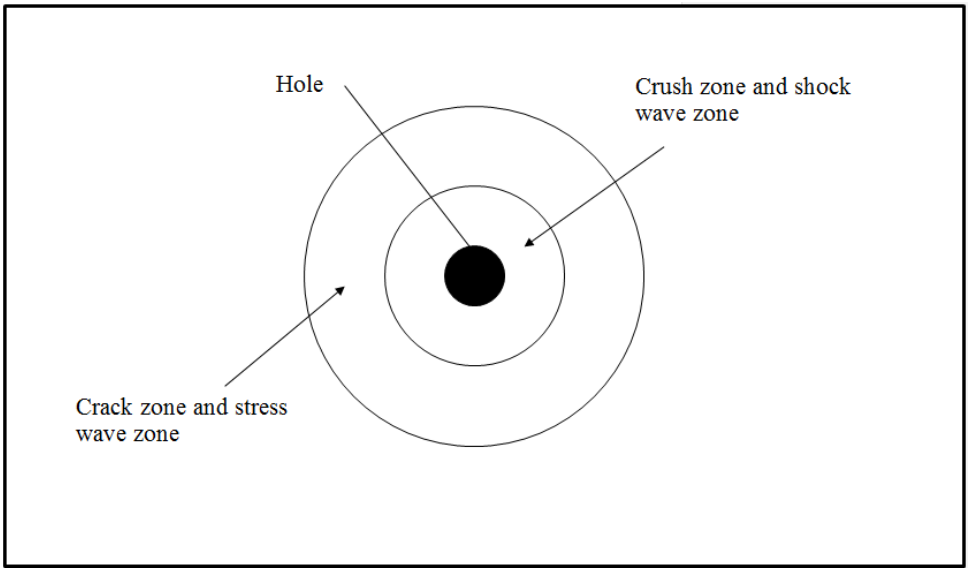

Figure 3.3. Different zones for a spherical charge applied to the borehole model

adapted from a spherical charge by changing the exponent from α to α1:

$$\sigma_r = P_h(\frac{r_h}{r})^{\alpha 1} \tag{3.8}$$

where: σ_r is pressure of the shock wave at the point of interest,

r is the radius of the point of interest,

r_h is the radius of the borehole,

$\alpha 1$ is the cylindrical attenuation exponent in the crush zone, and

P_h is the shock wave pressure on the wall of the borehole.

Dai (2002), in his publication written in Chinese, identifies two different zones: the shock wave zone in which the shock wave prevails, which extends to the limits of the crush zone, and the stress wave zone which extends beyond the crush zone. Because of the fundamental difference between the shock wave and the stress wave, he maintains that the attenuation factors for each zone are different. In the shock wave zone, the

attenuation exponent is estimated to be approximately 3. In the stress wave zone, the attenuation exponent is estimated to be approximately 1 to 2. The exponents for both the shock wave zone and stress wave zone are estimated by the following equations (Dai 2002): In the shock wave zone:

$$\alpha 1 = 2 + \frac{\nu}{1-\nu} \tag{3.9}$$

In the stress wave zone:

$$\alpha 2 = 2 - \frac{\nu}{1-\nu} \tag{3.10}$$

To agree with the values presented in his text, Equations 3.9 and 3.10 must be modified as follows:

In the shock wave zone:

$$\alpha 1 = 2(1 + \frac{\nu}{1-\nu}) \tag{3.11}$$

In the stress wave zone:

$$\alpha 2 = 2(1 - \frac{\nu}{1-\nu}) \tag{3.12}$$

So, combining equations 3.7, 3.8 and 3.11, the crush zone should be:

$$R_{crush} = (\frac{P_h}{\sigma_{cConfd}})^{\frac{1-\nu}{2}} r_h \tag{3.13}$$

where: σ_{cConfd} is dynamic confined compressive strength of rock. In the crack or stress wave zone, the crack extent is defined by:

$$R_{crush} \le R_{crack} \le r(\sigma_r = \sigma_{Td}) \tag{3.14}$$

where: σ_{Td} is the dynamic tensile strength of the rock.

The pressure of the stress wave at the interface between the shock wave zone and stress wave zone propagates outward in the radial direction according to the following equation:

$$\sigma = (\frac{R_{crush}}{r})^{\alpha 2} \sigma_{cd} \tag{3.15}$$

where: σ is the stress at any distance r, and

$\alpha 2$ is the cylindrical attenuation exponent in the stress zone from Equation 3.12

By combining equations 3.12 and 3.15, the crack zone should then be:

$$R_{crack} = (\frac{\sigma_{cd}}{\sigma_{Td}})^{\frac{1-\nu}{2(1-2\nu)}} R_{crush} \tag{3.16}$$

So, the extent of the crush zone is estimated by Equation 3.13 and the extent of the crack zone by Equation 3.16. According to these equations the borehole pressure, a confinement factor to connect σ_{Td} to σ_{cConfd}, and the dynamic compressive and tensile strengths of the rock surrounding the borehole need to be determined to predict the extend of the crush zone and the crack zone.

4. SHOCK WAVE PARAMETERS FOR FULLY-COUPLED CHARGES

The shock wave parameters include the shock wave pressure, the particle velocity, and the shock wave velocity. The shock wave pressure of an explosive is the detonation pressure [pressure at the Chapman-Jouquet (C-J) plane]. The shock wave pressure on the borehole wall is produced by the detonation of the explosive and is estimated by the interaction of the shock wave with the rock surrounding the borehole.

Many researchers assume the explosion pressure to be the pressure acting on the wall of the borehole, i.e., one half of the detonation pressure. This is appropriate only when conducting a quasistatic pressure analysis. However, if one is conducting a dynamic shock wave analysis, the shock wave pressure on a borehole depends on the detonation properties of the explosive and the dynamic mechanical properties of the surrounding rock.

Some researchers use the impedance mismatch method [see Section 2.2(3)] to calculate the borehole pressure. This method is not correct since the impedance mismatch is based on the condition of stress wave propagation in surrounding materials. In the case of rock blasting, shock wave propagation in air and rock should be considered. In the following sections, both theoretical and empirical methods are developed for estimating the pressure, particle velocity and extent of the damage zone in

rock blasting based on shock wave transfer (SWT). The theoretical basis for the SWT method will be presented first and then compared with an empirical method for a specific set of conditions found in the literature.

4.1 Development of the SWT Approach for Fully-coupled Loading (Theoretical Analysis)

The SWT approach is based on shock wave mechanics (Cooper 1996; Henrych 1979). The approach was used by researches to estimate the detonation interactions between explosives and other materials, such as rock, air, concrete, steel, etc.

The analytical method used to estimate the shock wave parameters for an interaction between the explosive detonation wave and shock wave in the surrounding rock is based on the work of Henrych (1979) and Zhang (1993) (Zhang includes a Chinese compilation of the work by Henrych). Their works help to construct the Hugoniot equation of explosives when detonation parameters of explosives interact with the shock wave parameters of rock. Henrych (1979) presented the shock wave mechanics that will be used to formulate the SWT method. The theoretical analysis for estimating shock wave parameters is based on the assumption of perpendicular transfer into the wall of the borehole. This assumption is true for a spherical charge. For a cylindrical charge, it may be assumed that the cylindrical charge can be reasonably approximated by a linear alignment of just-touching spherical charges each representing a unit part of the whole (Hustrulid 1999). In this way, the shock wave of the cylindrical charge can be assumed to act perpendicular to the borehole wall.

In fully-coupled borehole blasting, two media are considered:

- Explosives

- Rock

The detonation and shock wave transfer for fully-coupled rock blasting is illustrated in Figure 4.1. Figure 4.1(a) indicates that the shock wave is created and propagated outward from the axis in the explosive. Figure 4.1(b) shows that the shock wave is transmitted from the explosive into the rock. When the detonation wave impinges on the rock (impingement), the reflected wave propagating through the explosion gases after impingement may be a rarefaction wave or a shock wave depending on the properties of the explosive and rock. The criterion determining the type of wave is:

Case 1: When $P_{CJ} > P_x$ or $Z_{CJ} > Z_x$, the reflected wave is a rarefaction wave.

Case 2: When $P_{CJ} < P_x$ or $Z_{CJ} < Z_x$, the reflected wave is a shock wave.

Where: P_x is the shock wave pressure on the rock side of the interface of explosive and the wall of the borehole,

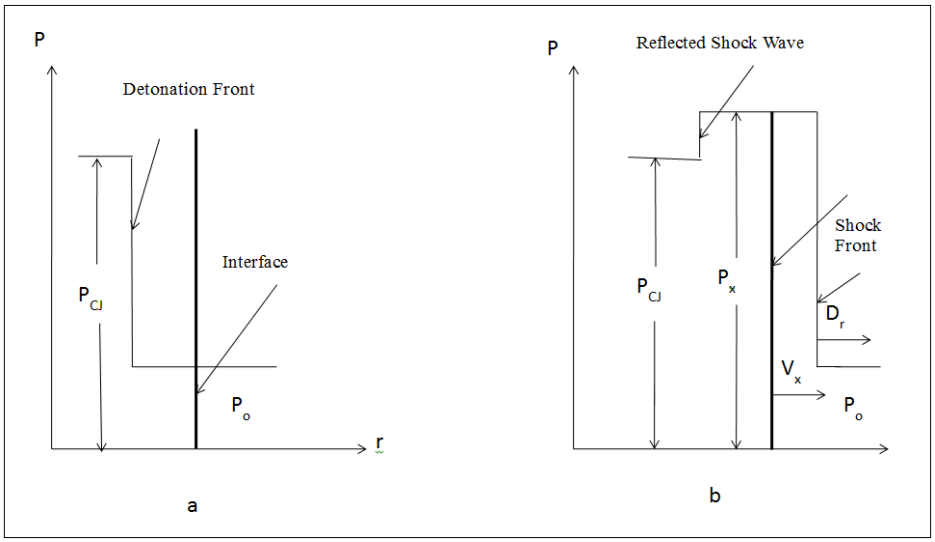

Figure 4.1. Initial shock front at the interface ($Z_{CJ} < Z_x$), modified from Henrych (1979)
a: Before arrival of the detonation wave
b: Following arrival of the detonation wave

Z_{CJ} is the impedance of the explosive, determined by density and VOD of the explosive:

$$Z_{CJ} = \rho_o D \tag{4.1}$$

Z_x is the impedance of the rock, determined by density and p-wave velocity of the rock:

$$Z_x = \rho_r V_p \tag{4.2}$$

when blasting with fully-coupled charges, Case 2 regularly happens because, in most cases, the impedances of the rocks are larger than those of explosives.

For explosives, the following equation of state is considered:

$$P = \frac{A}{sv^{\gamma}} \tag{4.3}$$

where: A is constant,

P is the pressure

sv is the specific volume ($1/\rho_0$) and

γ is the isentropic exponent, (≈3.0).

The detonation properties: pressure P_{CJ}, density ρ_{CJ}, particle velocity V_{CJ}, and shock velocity c_{CJ}, can be calculated by the following equations (Henrych 1979; Song et al. 1997; and Zhang 1993):

$$P_{CJ} = \frac{1}{1+\gamma}\rho_o D^2 \tag{4.4}$$

$$\rho_{CJ} = \frac{\gamma + 1}{\gamma} \rho_o \tag{4.5}$$

$$V_{CJ} = \frac{1}{1+\gamma} D \tag{4.6}$$

$$c_{CJ} = \frac{\gamma}{1+\gamma} D \tag{4.7}$$

When $P_x > P_{CJ}$, for fully-coupled detonation, the impedances of explosives are smaller than those for most rocks. Henrych (1979) provides the following relationship for the particle velocities on the wall of the borehole, expressed in terms of the detonation wave and the reflected shock:

$$V_x = V_{CJ} - V_r \tag{4.8}$$

where: V_x is the particle velocity at the interface of explosive and the wall of the borehole,

V_{CJ} is the particle velocity in the detonation wave, and

V_r is the particle velocity in the reflected shock wave

V_r is also given by Henrych (1979):

$$V_r = \sqrt{(P_x - P_{CJ})(sv_{CJ} - sv_x)} \tag{4.9}$$

where: sv_x is the specific volume of the explosive gasses at the wall of the borehole and sv_{CJ} is the specific volume of explosive gasses at the CJ plane.

Henrych (1979) considered the shock wave Hugoniot equation and equation of state and produced the following equation:

$$e_x - e_{CJ} = \frac{1}{2}(P_x + P_{CJ})(sv_{CJ} - sv_x) \tag{4.10}$$

where: e_x, e_{CJ} are internal energies at the interface and the explosive, respectively.

$$e = \frac{P(sv)}{(\gamma - 1)} \tag{4.11}$$

Substituting Equation 4.11 into 4.10:

$$\frac{P_x(sv_x)}{\gamma - 1} - \frac{P_{CJ}(sv_{CJ})}{\gamma - 1} = \frac{1}{2}(P_x + P_{CJ})(sv_{CJ} - sv_x) \tag{4.12}$$

Reorganizing Equation 4.12:

$$\frac{sv_x}{sv_{CJ}} = \frac{(\gamma - 1)\dfrac{P_x}{P_{CJ}} + \gamma + 1}{(\gamma + 1)\dfrac{P_x}{P_{CJ}} + \gamma - 1} \tag{4.13}$$

Applying Equation 4.5, 4.6, 4.8, 4.9 and 4.13, Henrych (1979) presents the following Hugoniot equation of the explosive detonation:

$$V_x = \frac{D}{1+\gamma}\left(1 - \frac{\dfrac{P_x}{P_{CJ}} - 1}{\left(\dfrac{1+\gamma}{2\gamma}\dfrac{P_x}{P_{CJ}} + \dfrac{\gamma - 1}{2\gamma}\right)^{\frac{1}{2}}}\right) \tag{4.14}$$

Cooper (1996) presents the Hugoniot equation for rock and other solids as:

$$D_r = c_o + sV_{hr} \tag{4.15}$$

where: D_r is shock velocity in the rock,

s is a constant determined by experiment,

c_o is the sound velocity in the rock, and

V_{hr} is particle velocity in the rock.

Some Hugoniot parameters of rocks, metals, and other materials are shown in Table 4.1 and Figure 4.2.

Let the initial density and pressure for a particular rock be ρ_{ho} and P_{ho}, respectively. When the shock wave propagates into the medium, the pressure, particle velocity, and shock wave velocity of the rock are P_{hr}, V_{hr} and D_r, respectively. Based on conservation of momentum, the pressure, P_{hr} can be obtained (P_{ho}=0):

$$P_{hr} = \rho_{ho} D_r V_{hr} \tag{4.16}$$

Table 4.1. Hugoniot parameters of rocks, metals, and other materials

Material	Density (g/cc)	c_o (m/s)	s	Reference
Limestone	2.6	3500	1.43	Zhang (1993)
Tuff	1.65	1320	1.41	Marsh (1980)
Alluvium	1.8	1185	1.47	Marsh (1980)
Gabbro (Anorthosite)	2.73	5196	0.54	Marsh (1980)
Gabbro	2.92	5060	0.63	Marsh (1980)
Diabase	3.01	5106	0.73	Marsh (1980)
Dunite	3.24	5894	1.29	Marsh (1980)
Marble	2.7	4000	1.32	Zhang (1993)
Granite	2.63	4140	0.83	Marsh (1980)
Oil shale	2.192	3780	1.15	Marsh (1980)
Sand	1.65	1300	1.35	Marsh (1980)
Concrete	1.16	2340	1.32	Marsh (1980)
Steel 304	7.89	4580	1.49	Marsh (1980)
Copper	8.93	3910	1.51	Marsh (1980)
Aluminum 921T	2.82	5150	1.37	Marsh (1980)

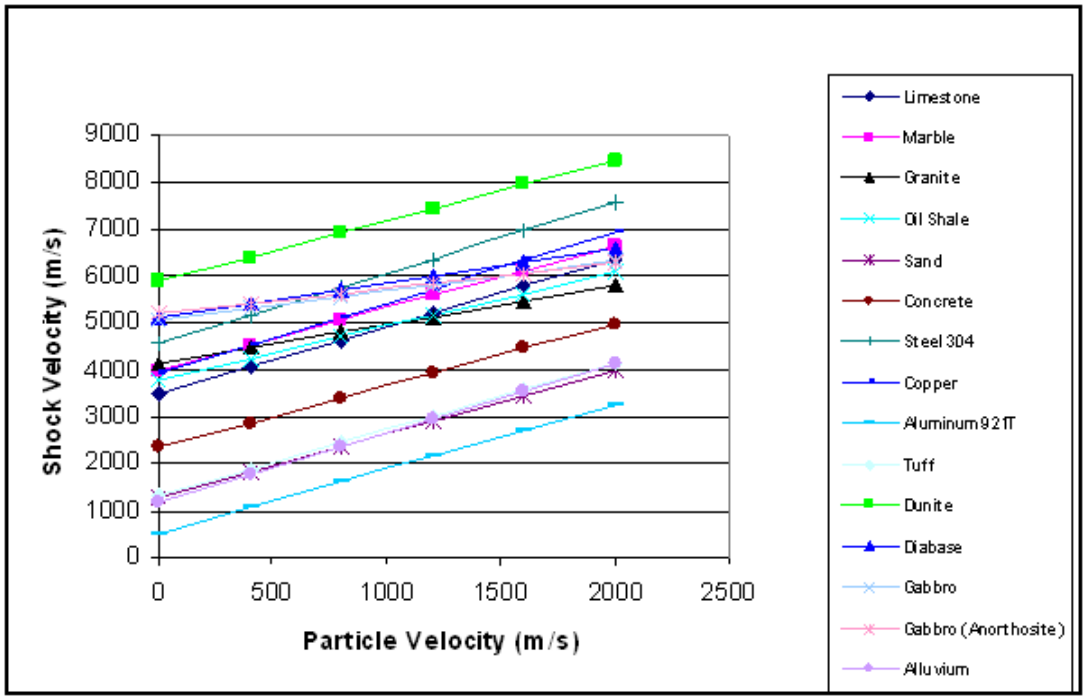

Figure 4.2. Some Hugoniot parameters of rocks, metals and other materials, modified from Marsh (1980)

Substituting Equation 4.15 into 4.16, the Hugoniot equation of rock can be expressed as:

$$P_{hr} = \rho_{ho}(c_o + sV_{hr})V_{hr} \tag{4.17}$$

Based on force and velocity continuity at the interface, the parameters in the explosive Hugoniot equation and rock Hugoniot equation in the interface should be equal. That is:

$$V_x = V_{hr} \tag{4.18}$$

and

$$P_x = P_{hr} \tag{4.19}$$

So, by applying Equations 4.15, 4.16, 4.18, and 4.19 the shock wave parameters on the wall of the borehole can be calculated. A direct analytical solution for these equations is difficult to obtain. A numerical program has been developed to solve these equations (Appendix A).

The following is an example for ANFO detonating in a borehole in marble. Based on Equation 4.15, the shock wave Hugoniot of the detonation for ANFO is shown in Figure 4.3. The given parameters of ANFO are:

Density, ρ_o: 0.8 g/cc

VOD, D: 4500 m/s

Detonation pressure, P_{CJ}: 4050 MPa and

Isentropic exponent, γ: 3

The shock wave Hugoniot of marble is shown in Figure 4.4. The given parameters of marble are:

Density, ρ_o: 2.7 g/cc

Longitudinal wave speed, c_o: 4000 m/s and

Hugoniot constant, s: 1.32

Based on the intersection, P_{hr} and V_{hr} can be calculated. The solution is:

Pressure on marble: 6634 MPa

Particle velocity on the marble: 523.8 m/s and

Shock wave velocity on marble: 4691.4 m/s

Superposition of the two figures is shown in Figure 4.5. Obviously, the borehole pressure for hard rock blasting from the SWT method (6634 MPa) is much larger than (2025 MPa), which is obtained by assuming pressure on the borehole wall is one half of the detonating pressure.

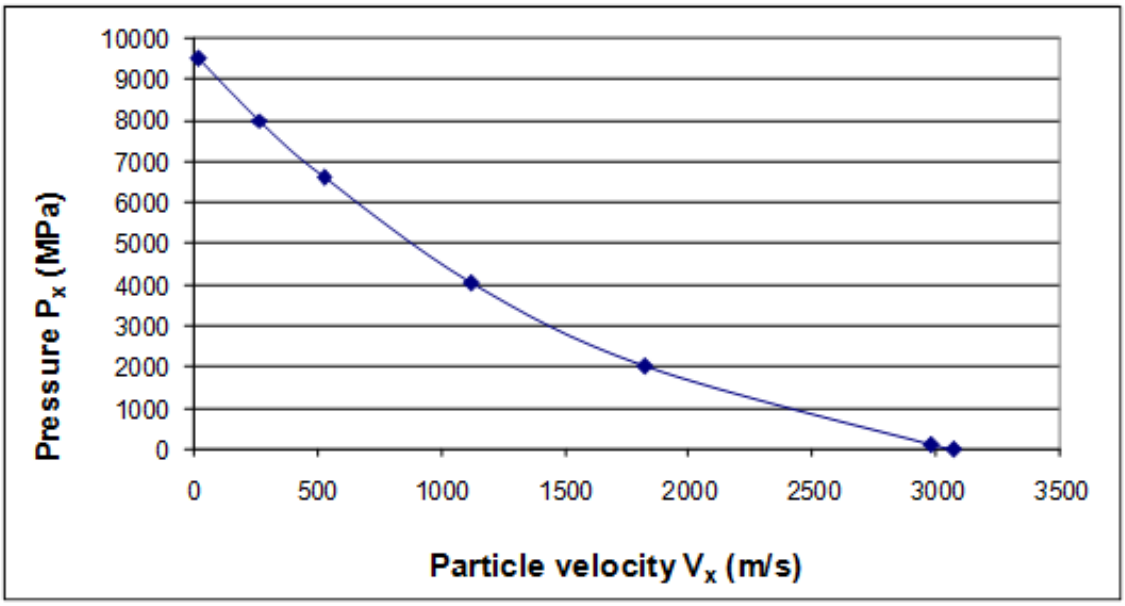

Figure 4.3. The shock wave Hugoniot for the detonation for ANFO

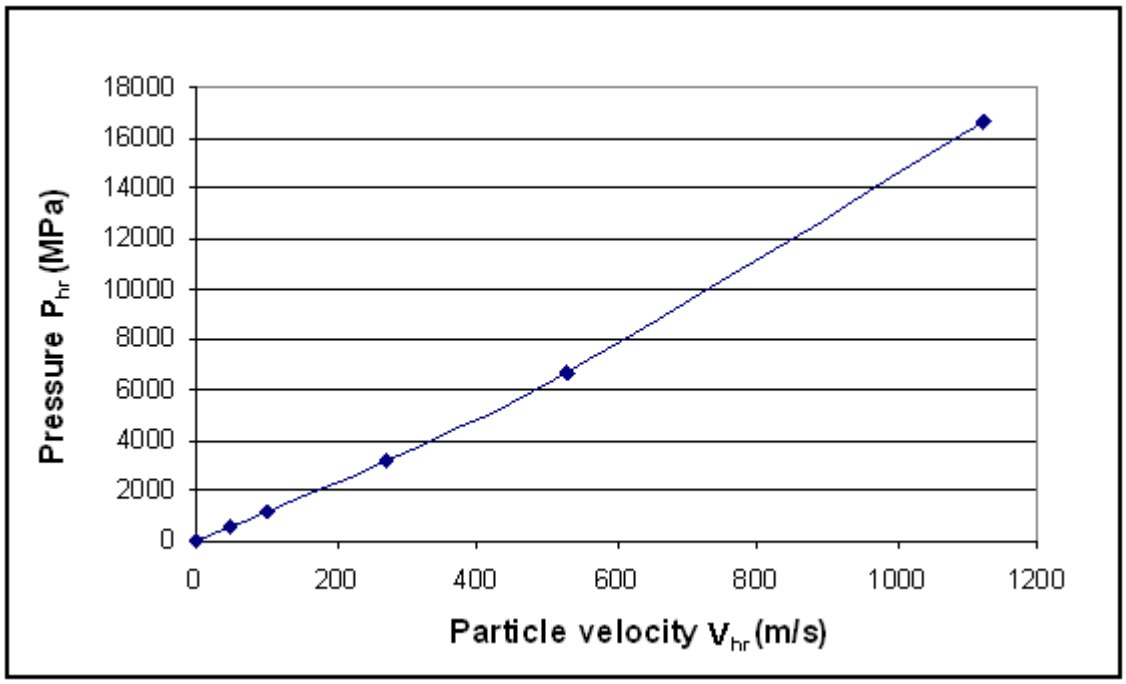

Figure 4.4. The shock wave Hugoniot for marble

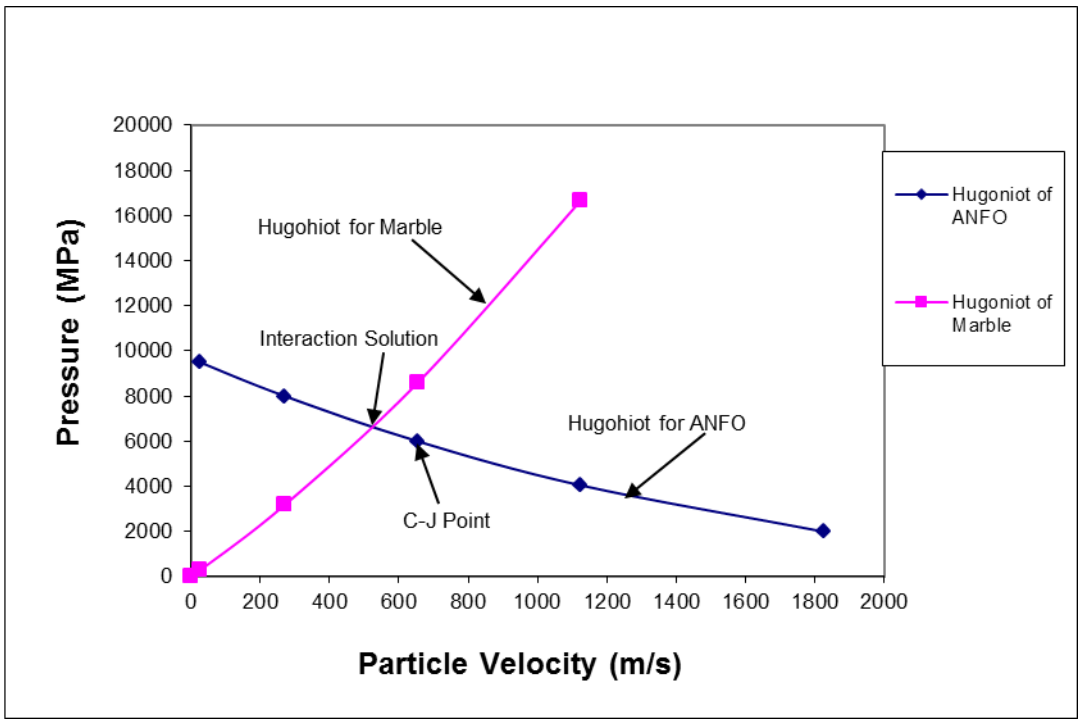

Figure 4.5. Solution for the ANFO and marble example, modified from Cooper (1996)

4.2 Fully-coupled Loading – Empirical Analysis

Following a similar process as the one described above, it is possible to use the empirical method to estimate the shock wave parameters for an interaction between the detonation wave of explosives and the shock wave of other solid materials. Based upon the experimental data, an empirical shock wave Hugoniot equation (the theoretical Hugoniot formulation is Equation 4.14) was constructed by Cooper (1996):

$$\frac{P_x}{P_{CJ}} = 2.412 - 1.7315\left(\frac{V_x}{V_{CJ}}\right) + 0.3195\left(\frac{V_x}{V_{CJ}}\right)^2 \tag{4.20}$$

where: P_{CJ} and V_{CJ} can be determined by Equations 4.4 and 4.6.

The equation of state for rock is the same as given by Equations 4.15 and 4.17. Selecting ANFO again as the example, the comparison of the empirical shock wave and the

theoretical Hugoniot for ANFO is shown in Figure 4.6. The interaction of the empirically derived Hugoniot for ANFO and that of marble is shown in Figure 4.7. The solution is:

Pressure on marble: 6745 MPa

Particle velocity on the marble: 531.5 m/s and

Shock wave velocity on marble: 4701.6 m/s

Comparing the empirical and theoretical solutions, the difference is only 1.5%, indicating that the theoretical analysis provides a reasonable value for this example.

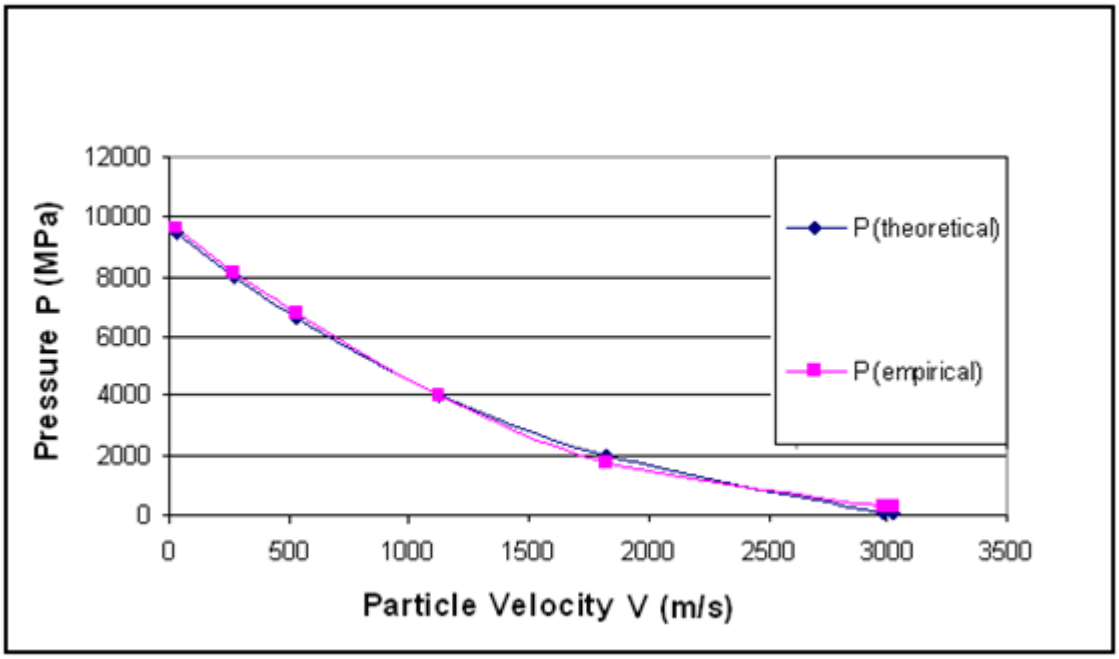

Figure 4.6. Comparison of the shock wave empirical and theoretical Hugoniots for ANFO

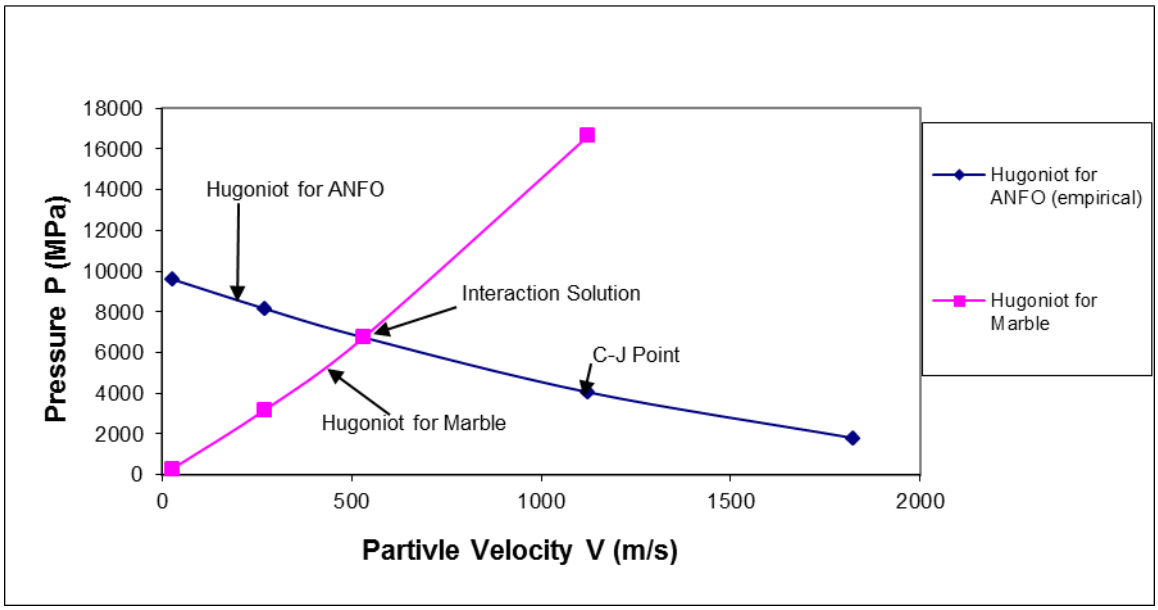

Figure 4.7. The interaction of Hugoniots of ANFO (empirical) and marble

5. SHOCK WAVE PARAMETERS

FOR DECOUPLED CHARGES

Similar to coupled charges as presented in Chapter 4, the shock wave parameters for decoupled charges include the shock wave pressure, the particle velocity, and the shock wave velocity. The shock wave pressure of an explosive is the detonation pressure [pressure at the Chapman-Jouquet (C-J) plane]. This pressure interacts with the air between the explosive and the borehole wall. The resulting pressure then transitions from the air to the rock surrounding the borehole.

5.1 Development of the SWT Approach for Decoupled Loading

Techniques for estimating shock wave parameters for decoupled conditions (illustrated on Figure 5.1) are difficult to find in the published literature. The method most often used is based on an assumption that the process involves adiabatic expansion of an ideal gas (no heat is gained or lost by the system) as presented by Persson et al. (1993):

$$P_e v_e^{\gamma} = P_h v_h^{\gamma} \tag{5.1}$$

where: P_e is pressure in explosive,

P_h is pressure in borehole,

v_e is volume of explosive,

v_h is volume of borehole, and

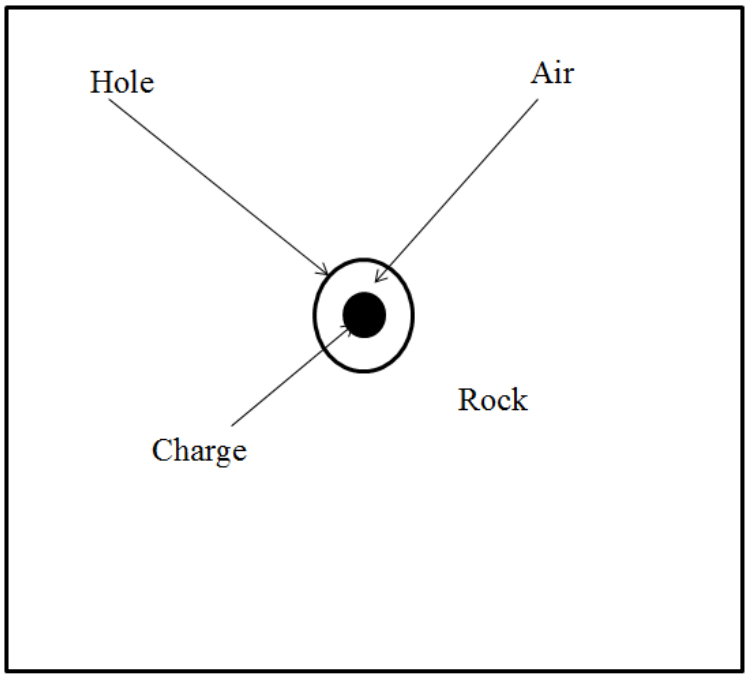

Figure 5.1. The geometry of decoupled loading of borehole

γ is the adiabatic exponent, γ=3.0 when $P_e \leq P_h$, and γ=1.2-1.4 when $P_e \geq P_h$.

By rearranging Equation 5.1 the borehole pressure for a cylindrical charge can be expressed as:

$$P_h = P_e \left(\frac{d_e}{d_h}\right)^{2\gamma} \tag{5.2}$$

where: d_e and d_h are the diameters of the charge and borehole, respectively.

Nowhere in Equation 5.2 is the shock wave pressure included. To properly analyze the pressures involved in detonation of a decoupled cylindrical charge, the change in the intensity of the shock wave from one medium into another medium should be considered. First, the explosive and air media are considered and then the air and rock media are dealt with.

5.2 Initial Parameters of the Shock Wave at the Explosive and Air Boundary

Estimation of shock wave parameters for decoupled loading is much more complex than estimating parameters for fully-coupled loading for the following reasons:

- Instead of two media, the explosive and the rock, as in the fully-coupled case, there are three media involved in the decoupled case, explosive, air and rock.
- Because of the very low density of air, high expansion of the explosive takes place at the explosive/air boundary. The expansion process is not isentropic. Under these conditions, an approximation is made by separating the expansion process into two stages, as illustrated in Figure 5.2 (Henrych 1979).
- Stage 1: the shock wave pressure decreases from the detonation pressure P_{CJ} to the critical pressure $P_{cr.}$ In this process, the isentropic exponent (k) has a constant value of 3. Beyond $P_{cr,}$ the isentropic exponent (γ) assumes a value between 1.2 and 1.4. The symbols k and γ are used to distinguish different stages of the process. In subsequent use, k equals 3 while λ equals 1.2 to 1.4.

$$P_{CJ} s v_{CJ}^{k} = P_{cr} s v_{cr}^{k} \tag{5.3}$$

- Stage 2: the shock wave pressure changes from the critical pressure P_{cr} at the explosive-air interface to the initial air shock wave pressure P_x. In this process, the isentropic exponent is constant (γ =1.2 - 1.4).

$$P_{cr} s v_{cr}^{\gamma} = P_x s v_x^{\gamma} \tag{5.4}$$

where: P_{CJ} is detonation pressure,

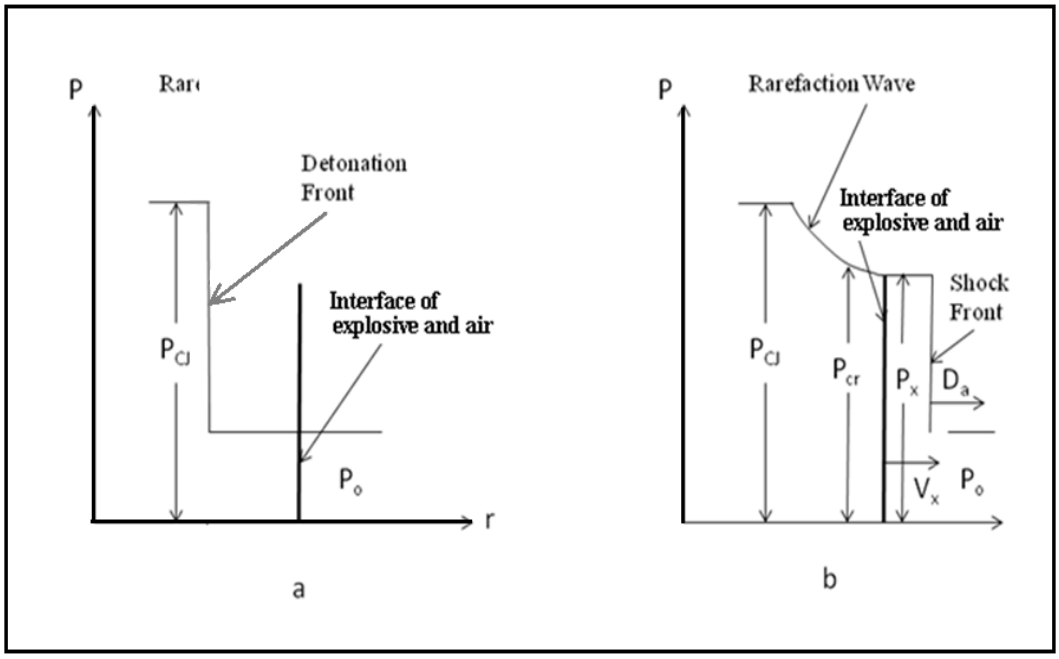

Figure 5.2. Initial shock front at the interface ($Z_{CJ} > Z_x$), modified from Henrych 1979):
a. before incidence of the detonation wave
b. after incidence of the detonation wave

P_{cr} is critical pressure,

P_x is initial air shock wave pressure,

sv_{CJ} is specific volume in C-J front,

sv_{cr} is specific volume at the critical pressure condition,

sv_x is specific volume of the initial air shock wave,

k is isentropic exponent, k=3.0. (the pressure between P_{CJ} to P_{cr}), and

γ is isentropic exponent, γ =1.2-1.4 (the pressure below P_{cr}).

The following equations outline the derivation presented by Henrych (1979), and Zhang (1993). The critical pressure, P_{cr} and critical specific volume, sv_{cr}, for the detonation wave are determined by the following Hugoniot equation:

$$\frac{P_{CJ} sv_{CJ}}{k-1} - \frac{P_{cr} sv_{cr}}{k-1} + \Delta Q = \frac{1}{2} P_{CJ} (sv_x - sv_{CJ}) + Q \tag{5.5}$$

where: ΔQ is the remaining energy for the state of detonation products changing from P_{CJ} and sv_{CJ} to P_{cr} and sv_{cr},

Q is available energy of the explosive .

Considering that

$$\frac{P_{CJ} sv_{CJ}}{k-1} >> \frac{P_{cr} sv_{cr}}{k-1} \tag{5.6}$$

the term

$$\frac{P_{cr} sv_{cr}}{k-1}$$

can be ignored in Equation 5.5. Referring to Equations 4.4, 4.5, and recognizing that γ must be replaced by k, $sv_{CJ} = 1/\rho_{CJ}$, $sv_{cr} = 1/\rho_{cr}$, $sv_x = 1/\rho_x$, Equation 5.5 can be reduced to:

$$\Delta Q = Q - \frac{D^2}{2(k^2 - 1)} \tag{5.7}$$

where: D is velocity of detonation (VOD).

ΔQ can be written as:

$$\Delta Q = c_v T_{cr} \tag{5.8}$$

where: T_{cr} is the temperature and

c_v is the specific heat capacity under constant volume or:

$$c_v = \frac{R}{k+1} \tag{5.9}$$

Based on the work of Henrych (1979) and Zhang (1993), the explosion gases may be considered to obey the ideal gas laws for pressures less than P_{cr}

$$P_{cr} sv_{cr} = RT_{cr} \tag{5.10}$$

Combine Equations 5.7 through 5.10, and Equation 5.11can be obtained.

$$P_{cr} sv_{cr} = RT_{cr} = \frac{R\Delta Q}{c_v} = (\gamma - 1)\Delta Q \tag{5.11}$$

Then combining Equations 5.3 and 5.11, and substituting P_{CJ} and sv_{CJ}, with Equations 4.4 and 4.5, the critical pressure, P_{cr} and critical specific volume, sv_{cr} can be obtained:

$$P_{cr} = \rho_o D^2 (k+1)^{\frac{k+1}{k-1}} \left\{ \frac{\gamma - 1}{k} \left[\frac{Q}{D^2} - \frac{1}{2(k^2 - 1)} \right] \right\}^{\frac{k}{k-1}} \tag{5.12}$$

$$sv_{cr} = \frac{1}{\rho_o} \left[\frac{k^k}{(k+1)^{k+1}} \right]^{\frac{k}{k-1}} \left[\frac{Q}{D^2} - \frac{1}{2(k^2 - 1)} \right]^{-\frac{1}{k-1}} \tag{5.13}$$

For decoupled loading in rock blasting, the condition of $P_{CJ} > P_x$ is satisfied. When $P_{CJ} > P_x$, the following relationship for the particle velocities at the explosive-air interface, expressed in terms of the detonation wave and the reflected shock wave is given by Henrych (1979) as:

$$V_x = V_{CJ} + V_r \tag{5.14}$$

where: V_x is the particle velocity at the interface of explosive and air,

V_{CJ} is the particle velocity in the detonation wave from Equation 4.6, and

V_r is the particle velocity in the rarefaction wave.

From the theory dealing with change of momentum for an element of an arbitrary medium:

$$dV_r = \frac{dP}{\rho C} \tag{5.15}$$

The velocity, V_r, can be obtained by

$$V_r = \int_{P_x}^{P_{CJ}} \frac{dP}{\rho C} \tag{5.16}$$

where: ρ and C are the density and the speed of sound in the gas–air mixture, respectively.

Henrych (1979 and Zhang (1993) integrate Equation 5.16 over two sections:

$$\begin{aligned} V_r &= \int_{P_{cr}}^{P_{CJ}} \frac{dP}{\rho C} + \int_{P_x}^{P_{cr}} \frac{dP}{\rho C} = \int_{C_{cr}}^{C_{CJ}} \frac{2}{k-1} dC + \int_{C_x}^{C_{cr}} \frac{2}{\gamma - 1} dC \\ &= \frac{2}{k-1}(C_{CJ} - C_{cr}) + \frac{2}{\gamma - 1}(C_{cr} - C_x) \end{aligned} \tag{5.17}$$

where:

$$C_{CJ} = \frac{k}{k+1} D \tag{5.18}$$

$$\frac{C_{cr}}{C_{CJ}} = \left(\frac{P_{cr}}{P_{CJ}}\right)^{\frac{k-1}{2k}} \tag{5.19}$$

$$\frac{C_x}{C_{cr}} = \left(\frac{P_x}{P_{cr}}\right)^{\frac{k-1}{2k}} \tag{5.20}$$

Substituting Equations 4.6, 5.17, 5.18, 5.19 and 5.20 into Equation 5.14, the particle velocity of the interface, V_x, can be obtained.

$$\begin{aligned} V_x = {} & \frac{D}{k+1}\left\{1+\frac{2k}{k-1}\left[1-\left(\frac{P_{cr}}{P_{CJ}}\right)^{\frac{k-1}{2k}}\right]\right\} \\ & +\left[\frac{2kD}{(\gamma-1)(k+1)}\left(\frac{P_{cr}}{P_{CJ}}\right)^{\frac{k-1}{2k}}\right]\left[1-\left(\frac{P_x}{P_{cr}}\right)^{\frac{\gamma-1}{2\gamma}}\right] \end{aligned} \tag{5.21}$$

The shock wave generated in the air by the explosion is characterized by the following parameters: particle velocity, V_m, pressure, P_m, density, ρ_m, and shock wave velocity D_a. The corresponding equations are defined by Henrych (1979) and Zhang (1993) as:

$$V_m = \sqrt{\frac{2P_m}{(\gamma_m+1)\rho_{mo}}} \tag{5.22}$$

$$\rho_m = \frac{1}{\left(\frac{1}{\rho_{mo}} - \frac{V_m{}^2}{P_m}\right)} \tag{5.23}$$

$$D_a = \frac{\gamma_m+1}{2}V_m \tag{5.24}$$

where: γ_m is the isentropic exponent for air, 1.2.

ρ_{mo} is initial density of air.

Based on the boundary continuity, the following relationships can be satisfied:

$$V_x = V_m \tag{5.25}$$

$$P_x = P_m \tag{5.26}$$

So, the initial shock wave parameters in the air are given by Equations 4.4, 5.12, 5.21, 5.22, 5.23, 5.24, 5.25, and 5.26.

To illustrate the process, an emulsion explosive detonating in a decoupled hole with arbitrary diameters of explosive and hole will be considered. The properties of the explosive are:

Density: 1.15 g/cc

VOD: 4500 m/s

Detonation pressure: 5821 MPa and

Relative weight strength: 0.9

The properties of air are:

Initial density: 0.001225 g/cc

k: 3(first stage)

γ: 1.4(second stage) and

γ_m: 1.2(air)

The results for air shock are:

Pressure on the air-explosive interface: 33.2 MPa

Particle velocity: 4969 m/s

Shock wave velocity: 5466 m/s and

Density: 0.001377 g/cc

The pressure on the air in the borehole (33.2 MPa) is much smaller than the detonating pressure (5821 MPa). However, the shock wave velocity in the air (5466 m/s) is larger than the VOD of the explosive (4500 m/s). This difference can cause channel effect because the air shock wave propagates ahead of the detonation front. Unreacted segments of the explosive charge may become over compressed and desensitized by the air shock pressure. Although the air shock pressure is much smaller than the detonation pressure, it may be high enough to desensitize some industrial explosives, such as emulsions sensitized by gas or plastic microspheres. Channel effect can cause explosive charge failure in decoupled rock blasting.

5.3 Shock Wave Parameters on the Borehole Wall

When the shock wave is transmitted from one medium (air-gas) into another medium (rock), both reflection and transmission occur at the interface. This is illustrated in Figure 5.3, where subscripts (A) and (B) represent medium A and medium B, respectively; 0 represents the initial condition; 1 is the condition at the shock wave front; and 2 is the condition at the reflected wave front; P is shock wave pressure and V is particle velocity.

To solve for the shock wave parameters at the interface between different media, a method of interactions of shock waves is applied as presented by Cooper (1996). The term “air-gas” refers to the mixed materials from detonated explosive and air in the decoupled borehole. First, a Hugoniot for the air-gas is constructed (Cooper, 1996).

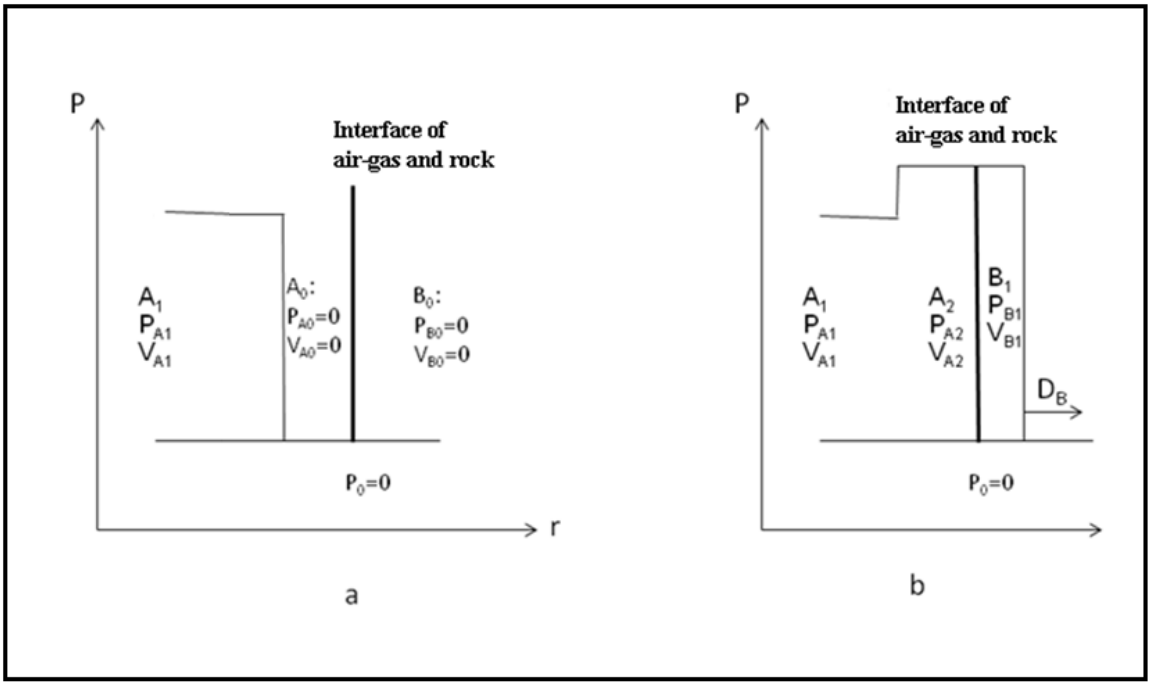

Figure 5.3. Shock wave transfer from medium A (air-gas) into medium B (rock), modified from Henrych (1979):
a: mefore incidence of the detonation wave
b: after incidence of the detonation wave

$$P_{ma} = \rho_{ma} c_a (2V_{ma} - V_a) + \rho_{ma} s_a (2V_{ma} - V_a)^2 \qquad (5.27)$$

where: P_{ma} is the shock wave pressure at the air-gas shock wave front,

ρ_{ma} is the density at the air-gas shock wave front,

c_a is the speed of sound in the air-gas,

s_a is the Hugoniot constant of the air-gas,

V_a is the particle velocity at a point in the air-gas, and

V_{ma} is the particle velocity at the air-gas shock wave front.

The change in density at the air-gas shock zone in the decoupled borehole is very complicated. For a cylindrical charge, it is proposed that the density in this zone can be estimated using the decoupled ratio and velocity of detonation according to the following:

$$\rho_{ma} = \frac{D}{k_v}\rho_m\left(\frac{r_e}{r_h}\right)^{2\gamma} \tag{5.28}$$

where: k_v is an assumed constant (800 m/s) which proves reasonable when compared to empirical results (Esen et al. 2003). Experimental data of decoupled loading by Esen et al. are obtained using concrete samples with the decoupling ratio from 1.25 to 2 (see Section 8.4) , and r_e and r_h are the radius of the charge and borehole, respectively. Then, the Hugoniot for the rock (B) can be expressed (Cooper 1996) as:

$$P_r = \rho_r c_r V_r + \rho_r s_r V_r^2 \tag{5.29}$$

where: P_r is the shock wave pressure at the shock wave front in the rock,

ρ_r is the density at the shock wave front in the rock,

V_r is the particle velocity at the shock wave front in the rock,

c_r is the speed of sound in the rock,

s_r is the Hugoniot constant of the rock, and

V_r is the particle velocity at the point of interest in the rock.

Based on boundary continuity, at the air-gas and rock interface:

$$P_r = P_{ma} \tag{5.30}$$

$$V_r = V_a \tag{5.31}$$

So, by combining Equations 5.14, 5.21, 5.22, 5.23, 5.24, 5.25, 5.26, 5.27, 5.28, 5.29, 5.30, and 5-31, the pressure and particle velocity on the wall of the borehole can be calculated.

As an example, consider a borehole with 51 mm diameter in marble using a centered emulsion explosive charge 32 mm in diameter. The properties of the explosive are:

Density:	1.15 g/cc
VOD:	4500 m/s
Relative weight strength:	0.9 and
Charge diameter:	32 mm

The properties of air are:

Initial density:	0.001225 g/cc
k:	3
γ:	1.4 and
γ_m:	1.2

The properties of the air-gas are:

c_a:	899 m/s and
s_a:	0.939

The given parameters of marble are:

Density, ρ_o:	2.7 g/cc
Longitudinal wave speed, c_r:	4000 m/s
Hugoniot constant, s_r:	1.32 and
Borehole diameter:	51 mm

The pressure and particle velocity on the wall of the borehole are:

Pressure:	2158 MPa and
Particle velocity:	188.2 m/s

The borehole pressure is 2158 MPa for marble from the SWT method. This pressure is substantially different than 1578 MPa resulting from Equation 5.2 (γ=1.4). Clearly, the borehole pressure from the SWT model depends on the properties of both explosive and rock. In contrast, the results from Equation 5.2 do not consider the properties of the rock.

6. PREDICTION OF DYNAMIC STRENGTH OF ROCK

Under different loading conditions, rock is reported to exhibit different behaviors. As indicated in Chapter 2 researchers report that both dynamic compressive strength and tensile strength increase as the strain rate increases (Prasad 2000; Lama 1978). The dynamic factor is the ratio of the dynamic strength of rock to the static strength of rock. The dynamic factor for tensile strength and the dynamic factor for compressive strength are different for the same rock. The dynamic factor is given by:

$$K_{cd} = \frac{\sigma_{cd}}{\sigma_c} \tag{6.1}$$

$$K_{Td} = \frac{\sigma_{Td}}{\sigma_T} \tag{6.2}$$

where: K_{cd} is dynamic factor for compressive strength,

K_{Td} is dynamic factor for tensile strength,

σ_{cd} is dynamic compressive strength,

σ_c is static compressive strength,

σ_{Td} is dynamic tensile strength and

σ_T is static tensile strength.

6.1 Dynamic Compressive Strength of Rock

As indicated in Section 2.1, it is reasonable to multiply the static compressive strength values by a factor of 1.5-2.5 to estimate the dynamic compressive strength. In the crush zone around the borehole, the ultimate compressive strength of rock under confined conditions is used. Under confined conditions, the compressive strength of rock is larger than its uniaxial compressive strength. Practically speaking, the confined compressive strength of rock is 2 to 4 times its uniaxial compressive strength, and frequently even more (Jaeger and Cook 1976; Hoek and Brown 1980). As illustrated in Figure 6.1, compressive strength of Carrara marble increases as the confining stress increases (Jaeger and Cook 1976). In Figure 6.1, the unconfined uniaxial compressive strength (p=0) is about 20,000 psi (134 MPa). The confined compressive strengths are 33,000 psi (227 MPa), 47,000 psi (324 MPa), 87,000 Psi (600 MPa) when confining pressures are 3,400 psi (23 MPa), 7250 psi (50 MPa) and 24,000 Psi (165 MPa), respectively.

Because the uniaxial compressive strength of rocks is conveniently obtained, it can be used to estimate the dynamic compressive strength of rocks (σ_{cConfd}):

$$\sigma_{ctrid} = K_{cd} K_{Conf} \sigma_c \tag{6.3}$$

where: K_{cd} is dynamic factor for compressive strength (at high level strain rate K_{cd}=2). K_{Conf} is confined pressure condition factor. K_{Conf} can be determined by the method documented by Hoek and Brown (1997):

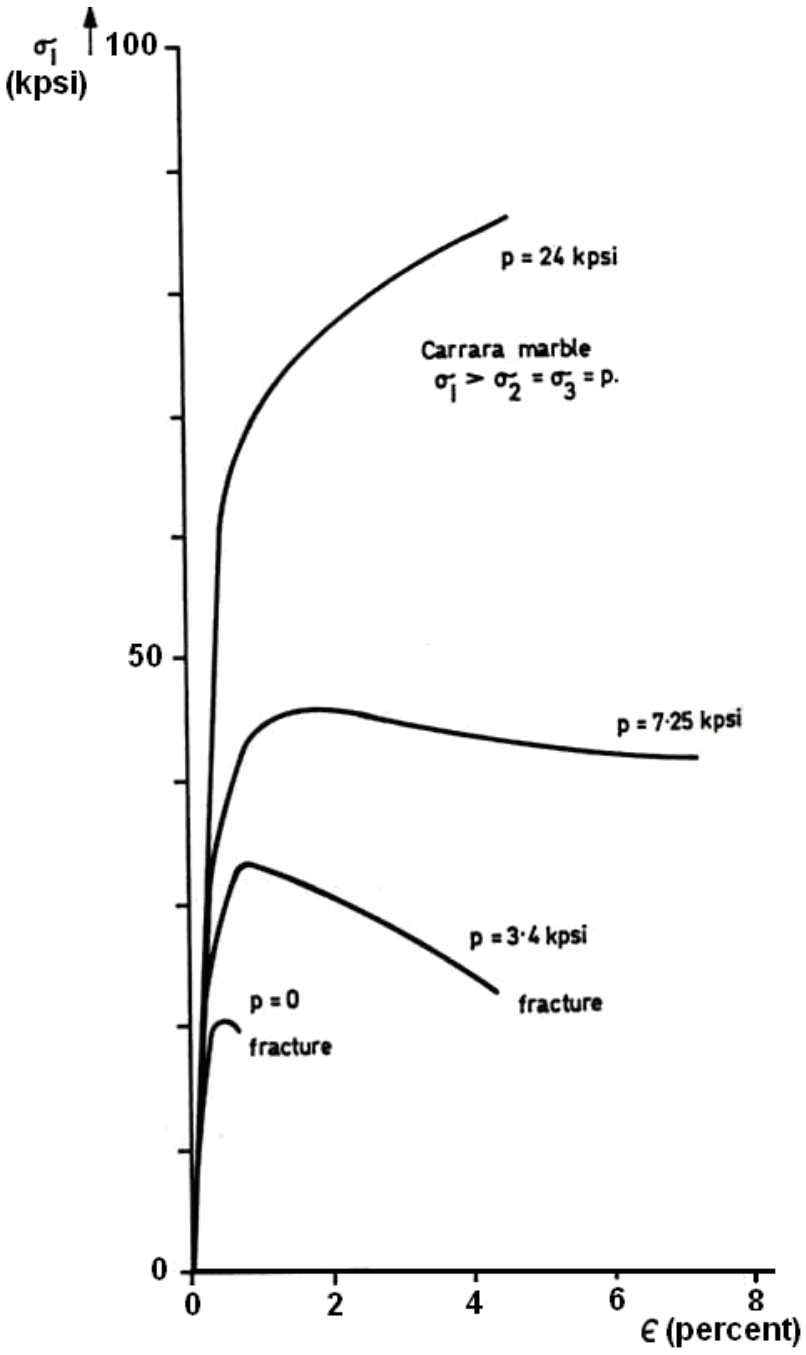

Figure 6.1. Compressive strength of rock under confined conditions, modified from Jaeger and Cook (1976)

$$K_{Conf} = \frac{\sigma_3}{\sigma_c} + (m\frac{\sigma_3}{\sigma_c} + 1)^{\frac{1}{2}} \quad (6.4)$$

where: m is a constant, presented on Table 6.1, and σ_3 is the minimum effective stress, in the range of $0 < \sigma_3 < 0.5\ \sigma_c$. When $\sigma_3 = 0.4\ \sigma_c$, the factor K_{Conf} is between 2.0 and 4.2.

6.2 Dynamic Tensile Strength of Rock

Generally, the increase in magnitude for dynamic tensile strength of rock at high strain rates is greater than the increase in dynamic compressive strength with high strain rates. Section 2.3 shows that the dynamic tensile strengths of rocks are about 2 to 13 times the static tensile strengths. The tensile dynamic factors presented by different researchers vary considerably. The reasons for this include the microstructure of rocks

Table 6.1. Value of the constant *m*, modified from Hoek and Brown (1997)

Rock	Texture	m	K_{Conf}	Rock	Texture	m	K_{Conf}
Claystone	Very fine	4	2	Sparitic limestone	Medium	10	2.6
Slate	Very Fine	9	2.5	Gypstone	Medium	16	3.1
Obsidian	Very Fine	19	3.3	Holnfels	Medium	19	3.3
Siltstone	Fine	9	2.5	Amphibolite	Medium	25-31	3.3
Mictitic limestone	Fine	8	2.4	Schists	Medium	8	2.2
Anhydrite	Fine	13	2.9	Dolerite	Medium	19	3.3
Quartzite	Fine	24	3.7	Breccia	Medium	18	3.3
Mylonites	Fine	6	2.2	Conglomerat	Course	22	3.5
Phyllites	Fine	10	2.6	Breccia	Course	20	3.4
Rhyolite	Fine	16	3.1	Marble	Course	9	2.5
Dacite	Fine	17	3.2	Migmatite	Course	30	4
Andesite	Fine	19	3.3	Gneiss	Course	33	4.2
Basalt	Fine	17	3.2	Granite	Course	33	4.2
Tuff	Fine	15	3	Granodiorite	Course	30	4
Sandstone	Medium	19	3.3	Diorite	Course	28	3.9
Creywacke	Medium	18	3.3	Gabbro	Course	27	3.8
Chalk	Medium	7	2.3	Norite	Course	22	3.5
Coal	Medium	21	2.4	Agglomerate	Course	20	3.4

and the strain rates used in experimental work. Usually, large dynamic factors result from high strain rate tests in the range of 10^2 to 10^4/sec. Smaller values result from the low strain rate tests in the range of 10^0 to 10^2/sec, Cho et al. (2003).

6.3 Estimation of Strain Rate for Rock Blasting

Higher level strain rates (10^2 to 10^4/sec) occur near the borehole crush zone. The dynamic compressive strength factor is about 2 at this strain rate. Beyond the crush zone, the strain rate is much lower. Favreau (1969) presents a theoretical analysis for the detonation of a spherical charge in an infinite, isotropic, and homogeneous medium. To estimate the tensile strain rate, the tangential strain can be expressed as:

$$\varepsilon_\theta = \frac{{r_h}^3 P}{2\alpha^2 r^3} + e^{\frac{-\alpha^2\tau}{\rho_r V_p r_h}} \left[\begin{array}{l} \left(\frac{{r_h}^2 P}{\alpha\beta r^2} - \frac{{r_h}^3 P}{2\alpha\beta r^3} \right) \\ \sin\left(\frac{\alpha\beta\tau}{\rho V_p r_h} \right) - \frac{{r_h}^3 P}{2\alpha^2 r^3} \cos\left(\frac{\alpha\beta\tau}{\rho V_p r_h} \right) \end{array} \right] \tag{6.5}$$

The definitions of parameters in Equation 6.5 are presented in Section 2.3.3. The tangential strain rate is

$$\begin{aligned} \varepsilon_\theta' = \frac{d\varepsilon_\theta}{d\tau} = -\frac{\alpha^2}{\rho_r V_p r_h} e^{\frac{-\alpha^2\tau}{\rho_r V_p r_h}} & \left[\begin{array}{l} \left(\frac{{r_h}^2 P}{\alpha\beta r^2} - \frac{{r_h}^3 P}{2\alpha\beta r^3} \right) \\ \sin\left(\frac{\alpha\beta\tau}{\rho V_p r_h} \right) - \frac{{r_h}^3 P}{2\alpha^2 r^3} \cos\left(\frac{\alpha\beta\tau}{\rho V_p r_h} \right) \end{array} \right] + \\ e^{\frac{-\alpha^2\tau}{\rho_r V_p r_h}} & \left[\frac{\alpha\beta}{\rho V_p r_h} \left(\frac{{r_h}^2 P}{\alpha\beta r^2} - \frac{{r_h}^3 P}{2\alpha\beta r^3} \right) \cos\left(\frac{\alpha\beta\tau}{\rho V_p r_h} \right) - \frac{\beta {r_h}^2 P}{2\alpha\rho_r V_p r^3} \sin\left(\frac{\alpha\beta\tau}{\rho V_p r_h} \right) \right] \end{aligned} \tag{6.6}$$

For τ=0, the strain rate is maximum. So

$$\varepsilon_{\theta}^{'} = -\frac{\alpha^2}{\rho_r V_p r_h}\left[-\frac{r_h^{\,3} P}{2\alpha^2 r^3}\right] + \left[\frac{\alpha\beta}{\rho V_p r_h}\left(\frac{r_h^{\,2} P}{\alpha\beta r^2} - \frac{r_h^{\,3} P}{2\alpha\beta r^3}\right)\right] = \frac{\mathrm{Pr}_h}{\rho_r V_p r^2} \tag{6.7}$$

Using ANFO and marble presented in the previous examples, the parameters for cylindrical explosive charges are:

	ANFO #1	ANFO #2	ANFO #3
Density:	0.8 g/cc	0.8 g/cc	0.8 g/cc
VOD:	4500 m/s	3000 m/s	2200 m/s
Charge diameter:	104 mm	104 mm	104 mm
Explosion pressure:	2025MPa,	900MPa	484MPa

The parameters for a typical rock and borehole are

Density: 2.7 g/cc

P-wave velocity: 4000 m/s

Poisson's ratio: 0.25 and

Diameter of borehole: 104 mm

Using Equation 6.7, the tensile strain rate as a function of distance from the charge center is shown in Table 6.2 and Figure 6.2. When different explosives are used, the strain rates are also different. However, the differences are not great. The results indicate that the region very close to the borehole, 1 to 5 times the diameter of the hole, has a high strain rate (10^2-10^3/sec). However, the region of 20 to 50 times the diameter of the hole has a low strain rate (10^0-10^1/sec). This low strain rate area is important because the boundary

Table 6.2. Comparison of strain rates as a function of VOD by Equation 6.7

Scale distance (r/rh)	Distance to charge center (r, m)	Strain rate (/sec, VOD=4500 m/s)	Strain rate (/sec, VOD=3000 m/s)	Strain rate (/sec, VOD=2200 m/s)
1	0.052	7211.5	3205.1	1723.6
2	0.104	1802.9	801.3	430.9
2.5	0.13	1153.8	512.8	275.8
2.8	0.1456	919.8	408.8	219.9
3	0.156	801.3	356.1	191.5
5	0.26	288.5	128.2	68.9
10	0.52	72.1	32.1	17.2
20	1.04	18.0	8.0	4.3
30	1.56	8.0	3.6	1.9
50	2.6	2.9	1.3	0.7
100	5.2	0.7	0.3	0.2

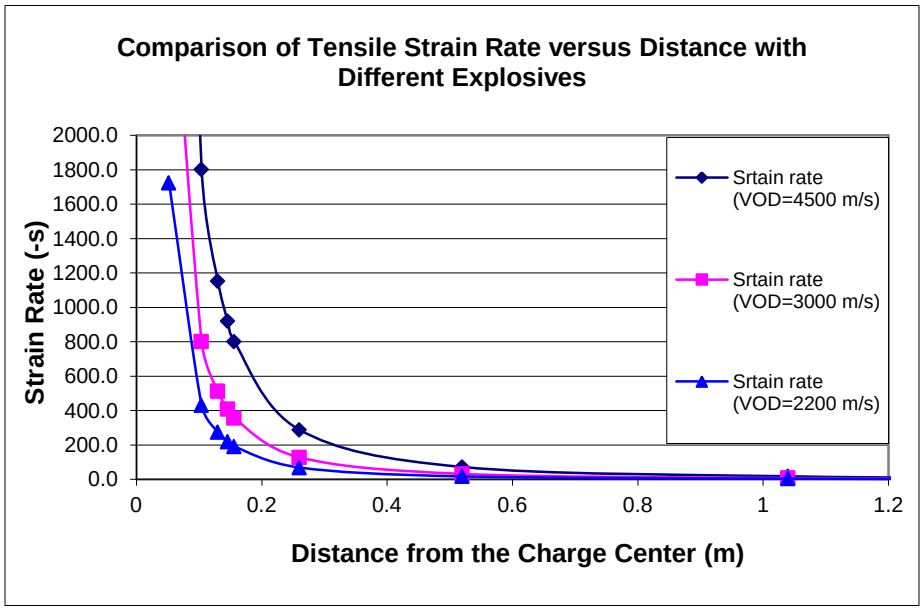

Figure 6.2. Comparison of strain rates as a function of VOD by Equation 6.7 for spherical charges

between damage and non-damage due to blasting occurs here. Generally, the extent of the crack zone for a cylindrical charge of regular ANFO is larger than 20 times the radius of the borehole based on SWT prediction (presented in Chapter 12). So, the strain rate range for this region is 10^0 to 10^1 /sec.

The dynamic tensile strength of rocks can be expressed as:

$$\sigma_{Td} = K_{Td}\sigma_T \tag{6.8}$$

where: K_{Td} is dynamic factor for tensile strength. A value of 2 can be assumed for K_{Td} Two is a conservative estimate given the values reported in the literature (see Section 2.1.2) for the dynamic tensile strength factor. This conservative value is selected because the crack zone is likely to occur in the lower strain rate area. The radius of the crack zone is 36 to 62 times borehole radius in limestone using TNT (Vovk et al. 1973).

7. SHOCK WAVE TRANSFER MODEL FOR PREDICTING THE DAMAGE ZONE IN ROCK BLASTING

Based on the principle of Shock Wave Transfer (SWT) in different media, the extent of the crush and crack zones can be predicted using the properties of the explosive and rock. A step by step explanation of the SWT model is as follows:

1. Using the properties of explosives, the detonation parameters can be estimated using Equations 4.4, 4.5, 4.6, and 4.7.
2. The shock wave parameters for a given rock can be calculated using the detonation parameters and the properties of the rock. In the fully-coupled condition, Equations 4.4, 4.14, 4.17, 4.18 and 4.19 are used to estimate the shock wave parameters in the rock. In the decoupled condition, Equations 4.4, 5.12, 5.21, 5.22, 5.23, 5.24, 5.25, 5.26, 5.27, 5.28, 5.29, 5.30, and 5.31 are employed to estimate the shock wave parameters in the rock.
3. The extent of a crush zone can be estimated by borehole pressure and the properties of the rock utilizing Equations 3.13 and 6.3. Once the extent of the crush zone is known, the extent of the crack zone can be estimated by using the properties of the rock and Equations 3.13, 3.16 and 6.8.

The properties relating to the explosive include:

- Density
- VOD

- Relative weight strength
- Diameter of charge

The properties relating to the rock include:

- Density
- P-wave velocity
- S-wave velocity
- Uniaxial static compressive strength
- Uniaxial static tensile strength
- Hugoniot constants
- Dynamic factor K_{cd}
- Dynamic factor K_{Td}
- Confined loading condition constant K_{Conf}
- Diameter of the borehole

In the SWT model, prediction models for fully-coupled and decoupled conditions can be developed for the crush zone and the crack zone. The conditions are shown in Figures 7.1 and 7.2. The computer code for SWT damage predictions is written in Visual Basic. This code provides the extent of the crush and the crack zones for a given set of parameters. The flow diagram for the SWT computer code is presented in Figure 7.3. The code may be found in Appendix A.

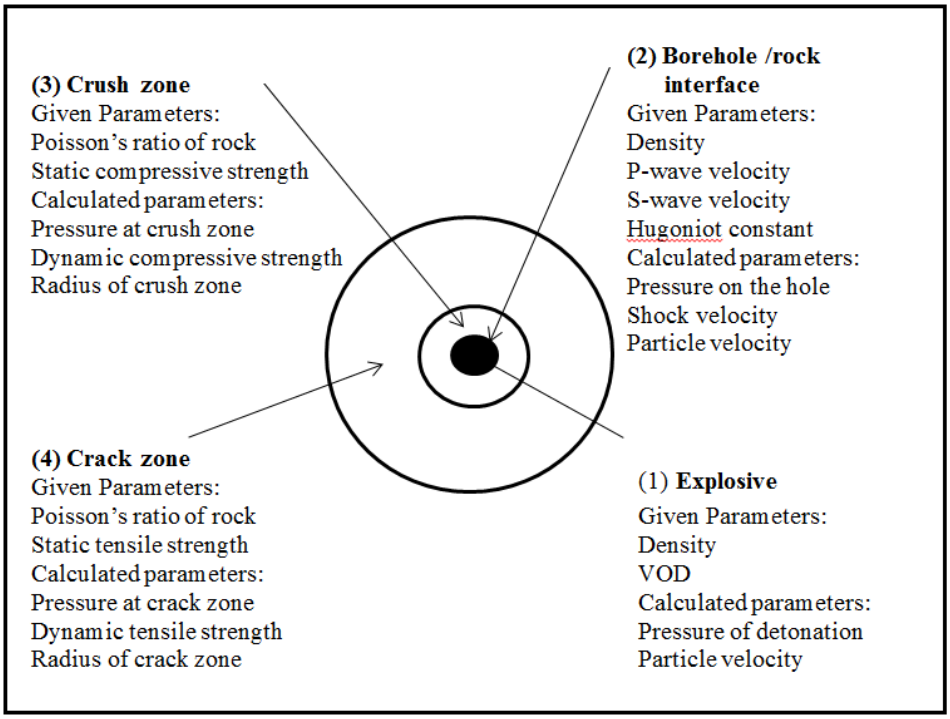

Figure 7.1. Schematic process for solving the fully-coupled condition for rock blasting

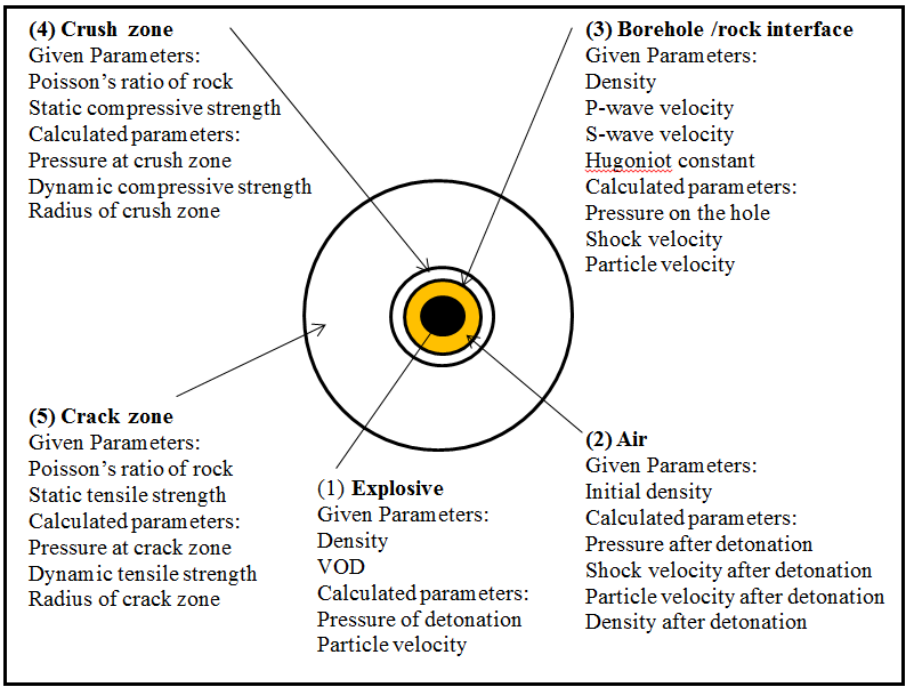

Figure 7.2. Schematic process for solving the decoupled condition for rock blasting

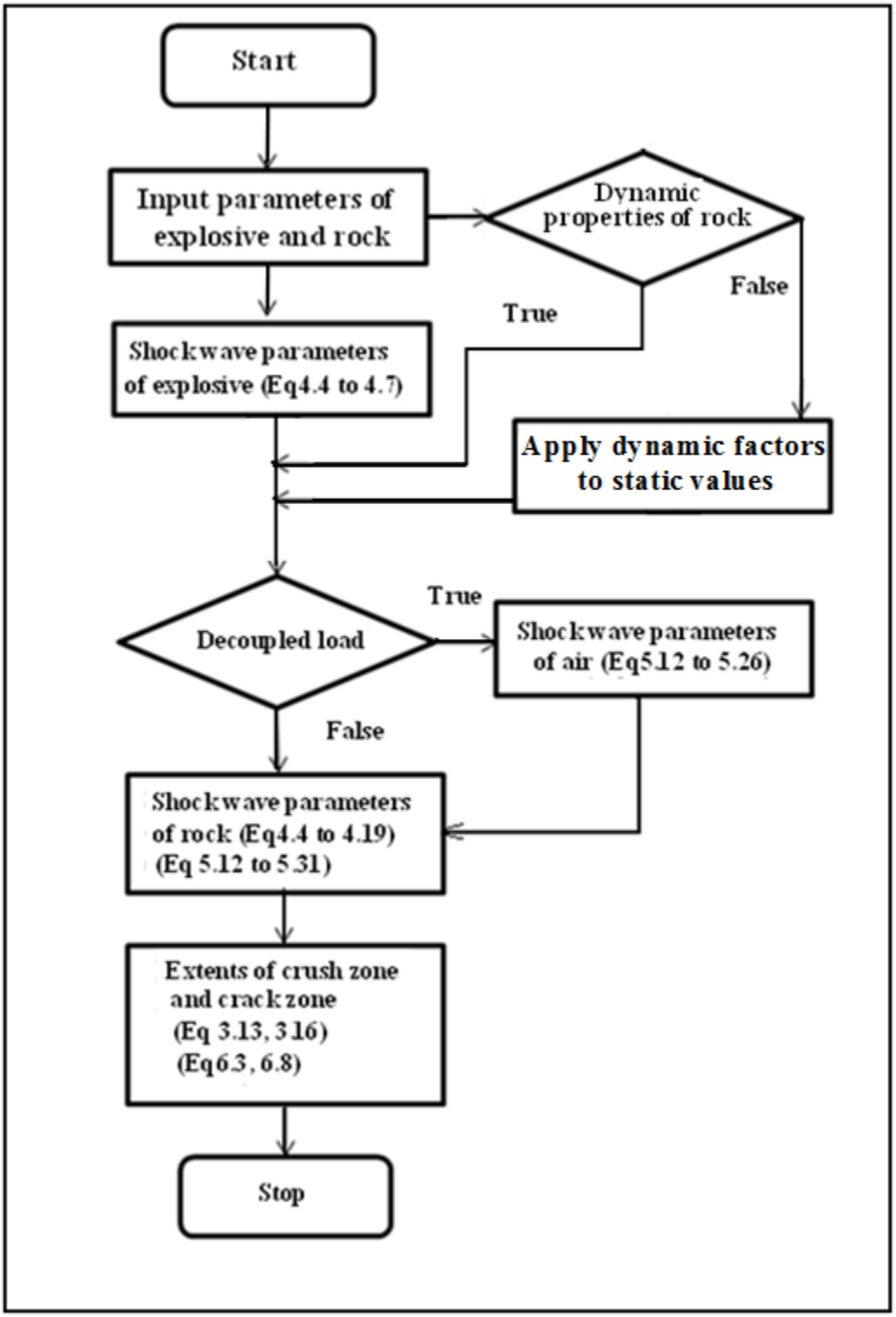

Figure 7.3. Computational flow diagram for the SWT computer code

8. VALIDATION OF SWT WITH EXISTING EXPERIMENTAL DATA

As a damage zone prediction model, SWT is different from any other approach published in current literature. To validate this approach, existing experimental data will be used to compare predicted versus actual extent of crush and crack zones for rock and concrete.

8.1 Comparison Involving Pressure Estimation

In rock blasting, pressure measurement near the borehole wall is difficult to accomplish. However, Liu (2002) has published some experimental data for pressure measurements at this interface. He used a fully-coupled emulsion explosive in a 32 mm hole to blast granodiorite. The parameters relating to the explosive are

Density:	1.18 g/cc
VOD:	4300 m/s and
Diameter of cylindrical charge:	32 mm

The parameters relating to the rock are

Density:	2.72 g/cc
P-wave velocity:	5600 m/s
Hugoniot constant (assumed):	1.4
Poisson's ratio:	0.25

Uniaxial compressive strength: 153 MPa

Constant K_{Conf} (assumed): 4

Dynamic factor K_{cd} (assumed): 2

Dynamic factor K_{Td} (assumed): 2 and

Tensile strength: 14 MPa

The pressure near the borehole was measured using an indirect method. The pressure gauges were inserted in water-filled receptor holes around the borehole (see relative distance from borehole – Table 8.1). Then, the pressure in the rock was calculated using an impedance mismatch method (Liu 2002):

$$P_r = \frac{\rho_w c_w + \rho_r c_r}{2\rho_w c_w} P_w \tag{7.1}$$

where: P_r is the pressure in rock,

P_w is the pressure in water,

ρ_r is the density of rock,

ρ_w is the density of water,

c_r is the velocity of sound in rock, and

c_w is the velocity of sound in water.

To predict the pressure near the borehole with the SWT method, Equations 3.8, 3.13, 3.16, 4.4, 4.14, 4.17, 4.18 and 4.19 are used. A comparison of results obtained by SWT and Liu's empirical measurements are shown in Table 8.1 and Figure 8.1. The results indicate that this approach satisfactorily estimates conditions for granodiorite. In this example, the crush zone and the crack zone were not measured. Based on the

Table 8.1. Comparison SWT pressure estimates and measurements, modified from Liu (2002)

Scale distance (r_h/r)	Distance to charge center (r, m)	Calculated pressure by SWT (MPa)	Measured by Liu (MPa)
1.0	16	8837.0	
2.1	33	1221.9	
11.3	180	517.5	
12.3	197	115.7	135.7
13.1	210	106.4	105.6
15.1	241	88.0	90.86
15.9	254	82.2	94.4
15.9	254	82.2	119.2
16.3	260	79.5	73.2
18.6	298	66.7	80.2
19.1	305	64.4	91.5
19.1	305	64.4	49
19.4	311	63.0	60.1
19.4	311	63.0	40.1
24.6	394	45.9	59.6
25.4	406	44.0	71.3
31.3	500	33.3	

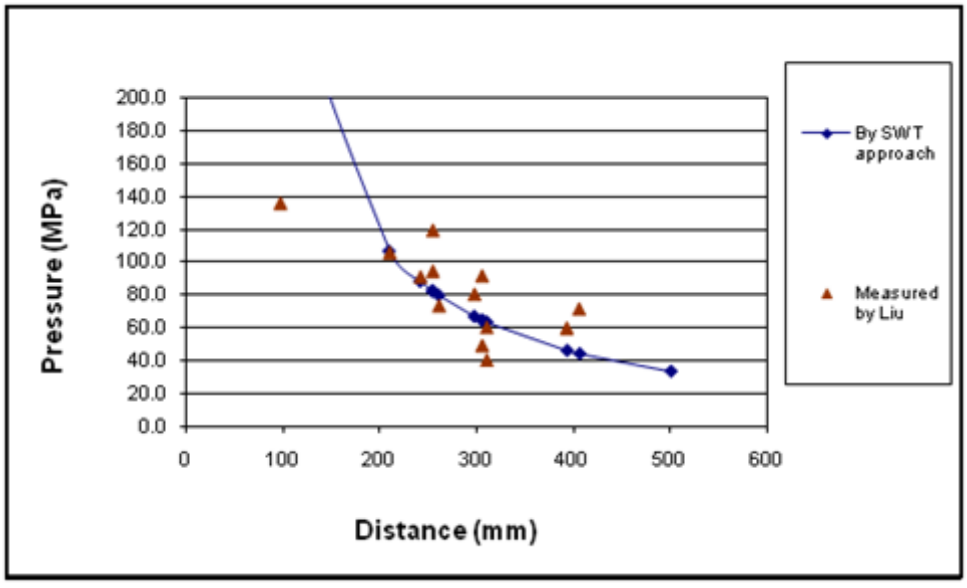

Figure 8.1. Comparison of pressures by SWT and measurements, modified from Liu (2002)

calculated values using the SWT model, the crush zone is 37 mm (2.3 times the radius of the borehole) and crack zone is 512 mm (32 times the radius of the borehole).

8.2 Comparison of Peak Particle Velocity Estimation and Experimental Data

Because the peak particle velocity (PPV) is easily measured, it is broadly applied in predicting damage caused by rock blasting. A large amount of PPV data are available for points located at some distance from the borehole or blasting site. Constants in Equation 2.11 (K, α, and β) can be determined by regression of experimental data. However, it is difficult to obtain the PPV close to the borehole, particularly at a distance of 1 to 20 times the borehole radius. Some available PPV data are presented by Holmberg and Persson (1978). A comparison of data from Holmberg and Persson with that predicted by SWT is presented below.

The parameters of the explosive (aluminized TNT-based watergel) are:

Density:	1.5 g/cc
VOD:	5000 m/s
Charge diameter:	171 mm and
Charge density:	34 kg/m

The assumed parameters of the rock are:

Density:	2.6 g/cc
P-wave velocity:	4000 m/s
Poisson's ratio:	0.28
Hugoniot constant:	1.4
S-wave velocity:	2200 m/s

Uniaxial compressive strength: 170 MPa

Tensile strength: 8 MPa

Constant K_{Conf}: 3.0

Dynamic factor Kcd: 2.0

Dynamic factor K_{Td}: 2.0 and

Hole diameter: 171 mm

Equations 3.8, 3.13, 3.16, 4.4, 4.14, 4.17, 4.18 and 4.19 are employed by SWT to calculate the PPV around the borehole. The comparison is summarized in Table 8.2 and Figure 8.2. The SWT approach agrees with the measured data for 99 to 315 times the radius of the borehole.

8.3 Comparison of the Crack Zone Estimation and Experimental Data

Direct visual measurement of the extent of the crack zone by wire-sawing is expensive, and data are very limited. The most complete available data set for crack measurement for rock blasting was produced by Olsson et al. (1993). Their experiments were carried out in a quarry for dimension stone in southern Sweden. This quarry contains fine grain granite with very few natural cracks. The granite is very competent and has a compressive strength of 197 MPa and a tensile strength of 12 MPa. In their experiments, six kinds of explosives were used. The parameters of the explosives are shown in Table 8.3 and the properties of the granite are presented in Table 8.4.

The comparison of experimental data developed by Olsson et al. (1993) and SWT is presented in Table 8.5 and Figure 8.3. The results indicate that the SWT provides reasonable values. Only two prediction results show a large deviation compared to the

Table 8.2. Comparison of SWT with Holmberg and Persson empirical measurements of PPV, modified from Holmberg and Persson (1978)

Scale Distance	Distance (m)	Calculated by SWT (m/s)	Measured (Holmberg and Persson 1978)
2.5	0.2	126.330	
4.9	0.4	54.608	
11.5	1.0	19.421	
14.2	1.2	15.058	
17.2	1.5	11.993	
24.5	2.1	7.789	
36.8	3.1	4.769	
49.0	4.2	3.367	
61.3	5.2	2.570	
73.5	6.3	2.062	
99.2	8.5	1.434	1.442
122.5	10.5	1.111	
147.0	12.6	0.891	
164.2	14.0	0.780	0.562
196.0	16.8	0.629	
314.9	26.9	0.355	0.283
490.1	41.9	0.208	

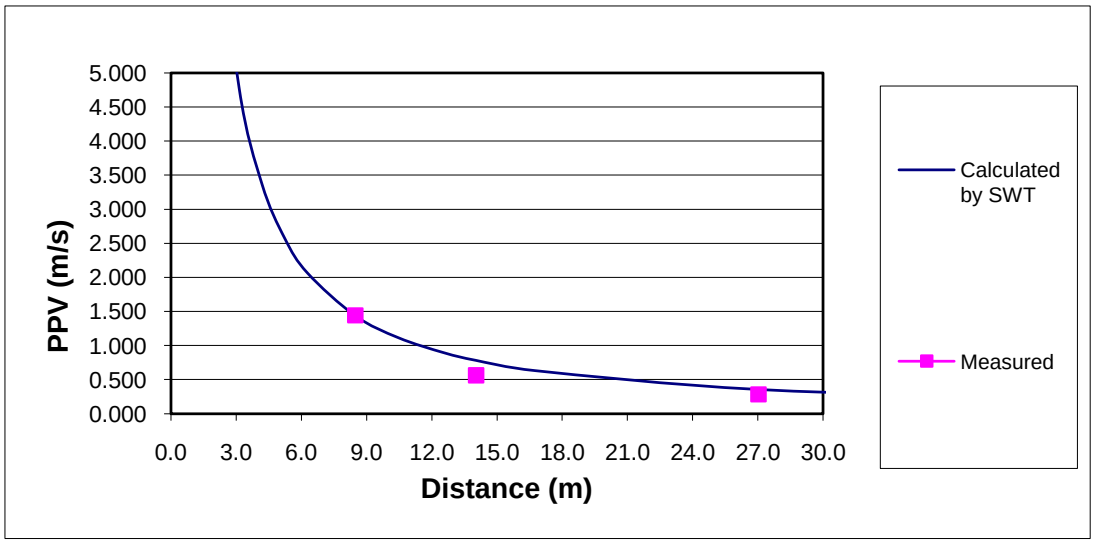

Figure 8.2. Comparison of SWT and empirical calculations and measurements, modified from Holmberg and Persson (1978)

Table 8.3. Explosive parameters, modified from Olsson et al. (1993)

Explosive	Density (g/cc)	Energy (MJ/kg)	Diameter of explosive (mm)	VOD (m/s)	Relative weight strength *
Gurit	1	3.4	17	2200	1.1
Kimulux	1.15	3.2	22	4800	1.2
Emullet 20	0.25	2.6	Bulk	1850	0.2
Emullet 50	0.5	2.6	Bulk	2650	0.4
Detonex	1.05	5.95	8.3	6500	2.0
Detonex	1.05	5.95	10.6	6500	2.0

*Weight strength relative to standard ANFO (energy of ANFO: 3.9 MJ/kg, and density: 0.82 g/cc)

Table 8.4. Rock parameters for granite, modified from Olsson et al. (1993)

Parameter	Value
Density (g/cc)	2.67
P-wave velocity (m/s)	4800
S-wave velocity (m/s)	2550
Compressive strength (MPa)	200
Tensile strength (MPa)	10-15
Constant K_{Conf} (Assumed)	3.5
Dynamic factor K_{cd} (Assumed)	2
Dynamic factor K_{Td} (Assumed)	2
Hugoniot constant s (Assumed)	1.4

Table 8.5. Crack length comparison with data, modified from Olsson et al. (1993)

Hole # and explosive	Density (g/cc)	Diameter explosive (mm)	VOD (m/s)	Diameter hole (mm)	Measured crack Length (cm)	Predicted crack Length by SWT (cm)
#1 Gurit	1	17	2200	38	44	29
#2 Gurit	1	17	2200	51	28	22
#3 Gurit	1	17	2200	64	20	17
#4 Kimulux	1.15	22	4800	38	45	88
#5 Kimulux	1.15	22	4800	51	35	89
#6 Emullet 20	0.25	Bulk	1850	38	40	32
#7 Emullet 50	0.5	Bulk	2650	38	80	82
#8 Detonex	1.05	8.3	6500	38	22	25
#9 Detonex	1.05	10.6	6500	38	30	42

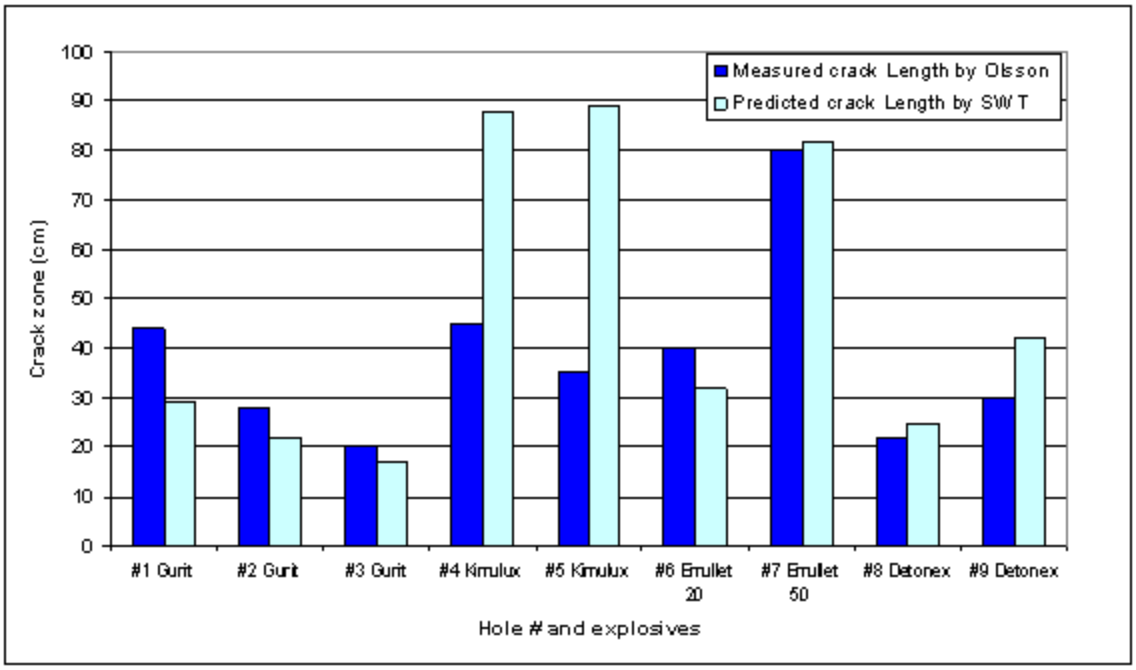

Figure 8.3. Comparison of Olsson et al. (1993) data and SWT prediction

experimental data, i.e., experiment # 4 and #5 (see Table 8.5). SWT appears to over-predict the extent of cracks. The other values are fairly reasonable. The explosive, Kimulux (22 mm in diameter) was used in test #4 and #5. From the manufacturer's specifications, the VOD of Kimulux is 4800m/s under the condition of no confinement. Unfortunately, the VOD was not verified under field conditions.

8.4 Comparison of SWT Crush Zone Estimate with Experimental Data

Esen et al. (2003) conducted a large number of experiments in which the crush zone was experimentally measured. In their study, two kinds of explosives were used, Gelatin dynamite and Elbar 1 dynamite. Ninety-two concrete samples were tested. The sample dimensions were 1.5 m x 1.0 m in cross section and 1.1 m in height. Different concrete strengths were employed. Physical and mechanical properties of the concrete

samples are shown in Table 8.6. Properties of the explosives are shown in Table 8.7. Experiments included both fully-coupled and decoupled loading conditions. The experimental results are shown in Table 8.8.

The data obtained by Essen et al. (2003) are very appropriate for validating the SWT approach, because all input parameters needed for SWT calculations were measured or otherwise available. Figure 8.4 presents measured and predicted relative distance r/r_h for the extents of the crush zone using Gelatin dynamite versus the compressive strength of samples. Figure 8.5 presents the same values for Elbar 1 dynamite. Both Figure 8.4 and Figure 8.5 are fully-coupled conditions. Figure 8.6 shows both measured and predicted relative distance r/r_h using Elbar 1 dynamite for the crush

Table 8.6. Physical and mechanical properties of concrete samples, modified from Esen et al. (2003)

Sample	UCS (MPa)	Static Tensile strength (MPa)	Density (g/cc)	V-wave velocity (m/s)	S-wave velocity (m/s)	Young's modulus (GPa)	Poisson's ratio
Low strength (-)	6.7	0.3	2.26	3372	1871	20.2	0.278
Low strength (+)	10.5	0.8	2.27	3752	2064	24.8	0.283
Medium strength (-)	16.3	1.2	2.29	3935	2157	27.3	0.285
Medium strength (+)	24.6	2.9	2.38	4553	2471	37.5	0.291
High strength (-)	42.1	2.2	2.34	4341	2363	33.7	0.29
High strength (+)	56.5	4.3	2.46	4891	2642	44.4	0.294

Table 8.7. Properties of explosives, modified from Esen et al. (2003)

Property	Gelatin dynamite	Elbar 1 dynamite	Remarks
Density (g/cc)	1.5	1.0	
Velocity of detonation (m/s)	1278	1081	Unconfined 16 mm diameter charge
Energy (kj/kg)	4700	3760	
Relative weight strength	2.1	1.18	

Table 8.8. Experimental measurements, modified from Esen et al. (2003)

Parameter	Fully-coupled tests	Decoupled tests
Explosives	Gelatin dynamite, Elbar 1 dynamite	Elbar 1 dynamite
Decoupled ratio	1	1.25, 1.5, 1.75, 2.0
Borehole diameter (mm)	16 -20	20, 24, 28, 32
Burden (cm)	22.7-46.2	18.2-31.3
Hole depth (cm)	40.4-45.4	39.8-45.0
Specific charge (kg/m^3)	0.11-0.25	0.15-0.175
Explosive amount (g)	8.0-22.8	7.8-16.1
Stemming material	1.18-3 mm aggregate	1.18-3 mm aggregate
Stemming length (cm)	26.5-40.3	20.0-39.6

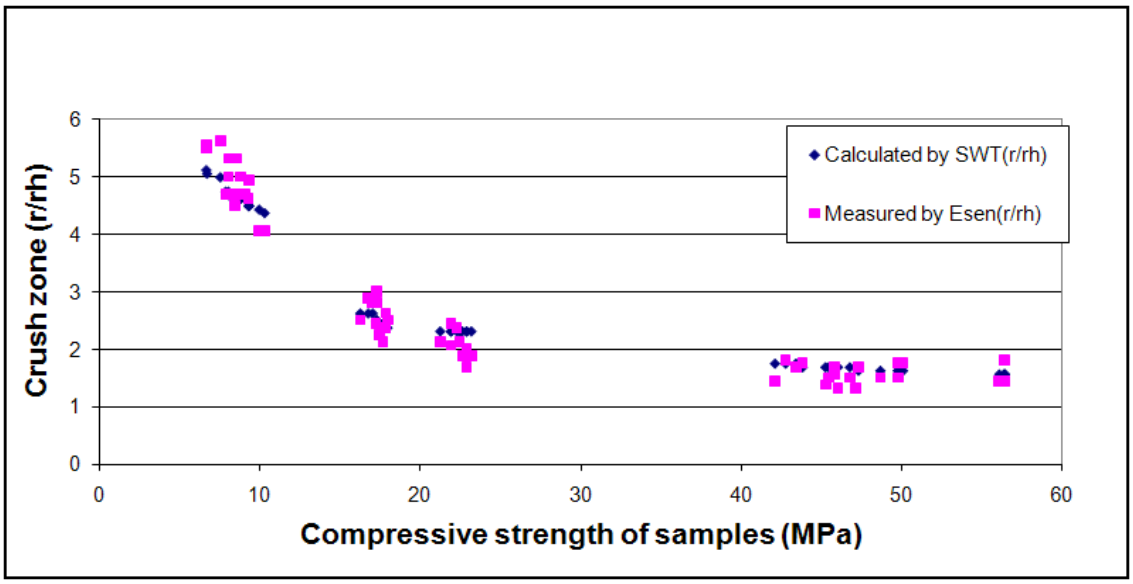

Figure 8.4. Comparison of measured and SWT predicted crush zone (scale distance) (fully-coupled condition using gelatin dynamite). Data source: Sedat Esen

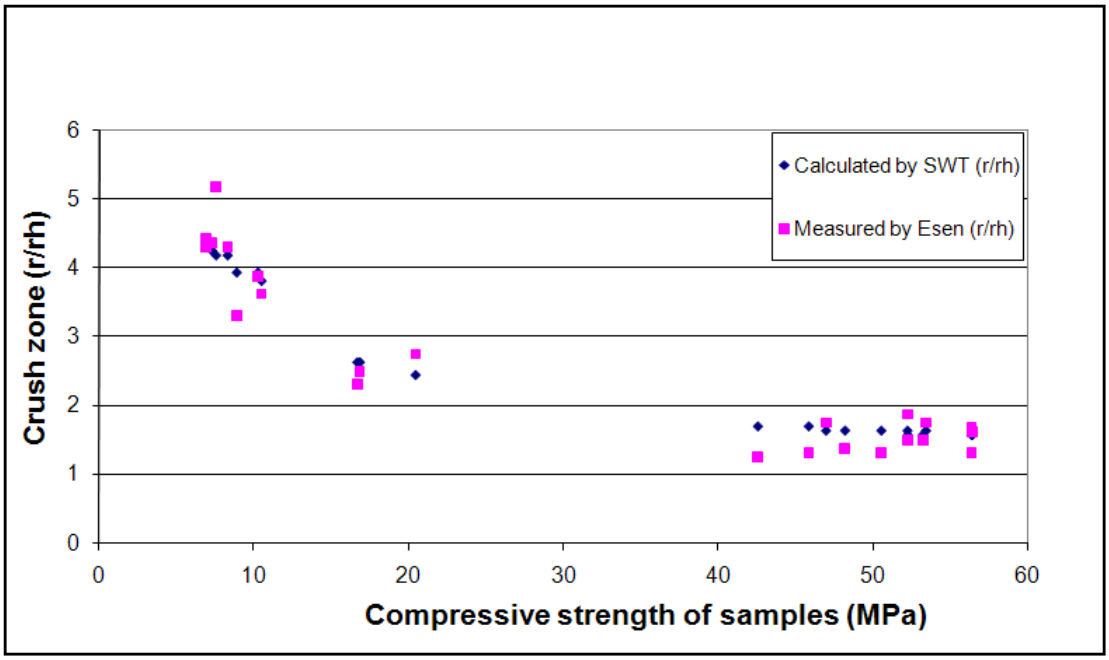

Figure 8.5. Comparison of measured and SWT predicted crush zone (scale distance) (fully-coupled condition using Elbar 1 dynamite). Data source: Sedat Esen

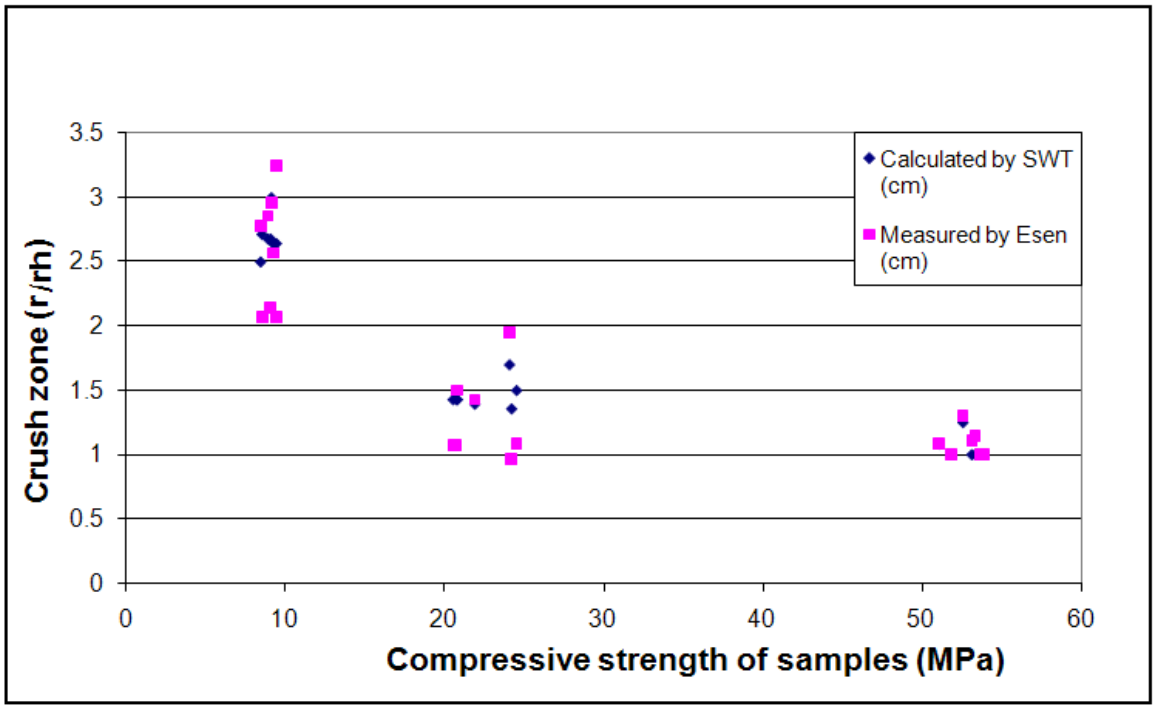

Figure 8.6. Comparison of measured and SWT predicted crush zone (scale distance) (decoupled condition using Elbar 1 dynamite). Data source: Sedat Esen

zone versus the compressive strength of samples, under decoupled conditions. From these comparisons, it can be seen that SWT predictions agree very well with the measurements reported by Esen et al. (2003).

8.5 Validation of SWT with Existing Approaches

Hustrulid (2010) evaluates an actual blast design using five different approaches. These five approaches include the Modified Ash (Energy-based), Modified Ash (Pressure-based), Holmberg Explosive Factor, Neiman Hydrodynamic, and Sher Quasi-Static. The objective was to compare the estimated radius of the damage zone for easer holes and perimeter holes in a drift design. The properties of rock and explosive are shown in Tables 8.9, and 8.10. For comparison, the same rock and explosive properties were used in the SWT method. The results of all six methods are reported in Tables 8.11, and 8.12. As can be seen the results of the SWT model are very close to all methods with exception of the Neiman Hydrodynamic model. However, one of the advantages of the SWT model over the five methods presented is the ability to estimate the crush zone. This ability provides a unique design option for engineers. By constraining the crush zone to a small value or zero, an improved perimeter blast is possible which can be validated by the "half-casts" displayed on the walls and back of the tunnel.

8.6 Summary of SWT Prediction with Existing Experimental Data

Based on the comparison of calculated values with existing experimental data, the results for the extent of crush zone are very encouraging. SWT estimates coincide fairly well with Olsson's experimental data, but the properties of the explosive were obtained

Table 8.9. Rock properties

Parameter	Value
Rock type	Monzonite
Density (g/cc)	2.8
Young's modulus (MPa)	72000
Poisson's ratio	0.28
P-wave velocity (m/s)	5900
Unconfined compressive strength (MPa)	150
Tensile strength (MPa)	22
Friction angle	45°
Diameter of borehole (mm)	48

Table 8.10. Explosive properties

Parameter	Value
Explosive type	Site sensitize emulsion
Density (g/cc)	0.85
VOD (m/s)	4300
Energy (MJ/kg)	3.1
Gas volume (L/kg)	950
Relative weight strength (RWS) s_{ANFO}	0.84
Adiabatic constant	3
Diameter of charge	48 mm for easer hole, 34 mm for perimeter hole

Table 8.11. Damage radius for easer hole

Approach	Damage radius (R_d/r_h)	Damage radius (m)	Extent of crush zone (mm)
Modified Ash Energy-based	22	0.5	NA
Modified Ash Pressure-based	30	0.7	NA
Holmberg Explosive Factor	24	0.6	NA
Neiman Hydrodynamic	33	0.8	NA
Sher Quasi-Static	28	0.7	NA
SWT	25	0.6	26

Table 8.12. Damage radius for perimeter hole

Approach	Damage radius (R_d/r_h)	Damage radius (m)	Extent of crush zone (mm)
Modified Ash Energy-based	17	0.4	NA
Modified Ash Pressure-based	17	0.4	NA
Holmberg Explosive Factor	17	0.4	NA
Neiman Hydrodynamic	23	0.6	NA
Sher Quasi-Static	14-18	0.3-0.4	NA
SWT	17	0.4	11

from manufacturers' specification rather than field measurements. Also, the properties for the rock involved in the experiments were not systematically measured at the experimental site. Esen's 92 large-scale concrete specimens provide a robust sample set for comparison. However, even this work does not include dynamic properties of concrete or explosive properties measured in the detonating holes, and concrete is used rather than actual rock. Esen's data set also does not provide the extent of the crack zones surrounding the boreholes. Therefore, additional experiments are needed to provide all data required for calculations using the SWT method. Based on the comparison with other approaches, the SWT model is close to the Modified Ash (Energy-based), Modified Ash (Pressure-based), Holmberg Explosive Factor, and Sher Quasi-Static models, the exception is the Neiman Hydrodynamic model. One of the advantages of the SWT model over the five methods presented is the ability to estimate the crush zone.

9. PRELIMINARY LABORATORY EXPERIMENTS

Very little existing experimental data are available for the extent of the crush and crack zones. Data that can be found in the literature are generally lacking the properties of explosives and rocks specific to the experimental site. Therefore, in this dissertation, new laboratory experiments are designed in an attempt to provide data necessary to validate the SWT model.

Preliminary laboratory tests were necessary to investigate the static and dynamic parameters of specimens as well as the properties of the explosives. In addition, the preliminary work provided experience for preparing grout samples, explosive loading methods, VOD measurements, and strain measurements for the subsequent large-scale laboratory experiments. Grout was selected to make the large-scale models because it has relatively high strength, low cost and can be molded into appropriate shapes. The large-scale experiments are needed to produce damage zones under various blasting conditions.

Based on the theoretical model described in the flow chart (Figure 7.3), prediction of the extent of damage in rock blasting requires knowledge of the properties of explosives and rocks used in the models. Explosive parameters may be determined by laboratory experiments or from data provided by the makers of the explosives. Estimates of static rock/grout properties can be determined by conventional laboratory tests. Table 9.1 summarizes the explosive properties and the respective calculated parameters. The

Table 9.1. Properties of explosives

Explosive parameters	PETN	207X	Parameter usage
Density (g/cc)	Specification From manufacture	Measured	For P_h, V_h calculation
Velocity of detonation (m/s	Measured	Measured	For P_h, V_h calculation
Relative energy	Calculated	Specification From manufacture	For P_h, V_h calculation (decoupled condition)
Diameter of charge (mm)	Measured	Measured	For R_{crush}, R_{crack} calculation
γ, γ_m, k	Assumed	Assumed	For R_{crush}, R_{crack}calculation (decoupled condition)

material properties and their usage in the SWT model are summarized in Table 9.2.

9.1 Selection of Appropriate Modeling Material

To select an appropriate material for laboratory experiments, five brands of grout were tested. The tests include set time, volume change, and cracking. The compressive strength reported by the manufacturer and availability are also factors to be considered. The primary test results and manufacturer specifications of these grout types are shown in Table 9.3. It indicates that Horn Grout (Tamms Industries), Premier Grout (L&M Construction Chemicals), and Supreme Grout (Cormix Construction Chemicals) have compressive strengths approaching those of rocks, the ability to cure without shrinkage or development of detrimental cracks, and reasonable setting time needed to mix

Table 9.2. Properties of rocks/grout

Rock parameters	Source	Parameter usage
Density (g/cc)	Measured	For P_h, V_h, R_{crush}, R_{crack} calculation
Poisson's ratio	Measured	For R_{crush}, R_{crack} calculation
Young's modulus (GPa)	Measured	
Compressive strength (MPa)	Measured	For R_{crush}, R_{crack} calculation
Tensile strength (MPa)	Measured	For R_{crush}, R_{crack} calculation
Dynamic compressive strength (MPa)	Measured	For R_{crush}, R_{crack} calculation
Dynamic tensile strength (MPa)	Measured	For R_{crush}, R_{crack} calculation
P-wave velocity (m/s)	Measured	For P_h, V_h, R_{crush}, R_{crack} calculation
S-wave velocity (m/s)	Measured	For R_{crush}, R_{crack} calculation
Hugoniot constant	Estimated	For P_h, V_h, R_{crush}, R_{crack} calculation
Diameter of borehole (mm)	Measured	For R_{crush}, R_{crack} calculation

Table 9.3. Grout characteristics

Grout	Set time	Volume change	Cracks	Compressive strength from manufacture's specification (MPa)	Availability
1107 Advantage Grout (DaytonSuperior)	Too fast	Expansion	Sample fractured when mold was removed	35-62	Local supplier
Premier Grout (L&M Construction Chemicals)	Work -able	OK	Random cracks develop on the surface of sample when thickness exceeds 4 in	41-65	Out of state
Pakmix Grout (Pakmix)	Too fast	Expansion	Sample fractured when mold was removed	25-35	Local supplier
Horn Grout (Tamms Industries)	Work -able	OK	Similar to Premier grout	35-52	Local supplier
Supreme grout (Cormix Construction Chemicals)	Work -able	OK	Similar to Premier grout	54-68	Existing stock not sufficient. No longer manufactured

*Workable indicates that the mixed grout will begin to harden in about 30 minutes or more

and pour desired shapes. Finally, Horn Grout (Tamms Industries) was selected because of its availability.

Because of the chemical reaction of hardening and hydration in the grout sample, internal forces are produced as the material sets. Because of the effect of internal forces, cracks occur in grout castings that exceed 102 mm in thickness. The large-scale samples needed for laboratory experiments must exceed 102 mm thick. The method used to eliminate these cracks will be described in Section 9.4.2.

9.2 Static Experiments

Horn grout samples with 57 mm in diameter and 127 mm in length were prepared for static compressive strength, Young's modulus, and Poisson's ratio experiments.

Biaxial strain gages were attached on diametrically opposite sides of each sample. The details are described in the following sections.

9.2.1 Strain Gage

Strain gage selection is based on the static or dynamic loading conditions, test materials, and specimen structure. Generally, the use of small strain gages is better for approximating the specific point strain value. For dynamic measurement, the length of strain gages used should satisfy the following relationship, (Dai 2002):

$$l \le \frac{V}{20 f} \tag{9.1}$$

where: V is P-wave velocity of the material (m/s),

f is the frequency of the wave (Hz), and

l is length of strain gage (m).

For strain rates on the order of 20 to 25 KHz and V= 4600 m/s, the length of the strain gage should be less than 8.2 to 11.5 mm. The average particle size in the grout is less than 1 mm. The optimum gage must be small enough to accurately record the dynamic strain and not to alter the properties of the specimen when embedded within the sample but large enough to average the strain over multiple particles. A review of available gages resulted in selecting CEA-05-125UW-350, manufactured by Micro-Measurements Group, Inc. was considered to be the best choice. This gage is shown in Figure 9.1, and its dimensions are presented in Table 9.4.

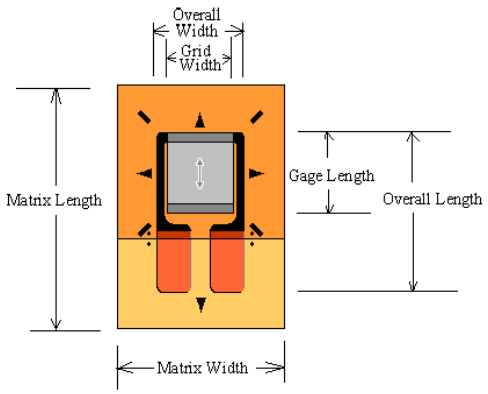

Figure 9.1. The CEA-05-125UW-350 strain gage,
modified from Micro-Measurements (2005)

Table 9.4.The dimensions of the strain gage CEA-05-125UW-350

Dimensions	mm
Gage Length	3.18
Overall Length	8.26
Grid Width	4.57
Overall Width	4.57
Matrix Length	10.7
Matrix Width	6.9

9.2.2 Test Specimen Preparation

The test specimen preparation includes casting the grout sample and installing the strain gages in samples. The manufacturer's instructions were followed for grout sample preparation and strain gage installation.

Cylindrical specimens were cast measuring 57 mm in diameter and 127 mm in length. After curing for 7 days, the ends of the specimens were cut with a diamond saw producing a length-to-diameter ratio of 2:1. The ends of the specimen were then ground parallel within 400 μm/cm on a semi-auto feeding grinding machine. For static tensile strength (Brazilian method), specimens were cut with a diamond saw producing disks with dimensions of 57 mm in diameter and 19 mm in thickness. A grout sample with stain gages attached is shown in Figure 9.2.

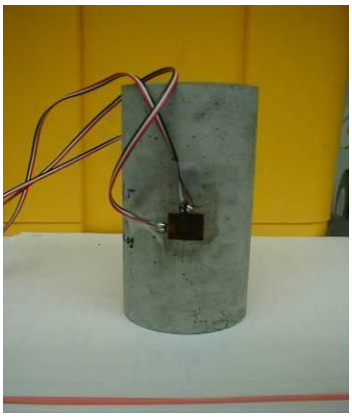

Figure 9.2. Grout sample with strain gages

9.2.3 Density of Grout Samples

Densities of grout samples were determined by measuring the dimensions of cylindrical samples and the mass of the cylinders. The samples were dried in an oven for 4 hours at a temperature of 40^{o}C. The resulting measurements are shown in Table 9.5.

9.2.4 Compressive Strength, Young's Modulus, and Poisson's Ratio

Compressive strength, Young's modulus, and Poisson's ratio of grout specimen were determined using a uniaxial testing machine capable of producing 2672.725 kN maximum axial compressive force. The control system for the testing machine is a TestStar IIm, manufactured by MTS. The computer program, MultiPurpose TestWare®, is also produced by MTS. Digital strain indicators by Micro Measurements Group,

Table 9.5. The dimensions and densities of grout specimens

Specimen	Diameter (mm)	Length (mm)	Density (g/cc)
#1	61.78	110.40	2.267
#2	62.07	111.88	2.243
#3	62.01	122.49	2.313
#4	60.49	126.59	2.289
Aaverage			2.278

Model of P-3500 were used to measure strains in the specimens. Test procedures are described:

The loads on the specimens were applied continuously at a constant stress rate of 0.5-1.0 MPa/sec, and both the loads and strains were automatically recorded by the testing machine control system and computer. Each sample was loaded to failure. The maximum recorded stress provided the uniaxal compressive strength. Young's modulus was obtained by the secant method, (Bieniawski et al. 1981). When stress, σ, is equal to 50% of the uniaxal compressive strength, the Young's modulus, E, is calculated by the following equation:

$$E = \frac{\sigma}{\varepsilon} \tag{9.2}$$

where: σ is stress, and

ε is strain.

Poisson's ratio of the grout sample was obtained from the circumferential and longitudinal biaxial strain gages mounted on the sample. It was calculated by:

$$\nu = \frac{\varepsilon_{lat}}{\varepsilon_{long}} \tag{9.3}$$

where: ν is Poisson's ratio,

ε_{lat} is transverse (circumferential) strain, perpendicular to the load direction, and

ε_{long} is axial strain, parallel to the load direction.

Poisson's ratio is that value determined by Equation 9.3 using ε_{lat}, and ε_{long} at 50%

of the uniaxal compressive strength. Test data from a typical grout sample are shown in Figure 9.3. A summary of the numerical data is shown in Table 9.6. A typical posttest grout sample is shown in Figure 9.4.

9.2.5 Tensile Strength Measurements

Tensile strength of the grout samples was measured using the Brazilian test method. The tensile strength can be obtained by the following equation (ASTM C496-96):

$$\sigma_T = \frac{2P}{\pi\, lD} \tag{9.4}$$

where: P is load on the sample (N),

π is the constant (3.14) Pi,

D is the diameter of the sample (m), and

l is the length of the sample (m).

The tensile strength results are shown in Table 9.7. The posttest grout samples are shown in Figure 9.5.

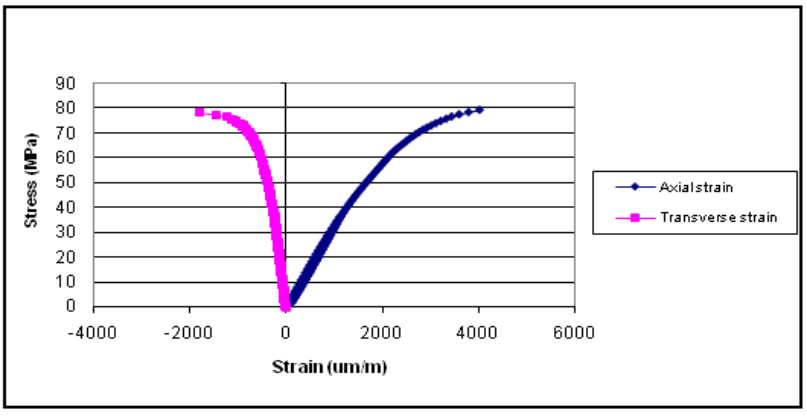

Figure 9.3. Stress versus strain for Horn grout sample #1

Table 9.6. Density, Young's modulus, Poisson's ratio, and compressive strength of grout specimens

Specimen	Density (g/cc)	Young's modulus (GPa)	Poisson's ratio	Compressive strength (MPa)
#1	2.267	31.6	0.21	79.2
#2	2.313	41.6	0.25	81.0
#3	2.289	32.0	0.24	80.0
Average	2.278	34.1	0.23	80.1

Figure 9.4. Posttest grout sample #1, uniaxal compressive strength test

Table 9.7. Tensile strength of grout samples

Sample	Thickness (mm)	Diameter (mm)	Load (N)	Tensile strength (MPa)
#1	17.75	60.55	9354.55	5.53
#2	17.54	60.58	9354.55	5.60
#3	19.71	60.7	9800.00	5.21
#4	21.22	60.57	9911.36	4.90
Average				5.31

Figure 9.5. Posttest grout samples, tensile strength test

9.3 Dynamic Experiments

Dynamic experiments include measuring P-wave velocity, S-wave velocity, dynamic tensile strength, dynamic compressive strength, dynamic Young's modulus, and dynamic Poisson's ratio.

9.3.1 P-wave and S-wave Velocity Measurements

P-wave and S-wave velocities are measured in the lab with a Tektronix 221A digital storage oscilloscope and Olympus NDT Model 5073PR Pulser/Receiver. Four samples were tested.

Dynamic Young's modulus and Poisson's ratio can be calculated using P-wave and S-wave velocities by the following equations (Dai 2002):

$$E_d = V_p{}^2 \rho \tag{9.5}$$

$$\nu_d = \frac{V_p{}^2 - 2V_s^2}{2(V_p^2 - V_s^2)} \tag{9.6}$$

where: V_p is P-wave velocity (m/s),

ρ is density of sample (kg/m^3), and

V_s is S-wave velocity (m/s).

The results are shown in Table 9.8.

9.3.2 Dynamic Compressive Strength Measurement

Dynamic compressive strength measurement was determined using a Split Hopkinson Pressure Bar (SHPB). The tests described in this section and in Section 9.3.3

Table 9.8. P-wave and S-wave velocities for grout specimens.

Sample	Length (mm)	Time for P-wave (μs)	P-wave velocity (m/s)	Time for S-wave (μs)	S-wave velocity (m/s)	Dynamic Young's modulus (GPa)	Dynamic Poisson's ratio
Grout #1	110.40	24.85	4442.66	40.20	2746.27	44.74	0.19
Grout #2	111.88	25.20	4439.68	39.35	2843.20	44.21	0.15
Grout #3	122.60	26.05	4706.33	42.00	2919.05	51.23	0.19
Grout #4	126.59	27.25	4645.50	43.60	2903.44	49.40	0.18
Average			4599.83		2852.99	47.57	0.18

were performed by Jeffrey Johnson (Mining Engineer, NIOSH Spokane Research Laboratory, Washington), using a 60 mm SHPB. A diagram of the SHPB device is shown in Figure 9.6. Axial compression results from the striker bar impacting the incident bar. When this occurs, an incident stress pulse is developed. The pulse propagates along the incident bar to the interface between the bar and the specimen. At this point, the pulse is both reflected and transmitted. The reflected wave propagates back along the incident bar, and the transmitted wave attenuates in the specimen and continues into the transmission bar. Both the incident and the reflected waves are measured by strain gauges mounted at midlength of the incident bar surface. Similarly, the transmitted wave is measured by strain gauges on the surface at midlength of the transmission bar (Li and Meng 2003).

Based on wave propagation theory and with a one-dimensional stress assumption, velocities at interfaces 1 and 2 can be calculated using the following equations, (Shan et al. 2000):

$$V_1 = c(\varepsilon_i - \varepsilon_r) \tag{9.7}$$

$$V_2 = c\varepsilon_t \tag{9.8}$$

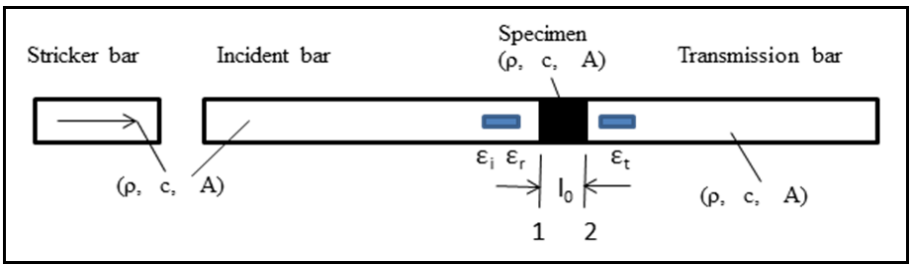

Figure 9.6. Schematic of the Split Hopkinson Pressure Bar

where: V_1 and V_2 are the particle velocities at the sample-bar interfaces,

c is P-wave velocity of the bars, and

ε_i, ε_r, ε_t are incident, reflected and transmitted strains in the bars.

The strain rate of the sample is given by:

$$\dot{\varepsilon}_s = \frac{V_1 - V_2}{l_0} \tag{9.9}$$

where: l_0 is the length of the sample.

Combining Equations 9.7, 9.8 and 9.9:

$$\dot{\varepsilon}_s = \frac{c}{l_0}(\varepsilon_i - \varepsilon_r - \varepsilon_t) \tag{9.10}$$

Forces at the ends of the sample are

$$P_1 = EA(\varepsilon_i + \varepsilon_r) \tag{9.11}$$

$$P_2 = EA\varepsilon_t \tag{9.12}$$

where: E is the Young's modulus of bars, and

A is the area of the sample cross-section.

Stresses at the ends of the sample are

$$\sigma_1 = \frac{EA}{A_s}(\varepsilon_i + \varepsilon_r) \tag{9.13}$$

$$\sigma_2 = \frac{EA}{A_s}\varepsilon_t \tag{9.14}$$

where: σ_1, σ_2 are the stresses at the ends of the sample, and

A_s is the area of cross-section of the sample.

The average force is

$$P_a = \frac{EA}{2}(\varepsilon_i + \varepsilon_r + \varepsilon_t) \tag{9.15}$$

The average stress is

$$\sigma_s = \frac{EA}{2A_s}(\varepsilon_i + \varepsilon_r + \varepsilon_t) \tag{9.16}$$

When forces at the ends of the sample reach dynamic equilibrium, the following condition is satisfied:

$$P_1 = P_2 \tag{9.17}$$

and also

$$\varepsilon_t = \varepsilon_i + \varepsilon_r \tag{9.18}$$

Finally, the stress, strain rate and strain of the sample are given by:

$$\sigma_s = \frac{EA}{A_s}\varepsilon_t \tag{9.19}$$

$$\dot{\varepsilon}_s = \frac{-2c}{l_0}\varepsilon_r \tag{9.20}$$

$$\varepsilon_s = \frac{-2c}{l_0}\int_0^t \varepsilon_r(\tau)d\tau \tag{9.21}$$

The dimensions of the grout sample tested using the SHPB were 60.33 mm in diameter and 73.94 mm in length (the effect of length was assumed negligible). The longitudinal velocity and the density of the grout sample were 4600 m/s and 2.28 g/cc, respectively. The parameters of SHPB are as follows:

- Diameter of incident and transmission bars (d) is 60.325 mm.
- Area of bar cross-section (A) is 28.567 cm^2.
- Bar Young's modulus (E) is 200 GPa.
- Bar longitudinal wave velocity (c) is 4974 m/s.
- Strain gage resistance is 1000 Ohm (½ bridge configration).
- Bridge excitation voltage (V_i) is 22 volts.
- Amplifying factor (AF) is 5.
- Strain gage factor (GF) is 2.115.

The dynamic compressive strength of the grout sample was determined to be approximately 300 MPa by adjusting the curve shown in Figure 9.7 upward to account for the negative value reported as the beginning and end of the test. The static compressive strength of the Horn grout sample was found to be 80 MPa. The same

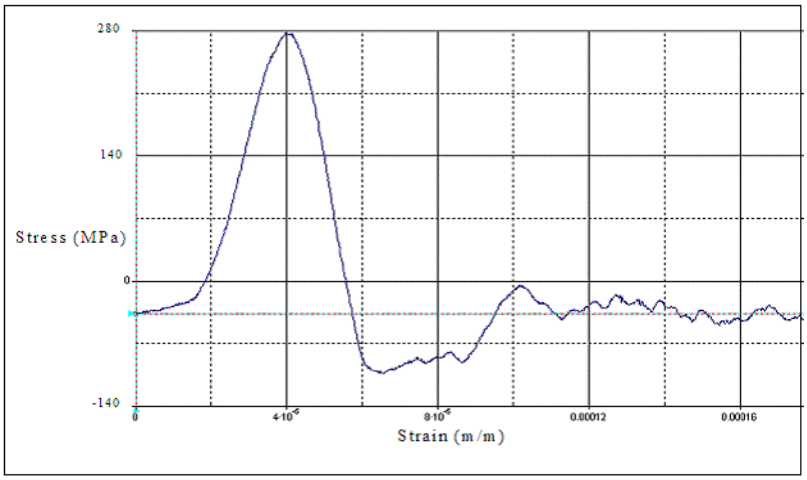

Figure 9.7. Stress-strain curve of Horn grout sample

diameter of samples was used for both static and dynamic tests. The length of the static test sample is 127 mm while that of the dynamic test sample is 73 mm. Consequently, the ratio of dynamic to static compressive strength of Horn grout is about 3.8.

9.3.3 Dynamic Tensile Strength Measurement

The dynamic tensile strength measurement was also determined using the NIOSH SHPB (tests performed by Jeffrey Johnson). The indirect tensile test (Brazilian Test) with the SHPB was employed (Zhao and Li. 2000). A schematic of the tensile test is shown in Figure 9.8. The principle and data reduction method are described in Section 9.3.2. The tensile stress of a sample can be calculated by the following equation:

$$\sigma_T = \frac{2P_a}{\pi\, l_0 D} \tag{9.22}$$

where: P_a is average force on the sample, determined by Equation 9.15.

π is 3.14,

D is the diameter of the sample, and

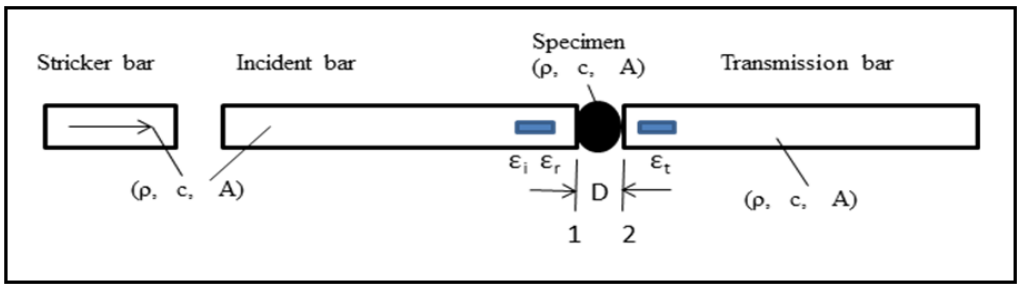

Figure 9.8. Schematic of tensile test with Split Hopkinson Pressure Bar using Brazilian method

l_0 is the length of the sample.

Horn grout samples with dimensions of 50.8 mm in diameter and 25.4 mm in length were tested. The measured dynamic tensile strength for Horn grout is 16.26 MPa. The static tensile strength reported in Table 9.7 is 5.31 MPa. As indicated, the dynamic tensile strength of the grout is approximately three times the static value. This ratio is in good agreement with values reported in the literature in Section 2.1.

9.4 Dynamic Strain Measurement

To verify the ability to measure dynamic strain in the laboratory, a cylindrical grout sample approximately 52 mm in diameter and 280 mm in length was fabricated.

The objective of this experiment was to explore ways of mounting appropriate strain gages and to develop a protocol for acquiring data under dynamic conditions. To measure strain in the grout sample, a CEA-05-125UW-350 (350 Ohm, Micro-Measurements Group, Inc.) strain gage was employed. To install the strain gage inside the sample, a grout slab approximately 12 mm by 30 mm and 5 mm thick was cut using a diamond saw from hardened grout of the same composition used for the experimental cylinder. The strain gage was then cemented to the slab, and the slab was cast into the

larger sample. Details for the grout strain slab preparation are described in Appendix B. The strain gage slab was positioned at the center of the cylindrical sample. A cap hole was located at one end of the cylinder, as shown in Figure 9.9.

A quarter bridge circuit shown in Figure 9.10 was designed to measure the dynamic strain of the specimen. In this figure, R represents fixed resistances of the bridge arms and remains constant. The input voltage and output voltage are measured by V_i, and V_o. The strain, ε, results in a change of resistance ΔR.(constant), input voltage,

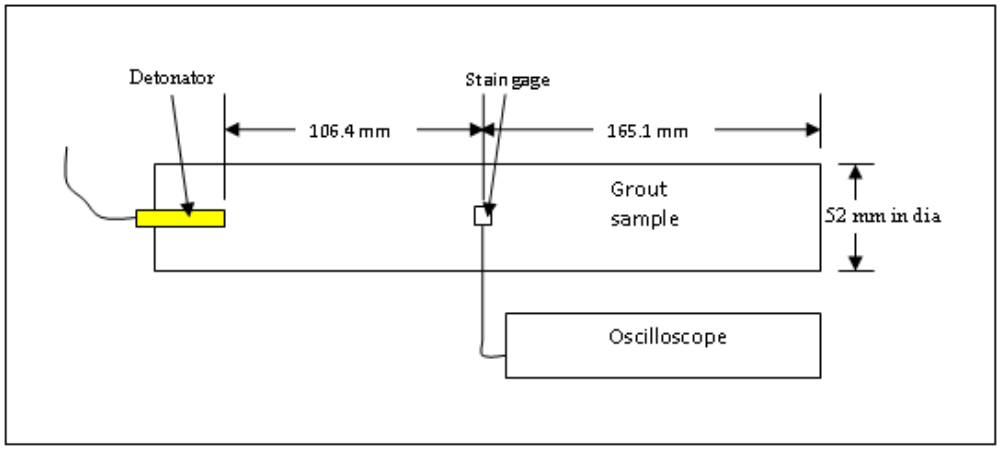

Figure 9.9. Schematic of strain measuring experiment
for a cylindrical sample.

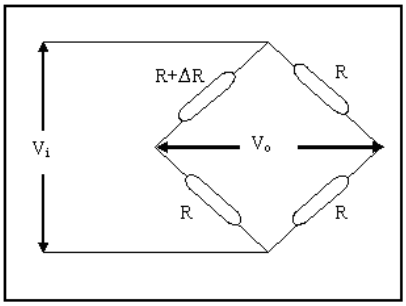

Figure 9.10. Quarter bridge circuit for dynamic strain measurement

output voltage and the strain in the strain gage, respectively. The strain can be expressed as

$$\varepsilon = \frac{\Delta R}{R\,F} \tag{9.23}$$

where: ΔR is the resistance change of strain gage, and F is the strain gage factor.

Then the relationship between strain and the output of the gage is

$$\frac{V_o}{V_i} = \frac{F\varepsilon}{4}\left(\frac{2}{2+F\varepsilon}\right) \tag{9.24}$$

Solving Equation 9.24, the strain can be obtained.

$$\varepsilon = \frac{4V_o}{F(V_i - 2V_o)} \tag{9.25}$$

Based on the energy dissipation capacity of the strain gage from the manufacturer's specification, the range of excitation voltage for the strain gages can be 10 to 12 volts. The output voltage of the strain measuring system, V_o, was recorded by a 2-channel Nicolet 3091 digital storage oscilloscope. Finally, the strain was calculated by Equation 9.25.

The strain measurement results for the cylindrical sample are shown in Figure 9.11. The pretrigger time was set for 0.02 microseconds. The shock wave propagated from cap to gage in an axial direction. The measured maximum strain was 2343 μm/m. This experiment verified that dynamic strain could be measured with available

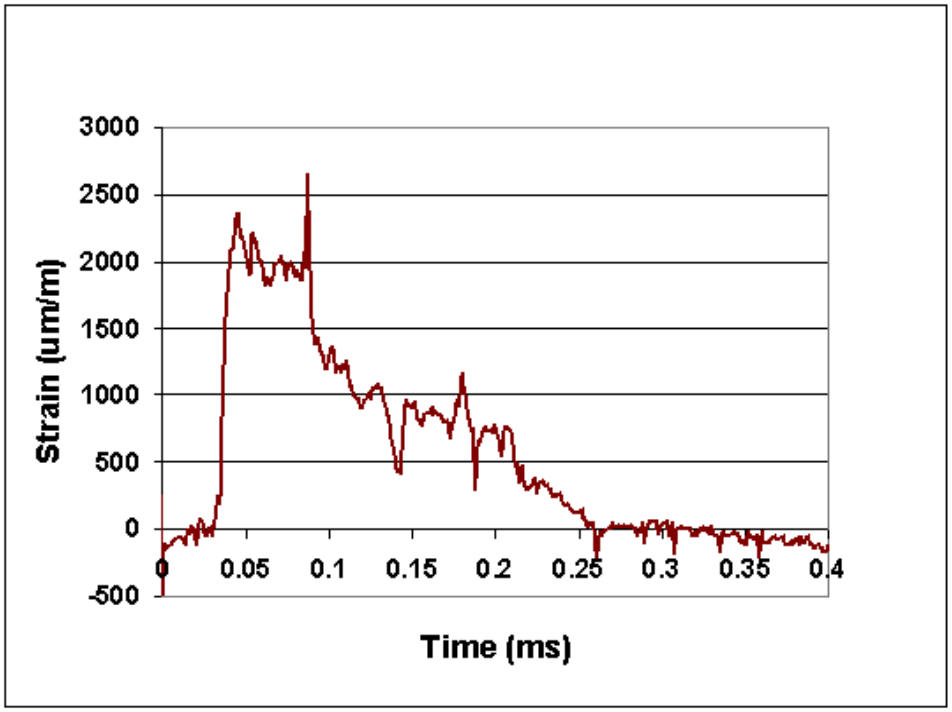

Figure 9.11. Strain versus time for the cylindrical sample

equipment. The signal, however, displayed noise characteristic of strain gages located near detonating explosives.

9.5 Explosive Selection and Laboratory Tests

9.5.1 Explosive Selection

The selection of explosives is limited by the scale of laboratory experiments. The small diameter borehole of a lab test is usually less than the critical diameter of most commercial explosives necessitating the use of more sensitive agents to achieve full order detonation. A practical laboratory explosive should, however, be well-characterized and present little safety hazard. Two explosives, pentaerythritol tetranitrate (PETN) and IRECO 207X seem to fulfill these requirements.

Pentaerythritol tetranitrate (PETN), a molecular explosive, has proven readily detonable with no minimum charge diameter required to achieve full order detonation. Detonating cord consists of a PETN core surrounded by a covering to facilitate handling and to protect the explosive from the surrounding environment. Cords of different explosive strength are manufactured. The "strength" is designed by the amount of PETN per unit length. In the English system of units, the strength is given in grains/ft; whereas, in the metric system it is grams/m. The conversion from one system to the other is 1g/m=5grains/ft. The density of PETN in detonating cord manufactured by Dyno Nobel is 1.4 g/cc. The various products produced by Dyno Nobel are summarized in Table 9.9.

The weight strength of PETN is 1375 cal/g. The VOD of PETN cords (3.6 gram/m and 5 gram/m) is about 7036 m/s by measurement in the laboratory (VOD measurement described in Section 9.5.3). IRECO 207X is a slurry explosive manufactured by IRECO Inc. (now Dyno Nobel). This cap sensitive explosive consists of a continuous aqueous phase containing the oxidizer and a suspended fuel phase consisting primarily of aluminum powder referred to as premix. The two separate components were combined in proportions of 15% premix and 85% solution, agitated, and loaded directly into the specimen boreholes. Lengthening the agitation time heightens the degree of polymer crosslinking and increases the viscosity of the final

Table 9.9. PETN cord diameter, modified from Meng 2004)

Cord (gram/m)	Core diameter (cm)	Outside diameter (cm)
10	0.308	0.470
80	0.252	0.447
5	0.226	0.399
3.6	0.205	0.361
1.5	0.143	0.318
Density	1.4 g/cc	

mixture. The critical diameter of 207X was found to be less than 9 mm, Manufacturer's data suggest a VOD for 207X in a 16 mm borehole of 3500 m/s and calculated energy of 1418 cal/g. Loading densities ranged from 1.16 to 1.20 g/cm^3.

9.5.2 Explosive Loading Method

The smallest hole consistent with the practical diameter for the large-scale samples to be tested is 5.4 mm. For the fully-coupled borehole, this is a very small hole. The surface tension of the small hole is great enough to keep the 207X from running into the hole under gravity alone. To insure a continuous explosive column, a vacuum was used, as shown in Figure 9.12. The evacuation tube is inserted in the bottom of the borehole, and the bottom of the hole is sealed with paper packing. The explosive is then filled from the top of the borehole while the vacuum is applied at the bottom of the borehole. The process is continued until some explosive appears in the evacuation tube. Complete

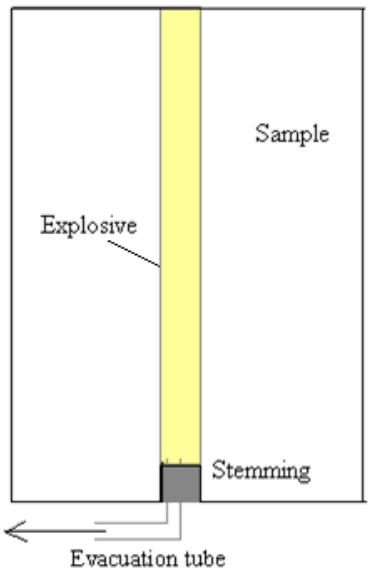

Figure 9.12. Explosive loading process

loading of the hole was confirmed by checking the mass of the explosive loaded into the hole compared to the volume of the hole.

9.5.3 VOD Measurement in the Borehole

Considering that the VODs of explosives are controlled by density, diameter, and confinement of the charge, the VODs of both explosives under anticipated experimental conditions needed to be measured.

To measure the VODs for PETN and 207X, two cylindrical grout samples with a central borehole were fabricated (shown in Figure 9.13). The diameter and length of the samples were 102 mm and 305 mm, respectively. The diameter of the borehole for 207X was 5.4 mm. A 5 gram/m PETN cord was cast in the center of grout sample for the PETN VOD test. A VODEX-100A (DannTech, South Africa) timer was used to measure the rate of detonation. A schematic representing the placement of target wires is shown in Figure 9.14. This figure shows three target wires positioned in the borehole for 207X and for the PETN cord. The distances (d_1, d_2) between the ends of target wires were measured first. Then when explosives were detonated, the arrival time (t) of detonation front at each target wire was measured by the VODEX-100A. The VOD was then calculated by the following equation:

$$D = \frac{d}{\Delta t} \tag{9.26}$$

where: Δt is the difference in arrival time for consecutive target wires.

The VOD results for the explosives are shown in Table 9.10.

Figure 9.13. Grout sample for VOD measurement

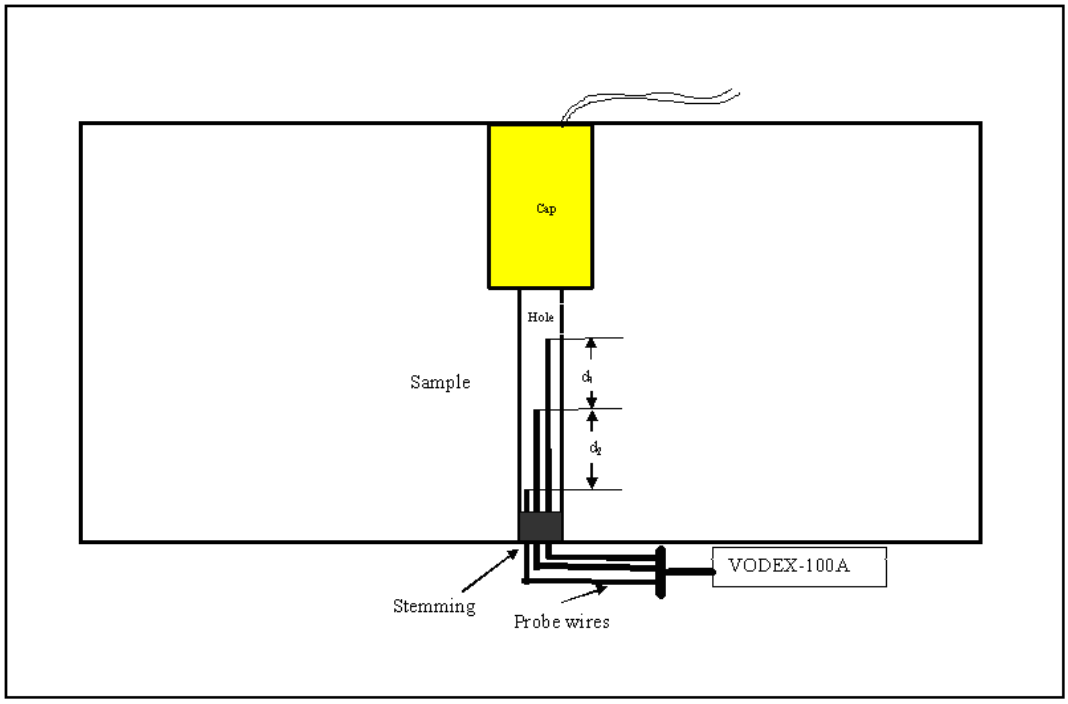

Figure 9.14. Placement of target wires in grout sample hole to measure VOD

Table 9.10. Basic properties for PETN and 207X

Explosive	Density (g/cc)	VOD (m/s)	Charge diameter
PETN (5 gram/m Det cord)	1.4	7000	3.1 mm
IRECO 207X	1.2	1960	5.4 mm

9.5.4 Explosive Detonation Test

On a practical basis, the smallest borehole diameter that can be drilled in large-scale experiments is 5.4 mm. It is important to guarantee that the selected explosive completely detonates in this hole size. Pentaerythritol tetranitrate (PETN) is a molecular explosive, and proven readily detonable with no minimum charge diameter required to achieve full order detonation under either confined or unconfined conditions. On the other hand, 207X is a mixed explosive. A critical detonation diameter test for 207X was conducted because both confined, fully-coupled, and unconfined (decoupled) critical diameters are unknown. For the confined (fully-coupled) condition, the critical diameter of 207X was less than 5.4 mm. It means that 207X with a diameter of 5.4 mm will reliably detonate under confined conditions. For the unconfined (decoupled) condition, the critical diameter for 207X was determined by a series of experiments. The experiments were designed to use thin wall plastic tubes having diameters of 5.4 mm, 6 mm, 7 mm and length of 305 mm to contain the explosives for unconfined VOD tests. Complete detonation is confirmed if the VOD meets product specifications as listed by the manufacturer. If the VOD value is much less, complete detonation is questionable. If a target wire fails to complete the circuit, detonation has failed. The results of the VOD measurements are summarized in Table 9.11.

Table 9.11. Results of critical diameter for IRECO 207X

Test	Critical diameter (mm)	VOD (m/s)
Confined	5.4	3000
Unconfined	5.4	failed
Unconfined	6	failed
Unconfined	7 (questionable)	2750

Based on the detonation test results under unconfined conditions, 207X failed to detonate in 5.4 mm and 6 mm diameter charges. The minimum critical diameter of 207X was found to be 7 mm. Complete detonation cannot be assured for unconfined charges at the critical diameter. Therefore, 207X, can only be used in fully-coupled blasting experiments conducted as part of this research.

9.6 Summary of Preliminary Laboratory Experiments

In preliminary laboratory experiments, five grout materials were tested. Horn grout was selected as an appropriate experimental material. The static and dynamic properties of Horn grout are summarized in Table 9.12.

The use of grout slabs to insert strain gages within large scale laboratory models appears practical. VOD measurements were conducted for two explosives, PETN and 207X. In addition, a method for loading 207X was developed and tested. Based on these preliminary tests PETN (detonating cord) can be used in large-scale grout sample laboratory experiments for both fully-coupled and decoupled conditions. However, 207X can be used only for the fully-coupled condition because of critical diameter limitations.

Table 9.12. The summary of static properties for Horn grout

Type of test	Density (g/cc)	Young's modulus (GPa)	Poisson's ratio	Compressive strength (MPa)	Tensile strength (MPa)	P-wave velocity (m/s)	S-wave velocity (m/s)
Static test	2.28	34.1	0.23	79.1	4.81		
Dynamic test		47.6	0.18	275.0	16.26	4600	2853

10. LARGE-SCALE LABORATORY EXPERIMENTS

In blasting, the crush zone has a fairly well defined concentric boundary within which the rock is pulverized. It extends to where the pressure wave no longer exceeds the dynamic compressive strength. The crack zone extends beyond the crush zone and has a less well-defined boundary. It extends to where the pressure wave no longer exceeds the dynamic tensile strength. These concepts are illustrated in Figure 10.1.

The objective of large-scale laboratory experiments is to establish the extent of damage zones, including the crush zone and the crack zone, for a given set of conditions. To explore the applicability of SWT, laboratory experimental models must include fully-coupled blasting and decoupled blasting. Specifically, the crush zone and the crack zone must be measured for a range of explosive types, borehole diameters, and charge diameters.

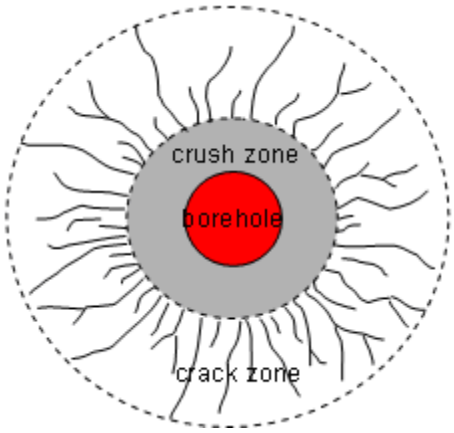

Figure 10.1. Damage zones surrounding a borehole

Large-scale laboratory blasting experiments involving a single-hole event are needed to verify applicability of the SWT method. In order to obtain the necessary information:

1. Measurement equipment with the capability of rapid data acquisition and storage is required to obtain strain data.
2. Subsequent to blasting, the sample must be cut apart to assess the extent of crush and crack zones.
3. Grout samples of sufficient size must be prepared to allow a borehole diameter within the constraints of the critical diameter for available explosives.
4. Particle size in the grout aggregates used in model construction must be minimized.
5. Dynamic strain measurements must be conducted in a hostile environment.
6. Visual records of the resulting damage zones must be obtained.
7. Safe experimental methods are required in the use of high explosives.

10.1 Grout Sample Size Determination for Large-scale Experiments

Investigation of the damage zone for rock blasting requires an appropriate grout sample size for large-scale experiments. Two methods were used to determine the sample size. One was to use the SWT model presented earlier. The other employed a commercial numerical simulation package, AUTOYDN®, produced by Century Dynamics Inc., to estimate the diameter needed to prevent cracks propagating to the surface. AUTODYN is a uniquely versatile explicit analysis tool for modeling the non-linear dynamics of solids, fluids, gasses and their interaction. Considering the available

explosives and solid materials in the AUTODYN software library, PETN with density 1.4 g/cc and grout with compressive strength of 80 MPa (concrete) were selected to estimate the required sample diameter. The simulation details are described in Appendix C.

The largest PETN cord (10 gram/m) was employed to simulate the crush and crack zone for a given size of grout sample. The properties of explosive are density at 1.4 g/cc (given by product provider) and VOD at 7100 m/s. The properties of grout (concrete) for these estimates are presented in Table 10.1.

The trial dimensions assumed for both methods are 500 mm in diameter and 500 mm in length with a borehole diameter of 3.1 mm (diameter of PETN cord with textile covering removed). The initial geometric model and postblast model for AUTODYN simulation are shown in Figures 10.2 and 10.3. Figure 10.2 is an AUTODYN representation of the cross section of a concrete cylinder showing the concentric drill hole. No confinement was applied to the perimeter of the cylinder. PETN was used as the explosive. Figure 10.3 represents the same cylinder following detonation of the PETN. The colored bands represent the degree of damage predicted by AUTODYN (see legend for interpretation). The low ratio for the blue area indicates little or no damage.

The results of both methods are shown in Table 10.2. Extents of the crush zones from SWT and AUTODYN are 7.2 and 4.9 mm, respectively. Extent of crack zones from SWT and AUTODYN are 87 and 101 mm, respectively. These results indicate that

Table 10.1. Properties of grout (concrete) for grout sample size estimations

Solid materials	Density (g/cc)	Compressive strength (MPa)	P-wave velocity (m/s)	S-wave velocity (m/s)	Poisson's ratio	Tensile strength (MPa)	Estimation method
Grout	2.28	80	4600	2853	0.18	5.3	SWT
Concrete	2.28	80					AUTODYN

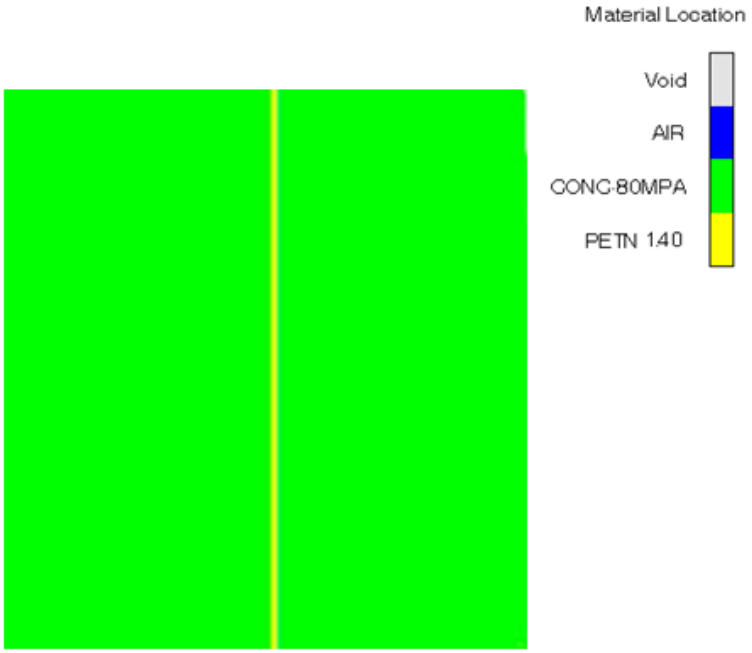

Figure 10.2. Initial geometric model of AUTODYN simulation

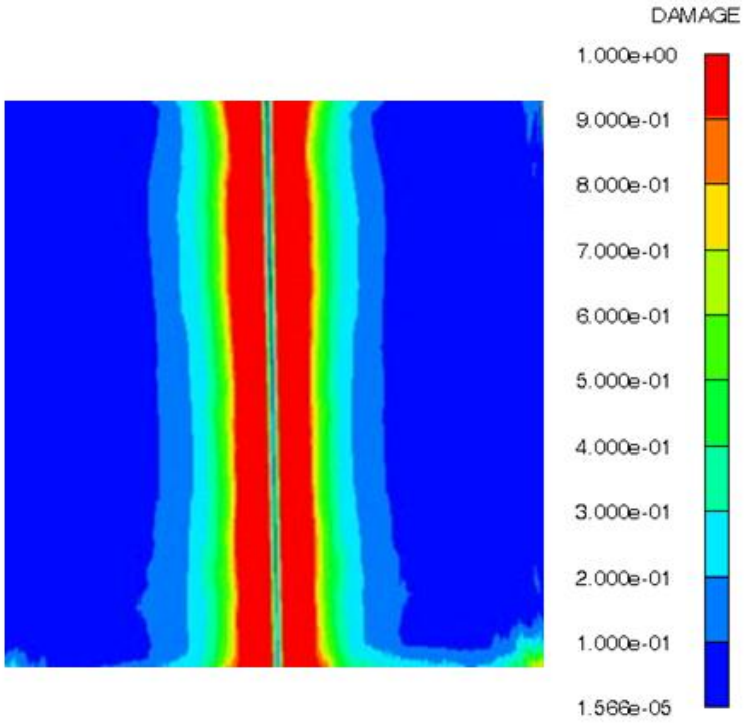

Figure 10.3. Postblast model of AUTODYN simulation

Table 10.2. Results of damage zones by both simulations

Simulation method	Extent of crush zone (mm)	Extent of crack zone (mm)	Remarks
SWT	7.2	87	Diameter is sufficient
AUTODYN	4.9	101	Diameter is sufficient

the crack damage (87 mm and 101mm) should not extend to the sides of the sample at 250 mm from the borehole. The perimeter was assumed to be confined for the SWT approach. For AUTODYN the perimeter was assumed to be unconfined. Based on the damage zone prediction by SWT and AUTODYN simulation, grout samples 500 mm in diameter and 400-500 mm high should be adequate to enclose all fractures generated by the borehole detonation for charge diameters from 2.1 to 10.8 mm. As an additional precaution, and to facilitate sample preparation, a confinement device composed of concrete was fabricated making the equivalent diameter close to 1 m.

10.2 Blasting Chamber

In order to protect personnel and measuring equipment, all experiments were conducted in an enclosed vessel. Personnel and instruments were located inside of the adjacent Ireco Laboratory. The test specimen, cap, and explosive were enclosed in a Kevlar chamber, located immediately outside of the laboratory. An overall view of the chamber is shown in Figure 10.4. The chamber is designed to be lowered over the experiment by an overhead hoist. The purpose of the chamber is to contain fragments resulting from detonation. The sample support frame is located in the center of the

Figure 10.4. Overall view of grout sample testing facility

chamber. The sample support frame consists of a 1.52 m diameter laminated plywood table covered with a piece of sheet metal. The table has a central hole, 2.54 cm in diameter. The table is supported by a steel and timber frame. The support frame is designed to allow all instrumental connections to be made from below the sample.

10.3 Instrumentation

Strain measurement in the grout sample was obtained using conventional foil strain gages mounted on grout slabs as described in Section 9.4 and Appendix B. Strain gage selection is based on the static or dynamic loading conditions, test materials, and specimen structure. In order to obtain specific point strain, the smallest possible gage

should be used. However, the length of the strain gages used should be at least five times the diameter of the largest particle in the grout. Based on these requirements a CEA-05-125UW-350 (Micro-Measurements Group, Inc.) gage was selected. The detail information is presented in Section 9.2.1.

Strain gages were affixed using an adhesive, M-Bond 200, following the manufacturer's recommendations. Measurement of the change in resistance caused by the passing strain waves was made by recording voltage change in an initially balanced Wheatstone bridge. Limited energy dissipation capacity of the small strain gages required usage of excitation voltages of about 12 volts. Strain data was converted from analog to discrete measurements by three dual-channel Nicolet 3091 digital storage oscilloscopes, capable of sampling at 1 MHz.

The VOD of the explosive was measured with a VODEX-100A timer, described in Section 9.5.3.

10.4 Grout Sample and Confinement Device

Seven large-scale experiments are outlined in Table 10.3. Experiments #2, #3, #5 and #6 were fully-coupled. PETN was used in # 2 and #3, and 207x was used in # 5 and #6. Experiments #1, #4 and #7 were decoupled with PETN used as the explosive.

10.4.1 Confinement Device

Confinement was provided by a segmented concrete pipe measuring 500 mm in internal diameter, 1000 mm in external diameter and 500 mm in length. The pipe was constructed using SONO tubes and sheet metal forming five chambers which were later filled with concrete. This form is shown in Figure 10.5. Pakmix, a premixed concrete

Table 10.3. Large-scale models

Sample	Charge diameter (mm)	Hole Diameter (mm)	Decoupled ratio	Explosive	Confinement condition
#1	3.1	10.8	3.48	PETN 10 gr*** detonating cord	Confinement
#2	2.3*	2.3	1	PETN 5 gr detonating cord	Confinement
#3	2.1*	2.1	1	PETN 3.6 gr detonating cord	Confinement
#4	2.3	8.5	3.5	PETN 5 gr detonating cord	Confinement
#5	5.4**	5.4	1	IRECO 207X	Non-confineme
#6	5.4**	5.4	1	IRECO 207X	Confinement
#7	2.1	10.8	5.14	PETN 3.6 gr detonating cord	Confinement

*Charge diameter is the diameter of the detonating cord with outer fabric removed with exception of the thin plastic covering. The explosive core is slightly less than that shown.
**Explosive was loaded directly into the hole and was fully coupled.
***gr is gram/m.

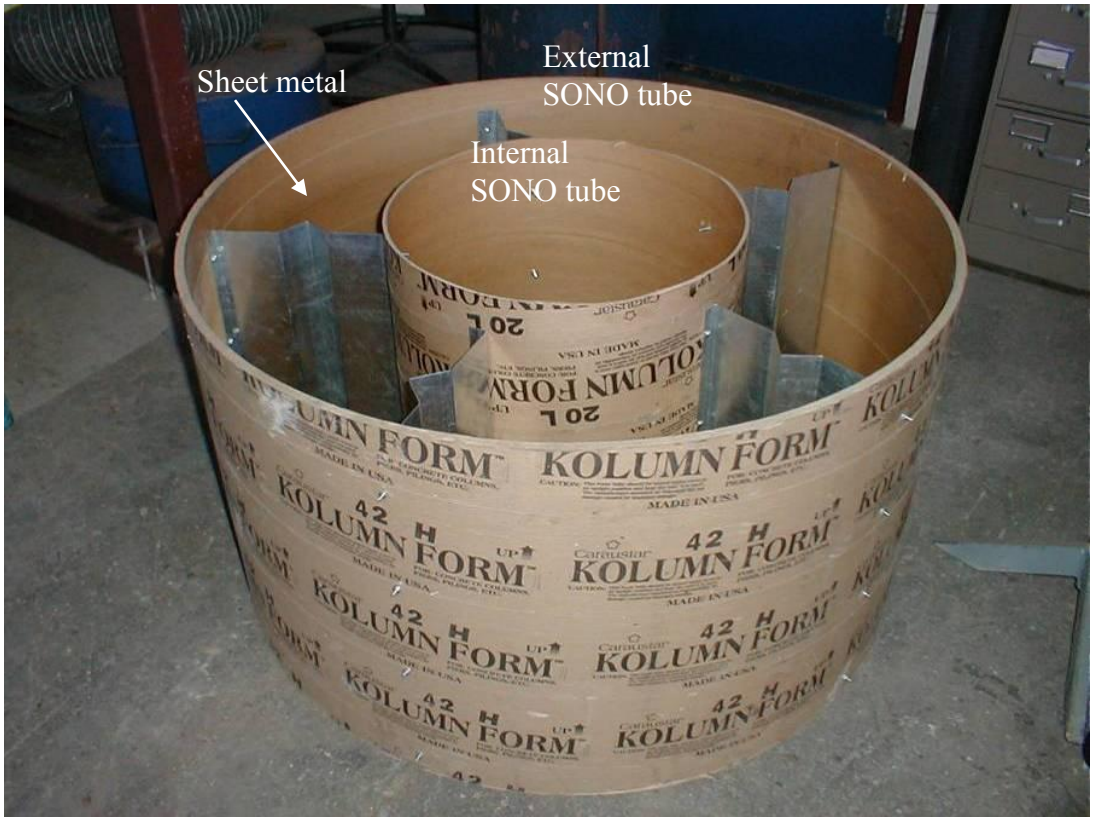

Figure 10.5. Form for the confinement device

was used to cast the confinement device. Two strain gages were installed in the confinement device at the locations shown in Table 10.4. The concrete confinement device was cured for 28 days. It was reused for subsequent experiments. The concrete segments are shown in Figure 10.6.

10.4.2. Grout Samples

As indicated in Section 10.4, a total of seven large scale experiments were conducted. To protect the grout samples from thermally-induced cracks, they were cast

Table 10.4. The locations of strain gages in confinement device

Gage	Gage factor	Resistance (Ohm)	Location in vertical direction from bottom	Location in radial direction from the center
#1	2.105	350	228.6 mm	330.76 mm to center
#2	2.105	350	228.6 mm	478.72 mm to center

Figure 10.6. Confinement device

in consecutive layers each less than 102 mm thick. The preparation procedure is described as follows:

1. Assemble the segments of the confinement device on the support table located within the blast chamber. Five segments were tightly held together with tie straps.
2. Paint the inside wall of the confinement device with paint and then apply paste wax to the painted surface to prevent the grout sample from bonding with the confinement device.
3. Center the core of the detonating cord in the form before filling the form with grout to produce a model representing a fully-coupled PETN blast. The PETN cord was carefully prepared by removing the textile covering leaving only a thin plastic tube to hold the explosive, so the ratio of the decoupling is slightly larger than 1 (the ratio of the decoupling=d_h/d_e) . Before casting, VOD target wires were tied to the cord at specific intervals. For decoupled charges, a borehole in the center of the sample was produced by precasting a plastic rod coated with wax. The grout was mixed with two bags (22.7 kg per bag) of Horn grout and approximately 4.5 lt of water to produce a mixture containing 10-11% water. Mixed grout was place into the form. Air was expelled from samples using a vibration tool. This was the first 102 mm layer of grout in the sample. The sample was allowed to set at room temperature for at least 4 hours.
4. Roughen the top surface of the sample with a chip hammer. Clean all loose materials from the surface with a vacuum.

5. Repeat steps 4, 5 and 6 to make each successive layer. Install strain gages in the third layer. Gage locations are presented in Table 10.5.

The confinement device is shown in Figure 10.7. The position of gages relative to the borehole and segments of the confinement are shown in Figure 10.8.

10.5 Preparations for Blasting

After curing for 2 weeks, the grout sample was ready for testing. Five Wheatstone ¼ bridges, described in Section 9.4, were assembled and connected to the Nicolet 3091 digital storage oscilloscopes. For decoupled experiments, VOD probe wires were tied onto the detonating cord first. The cord was centered in the precast hole using two short plastic sticks at ends of the hole to fix the cord in the center of the hole. For fully-coupled experiments, VOD probe wires were tied on the detonating cord before casting

Table 10.5. The locations of strain gages in the grout sample

Sample	Gage	Resistance/factor (Ohm/)	Location in vertical direction	Location in radial direction
#1	#1	350/2.105	230 mm	60 mm to center
	#2	350/2.105	230 mm	135 mm to center
	#3	350/2.105	230 mm	210 mm to center
#2	#1	350/2.105	230 mm	60 mm to center
	#2	350/2.105	230 mm	135 mm to center
	#3	350/2.105	230 mm	210 mm to center
#3	#1	350/2.105	230 mm	57 mm to center
	#2	350/2.105	230 mm	134 mm to center
	#3	350/2.105	230 mm	210 mm to center
#4	#1	350/2.105	230 mm	57 mm to center
	#2	350/2.105	230 mm	134 mm to center
	#3	350/2.105	230 mm	210 mm to center
#5	#1	350/2.105	230 mm	41 mm to center
	#2	350/2.105	230 mm	130 mm to center
	#3	350/2.105	230 mm	219 mm to center
#6	#1	350/2.105	230 mm	50 mm to center
	#2	350/2.105	230 mm	127 mm to center
	#3	350/2.105	230 mm	203 mm to center
#7	#1	350/2.105	230 mm	57 mm to center
	#2	350/2.105	230 mm	134 mm to center
	#3	350/2.105	230 mm	210 mm to center

Figure 10.7. The final grout sample and confinement device

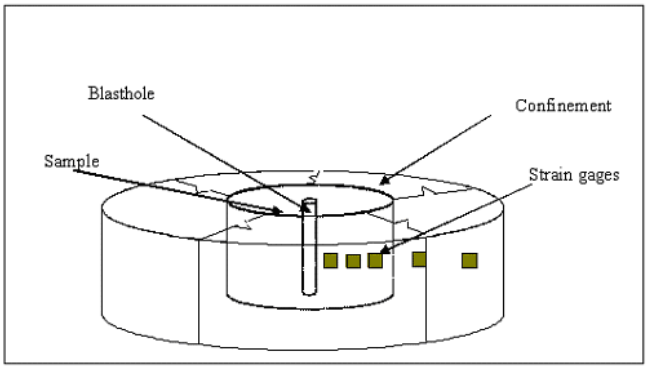

a. Schematic preparation of grout sample

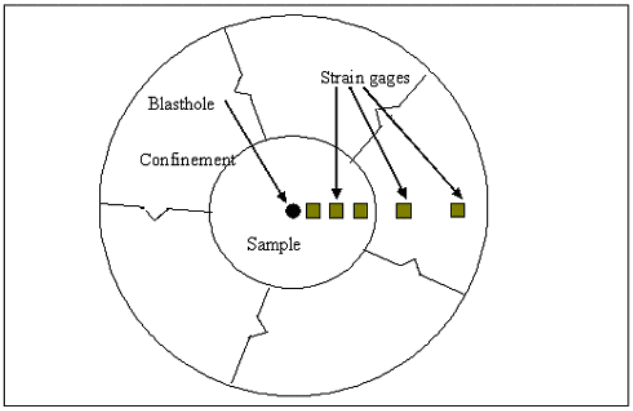

b. Plan view of the grout sample

Figure 10.8. Location of strain gages within the grout sample

the sample. For fully-coupled 207x, VOD probe wires were installed in the borehole of the sample, and then 207x was loaded into the borehole using the vacuum method previously described (Section 9.5.2).

An electric blasting cap was inserted into the hole in direct contact with the 207x. The cratering caused by the cap was limited to the upper surface. In the case of detonating cord, the cap was tied onto the detonating cord external to the hole. A 20 gage insulated twisted pair of wires was wrapped around the cap to provide a trigger wire. The trigger wire was connected from the cap to the trigger input of the Nicolet 3091 digital storage oscilloscopes. VOD probe wires were connected to the VODEX meter. Wheatstone bridges were then balanced, and the pretrigger time was set at 50 μs on the Nicolet 3091 digital storage oscilloscopes. The trigger sensitivity was tested at least twice to make sure the oscilloscope was responding properly. Immediately prior to blasting, the Nicolet oscilloscopes and the VODEX were armed. The Kevlar chamber was lowered, and from a safe position, the cap was connected to the blasting machine. An audible warning siren was turned on and the area was checked again to ensure that no one had entered the area. The explosive was then fired with a blasting machine (Fidelity Electric Co.). Upon detonation of the cap, the wires were fused forming a closed circuit and providing a voltage to the trigger circuit of the Nicolet 3091 digital storage oscilloscopes. The voltage served to initiate data collection by the digital oscilloscopes and timer. The chamber was raised and the sample was checked to make sure that all explosives had detonated. The data stored in the Nicolet 3091 oscilloscopes were transferred to a computer data base using WFread®, Waveform Basic version 2.3, produced by Blue Feather Software.

To check the damage extent of the crush zone and crack zone, the samples were cut diametrically as shown in Figures 10.9 to 10.23.

10.6 Results for Large-scale Laboratory Experiments

The conditions for each test are shown in Table 10.6. The VOD of 207X is around 3000 m/s, in fully-coupled conditions. As can be seen, the VOD for PETN is essentially the same for all diameters and fully-coupled/decoupled loading conditions. The results for sample #1, #2, #3, #4 and #7 indicate a VOD of approximately 7000 m/s.

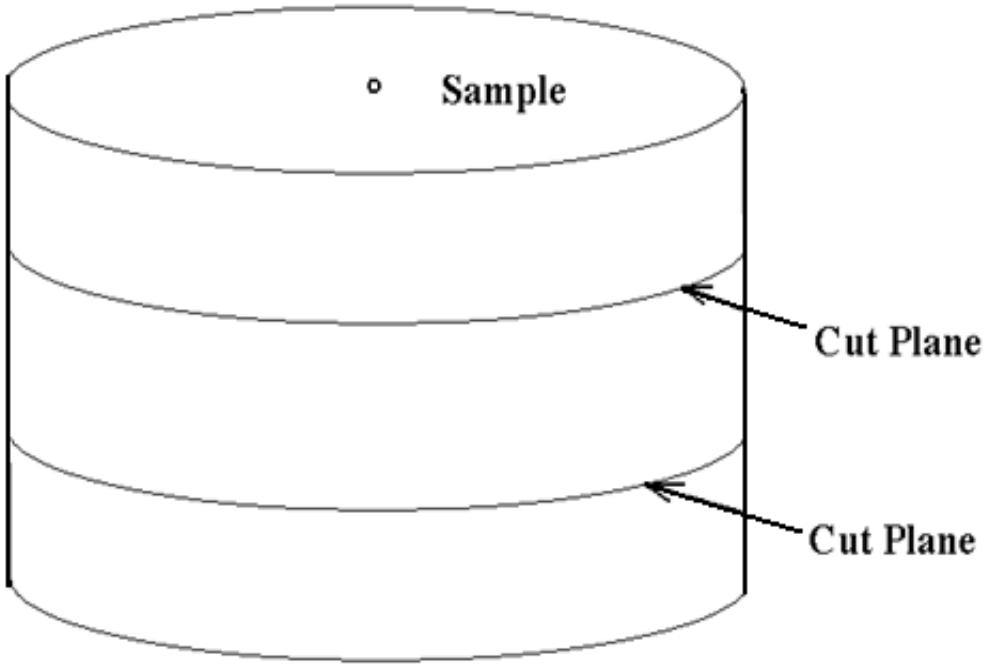

Figure 10.9. Position of diametrical cuts through grout cylinder

Figure 10.10. Postblast sample #1, 10 gram/m detonating cord, decoupled and confined

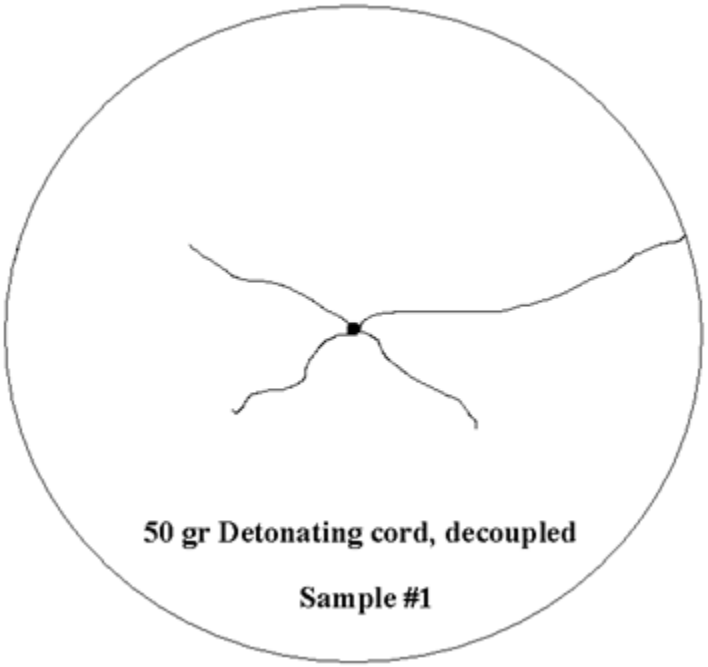

Figure 10. 11. Schematic of postblast sample #1, 10 gram/m detonating cord, decoupled and confined

Figure 10.12. Postblast sample #2, 5 gram/m detonating cord, fully-coupled and confined

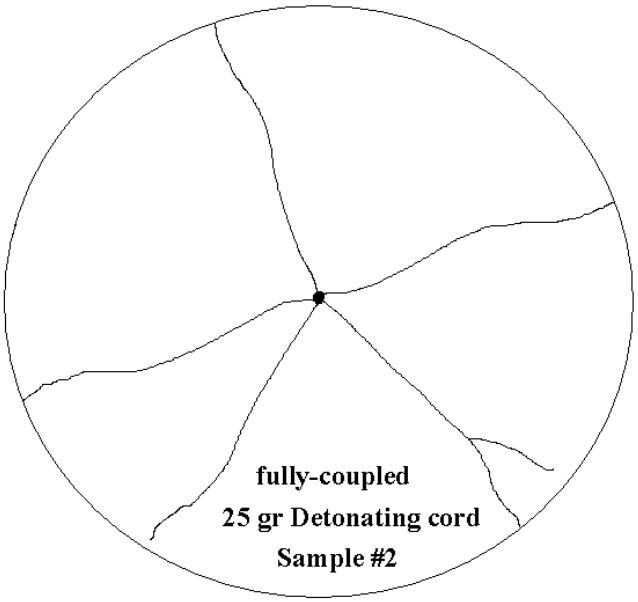

Figure 10.13. Schematic of postblast sample #2, 5 gram/m detonating cord, fully-coupled and confined

Figure 10.14. Postblast sample #3, 3.6 gram/m detonating cord, fully-coupled and confined

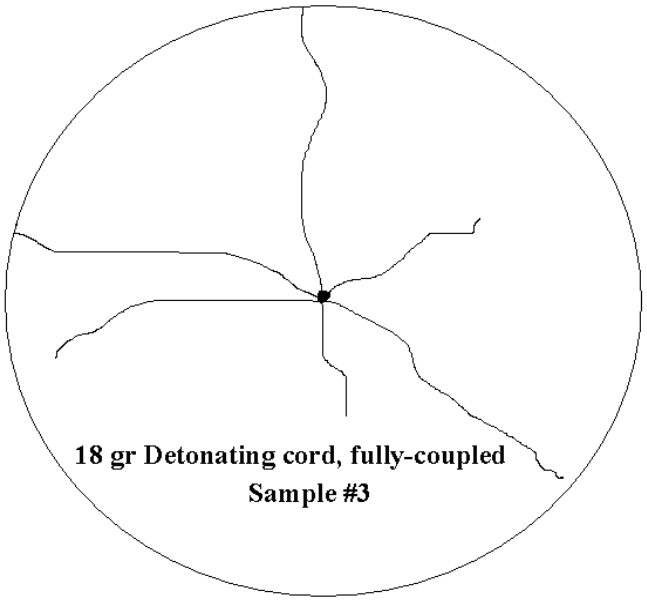

Figure 10.15. Schematic of postblast sample #3, 3.6 gram/m detonating cord, fully-coupled and confined

Figure 10.16. Postblast sample #4, 5 gram/m detonating cord, decoupled and confined

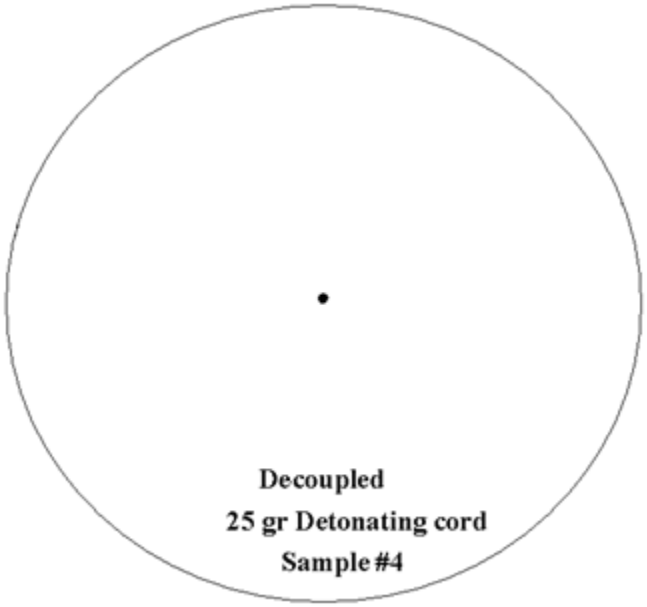

Figure 10.17. Schematic of postblast sample #4, 5 gram/m detonating cord, decoupled and confined

Figure 10.18. Postblast grout sample #5, fully-coupled explosive 207X, unconfined

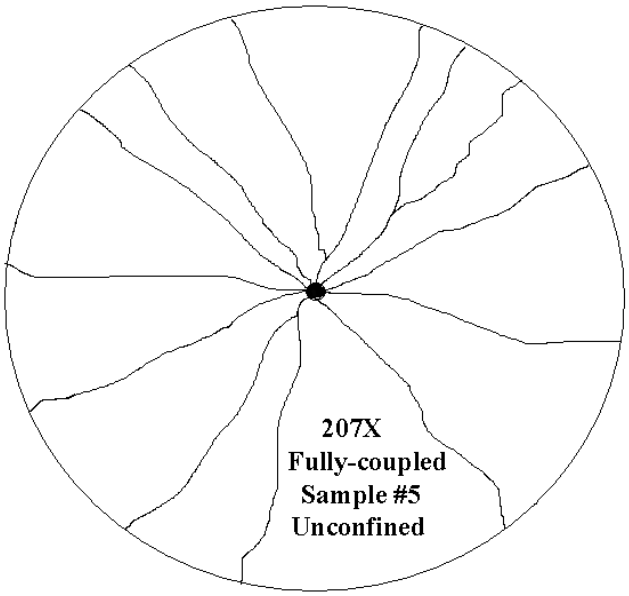

Figure 10.19. Schematic of postblast grout sample #5,
fully-coupled explosive 207X, unconfined

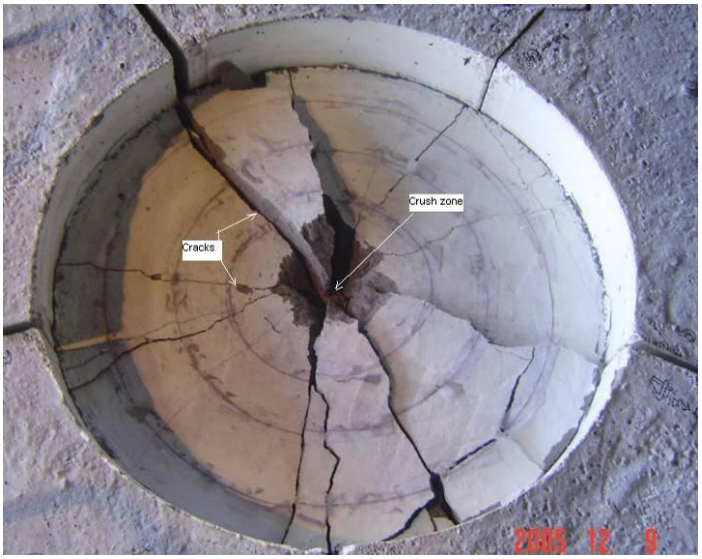

Figure 10.20. Postblast grout sample #6 fully-coupled explosive 207X and confined

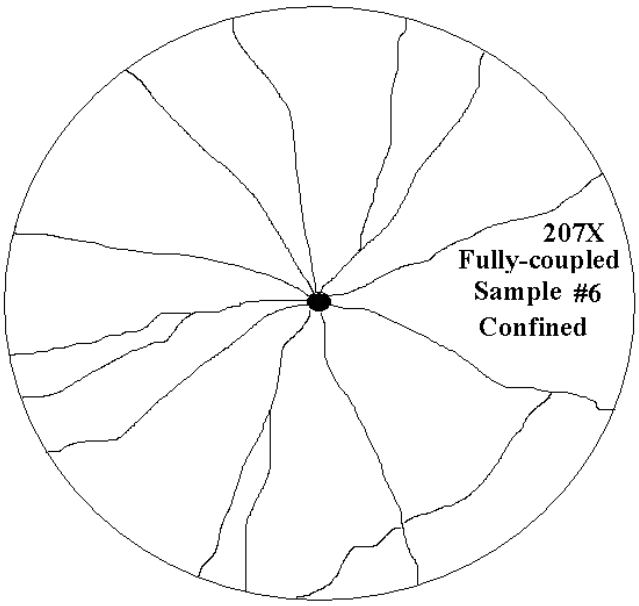

Figure 10.21. Schematic of postblast grout sample #6,
fully-coupled explosive 207X and confined

Figure 10.22. Postblast grout sample #7, decoupled 3.6 gram/m detonating cord and confined

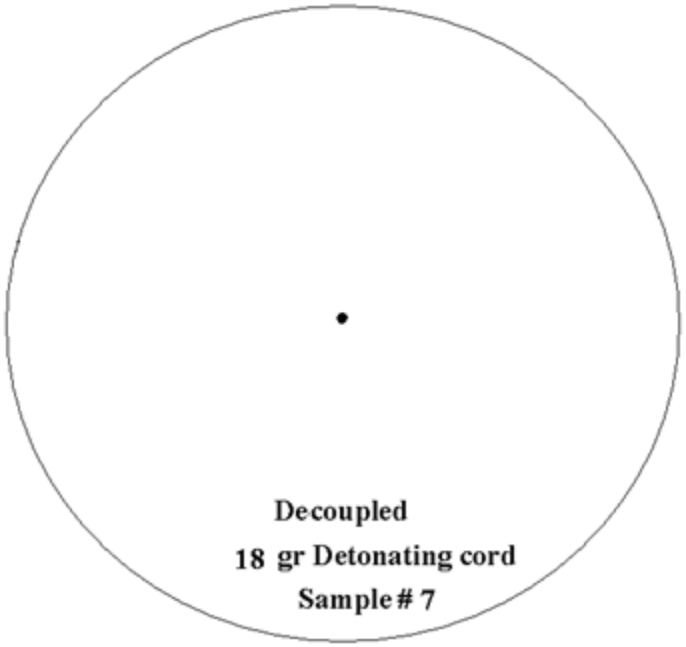

Figure 10.23. Schematic of postblast grout sample #7, decoupled 3.6 gram/m detonating cord and confined

Table 10.6. Explosives and parameters for each experiment

Sample	Explosive	Charge dia. (mm)	Hole dia. (mm)	Ratio of coupling	Charge density (g/cc)	VOD (m/s)
#1	PETN (10 gr deto-cord)	3.1	10.8	3.48	1.4	6996
#2	PETN (5 gr deto-cord)	2.3	2.3	1	1.4	7005
#3	PETN (3.6 gr deto-cord)	2.1	2.1	1	1.4	6937
#4	PETN (5 gr deto-cord)	2.3	8.5	3.7	1.4	7090
#5	207X	5.4	5.4	1	1.2	3098
#6	207X	5.4	5.4	1	1.2	3000
#7	PETN (3.6 gr deto-cord)	2.1	10.8	5.14	1.4	6990

The extents of crush zones and crack zones are shown in Table 10.7. The crush and crack zones versus ratio of decoupling are shown in Table 10.8. Crush zones were evident in samples #1, #2, #3, #5, and #6. No crush zone was generated in samples #4 and #7. The crack zones are evident in samples #1, #2, #3, #5 and #6 and no crack zones appeared in samples #4 and #7. The crush zones and crack zones are closely related to the ratio of coupling. Both crush zones and crack zones are largest when the ratio of coupling is 1 (fully-coupled). They decrease as the ratio of coupling increases, as shown in Table 10.8 and Figure 10.24 and 10.25. Notice that the extents of the crack zone of

Table 10.7. Damage extent for crush zone and crack zone

Sample	Hole Dia. (mm)	Radius of crush zone (mm)	Maximum crack zone (mm)	Average crack zone (mm)
#1	10.8	5.8	254	149
#2	2.3	2.8	254	249
#3	2.1	2.9	254	190
#4	8.5	4.3	---	---
#5	5.4	6.5	254	254
#6	5.4	7.0	254	254
#7	10.8	5.4	---	---

Table 10.8. Crush and crack zones versus ratio of coupling

Sample	Ratio of Coupling (r_h/r_e)	Radius of crush zon (r/r_h)	Radius of crack zone (r/r_h)
#2	1	2.4	217
#3	1	2.8	181
#5	1	2.4	94
#6	1	2.6	94
#1	3.48	1.1	28
#4	3.7	1	1
#7	5.14	1	1

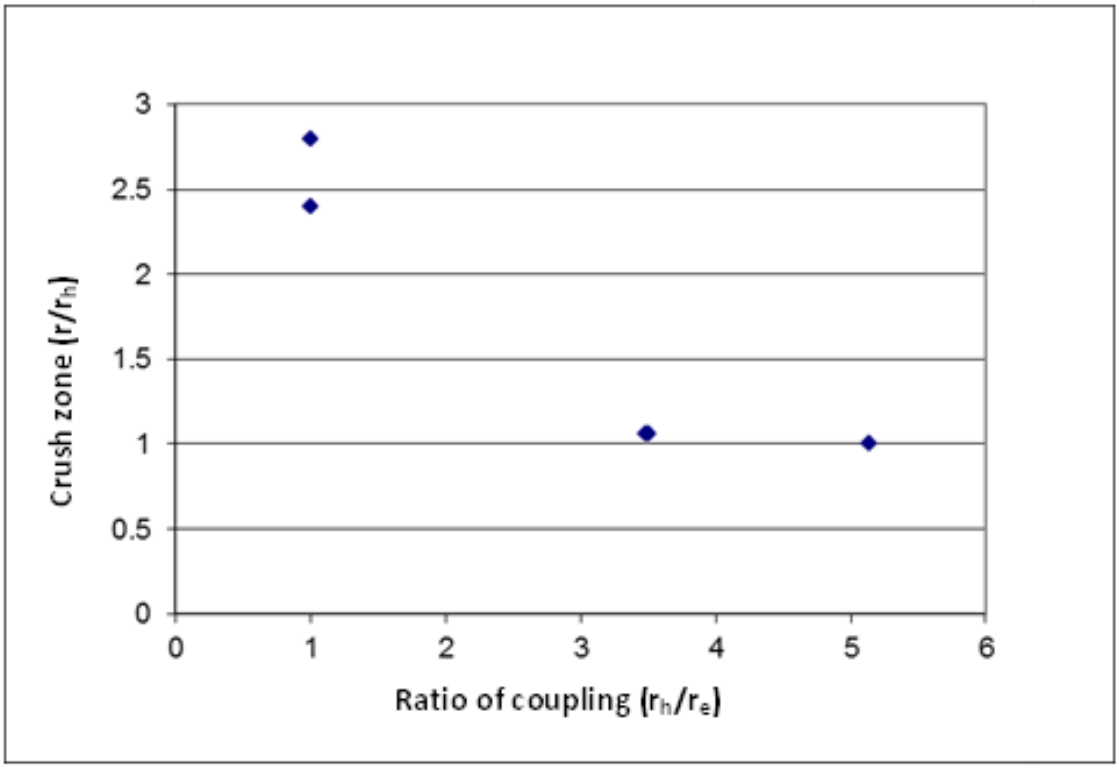

Figure 10.24. Crush zone versus ratio of coupling

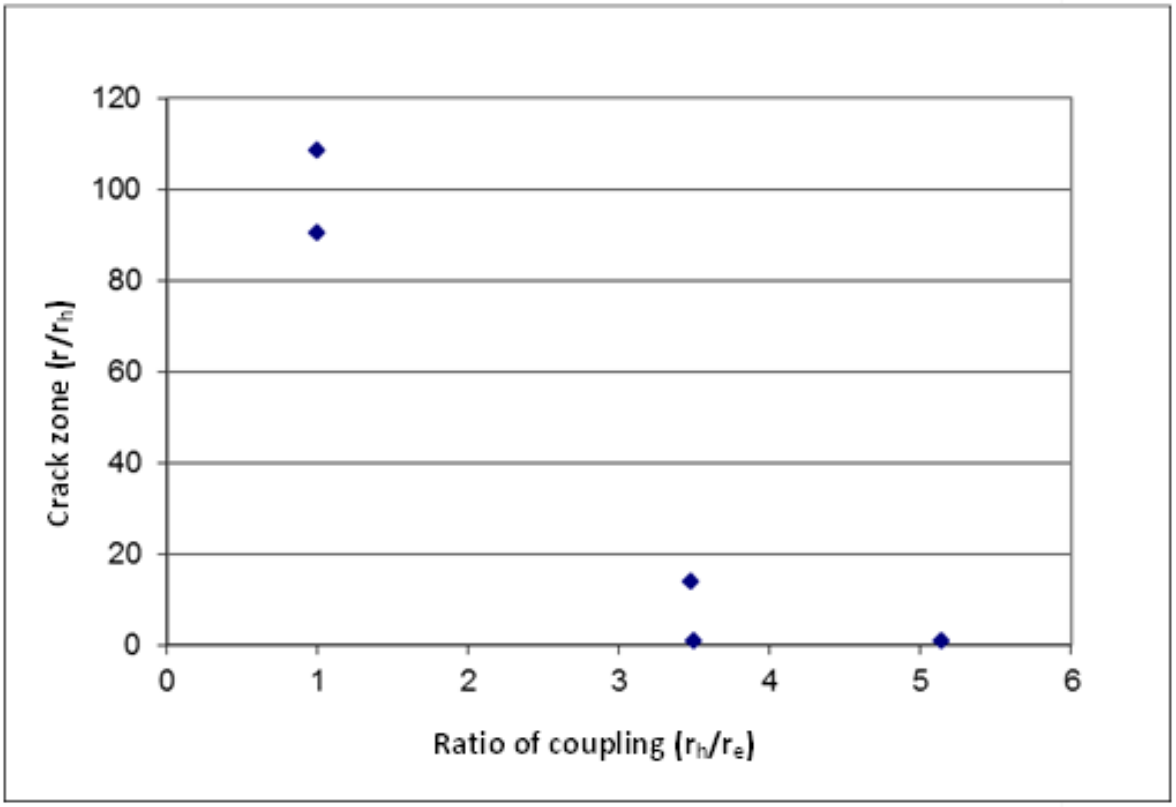

Figure 10.25. Crack zone versus ratio of coupling

some samples equal the radius of the sample, such as 94.1 to 216.8 times the borehole radii for fully-coupled conditions while no crack zones are produced for the samples with decoupled conditions with ratios of 3.7 and 5.14. The typical strains in the grout sample during blasting are shown in Figure 10.26 and 10.27. The maximum strains versus distances for all seven samples are summarized in Figure 10.28. The strain measurement was not very successful due to excessive noise.

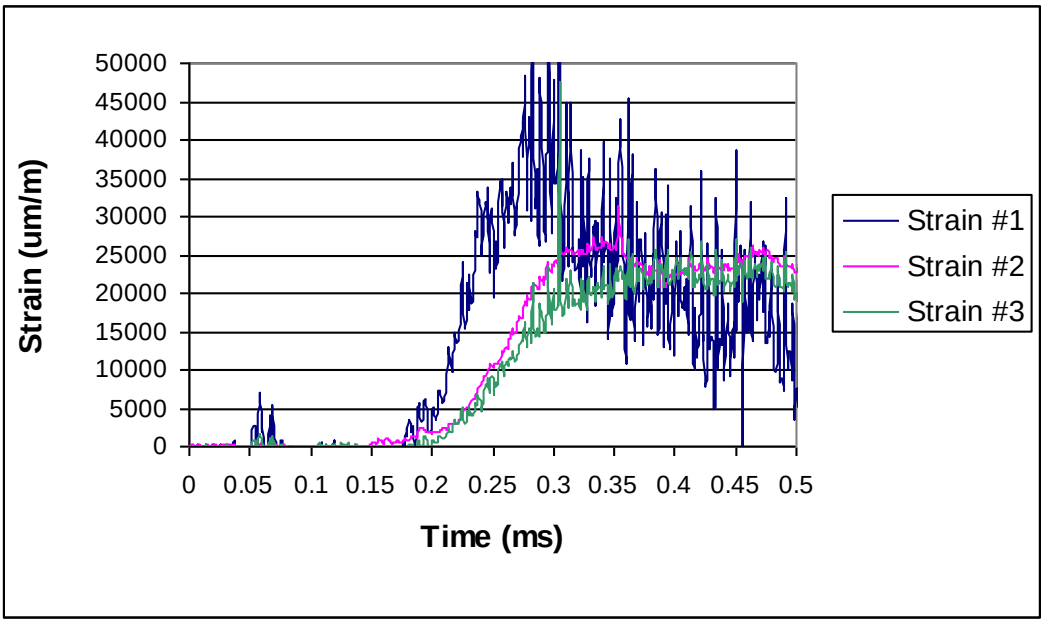

Figure 10.26. Strain versus time for sample #6

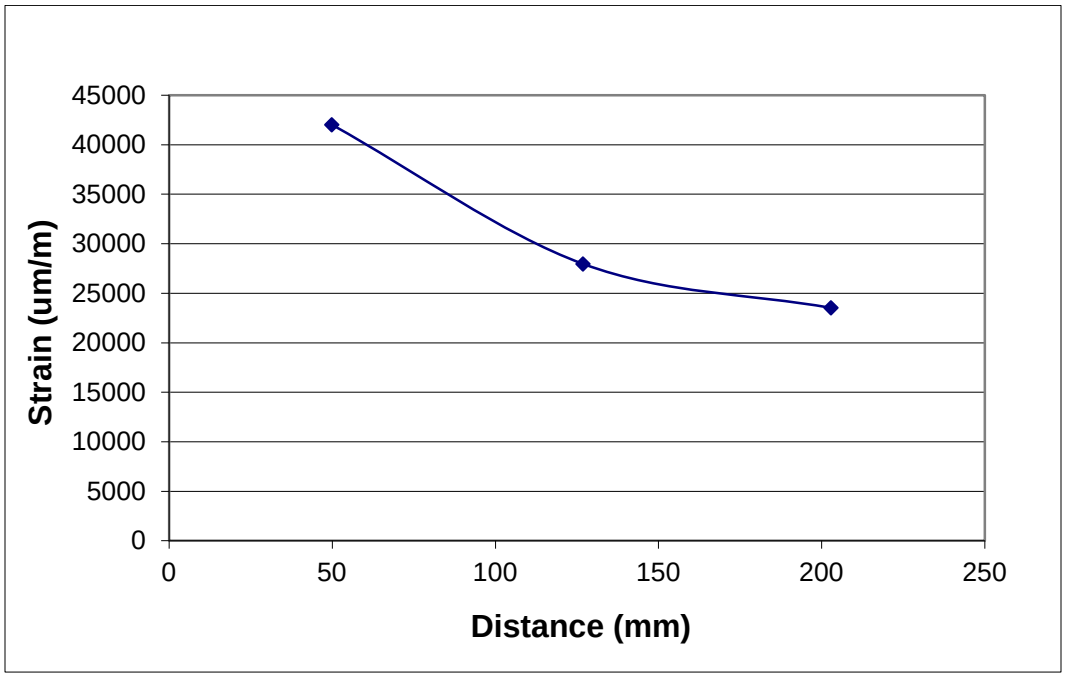

Figure 10.27. Maximum strain versus distance for sample #6

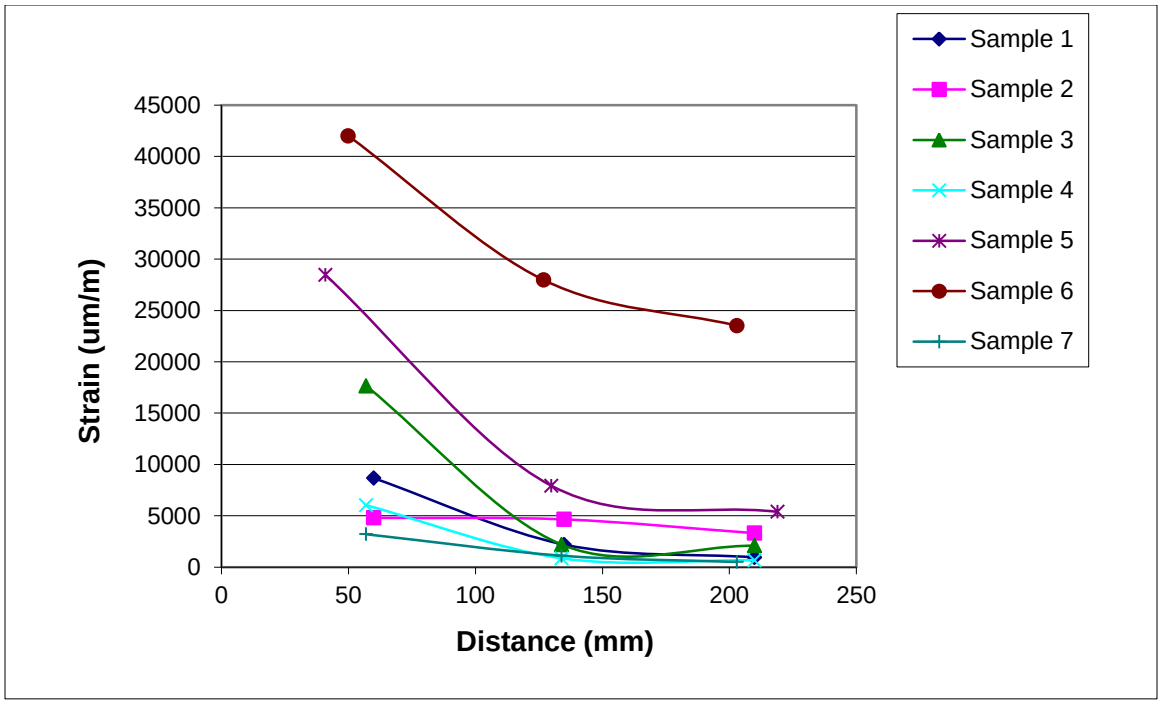

Figure 10.28. Maximum strains versus distances for all seven samples

11. COMPARISON OF SWT USING LARGE-SCALE LABORATORY EXPERIMENTAL DATA

11.1 Comparison of the Crush Zone Estimation with Large-scale Experimental Data

The input data for SWT model is shown in Tables 9.12 and 10.6. The Hugoniot constant of grout was assumed to be 1.32 (the same as concrete), and relative weight strength of PETN was calculated to be 1.54. Measured and predicted radii of the crush zone in large-scale samples are shown in Table 11.1 and Figure 11.1. SWT predicted crush zones are very close to the laboratory results for samples #1, #4, #5, #6 and #7. The predicted results for samples #2 and #3 are much larger than those observed in the experiments. This difference may be due to the effective decoupling resulting from the thin-walled plastic tube used to contain the PETN. Detonator cord includes two layers covering the PETN. The outer is a textile material which was removed as part of the experimental procedure.

Table 11.1. Crush zone results of laboratory and SWT

Sample	Dia. Explosive (mm)	Dia. Hole (mm)	Decouple ratio	Radius* of Crush zone (Lab, mm)	Radius of Crush zone (SWT, mm)	Scaled radius of Crush zone(Lab, r_{crush}/r_h)	Scaled radius of Crush zone (SWT, r_{crush}/r_h)
#1	3.1	10.8	3.5	5.8	5.7	1.1	1.1
#2	2.3	2.3	1.0	2.8	4.9	2.4	4.3
#3	2.1	2.1	1.0	2.9	4.5	2.8	4.3
#4	2.3	8.5	3.7	4.3	4.7	1.0	1.1
#5	5.4	5.4	1.0	6.5	6.5	2.4	2.4
#6	5.4	5.4	1.0	7.0	6.3	2.6	2.3
#7	2.1	10.8	5.1	5.4	5.4	1.0	1.0

*Radius determined by measuring the diameter of the crush zone and dividing by 2.

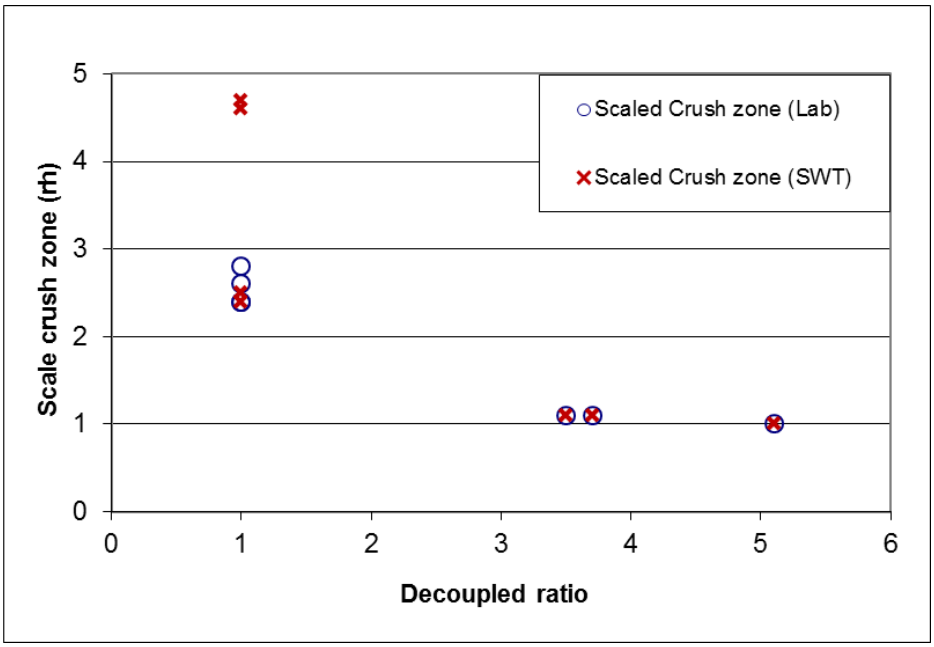

Figure 11.1. Comparison of experimental and predicted crush zone data

11.2 Comparison of the Crack Zone Estimation with Large-scale Experimental Data

Measured and predicted radii of the crack zone in laboratory experiments are shown in Table 11.2 and Figure 11.2. Measured extents of crack zones of samples #1, #2, #3, #5 and #6 were much larger than predicted. Using SWT, cracks were predicted for conditions represented by samples #4 and #7, but no cracks were observed in the corresponding models. Therefore, the extent of fracturing predicted by SWT is much different than measured in the large scale models. Extent of the crack zones in samples #1, #2, #3, #5 and #6 are extremely large (27 to 216 times the radius of borehole) compared with the predicted results (11 to 69 times borehole radius). One possible explanation is that the confinement device was ineffective in limiting crack growth,

Table 11.2. Comparison of laboratory data with SWT

Sample	Dia. Explosive (mm)	Dia. Hole (mm)	Decoupled ratio	Radius of Crack zone (Lab, mm)	Radius of Crack zone (SWT, mm)	Scale radius of Crack zone(Lab, r/r_h)	Scale radius of Crack zone(SWT, r/r_h)
#1	3.1	10.8	3.5	149	92	28	17
#2	2.3	2.3	1.0	249	79	217	69
#3	2.1	2.1	1.0	190	72	181	69
#4	2.3	8.5	3.7	0	75	1.0	18
#5	5.4	5.4	1.0	254	104	94	39
#6	5.4	5.4	1.0	254	101	94	37
#7	2.1	10.8	5.1	0	58	1.0	11

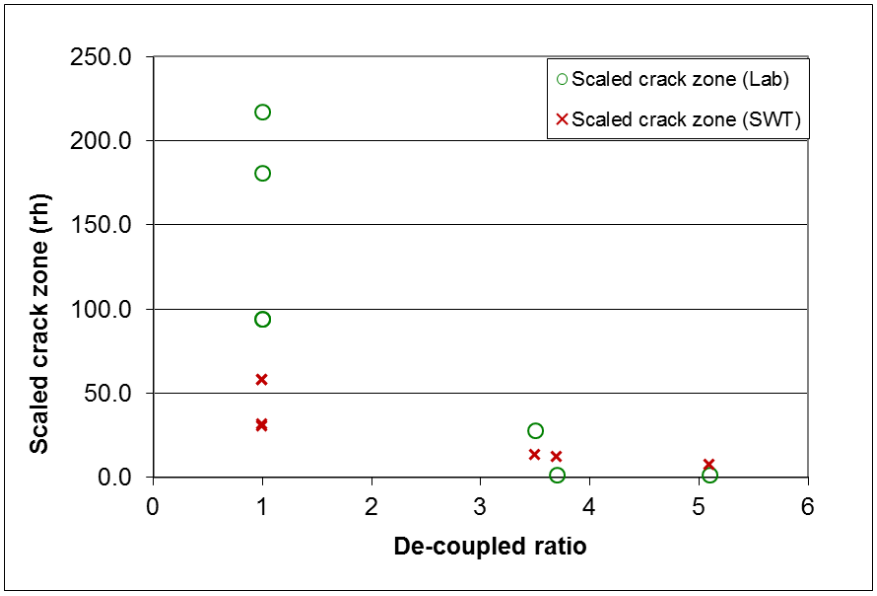

Figure 11.2. Comparison of laboratory data with SWT

assuming that the SWT provides reasonable values. Movement of the confinement device in the radial direction was noticed for each blast. One explanation may be that some of the strain wave is being reflected at the painted and waxed boundary. This soft confinement may promote growth of the crack zone in the laboratory samples. Another factor could be gas expansion into the cracks, driving them further than predicted by SWT. This seems unlikely because the gases are immediately vented to the atmosphere in laboratory experiments.

11.3 Summary of Laboratory and SWT Results

The extent of the crush zone for laboratory models is in good agreement with those predicted by SWT. However, the results show poor agreement for the extent of the crack zone. One factor that could contribute to unsatisfactory results in predicting the extent of the crack zone is the possibility that the high-pressure gasses produced by explosive detonation do not immediately vent to the atmosphere. In addition, reflection at the cylindrical discontinuity may also contribute to greater than expected crack lengths. Therefore, the SWT method provides reasonable estimates for the crush zone; estimation of the crack zones should be explored under field condition. An attempt was made to measure the strain in the radial direction at various points within the sample. However, attempts to reduce the noise in the measurements were unsuccessful; consequently no meaningful strain data were obtained.

12. FIELD EXPERIMENTS

To further explore the applicability of SWT, field experiments were conducted at Newmont's Leeville underground mine. The purpose of these field tests was to improve stope blast design by minimizing overbreak.

12.1 Problem Statement

After about 2 years of production at Leeville, many stopes in Zones 1, 3, 4, and 5 had been mined out. It was found that most of the ribs of these stopes failed during the production period (average 3 to 6 weeks). Progression of these rib failures compromised the stability of the roof because of an increase in span of the unsupported stope. Such failure was evident in stopes 140, 132 and 120 in Zone 1, and stopes 407, 410 in Zone 4. The severity of rib failures are closely related to the blast pattern.

12.2 Original Blast Design

The typical dimensions of the stopes are 6 m wide, 15-21 m high, and 30 m long. Boreholes employed at Leeville are typically 95 mm in diameter, and conventional ANFO is used. Original blasting designs include three different patterns in Zone 1.

1. For stope 120, 4 holes per row with 1.8 m burden and approximately 1.5 m spacing.
2. For stope 140, 3 holes per row with 1.8 m burden and approximately 2.1 m spacing.

3. For stope 132, 3 holes per row with 2.4 m burden and approximately 2.1 m spacing.The patterns corresponding to 1, 2, and 3 are shown in Figures 12.1, 12.2 and 12.3.

The powder factors for these designs are shown in Table 12.1.

Overbreak and rib failure were measured by the Cavity Monitoring System (CMS), produced by Optech International Inc. The measured overbreak profiles of each stope are shown in Figures 12.4, 12.5, 12.6, 12.7, 12.8 and 12.9. A severe overbreak and rib failure occurred in stope 120 and 140. Some overbreak and rib failure took place in stope 132. The maximum rib failures of stope 140, 120 and 132 extended to 5.2 m, 2.7 m and 2.4 m, respectively, and average overbreak for these stopes were 1.4 m, 1.1 m and 0.9 m, respectively. The overbreak results for these stopes are summarized in Table 12.2. The falls of ground in stope 120, 140 and 132 occurred due to the failure of ribs in these stopes.

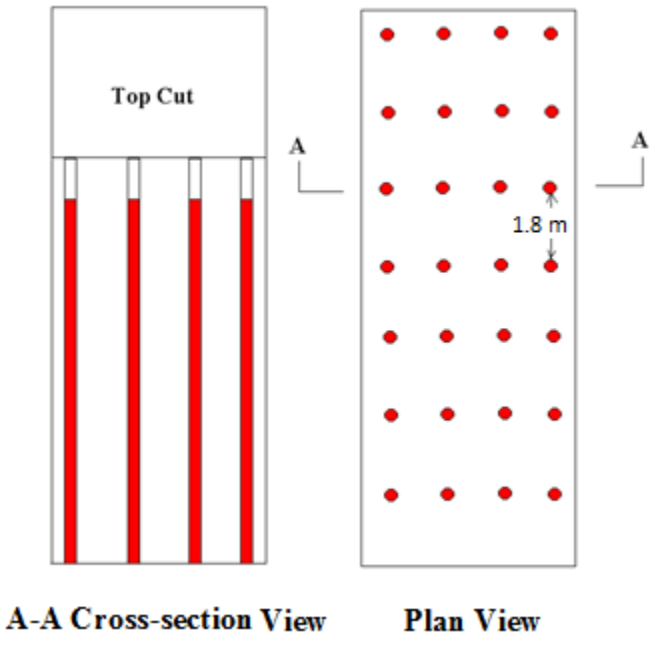

Figure 12.1. Original pattern 1

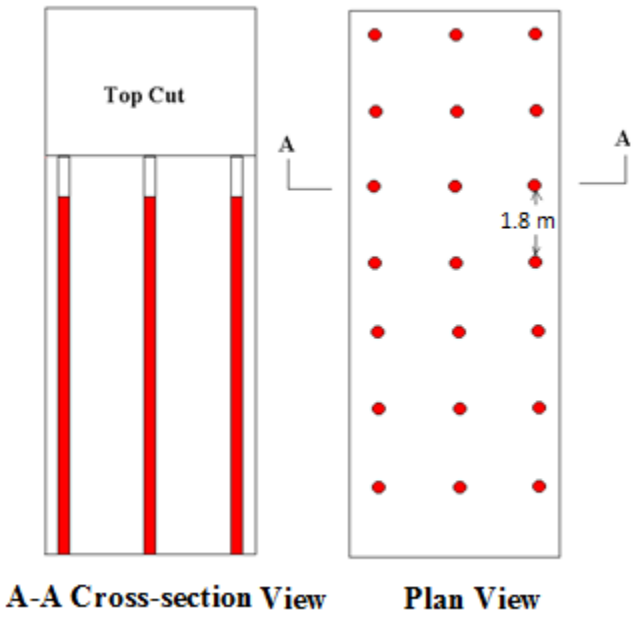

Figure 12.2. Original pattern 2

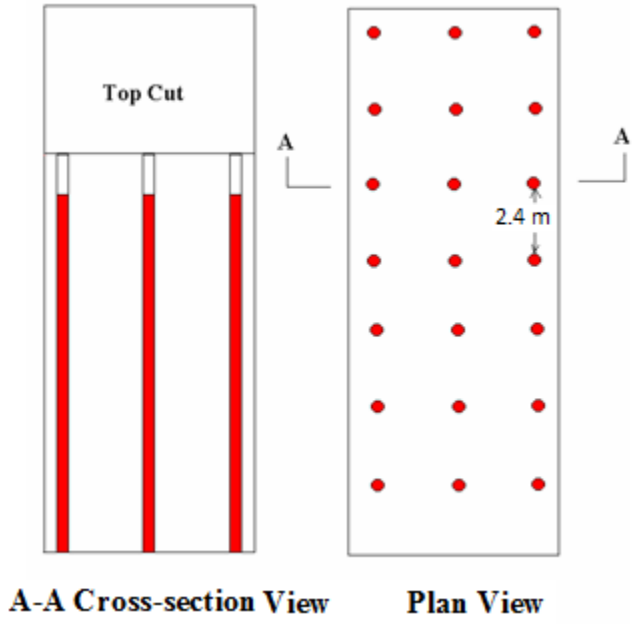

Figure 12.3. Original pattern 3

Table 12.1. Powder factors for original designs

Blast design	Powder factor (kg/m^3)	Powder factor for ribs (kg/m^2)*
1 Stope 120, (95 mm. hole, 4 holes/row, 1.8x1.5 m burden to spacing	2.10	3.17
2 Stope 140, (95 mm hole, 3 holes/row, 1.8X2.1 m burden to spacing	1.57	3.17
3 Stope 132, (3 ¾ in. hole, 3 holes/row, 2.4x2.1 m burden to spacing	1.17	2.39

* Weight of explosive in the holes closest to the rib per unit area of the rib.

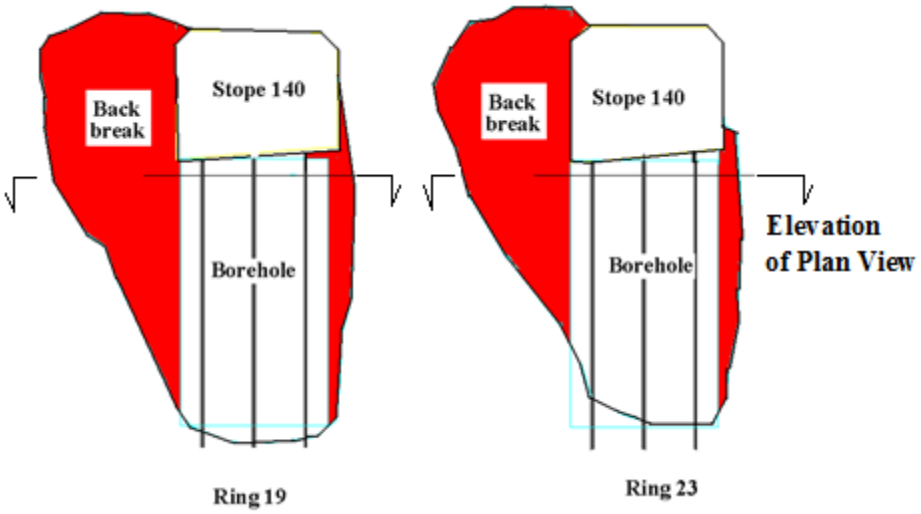

Figure 12.4. Overbreak and rib failure in stope 120
(Cross-section of ring 19 and 21)

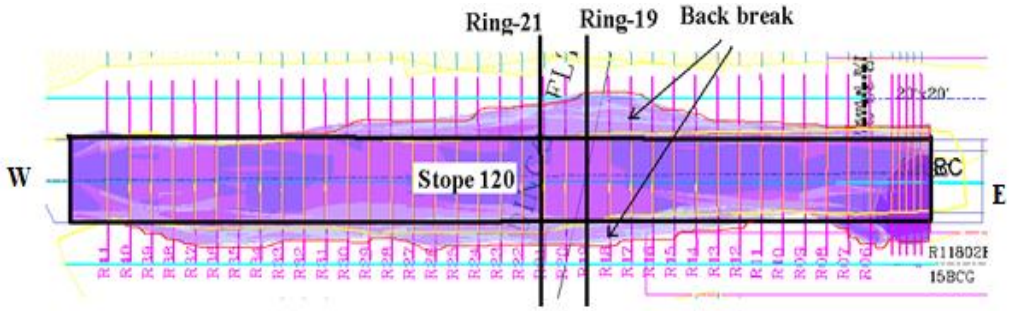

Figure 12.5. Overbreak and rib failure in stope 120 (plan view)

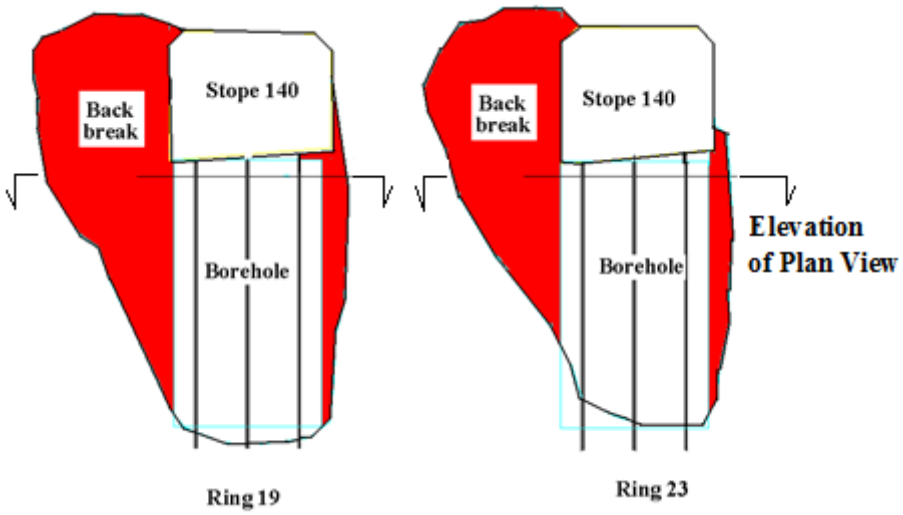

Figure 12.6. Overbreak and rib failure in stope 140
(Cross-section of ring 19 and 23)

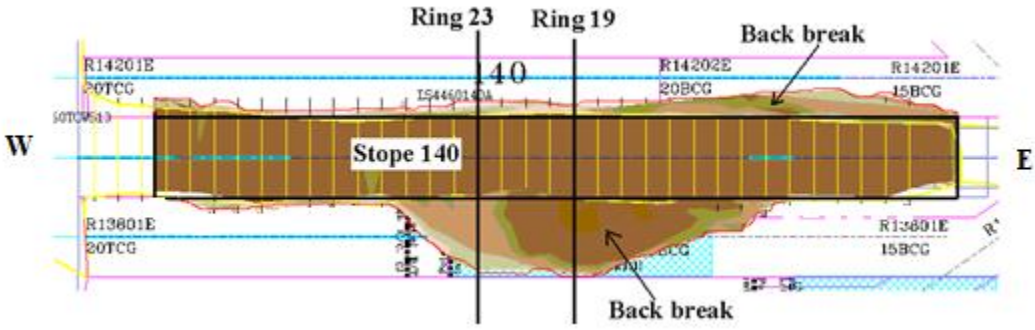

Figure 12.7. Overbreak and rib failure in stope 140 (plan view)

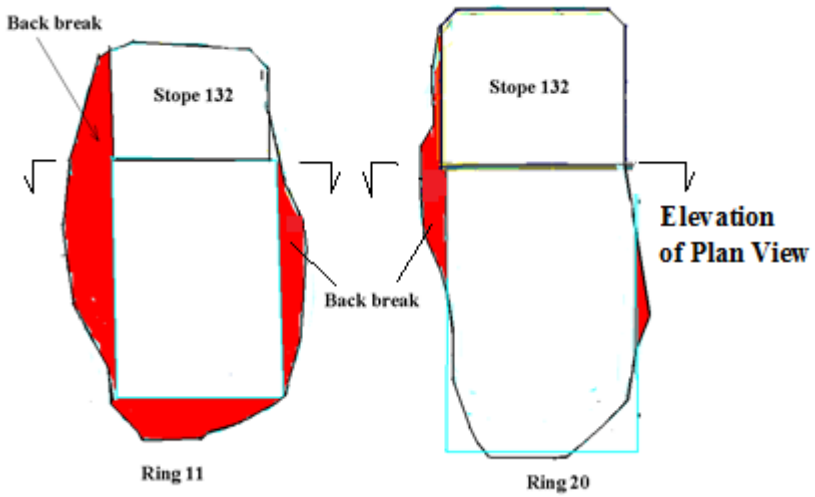

Figure 12.8. Overbreak and rib failure in stope 132
(Cross-section of ring 11 and 20)

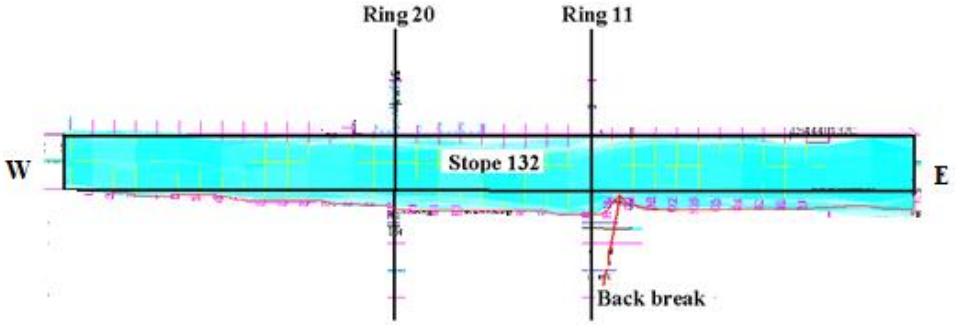

Figure 12.9. Overbreak and rib failure in stope 132 (plan view)

Table 12.2. Overbreak results for stopes 140, 120 and 132

Distance measuring from west end of stope (m/ft)	140 north rib (m)	140 south rib (m)	120 north rib (m)	120 south rib(m)	132 north rib (m)	132 south rib(m)
6 /20	1.04	0.00	0.91	1.22	0.49	0.52
13/40	1.74	0.00	1.07	0.15	0.40	0.82
18/60	1.59	2.35	1.07	0.15	0.30	0.73
24/80	1.25	3.84	2.77	1.16	0.00	1.55
30/100	0.61	5.34	2.47	1.25	0.00	1.74
37/120	0.76	3.48	1.55	1.80	0.27	2.38
43/140	0.58	0.00	0.76	1.13	0.00	2.20
49/160	0.30	0.73	0.15	1.34	0.00	1.98
55/180	0.30	0.61	0.30	0.64	0.00	1.71
Average overbreak of each rib	0.91	1.83	1.22	0.98	0.15	1.52
Average overbreak of both ribs for each stope	0.00	1.37	0.00	1.10	0.00	0.85

12.3 Proposed Pattern

To reduce blasting overbreak and improve stability, several new blast designs were proposed for current and future stopes. A logical adjustment to the pattern was to alternate three holes and two holes using a 1.8 m ring as shown in Figure 12.10. The hole size for this adjusted pattern was initially 95 mm. The powder factor for the adjusted blast design was still high, 1.3 kg/m^3. Therefore, four modifications were proposed using SWT:

1. Modification #1 employs decoupled holes. Decoupling is accomplished by using a 76 mm PVC tube installed in the rib holes. The tube is placed in contact with the wall of the borehole furthest from the rib as shown in Figure 12.11.
2. Modification #2 employs smaller diameter, 76 mm, rib holes drilled near the rib of the stope. All other holes remain at 95 mm.
3. Modification #3, all holes in the stope round are reduced to 76 mm.
4. Modification #4, all holes in the stope round, including rib holes, remain at 95 mm, but low energy explosive is used in the rib holes. All other holes are loaded with conventional ANFO. Modification #4 is shown in Figure 12.12.

The powder factors for all proposed new designs are shown in Table 12.3.

12.4 Damage Zone Prediction Using SWT

SWT was employed to predict the damage zone and select the best blast design pattern among the alternatives. The properties of explosives and rock are listed in Table 12.4 and 12.5. The predicted results for crack zone extent are shown in Table 12.6.

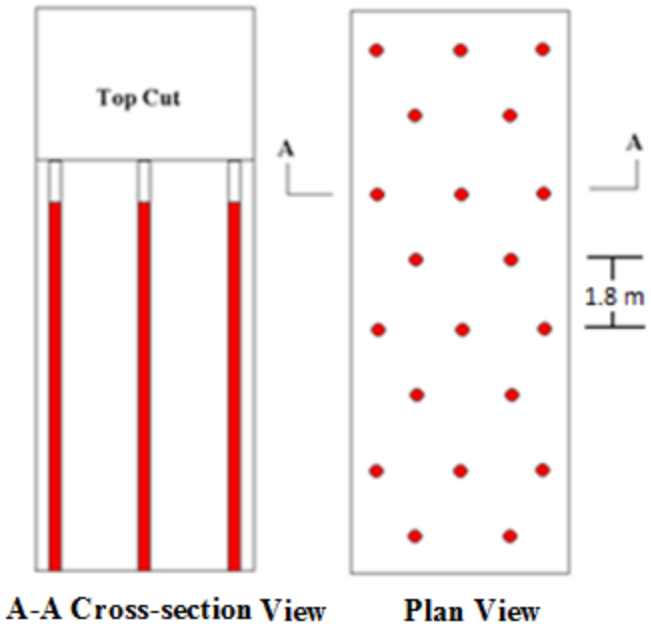

Figure 12.10. Stope with adjusted hole pattern

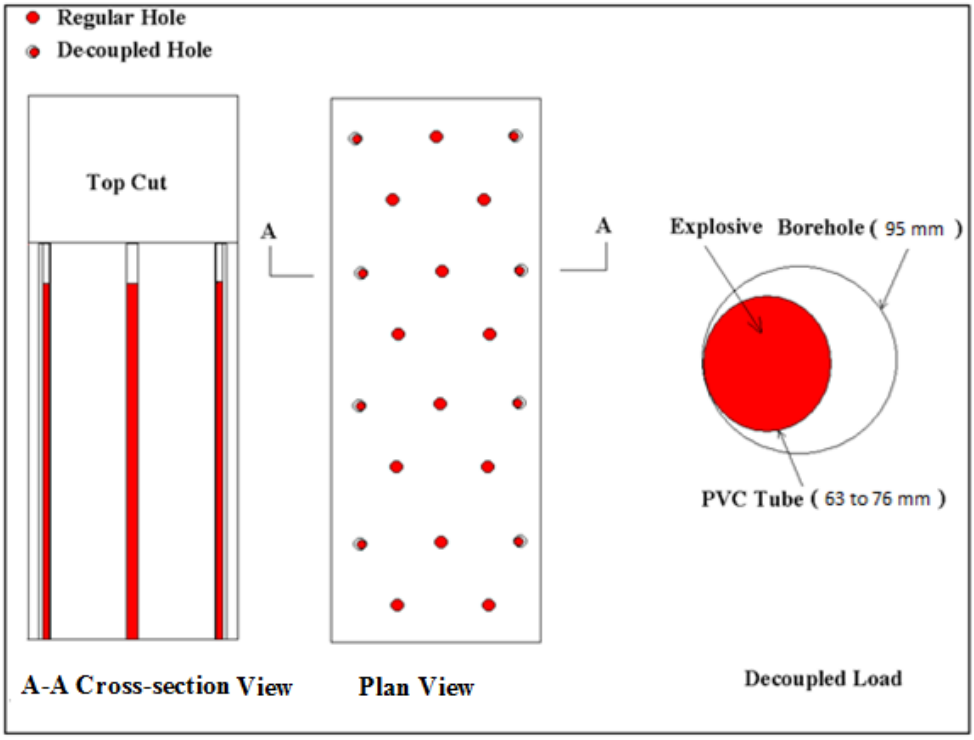

Figure 12.11. Modification blast design #1

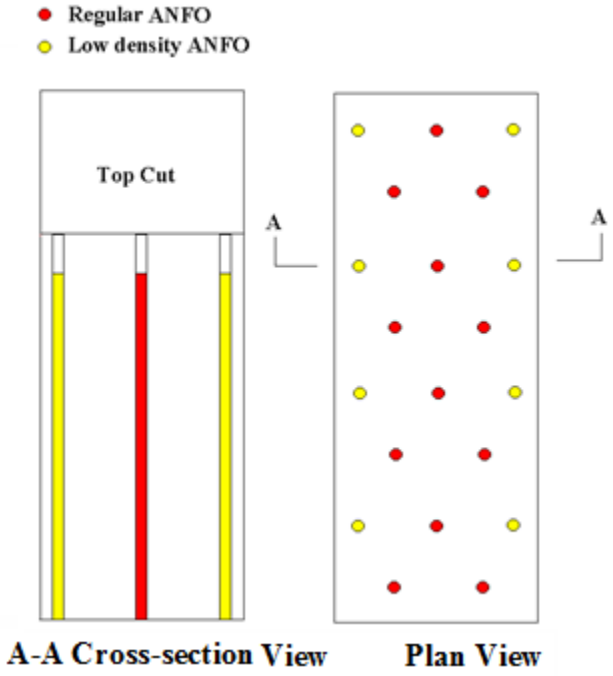

Figure 12.12. Modification blast design #4

Table 12.3. Powder factors for the modified pattern and four modifications

Blast design	Powder factor for entire stope (kg/m^3)	Powder factor for ribs (kg/m^2)
Modified pattern	1.31	1.61
Modification #1	1.12	1.02
Modification#2	1.12	1.02
Modification#3	1.00	1.02
Modification#4	1.10	0.98

Table 12.4. Properties of explosives

Explosive	Density (g/cc)	Velocity of detonation (m/s)	Diameter (mm)
ANFO (regular)	0.82	3500	95
ANFO (regular)	0.82	3350	76
ANFO (regular)	0.82	2800 (unconfined condition)	76
ANFO (low energy)	0.88	2000	95
ANFO (low energy)	0.88	1800	76

Table 12.5. Properties of rock

Parameter	Value
Density (g/cc)	2.65
Poisson's ratio	0.25
Compressive strength (MPa)	80
Tensile strength (MPa)	6
P-wave velocity (m/s)	4000
Hugoniot constant of rock	1.4

Table 12.6. Predicted extent of the damage zones around borehole for each blast design

Diameter of hole (mm)	Explosive	Extent of crack zone (m)
95	ANFO (regular)	1.71
76	ANFO (regular)	1.25
Decoupled with 76 mm charge and 95 mm hole	ANFO (regular)	1.22
95 mm	ANFO (low energy)	1.19

Based on the predictions, the extent of the damage zone (overbreak for all blast designs are illustrated in Figures 12.13, 2.14, 12.15, 12.16, 12.17, and 12.18. The worst case is for the original stoping pattern. Good results are achieved by modification #1, #2, #3 and #4. The #4 modification is the most practical method for the operation. This pattern employs low energy ANFO in rib holes.

The predicted overbreak for all blast designs are presented in Table 12.7. As shown, modification #4 decreases the largest overbreak more than 55% and average overbreak is reduced more than 72% compared to the original design. Based on this result, modification #4 was selected for field testing.

12.5 Field Experiments

Stope 145 and stope 153 in Zone 1, were selected for field testing. Because no low energy ANFO is produced in the United States, AmexK manufactured by Orica was ordered from Canada. Amex K is a low-energy blend of ammonium nitrate, inert material and refined oil designed for controlled blasting under dry conditions. The

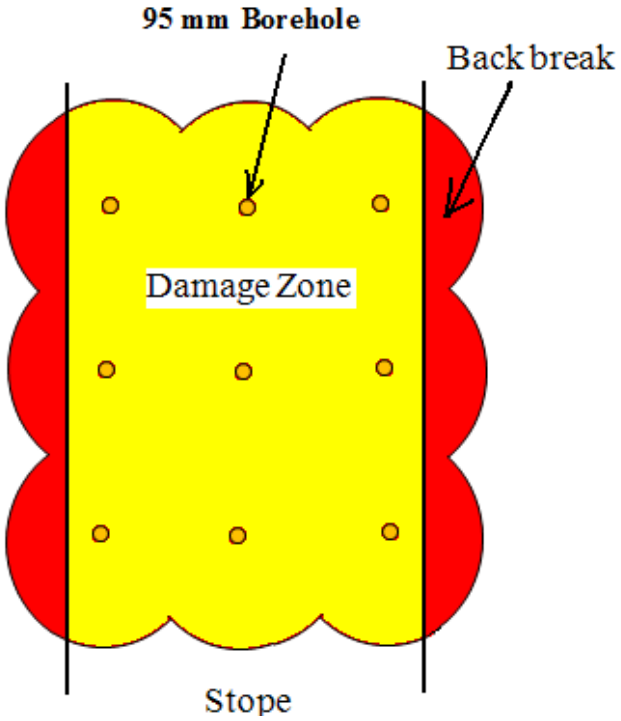

Figure 12.13. Prediction overbreak of original blast design

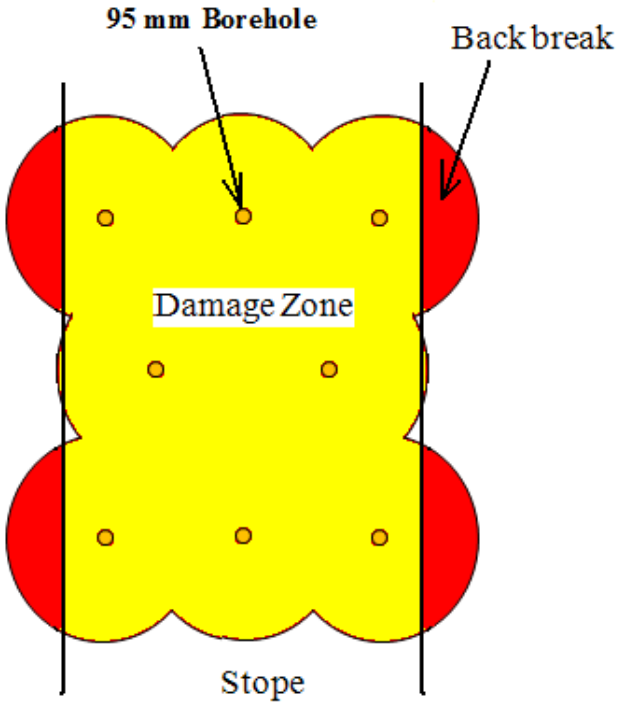

Figure 12.14. Prediction of overbreak using the modified hole pattern

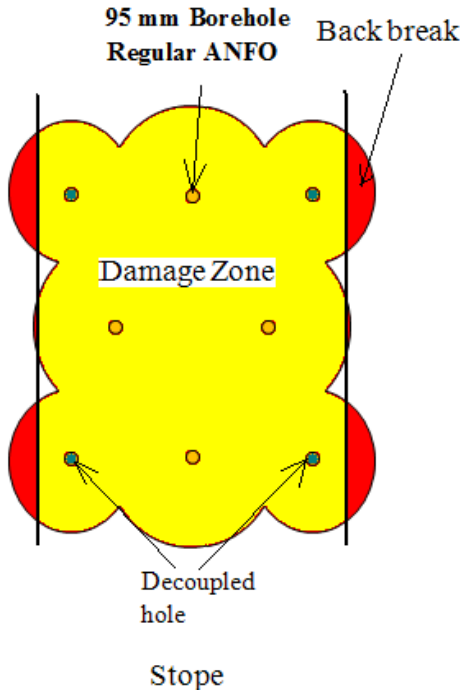

Figure 12.15. Prediction of overbreak produced by modification #1, decoupled explosives in the rib holes

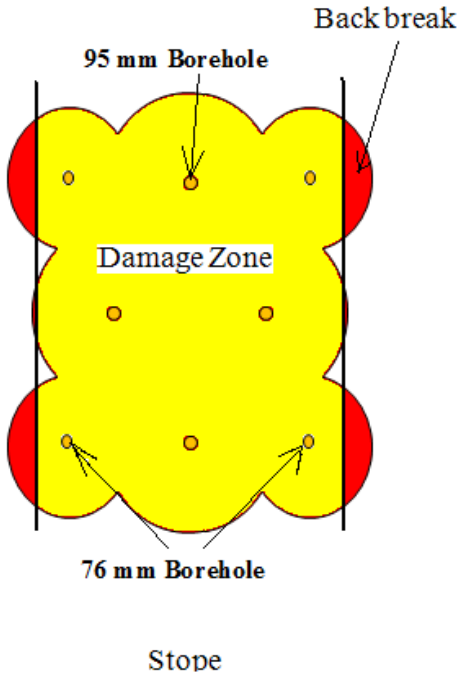

Figure 12.16. Prediction of overbreak produced by modification #2, using smaller boreholes along the rib

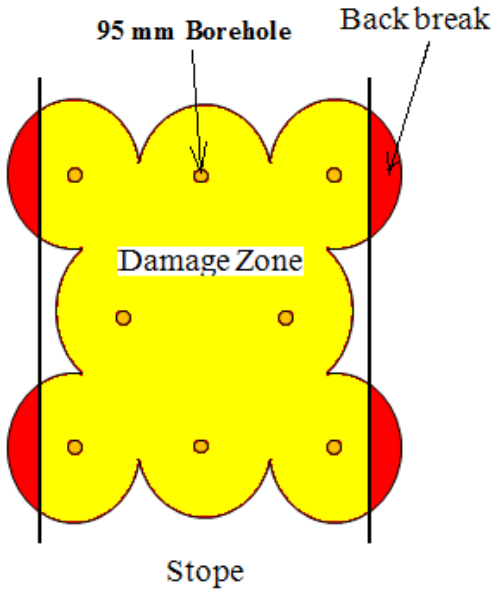

Figure 12.17. Prediction of overbreak produced by modification #3, using 76 mm holes throughout

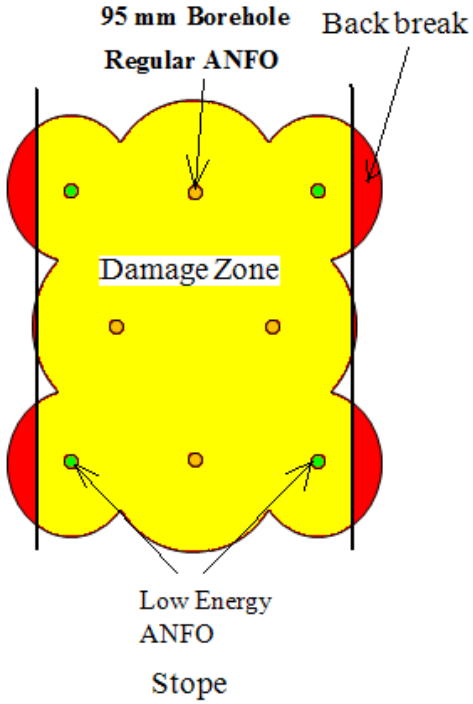

Figure 12.18. Prediction of overbreak produced by modification #4, using low energy ANFO for only rib side holes

Table 12.7. Predicted overbreaks for all blast designs

Blast design	Largest overbreak (m)	Average overbreak (m)
Original blast design	0.95-1.10	0.76-0.91
Modified hole pattern, all 95 mm holes	0.95-1.10	0.46-0.55
Modification #1, with decoupled explosives in the rib holes	0.45-0.61	0.24-0.30
Modification #2, with 76 mm holes for ribs and all other holes 95 mm	0.49-0.64	0.24-0.34
Modification #3, with 76 mm throughout	0.49-0.64	0.24-0.34
Modification #4, with 95 mm holes throughout and low energy ANFO in the rib holes	0.43-0.58	0.21-0.30

technical data of Amex K are shown in Table 12.8.

To confirm that Amex K was an appropriate low energy ANFO for modification #4, field borehole VOD measurements were conducted. A MicroTrap VOD recorder, MERL Kingston, Canada, was used to measure the VOD for explosives in the borehole. The measured VOD results of Amex K and regular ANFO are 2273 m/s and 3810 m/s, respectively, shown in Figure 12.19 and 12.20. The damage zone prediction for Amex K and regular ANFO was rechecked using SWT based on the measured VODs. The extent of the damage zones around the boreholes for Amex K and conventional ANFO by SWT is shown in Table 12.9. The results indicate that the extent of damage zone produced by Amex K is much less than that produced by conventional ANFO.

Table 12.8. Technical data for Amex K (Orica 2008)

Amex K	Poured in 100 mm holes
Loaded density (g/cc)	0.88
Typical velocity of detonation	1500 m/s
Water resistance	None
Relative Weight Strength	0.43

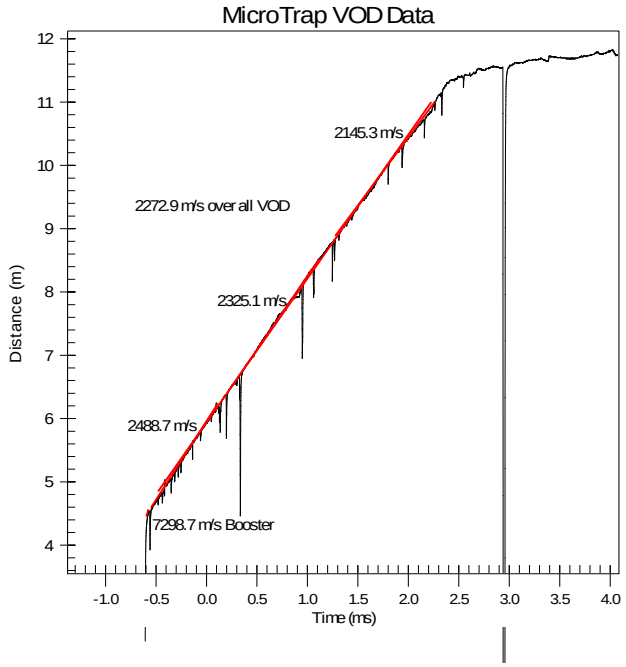

Figure 12.19. VOD of Amex K

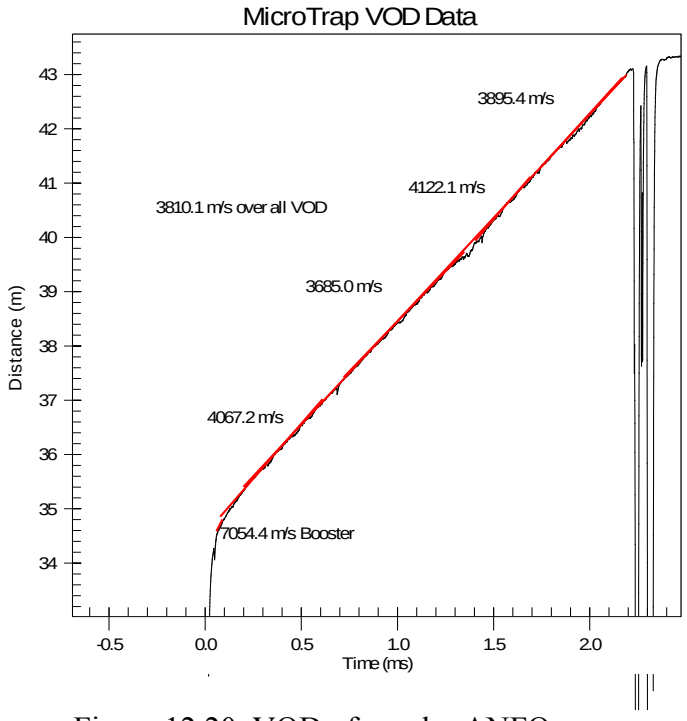

Figure 12.20. VOD of regular ANFO

Table 12.9. Extent of the damage zones around borehole for Amex K and regular ANFO by SWT

Diameter of hole (mm)	Explosive	Extent of crack zone (m) by SWT
95	ANFO (regular)	1.83
95	ANFO (low energy)	1.31

As shown in modification #4 (Figure 12.12), Amex K was loaded in all rib holes and conventional ANFO was loaded in all other holes in stopes 145 and 153. Exceptional results were achieved as indicated by CMS and shown in Figures 12.21, and 12.22. Overbreaks for the two stopes are tabulated in Table 12.10. Very little over break occurred in these two stopes. The largest overbreaks in stopes 140 and 153 were 0.85 m and 0.98 m, respectively, and average overreaks were 0.30 and 0.32 m, respectively. Comparing this new blast design with the original, the average overbreak decreased more than 63%.

12.6 Conclusions for Field Tests Compared to SWT Predictions

The overbreak results from SWT and field experiments are summarized in Table 12.11. The largest overbreaks in stope ribs experienced in the field tests are larger than those predicted by SWT. However, the average overbreak in stope ribs from field experiments are very close to those predicted by SWT. It is likely that geotechnical structures, such as joints, could make the extent of backbreak more variable but the usefulness of the SWT approach for average results has been confirmed for conditions at Leeville.

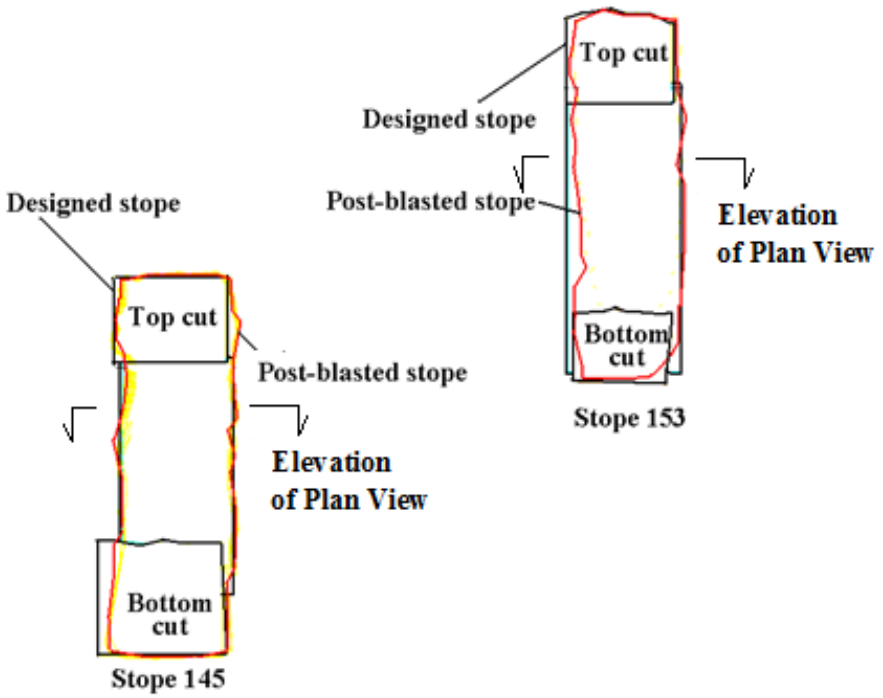

Figure 12.21. CMS results of postblasted stopes 145 and 153 (cross-section)

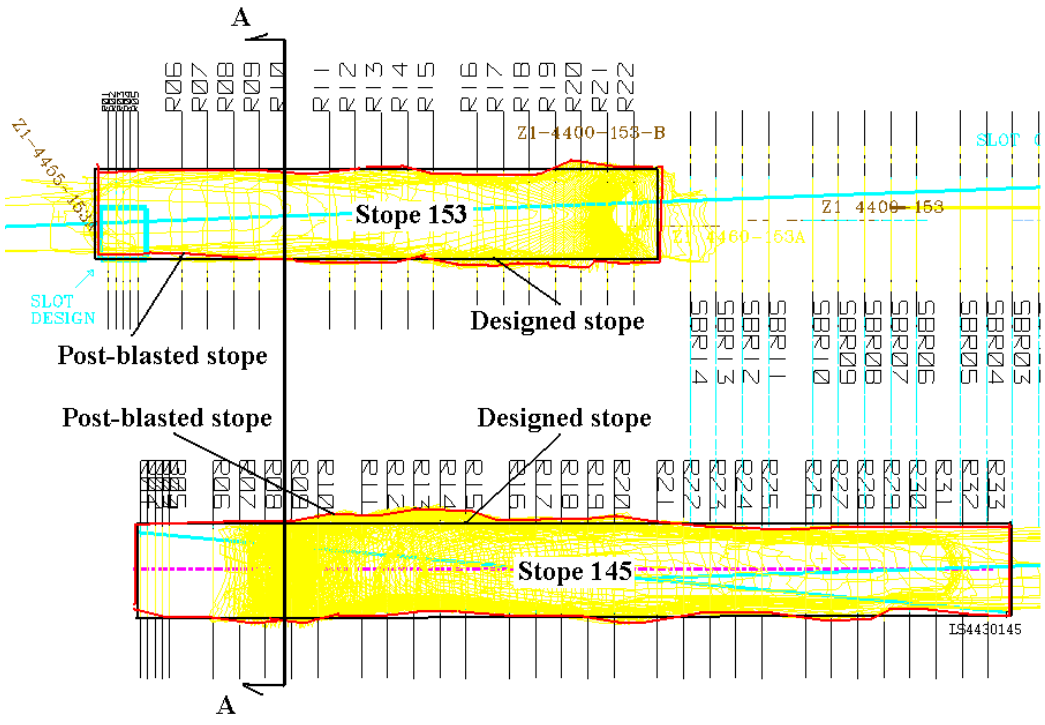

Figure 12.22. CMS results of postblasted stopes 145 and 153 (plan view at midheight)

Table 12.10. Overbreak results of stope 145 and 153 at midheight

Measuring location from west end of stope (m/ft)	145 north Rib (m)	145 south Rib (m)	153 north Rib (m)	153 south Rib (m)
6 /20	0.30	0.00	0.64	0.00
13/40	0.85	0.55	0.58	0.15
18/60	0.85	0.00	0.98	0.24
24/80	0.37	0.43	0.24	0.58
30/100	0.37	0.00	0.00	0.30
37/120	0.00	0.00	0.00	0.40
43/140	0.00	0.55	0.30	0.00
Average overbreak of each rib	0.40	0.21	0.40	0.24
Average overbreak of both ribs for each stope	0.00	0.30	0.00	0.32

Table 12.11. Overbreak comparison between SWT and field experiments

Stope	145		153	
Overbreak	Largest overbreak (m)	Average overbreak (m)	Largest overbreak (m)	Average overbreak (m)
SWT	0.55-0.70	0.27-0.37	0.55-0.70	0.27-0.37
Field experiment	0.85	0.30	0.98	0.32

13. PRACTICAL GUIDELINES FOR BLASTING USING SWT

In this chapter, the SWT model is used to produce an engineer-friendly approach to predict the damage zone in surface and underground rock blasting in granite based on the Shock Wave Transfer (SWT) model. The results are displayed in the form of convenient damage prediction charts. Both conditions of full loading and decoupled loading are considered. ANFO is the explosive of choice for full loading provided the boreholes are dry. Gurit is employed for decoupled loading rock blasting.

13.1 Prediction of the Crack and Crush Zones with Fully Loaded Boreholes

Most industrial explosives have nonideal explosion properties. This is especially true for ANFO. One characteristic of ANFO is that its VOD depends on the diameter of the explosive charge as shown in Figure 13.1. Because of the dependence of VOD on diameter, prediction of the extent of the crack zone is directly related to the borehole diameter. In practical rock blasting operations, smaller borehole diameters are used in underground mining, and larger borehole diameters are used in surface mining. Usually, the borehole diameters are 50.8 to 76.2 mm for underground mining, and 101.6 to 304.8 mm for surface mining.

To develop an engineer-friendly application of the SWT model for predicting the damage zone, convenient damage prediction charts are constructed for different rock types. By knowing the extent of damage, engineers can design blasts to protect the

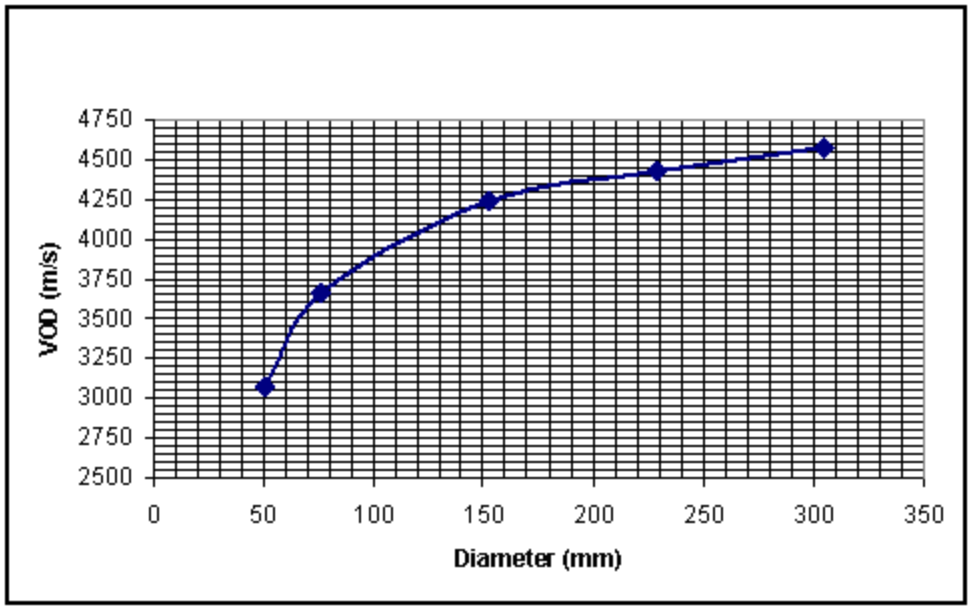

Figure 13.1. VOD versus borehole diameter for ANFO (density, 0.81 g/cc), modified from Atlas Powder Co. 1987)

integrity of rock beyond the excavation. Using the SWT computer program presented in Appendix A, appropriate properties for explosives and rocks can be entered into the program using the input page shown on Figure 13.2. By varying the compressive and tensile strength, tables can be prepared which provide the corresponding crush and crack zone radii. Other useful parameters are also obtained and can be summarized by tables or figures if needed.

Using explosive properties summarized in Table 13.1, (Atlas Powder Co. 1987) and rock properties (Lama and Vutukuri 1978), convenient design charts for three borehole diameters (50.8 mm, 152.6 mm, and 304.8 mm) are presented in Tables 13.2 to 13.4 for holes fully loaded with ANFO. The data presented in these tables is presented graphically in Figures 13.3 to 13.6. For other borehole diameters used in practice, the

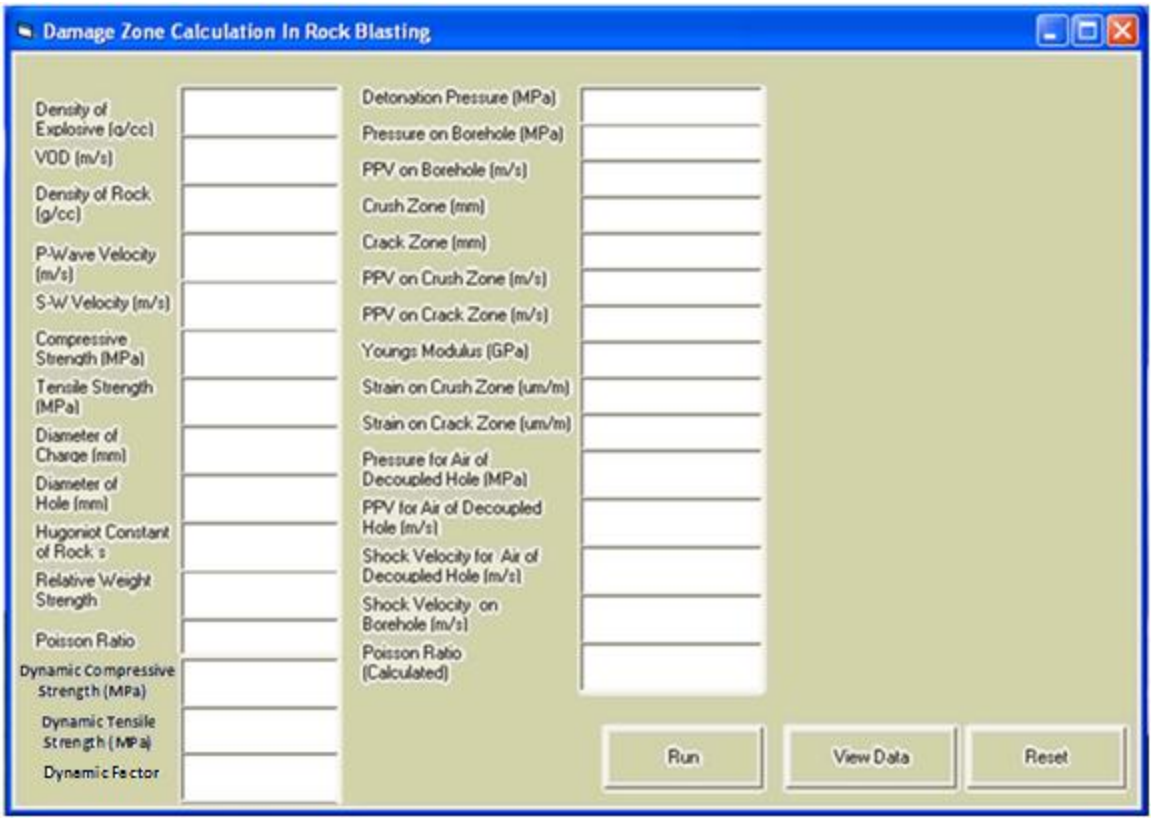

Figure 13.2. SWT computer program input page

crack and crush zones can be obtained by interpolation from the prediction tables or charts.

13.2 Prediction of the Crack and Crush Zones with Decoupled Boreholes

For smooth-wall, rock-blasting operations, decoupled loading techniques are often employed. These operations include smooth blasting in underground mining operations and presplit blasting in surface mining operations. However, damage predictions for decoupled rock blasting are not generally available.

The explosive, Gurit, is used for illustration. The density and VOD of Gurit are 1.0 g/cc and 2200 m/s, and the diameter is 22 mm.

Table 13.1. Rocks and their properties (Atlas Powder Co. 1987)

Material	Density g/cc	Vp (m/s)	Vs (m/s)	Compressive strength (MPa)	Tensile strength (MPa)
Granite	2.67	5029	2744	98-275	3.9-24.5
Gabbro	2.98	6555	3445	147-294	4.9-29.4
Baslt	3.00	5610	3049	78-412	5.9-29.4
Sandstone	2.45	3354	1982	49-167	5-24.5
Limestone	2.65	4573	2972	3.9-245	1-24.9
Shale	2.35	2896	1677	9.8-160	2-9.8
Diabase	2.98	6370	3740	118-245	5.9-12.7
Slate	2.30	4055	2866	24.5-196	6.9-19.6
Marble	2.80	5793	3506	51-280	4-29
Quartzite	2.75	6052	3500	85-353	3-35
Schist	2.85	4543	2896	31-251	5-11
Gneiss	2.80	5153	2800	78-245	3.9-19.6
Dolomite	2.65	5457	3000	14.7-245	2.5-24.5

Table 13.2. Crack and crush zones for 50.8 mm holes in granite fully loaded with ANFO

Tensile strength (MPa)	Crack zone (m)	Crack zone with scale distance (r/r_h)	Compressive strength (MPa)	Crush zone (mm)	Crush zone with scale distance (r/r_h)
3	1.6	64.2	50	61	2.4
5	1.4	55.5	90	50	2.0
10	0.9	35.8	120	45	1.8
15	0.7	29.1	160	40	1.6
20	0.7	25.6	200	37	1.5
25	0.6	23.2	240	35	1.4
30	0.5	21.3	280	33	1.3

Table 13.3. Crack and crush zones for granite by 152.6 mm holes in granite fully loaded with ANFO

Tensile strength (MPa)	Crack zone (m)	Crack zone with scale distance (r/r_h)	Compressive strength (MPa)	Crush zone (mm)	Crush zone with scale distance (r/r_h)
3	6.0	79.0	50	225	3.0
5	5.2	68.4	90	183	2.4
10	3.4	44.0	120	165	2.2
15	2.7	36.0	160	149	2.0
20	2.3	30.7	200	138	1.8
25	2.2	28.5	240	129	1.7
30	2.0	26.3	280	122	1.6

Table 13.4. Crack and crush zones for 304.8 mm holes in granite fully loaded with ANFO

Tensile strength (MPa)	Crack zone (m)	Crack zone with scale distance (r/r_h)	Compressive strength (MPa)	Crush zone (mm)	Crush zone with scale distance (r/r_h)
3	12.6	110.6	50	473	4.1
5	10.9	95.7	90	384	3.4
10	7.0	61.4	120	346	3.0
15	5.7	50.2	160	313	2.7
20	5.0	43.9	200	289	2.5
25	4.6	39.8	240	271	2.4
30	4.2	36.8	280	256	2.2

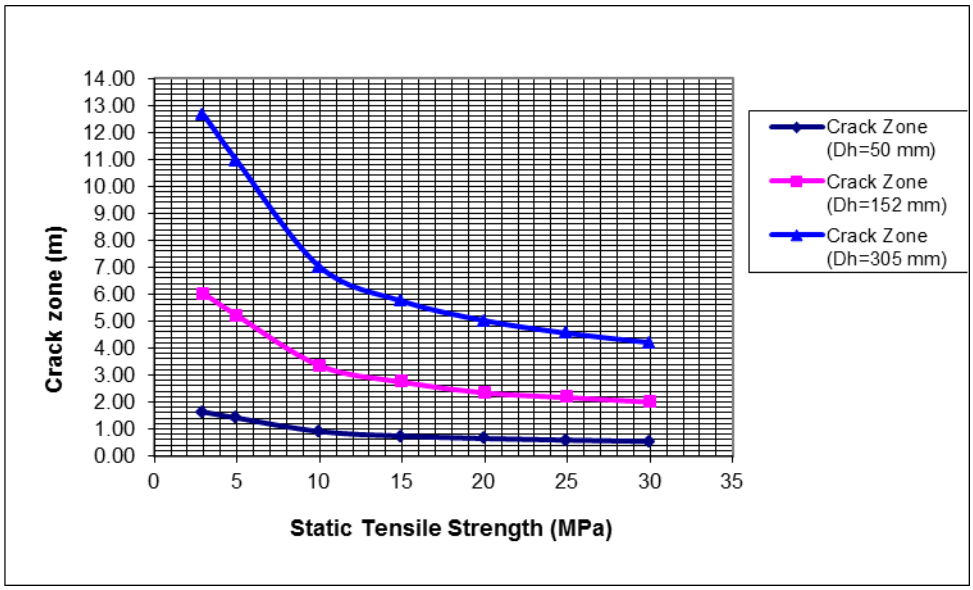

Figure 13.3. Crack zone for granite using ANFO

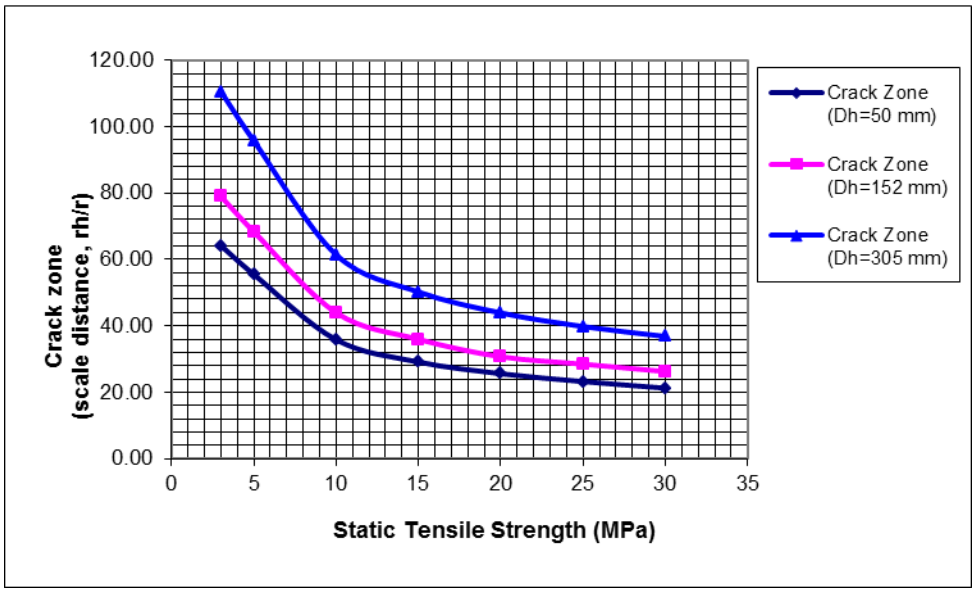

Figure 13.4. Crack zone in terms of scaled distance for granite using ANFO

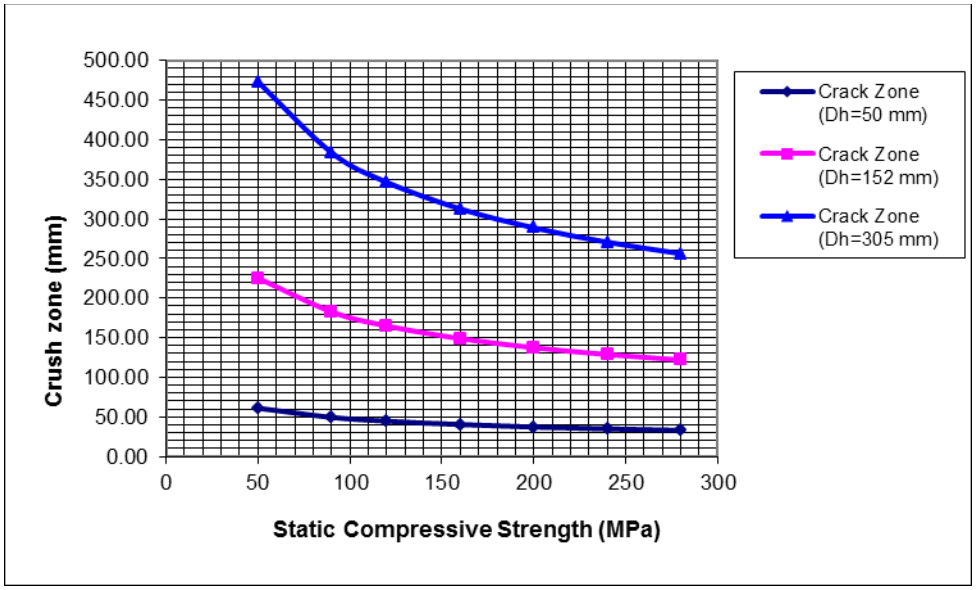

Figure 13.5. Crush zone for granite using ANFO

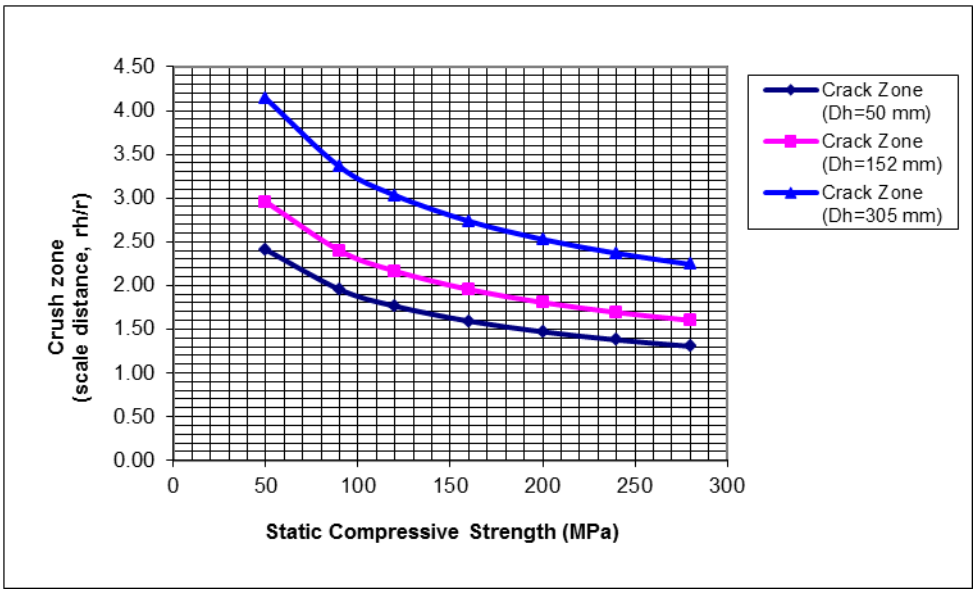

Figure 13.6. Crush zone in terms of scaled distance for granite using ANFO

To develop convenient damage prediction charts for granite, the SWT model is employed using the values for γ as defined in Section 5.1 (γ=3.0 when $P_e \leq P_h$, and γ=1.2-1.4 when $P_e \geq P_h$). The diameter of the explosive charge is kept constant at 22 mm. The diameters of the borehole, 32 mm, 50.8 mm and 76.2 mm are used. The results of the damage prediction for granite with decoupled blasting are shown in Tables 13.5 to 13.7 and Figures 13.7, to13.10 which are developed as explained in the previous section.

Table 13.5. Crack and crush zones in granite for decoupled 32 mm holes using 22 mm Gurit

Tensile strength (MPa)	Crack zone (m)	Crack zone with scale distance (r/r_h)	Compressive strength (MPa)	Crush zone (mm)	Crush zone with scale distance (r/r_h)
3	0.7	40.6	50	29	1.8
5	0.6	35.0	90	20	1.2
10	0.4	22.5	120	18	1.1
15	0.3	18.1	160	0	0
20	0.2	14.4	200	0	0
25	0.2	11.9	240	0	0
30	0.2	10.0	280	0	0

Table 13.6. Crack and crush zones in granite for decoupled 50.08 mm holes using 22 mm Gurit

Tensile strength (MPa)	Crack zone (m)	Crack zone with scale distance (r/r_h)	Compressive strength (MPa)	Crush zone (mm)	Crush zone with scale distance (r/r_h)
3	0.7	28.0	50	27	1.1
5	0.5	19.7	90	0	0
10	0.3	11.0	120	0	0
15	0.2	7.9	160	0	0
20	0.2	6.3	200	0	0
25	0.1	5.1	240	0	0
30	0.1	4.3	280	0	0

Table 13.7. Crack and crush zones in granite for decoupled 76.2 mm holes using 22 mm Gurit

Tensile strength (MPa)	Crack zone (m)	Crack zone with scale distance(r/r_h)	Compressive strength (MPa)	Crush zone (mm)	Crush zone with scale distance (r/r_h)
3	0.5	14.2	50	0	0
5	0.4	9.2	90	0	0
10	0.2	5.3	120	0	0
15	0.1	3.7	160	0	0
20	0.1	2.9	200	0	0
25	0.1	2.4	240	0	0
30	0.1	2.1	280	0	0

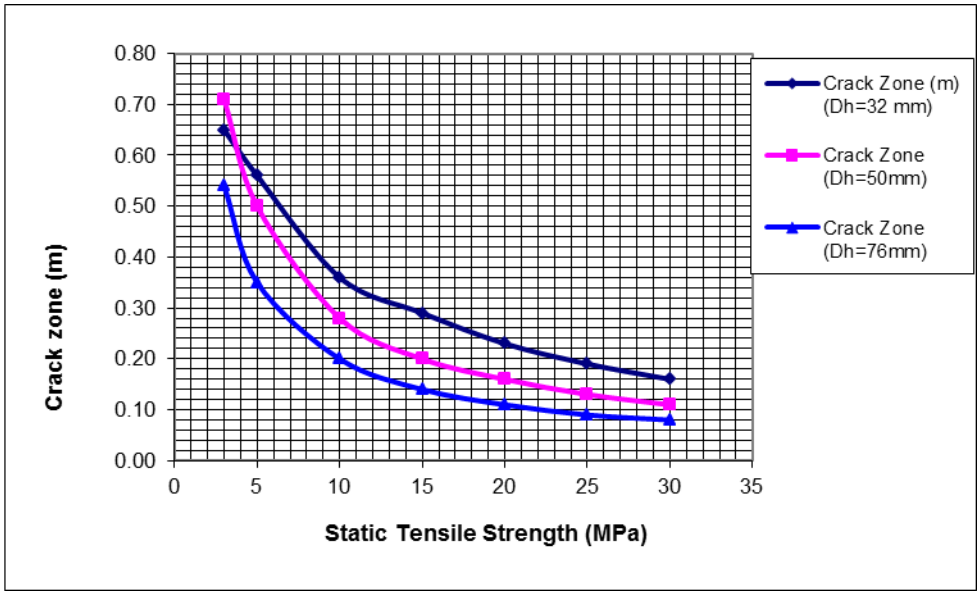

Figure 13.7. Crack zone in granite with decoupled 22 mm Gurit

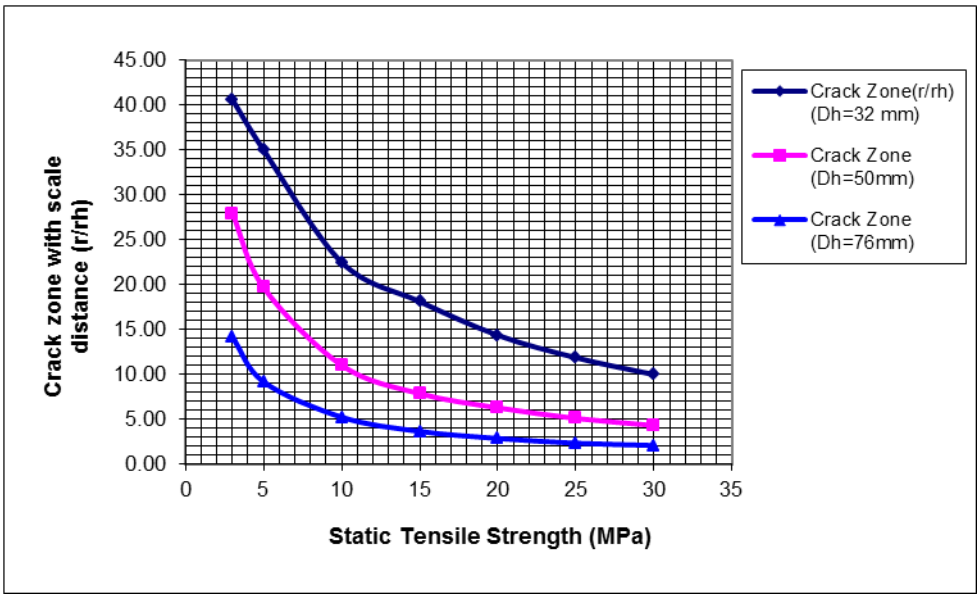

Figure 13.8. Crack zone in terms of scaled distance in granite with decoupled 22 mm Gurit

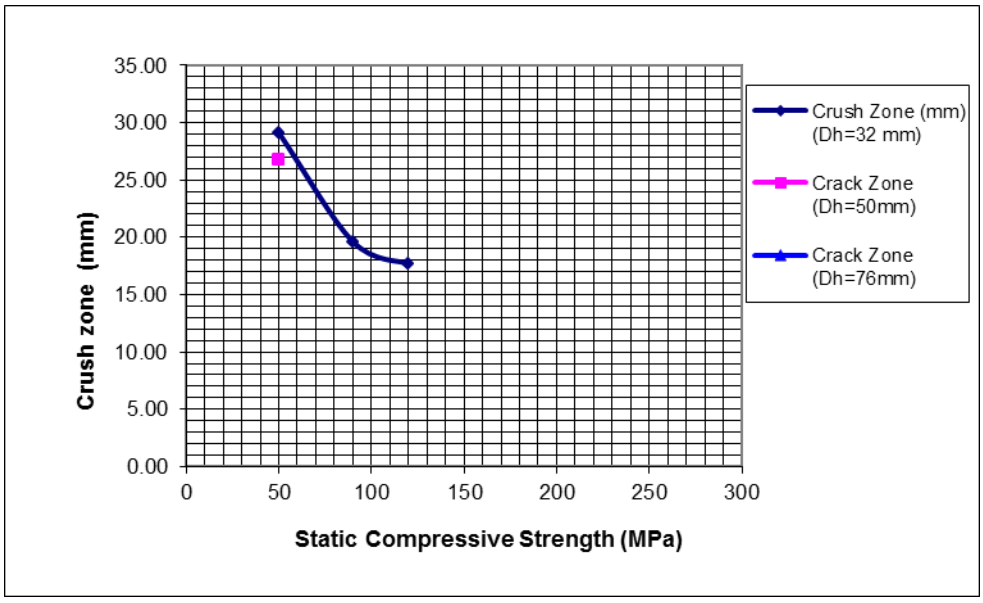

Figure 13.9. Crush zone in granite with decoupled 22 mm Gurit

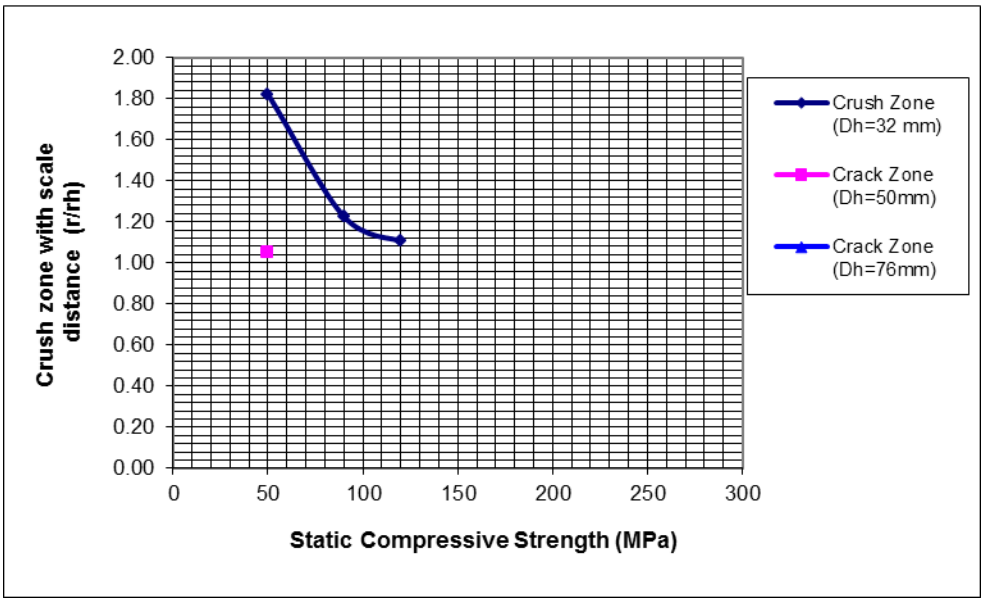

Figure 13.10. Crush zone in terms of scaled distance
in granite with decoupled 22 mm Gurit

14. CONCLUSIONS AND FUTURE RESEARCH

14.1 Conclusions

This dissertation presents a new damage zone prediction model for rock blasting based on Shock Wave Transfer (SWT). The SWT approach is based on shock wave mechanics (Cooper 1996; Henrych 1979). It is applied to estimate the detonation interactions between explosives and other materials, such as rock, air, concrete, and steel etc. To validate the SWT model, three validations are presented: (1) currently available experimental data in the literature; (2) large-scale laboratory experiments; and (3) results of a field application in an underground mine. Based on Esen's (2003) laboratory experiments and large-scale laboratory experiments, the SWT model successfully estimates the extent of the crush zone. The SWT model provides estimates similar to other approaches, i.e., the Modified Ash (Energy-based), Modified Ash (Pressure-based), Holmberg Explosive Factor, and Sher Quasi-Static models. One advantage the SWT model has over these approaches is the ability to estimate the crush zone. This ability provides a unique design option for engineers. By constraining the crush zone to a small value or zero, an improved perimeter blast is possible.

However, confirmation of crack zone prediction by the SWT model was unsuccessful for the large-scale laboratory experiments. It is likely that the relatively small size of the laboratory models and lack of complete confinement influenced the extent of the crack zone. In addition, Autodyn simulation may need further refinement.

An actual field application of this new method under field conditions, however, demonstrates the usefulness of the SWT model for practical blast design.

New insights and useful information produced by this research include:

- The borehole pressure calculated by the SWT model suggests that it is larger than one-half of the detonating pressure for fully-coupled holes (Section 4.2). The borehole pressure determined by the SWT model is a function of both explosive and rock properties. The explosion pressure determined by dividing the detonation pressure by 2 is a function of the explosive properties only and is independent of the properties of the rock surrounding the borehole. This simplification may not provide the best estimate for the borehole pressure. (Section 4.2).
- The theoretical basis of SWT provides an explanation for the channel effect in decoupled rock blasting (Section 5.2). The pressure on the air in the borehole for decoupled blasting is smaller than the detonating pressure. However, the shock wave velocity in the air surrounding the charge may be larger than the VOD of the explosive causing the air shock wave to propagate ahead of the detonation. The air pressure could be sufficient to desensitize the explosive leading to less than full-order detonation.
- The borehole pressure for decoupled blasting estimated by the SWT model is related to the properties of both the explosive and the rock surrounding a borehole. Estimates based on Equation 5.2, currently used, are related only to the properties of explosive (Section 5.3).
- Dynamic compressive and tensile strengths of grout used to simulate rock for laboratory experiments are larger than those for static conditions. The dynamic

compressive and tensile strengths were tested using Split Hopkinson Pressure Bar (SHPB, Section 9.3). The SHPB is more representative of the strain rates experienced in rock blasts.

- For rock blasting, the strain rate at a point in rock depends on the borehole pressure, P-wave velocity and density of the rock, and the distance between the borehole and the point to be considered (Equation 6.7). The strain rate decreases as the distance between the borehole and the point to be considered increases.
- The extents of the crush zone and the crack zone are determined by properties of the explosive, properties of the rock, and the degree of coupling. Dynamic compressive strength governs the extent of crush zone and dynamic tensile strength controls the extent of crack zone.
- In this research, dynamic tensile strength was assumed to apply over the extent of the crack zone, based on the laboratory results, the dynamic strength factor may be less than 2.0.
- A successful field trial confirmed that the SWT model can be used in practical blast design.
- A series of convenient charts can be created using the SWT model to predict the extents of crack zone and crush zone based on the properties of rock and explosive.
- The extents of the crack zone and crush zone predicted by SWT for decoupled models are similar to those predicted by AUTODYN for decoupling ratios of 3.5 to 5.0 (Appendix C).

14.2 Future Work

The SWT model provides reasonable estimates for the extent of the crush zone in rock blasting. This may be of value for perimeter blasting in underground mining and presplit blasting in surface mining. In these blasting operations, no crush zone, or only a minor crush zone, can be tolerated. Damage is not limited by crush zone alone. The extent of the crack zone must also be determined. Laboratory models employed in this research were inadequate in validating the extent of the crack zone predicted by the SWT model. The reason is likely because the laboratory models are too small and not well confined. Considering the requirements of size and confinement, verification in the field may be a better option than large and more complicated laboratory tests. The ideal experimental site would be a quarry or underground mine dedicated to research or training. In this case, static and dynamic properties of rock and presence or absence of geologic structures could be evaluated for the specific site rather than trying to simulate them under laboratory conditions. Commercially available explosives should be selected and all properties of explosives should be measured under the conditions at the experimental site. Sawing or grinding the rock in a direction perpendicular to the borehole could be used for the investigation of crush and crack zones in field experiments. In addition to homogenous and isotropic rock, future research should deal with rock masses containing geological discontinuities. More research for appropriate γ values should be conducted. The γ value for decoupled conditions could be different from those values assumed in Section 5.1

The present formulation of the SWT software employs a dynamic tensile strength factor of 2.0 to estimate the extent of the crack zone. It is reasonable to believe that the

strain rate decreases as the distance from the blast hole increases. If this is a case, using the static tensile strength to determine the extent of the crack zone may be more appropriate. Doing so would also provide a more conservative estimate of the extent to which tension cracks will propagate. Therefore, research should be done to determine the distance from a blast hole for which the static tensile strength should govern the SWT estimate of the extent of the crack zone.

Other future work could include additional charts for the extent of the crush zone and the crack zone for the most common rock types (see Section 12) so that explosives engineers can predict the extent of damage zones by simply referring to the appropriate chart. In addition, a stronger database for dynamic properties of rock should be developed. It may be more appropriate using SPHB to determine the dynamic compressive and tensile strengths in the blasting strain rate range. More research needs to be done to determine the attenuation factors for the stress wave and the shock wave beyond the borehole wall as they propagate outward in the radial direction. Furthermore, research is needed to determine the effect of charge shape (spherical attenuation factors. versus cylindrical) on the attenuation factors.

APPENDIX A

VISUAL BASIC PROGRAM FOR THE SWT MODEL

```
Dim Dense, VOD, Dr, SSD, YM, CS, Ts, Cd, Td, Kd, DE, DH, PCJ, Ph, Vh, Pcrit,
Ccrit, Q, Dair As Single
 Sub Newton4(x)
to1 = 0.00001
b = 100000000000#
a = 0 'b / 1000
Do
a1 = Cosec(ByVal a)
b1 = Cosec(ByVal b)
c = (a + b) / 2
c1 = Cosec(ByVal c)
If Abs(c1) < Abs(to1) Then GoTo 20
If Abs(c1 + a1) = Abs(c1) + Abs(a1) Then a = (a + b) / 2
If Abs(c1 + a1) <> Abs(c1) + Abs(a1) Then b = (a + b) / 2
Loop
20 x = c
End Sub
Public Function Cosec(ByVal x As Double)
```

```
Dee = Val(Formd1.TxtDee.Text)

VOD = Val(Formd1.TxtVOD.Text)

Dr = Val(Formd1.TxtDr.Text)

PW = Val(Formd1.TxtPW.Text)

'YM = Val(TxtYM.Text)

Cd = Val(Formd1.TxtCdText)

Td = Val(Formd1.TxtTd.Text)

Kd = Val(Formd1.TxtKd.Text)

CS = Val(Formd1.TxtCS.Text)

Ts = Val(Formd1.TxtTS.Text)

DE = Val(Formd1.TxtDe.Text)

DH = Val(Formd1.TxtDh.Text)

s = Val(Formd1.Txts.Text)

RWS = Val(Formd1.TxtRWS.Text)

Q = RWS * 3821000

PCJ = ((Dee * 1000 * VOD ^ 2) / 4)

Pcrit = Dee * 1000 * (VOD ^ 2) * 16 * ((0.4 / 3) * (Q / VOD ^ 2 - (1 / 16))) ^ (3 / 2)

Ccrit = (3 / 4) * VOD * (Pcrit / PCJ) ^ (1 / 3)

Cosec = (VOD / 4) * (1 + 3 * (1 - (Pcrit / PCJ) ^ (1 / 3))) + (3 * Ccrit / 0.8) * (1 - (x /

Pcrit) ^ (0.4 / 2.8)) - ((2 / 2.2) * x / 1.225) ^ 0.5

End Function
```

```
Dim Dense, VOD, Dr, SSD, YM, CS, Ts, Kd, DE, DH, PCJ, Ph, Vh, Pcrit, Pm, Ccrit,
Q, SKVair, Dair As Single
 Sub Newton5(x)
to1 = 0.00001
b = Val(Formd1.TxtPW.Text)
a = 0 'b / 1000
Call Newton4(X1)
Pm = X1 / 1000000
Vm = ((2 / 2.2) * X1 / 1.225) ^ 0.5
SKVair = (2.2 / 2) * Vm
Formd1.TxtPPVair.Text = Round(Vm, 6)
Formd1.TxtPair.Text = Round(Pm, 6)
Formd1.TxtSKVair.Text = Round(SKVair, 6)
Do
a1 = Cosec(ByVal a)
b1 = Cosec(ByVal b)
c = (a + b) / 2
c1 = Cosec(ByVal c)
If Abs(c1) < Abs(to1) Then GoTo 20
If Abs(c1 + a1) = Abs(c1) + Abs(a1) Then a = (a + b) / 2
If Abs(c1 + a1) <> Abs(c1) + Abs(a1) Then b = (a + b) / 2
Loop
20 x = c
```

```
End Sub


Public Function Cosec(ByVal x As Double)
Dee = Val(Formd1.TxtDee.Text)
VOD = Val(Formd1.TxtVOD.Text)
Dr = Val(Formd1.TxtDr.Text)
PW = Val(Formd1.TxtPW.Text)
'YM = Val(TxtYM.Text)
CS = Val(Formd1.TxtCS.Text)
Ts = Val(Formd1.TxtTS.Text)
Cd = Val(Formd1.TxtCd.Text)
Td = Val(Formd1.TxtTd.Text)
Kd = Val(Formd1.TxtKd.Text)
DE = Val(Formd1.TxtDe.Text)
DH = Val(Formd1.TxtDh.Text)
s = Val(Formd1.Txts.Text)
Pm = Val(Formd1.TxtPair.Text)
Vm = Val(Formd1.TxtPPVair.Text)
'Dair = 0.25 * Dee * 1000 * (DE / DH) ^ 2.4
Pm = Pm * 1000000
Kvod = VOD / 800 'density chang coefficient
If Kvod > 5 Then
Kvod = 5
```

```
End If


Kdec = 2 + 0.08 * Kvod
'Dair = 0.1 * Dee * 1000 * (DE / DH) ^ 2.8
Dair = Kvod * (1 / (1 / 1.225 - (Vm ^ 2) / Pm)) * (DE / DH) ^ Kdec
'Vm = Vm * (DE / DH) ^ 0.5
PCJ = ((Dee * 1000 * VOD ^ 2) / 4)
Cosec = Dair * 899 * (2 * Vm - x) + Dair * 0.939 * (2 * Vm - x) ^ 2 - Dr * 1000 * PW
* x - Dr * 1000 * s * x ^ 2
End Function
```

==========

```
Dim Dense, VOD, Dr, SSD, YM, CS, Ts, Kd, DE, DH, PCJ, Ph, Vh As Single
 Sub Newton(x)
to1 = 0.00001
b = Val(Formd1.TxtPW.Text)
a = 0 'b / 1000
Do
a1 = Cosec(ByVal a)
b1 = Cosec(ByVal b)
c = (a + b) / 2
c1 = Cosec(ByVal c)
If Abs(c1) < Abs(to1) Then GoTo 20
If Abs(c1 + a1) = Abs(c1) + Abs(a1) Then a = (a + b) / 2
```

```
If Abs(c1 + a1) <> Abs(c1) + Abs(a1) Then b = (a + b) / 2

Loop


20 x = c

End Sub

Public Function Cosec(ByVal x As Double)

Dee = Val(Formd1.TxtDee.Text)

VOD = Val(Formd1.TxtVOD.Text)

Dr = Val(Formd1.TxtDr.Text)

PW = Val(Formd1.TxtPW.Text)

'YM = Val(TxtYM.Text)

CS = Val(Formd1.TxtCS.Text)

Ts = Val(Formd1.TxtTS.Text)

Cd = Val(Formd1.TxtCd.Text)

Td = Val(Formd1.TxtTd.Text)

Kd = Val(Formd1.TxtKd.Text)

DE = Val(Formd1.TxtDe.Text)

DH = Val(Formd1.TxtDh.Text)

s = Val(Formd1.Txts.Text)

PCJ = ((Dee * VOD ^ 2) / 4) '* (DE / DH) ^ 3

'Ph = DR * (SSD + s * Vh) * Vh

'PCJ = (((Dee * VOD ^ 2) * (1 - 0.7125 * Dee ^ 0.04)) * (DE / DH) ^ 3)
```

```
Cosec = (VOD / 4) * (1 - ((Dr * (PW + s * x) * x / PCJ) - 1) / (((4 * Dr * (PW + s * x)
* x) / (6 * PCJ) + (1 / 3))) ^ 0.5) - x
End Function
```

```
Dim Dense, VOD, Dr, SSD, YM, CS, Ts, Kd, DE, DH, PCJ, Ph, Vh As Single
 Sub Newton2(x)
to1 = 0.00001
b = 900000000 * Val(Formd1.TxtPW.Text)
a = 1000
Do
a1 = Cosec(ByVal a)
b1 = Cosec(ByVal b)
c = (a + b) / 2
c1 = Cosec(ByVal c)
If Abs(c1) < Abs(to1) Then GoTo 20
If Abs(c1 + a1) = Abs(c1) + Abs(a1) Then a = (a + b) / 2
If Abs(c1 + a1) <> Abs(c1) + Abs(a1) Then b = (a + b) / 2
Loop
20 x = c
End Sub
Public Function Cosec(ByVal x As Double)
Dee = Val(Formd1.TxtDee.Text)
VOD = Val(Formd1.TxtVOD.Text)
```

```
Dr = Val(Formd1.TxtDr.Text)
PW = Val(Formd1.TxtPW.Text)
'YM = Val(TxtYM.Text)
CS = Val(Formd1.TxtCS.Text)
Ts = Val(Formd1.TxtTS.Text)
Cd = Val(Formd1.TxtCd.Text)
Td = Val(Formd1.TxtTd.Text)
Kd = Val(Formd1.TxtKd.Text)
DE = Val(Formd1.TxtDe.Text)
DH = Val(Formd1.TxtDh.Text)
s = Val(Formd1.Txts.Text)
PCJ = ((Dee * 1000 * VOD ^ 2) / 4) * (DE / DH) ^ 3
'Ph = DR * (SSD + s * Vh) * Vh
'PCJ = (((Dee * 1000 * VOD ^ 2) * (1 - 0.7125 * Dee ^ 0.04)) * (DE / DH) ^ 3)
If Dr * PW >Dee * VOD Then
Cosec = ((x / (Dr * 1000)) * (1 - 1 / (((5.5 * x) / (Dr * 1000 * PW ^ 2)) + 1) ^ 0.2)) ^
0.5 - (VOD / 4) + ((x - PCJ) * 6 ^ 0.5) / (Dee * 1000 * 2 * (4 * x + 2 * PCJ)) ^ 0.5
Else
Cosec = ((x / (Dr * 1000)) * (1 - 1 / (((5.5 * x) / (Dr * 1000 * PW ^ 2)) + 1) ^ 0.2)) ^
0.5 - (VOD / 4) - (6 * VOD / 8) * (1 - (x / PCJ) ^ (1 / 3))
'Cosec = (((x / (Dr * 1000)) * (1 - (1 / (((5.5 * x) / (Dr * 1000 * PW ^ 2)) + 1) ^ 0.2)) ^
0.5) - (VOD / 4) + (((x - PCJ) * 6 ^ 0.5) / (Dee * 1000 * 2 * (4 * x + 2 * PCJ)) ^ 0.5))
End If
```

```
End Function
```

```
Dim Dense, VOD, Dr, SSD, YM, CS, Ts, Kd, DE, DH, PCJ, Ph, fa3, fa0, m1, theta,
Vh As Single
 Sub Newton3(fa3)
to1 = 0.00001
b = 0.5
a = 0.1
Do
a1 = Cosec(ByVal a)
b1 = Cosec(ByVal b)
c = (a + b) / 2
c1 = Cosec(ByVal c)
If Abs(c1) < Abs(to1) Then GoTo 20
If Abs(c1 + a1) = Abs(c1) + Abs(a1) Then a = (a + b) / 2
If Abs(c1 + a1) <> Abs(c1) + Abs(a1) Then b = (a + b) / 2
Loop
20 fa3 = c
End Sub
Public Function Cosec(ByVal fa3 As Double)
Dee = Val(Formd1.TxtDee.Text)
VOD = Val(Formd1.TxtVOD.Text)
Dr = Val(Formd1.TxtDr.Text)
```

```
PW = Val(Formd1.TxtPW.Text)
'YM = Val(TxtYM.Text)
fa0 = Val(Formd1.TxtSW.Text)
Ts = Val(Formd1.TxtTS.Text)
DE = Val(Formd1.TxtDe.Text)
Cd = Val(Formd1.TxtCd.Text)
Td = Val(Formd1.TxtTd.Text)
Kd = Val(Formd1.TxtKd.Text)
DH = Val(Formd1.TxtDh.Text)
s = Val(Formd1.Txts.Text)
'a = (asin((1 / (6 * m1 ^ 2)) * (((Dr * 16 * Sin((3.14 / 180) * fa3)) /
'(Dee * s * Sin((3.14 / 180) * fa0))) * ((Sin((3.14 / 180) * fa3)) / (Sin((3.14 / 180) *
fa0)) - PW / VOD) + 2))) ^ 0.5
'b = Atn(((1 / (6 * m1 ^ 2)) * (((Dr * 16 * Sin((3.14 / 180) * fa3)) / _
'(Dee * s * Sin((3.14 / 180) * fa0))) * ((Sin((3.14 / 180) * fa3)) / (Sin((3.14 / 180) *
fa0)) - PW / VOD) + 2)) / Sqr(-((1 / (6 * m1 ^ 2)) * (((Dr * 16 * Sin((3.14 / 180) *
fa3)) / _
'(Dee * s * Sin((3.14 / 180) * fa0))) * ((Sin((3.14 / 180) * fa3)) / (Sin((3.14 / 180) *
fa0)) - PW / VOD) + 2)) * ((1 / (6 * m1 ^ 2)) * (((Dr * 16 * Sin((3.14 / 180) * fa3)) / _
'(Dee * s * Sin((3.14 / 180) * fa0))) * ((Sin((3.14 / 180) * fa3)) / (Sin((3.14 / 180) *
fa0)) - PW / VOD) + 2)) + 1))
theta = Atn(Tan((3.14 / 180) * fa0) / (1 + 3 * (1 + (Tan((3.14 / 180) * fa0)) ^ 2)))
m1 = (1 + ((4 / 3) ^ 2) * (1 / (Tan((3.14 / 180) * fa0)) ^ 2)) ^ 0.5
```

```
PCJ = ((Dee * 1000 * VOD ^ 2) / 4) * (DE / DH) ^ 3

'Ph = DR * (SSD + s * Vh) * Vh

'PCJ = (((Dee * 1000 * VOD ^ 2) * (1 - 0.7125 * Dee ^ 0.04)) * (DE / DH) ^ 3)

'a = (Sin(fa2 + theta)) ^ 2

bb = 1 / (6 * m1 ^ 2)

fa01 = (3.14 / 180) * fa0

cc = 2 + (Sin(fa3) / Sin(fa01) - PW / VOD) * (Dr * 16 * Sin(fa3)) / (Dee * s *
Sin(fa01))

aa = (bb * cc) ^ 0.5

aa3 = -aa * aa + 1

aa2 = Sqr(aa3)

aa1 = aa / aa2

fa2 = Atn(aa1) - theta

fa22 = fa2 + theta

D = 2 * Sin(fa22) - 4 * Tan(fa2) * Cos(fa22) + 2 / (Sin(fa22) * m1 ^ 2)

e = 2 * Sin(fa22) * Tan(fa2) + 4 * Cos(fa22) + (2 * Tan(fa2)) / (Sin(fa22) * m1 ^ 2)

f = Tan(fa3) * (1 - (PW * Sin((3.14 / 180) * fa0)) / (VOD * Sin(fa3)))

g = s + (s - 1 + (PW * Sin((3.14 / 180) * fa0)) / (VOD * Sin(fa3))) * (Tan(fa3)) ^ 2

Cosec = D / e - f / g

End Function
```

APPENDIX B

STRAIN GAGE SLAB PREPARATION

To cast stain gages into the test specimen, a small grout slab is prepared to mount the strain gage, shown in Figure B.1. Then the strain gage slab is installed in the designed location within the form used to contain the grout. Mixed grout is then poured around and over the slab and allowed to harden. Preparation of the grout strain slab is outlined below:

- Fabricate a grout slab by diamond-sawing a cured large grout sample. Slabs (approximately 200 x 15 x10 mm) were used for large laboratory samples, and slabs, 75 x 10 x 5 mm, were used for small scale samples.
- Prepare the surface of the grout slab by sanding with 320-grit abrasive paper
- Apply M-Prep Conditioner A, a mildly acidic solution, to the surface in the gage area. Reduce the surface acidity by scrubbing with M-Prep Neutralizer 5A. Dry the surface thoroughly.
- Use a ballpoint pen or round-pointed metal rod, to draw layout lines to properly align gages.
- Bond the strain gage with a quick-curing adhesive, M-Bond 200,.
- Solder leads directly to the strain gage. Then cover the gage area with quick setting Epoxy to protect the gage from damage and to minimize the effect of water absorption under the gage.

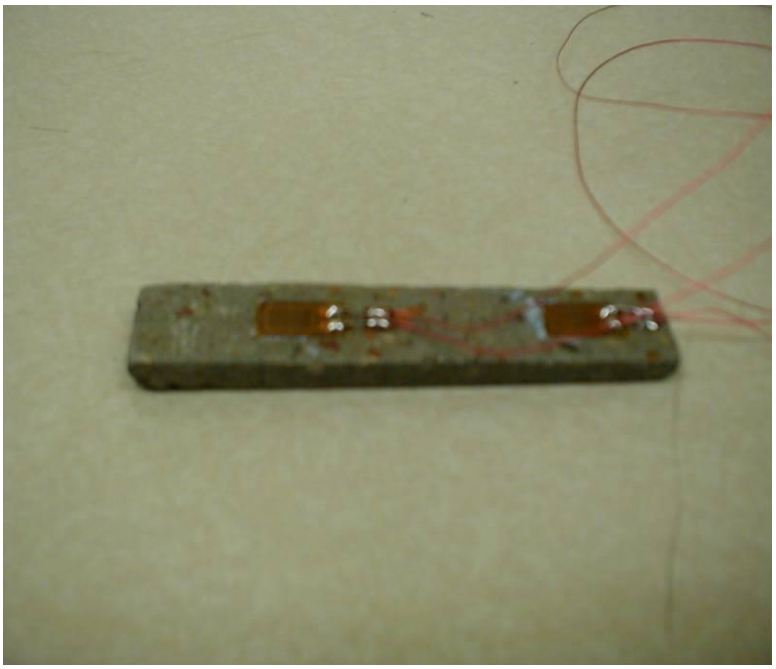

Figure B. 1. Grout slab with stain gage

APPENDIX C

BLAST MODELS SIMULATED WITH AUTODYN

ANSYS AUTODYN (ANSYS 2000) is an explicit analysis tool for modeling nonlinear dynamics of solids, fluids and gases and their interaction. This program was used to determine the physical size needed for the large scale experimental grout samples and to make sure that the length of the crack zone would not be larger than the diameter of the grout samples. It was also used in an attempt to duplicate the results from the SWT model presented in this dissertation. Six AUTODYN numerical models were constructed. Model #1 is to determine the minimum size specimen required for laboratory experiments. The other five models are used to simulate conditions tested in the laboratory. The SWT model is also used to estimate the extent of crush and crack zones for the six models with the properties of explosive and grout used in laboratory experiments so that the results of the SWT model can be used to compare with the results of AUTODYN. In order to simulate laboratory conditions, it was necessary to update the AUTODYN properties library for the explosive used and the grout used to construct the models. The PETN used in the laboratory has a density of 1.4 g/cc and the compressive strength of the grout/concrete used is 80 MPa. Based on communications with ANSYS (ANSYS 2000), appropriate properties of explosive and concrete for the laboratory experiments can be estimated from the AUTODYN properties library, shown in

Table C.1 and Table C.2. Table C.3 summarizes the laboratory conditions simulated by the six AUTODYN models. Each model is unconfined at the perimeter. In AUTODYN, to model the progressive crushing and subsequent weakening of the material like concrete, a damage factor D, which is usually related to the amount of material straining, is introduced. The damage factor ranges from zero to D_{max} with zero indicating no damage and D_{max} representing complete damage.

Model #1 represents an explosive load simulated by a 10 gram/m fully-coupled hole in the center of a 500 mm diameter grout sample, 500 mm in height. This condition is slightly different from the experimental conditions in which the detonation cord was stripped of the outer textile covering leaving only the thin-walled tube containing the PETN. Results are shown in Figure C.1. The radius of the crack zone is 101 mm, and the radius of the crush zone is 4.9 mm outward from the centerline of the sample.

Model #2 represents a 500 mm diameter, 500 mm high sample with a fully-coupled central charge equivalent to 5 gram/m detcord (PETN). Results are shown in Figure C.2. The extent of the crack zone is 85 mm, and the extent of the crush zone is 3.7 mm

Model #3 represents the equivalent of 3.6 gram/m detcord fully-coupled in a grout sample measuring 500 mm in diameter and 500 mm in height. Results are shown in Figure C.3. The extent of crack zone is found to be 79 mm, and the extent of the crush zone is 3.1 mm. Model #4 represents a 500 mm diameter, 500 mm high sample with a borehole charge equivalent to 10 gram/m detcord (PETN) decoupled charge in a 10.8 mm hole. Results are shown in Figure C.4. The extent of crack zone is 65 mm, and the extent of the crush zone is 6.0 mm.

Table C.1. Parameters for PETN

Parameters for Equation of State	PETN (0.88) Available in the software	PETN (1.26) Available in the software	PETN (1.4) Selected value	PETN (1.5) Available in the software	PETN (1.77) Available in the software
Reference density(g/cm3)	0.88	1.26	1.40	1.50	1.77
Parameter A (MPa)	348.62	573.10	603.60	625.30	617.05
Parameter B (MPa)	11.29	20.16	21.99	23.29	16.93
Parameter R1	7.0	6.0	5.6	5.25	4.4
Parameter R2	2.0	1.8	1.7	1.6	1.2
Parameter W	2.4	2.8	2.8	2.8	2.5
C-J Detonation velocity (m/s)	5170	6540	7100	7450	8300
C-J Energy / unit volume (MJ/m3)	5025	7190	8000	8560	10100
C-J Pressure (GPa)	6.2	14.0	17.6	22.0	33.5

Table C.2. Parameters for concrete

Concrete Strength (MPa)	Density (g/cc)	Speed of sound (m/s)	Initial compaction pressure (MPa)	Solid compaction pressure (GPa)	Shear modulus (GPa)	Compressive Strength (MPa)
35 Avai in the software	2.31	2.92	23.3	6	16.7	35
80 Selected value	2.40	3.1	60	6	18.0	80
140 Avai in the software	2.52	3.23	93.3	6	22.0	140

Table C.3.Summary for AUTODYN simulation models

Model	Charge diameter (mm)	Hole Diameter (mm)	Decoupled ratio	Explosive
#1	3.1	3.1	1	PETN 10 gr detonating cord
#2	2.3	2.3	1	PETN 5 gr detonating cord
#3	2.1	2.1	1	PETN 3.6 gr detonating cord
#4	3.1	10.8	3.48	PETN 10 gr detonating cord
#5	2.3	8.5	3.5	PETN 5 gr detonating cord
#6	2.1	10.8	5.14	PETN 3.6 gr detonating cord

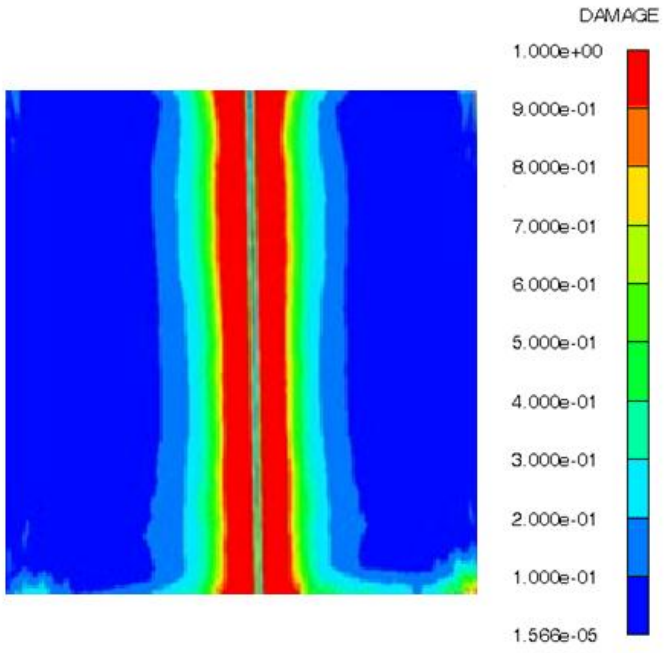

Figure C.1. Model #1, 10 gram/m PETN charge fully-coupled in a grout sample measuring 500 mm in diameter and 500 mm in height

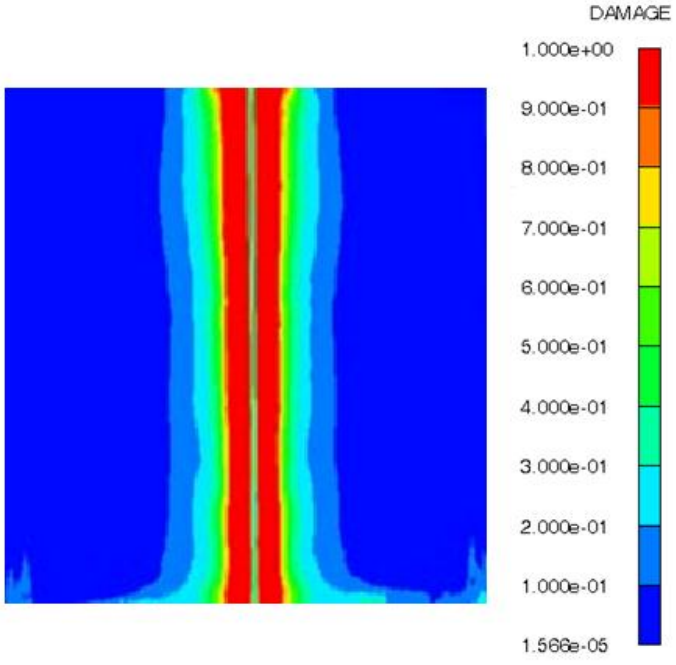

Figure C.2. Model #2, 5 gram/m PETN charge fully-coupled in a grout sample

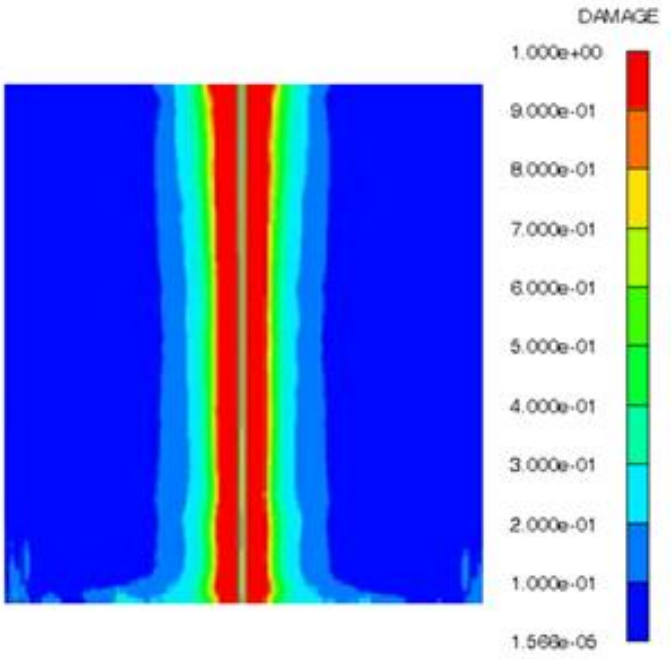

Figure C.3. Model #3, 3.6 gram/m PETN charge fully-coupled in a grout sample

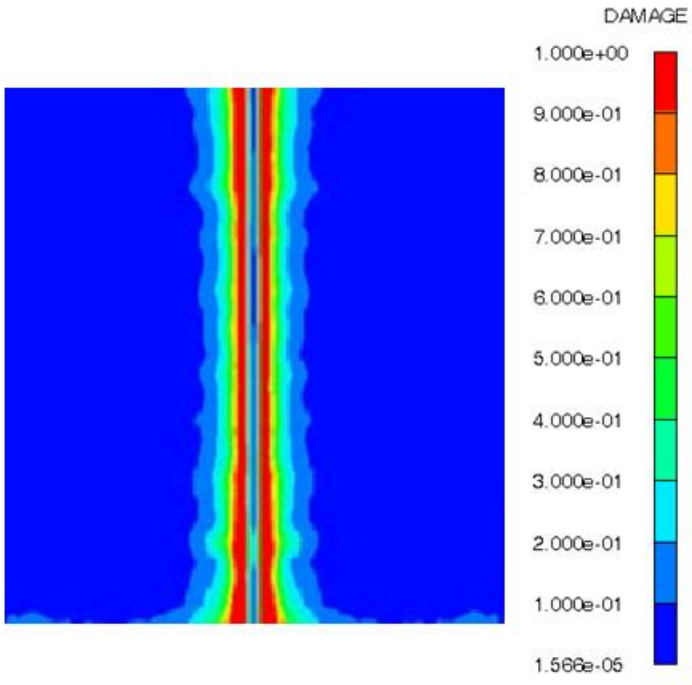

Figure C.4. Model #4, 10 gram/m PETN decoupled charge

Model #5 represents a 500 mm diameter and 500 mm high sample with the equivalent of a 5 gram/m detcord (PETN) decoupled charge in a 8.5 mm hole. Results are shown in Figure C.5. The extent of the crack zone is 48 mm, and the extent of the crush zone is 0 mm

Model #6 represents a 500 mm diameter, 500 mm high grout sample with the equivalent of a 3.6 gram/m PETN decoupled charge in a 10.8 mm hole. Results are shown in Figure C.6. The extent of the crack zone is 30 mm, and the extent of the crush zone is 0 mm.

The AUTODYN analysis was performed on models that were unconfined at the circumference. The results of Model 1 indicate that a diameter of 500 mm should be

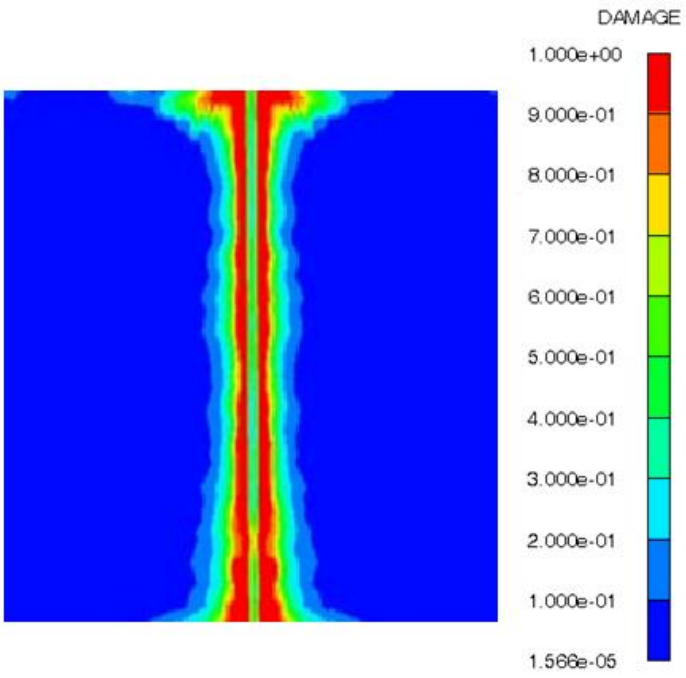

Figure C.5. Model #5, 5 gram/m PETN decoupled charge

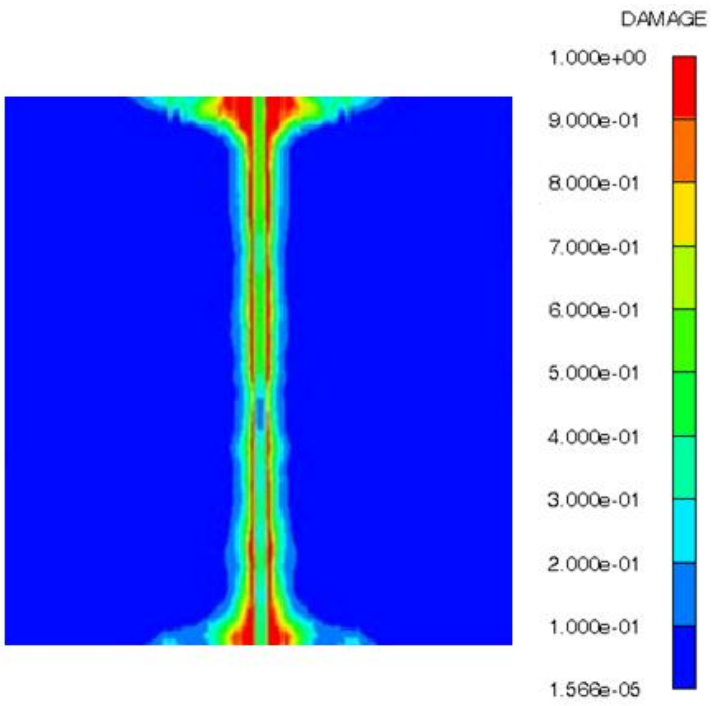

Figure C.6. Model #6, 3.6 gram/m PETN decoupled charge

sufficient to contain radial fractures within the model. If such is the case, then the selected diameter should have been sufficient to limit the extent of radial fractures to the model dimensions, especially since laboratory tests were conducted using lateral confinement. Unfortunately fractures did extend the model limits.

A comparison of the crack zone and crush zone extent predicted by AUTODYN and SWT are tabulated in Table C.4, Figures C.7 and C.8. The extent of the crack zone predicted by the SWT model for fully-coupled models are smaller than those predicted by AUTODYN while the extent of crack zone predicted by SWT for decoupled models are similar as those predicted by AUTODYN. The extent of the crush zone predicted by the SWT model for fully-coupled models are larger than those predicted by AUTODYN while the extent of the crush zone predicted by SWT for decoupled models are similar to those predicted by AUTODYN.

Table C.4. Comparison of extent of crack and crush zones from SWT prediction and AUTODYN simulations

Model	Charge diameter (mm)	Hole Diameter (mm)	Decoupled ratio	Crack zone by AUTODYN (mm)	Crack zone by SWT (mm)	Crush zone by AUTODYN (mm)	Crush zone by SWT (mm)
#1	3.1	3.1	1	101	87	4.9	7.2
#2	2.3	2.3	1	85	63	3.7	5.3
#3	2.1	2.1	1	79	58	3.1	4.8
#4	3.1	10.8	3.48	65	68	6.0	5.7
#5	2.3	8.5	3.5	48	51	4.3	4.3
#6	2.1	10.8	5.14	30	38	5.4	5.4

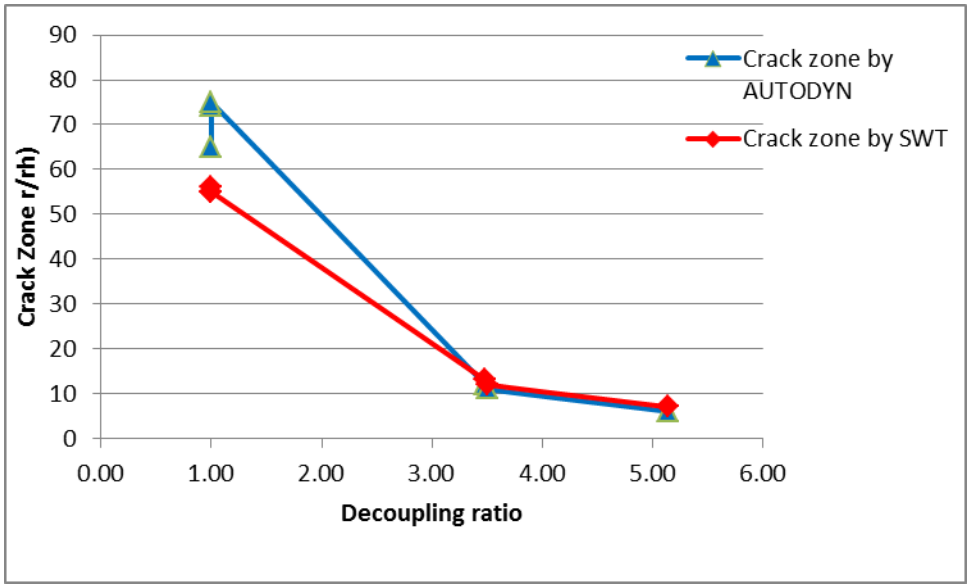

Figure C.7. Comparison of extent of crack zone from the SWT model prediction and AUTODYN simulations

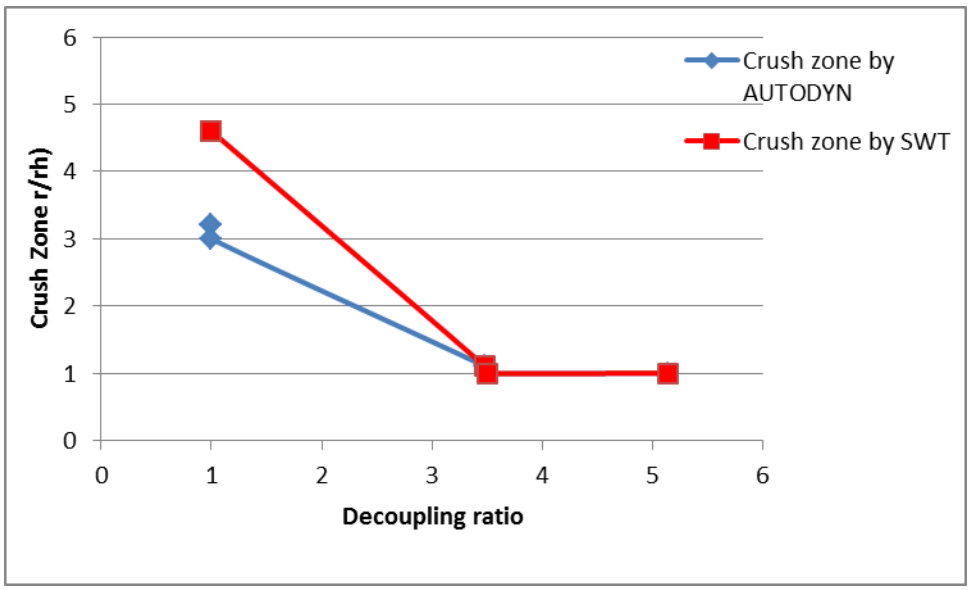

Figure C.8. Comparison of extent of crush zone from the SWT model prediction and AUTODYN simulations

SELECTED BIBLIOGRAPHY

Ash, R. L. 1963. The mechanics of rock breakage. *Pit and Quarry* I, (Aug) pp. 98-112. Part II, (Sept) pp. 118-123. Part III, (Oct) pp. 126-131. Part IV, (Nov): pp 109-118.

ASTM C496-96. 2004. Standard test method for splitting tensile strength of cylindrical concrete specimens. American Society of Testing and Materials. *Annual Book of ASTM Standards.* 04. 02: pp 281-284.

Atchison, T. C., and Tournay, W. E. 1959. *Comparative Studies of Explosives in Granite.* USBM RI 5509.

Atlas Powder Co. 1987. *Explosives and Rock Blasting.* Atlas Powder Co.

Ansys. 2000. *Autodyn User Manual.* Canonsburg, Pennsylvania.

Bacon, L. O. 1962. *A Method of Determing Dynamic Tensile Strength of Rock at Minimum Loading.*USBM. RI. 6067.

Bauer, A. 1961. Application of the Livingston theory. *Quarterly of the Colorado School of Mines.* 56(1): pp 171-182.

Bauer, A. and Calder, P. N. 1978. *Open pit and Blasting Seminar Mining Engineering Dept.* Queens University, Kinston Ontario.

Bedell, G. C. 1990. Effect of fractures on fragmentation. M.S.thesis, University of Utah, Salt Lake City, Utah.

Bieniawski, Z.T., Franklin, J. A., Bernede, M. J., Duffaut, P., Rummel, F., Horibe, T., Broch, E., Rodrigues, E., Van Heerden, W. L., Vogler, U. W., Hansagi, I., Szlavin, J., Brady, B. T., Deere, D. U., Hawkes, I. and Milovanovic, D. 1981. Suggested methods for determining the uniaxial compressive strength and deformability of rock materials. *Rock Characterization Testing and Monitoring ISRM Suggested Methods.* Edited by E. T. Brown. Pregamon Press: pp113-116, Oxford, United Kingdom.

Blanton, T. L. 1981. Effect of strain rates from 10^{-2}/sec-10^{-1}/sec on three rocks. *Int. J. Rock Mech. Min. Sci. and Geomech. Abstr.* 18: pp 47-62.

Blair, D. and Minchinton, A. 1997. On the damage zone surrounding a single blasthole. *Geomechanics Abstracts* 5: pp 320-320.

Borovikov, V. A. and Vanyagin, I. F. 1995. *Modelling the Effects of Blasting on Rock Breakage.* A. A. Balkema/Rotterdam/Broofied: pp 131-13

Brent, G. F. and Smith, G. E. 1996. Borehole pressure measurement behind blast limits as aid to determining the extent of rock damage. *Fragblast 5,* Edited by B. Mohandy. Balkema, Rotterdam: pp 103-112.

Brent, G. F. and Smith, G. E. 1999. The detection of blast damage by borehole pressure measurement. *Fragblast 6,* South African Institute of Mining and Metallurgy, Johannesburg: pp 9-13.

Brinkmann, J. R. 1987. Separating shock wave and gas expansion breakage mechanisms. *Proc.2nd Int. Symp. On Fragmentation by Blasting,* Keytone, Colorado USA: pp 6-15.

Brinkmann, J. R. 1990. An experimental study of the effects of shock and gas penetration in blasting. *Proc. 3rd Int. Symp.On Fragmentation by Blasting,* Brisbane, Australia: pp 55-66.

Cho, S. H., Otaga, Y. and Kaneko, K. 2003. Strain–rate dependence of the dynamic tensile strength of rock. *Int. J. Rock Mech. Min. Sci. and Geomech. Abstr.* Vol.40: pp 763-777.

Cook, Melvin A. 1958. *The Science of High Explosives.* Eeinhold Publishing Corp.

Cook, Melvin A. 1974. *The Science of Industrial Explosives.* Ireco Chemicals

Cooper, P. W. 1996. *Explosives Engineering*. Wiley-Vch.

Crandell, F.J. 1949. Ground vibrations due to blasting and its effect upon structures. *J. Boston Soc. Civil Engg.* 36(2): pp 225-245.

Dai, J. 2002. *Dynamic Behaviors and Blasting Theory of Rock.* Metallurgical Industry Press. (in Chinese).

Day, P. R. 1982. Controlled blasting to minimize overbreak with big boreholes underground. *Proc. 8th conf. Exp Blast Tech* ISEE: pp264-274.

Devine, F. J., Beck, R. H., Meyer, A. V. C. and Duwall, W. I. 1965. *Vibration Levels Transmitted Across a Presplit Fracture.* USBM RI 6695.

Devine, F. J., Beck, R. H., Meyer, A. V. C. and Duwall, W. I. 1966. *Effect of Charge Weight on Vibration Levels from Quarry Casting.* USBM RI 6774.

Divas, W. C. 1997. Shock waves; rarefaction waves equations of state. *Explosive Effects and Applications.* Edited by Zukas J. A. and Walters W. P. Springer: pp 47-113

Doucet, C., Paventi, M., Lizotte, Y. and Scoble, M. 1994. Structural control over blast fragmentation: Characterisation and case studies. *10th Symp.on Explosives and Blasting Research, Int. Soc. Explosive Engg.* Austin, Texas: pp 121-133.

Drukovanyi, M. F., Kravtsov, V. S., Chernyavskii, Y. E., Reva, V. V. and Zerkov, S. N., 1976. Calculation of fracture zones created by exploding cylindrical charges in ledge rocks. *Soviet Mining Science,* 12(3): pp 292-295.

Duvall, W. I. and Atchison, T. C. 1957. *Rock Breakage by Explosives.* USBM RI 5356.

Duvall, W. I. and Petkof, B. 1959. *Spherical Propagation of Explosion-generated Strain Pulses in Rock.* USBM RI 5483.

Duvall, W. I. and Fogelson, D. 1962. *Review of Criteria for Estimating Damage to Resistances from Blasting Vibrations.* USBM RI 5968.

Duvall, W. I., Johnson, C. F., Meyer, A. and Devine, J. 1963. *Vibrations from Instantaneous and Milli-second Delayed Quarry Blasts.* USBM RI 6151.

Edmond, J. M., and Paterson, M. S. 1972. Volume changes during the deformation of rock at high pressures. *Int. J. Rock Mech. Min. Sci.,* 9: 161.

Edward, A. T. and Northwood, T. D. 1960. Experimental studies of the effects of blasting on structures. *The Engineer* 211: pp 538-546.

Esen, S., Onederra I. and Bilgin H. A. 2003. Modelling the size of the crushed zone around a blasthole. *Int. J. Rock Mech. Min. Sci. and Geomech. Abstr*. 40: pp 485-495.

Farmer, I. W. 1968. *Engineering Properties of Rocks.* E. and F.N. Spon Ltd.

Favreau, R. F. 1969. Generation of strain waves in rock by explosion in a spherical cavity. *Journal of Geophysical Research,* 74: pp 4267-4280.

Floyd, J. L. 1998. The development and implementation of efficient wall control blast designs. *J. Explosive Engg.* May/June: pp 12-18.

Forsyth, W. W. 1993. A discussion on the blast induced overbreak around underground excavations. *Rock Fragmentation by Blasting Fragblast-4*: pp 161-166.

Franklin, J.F., Ibarra, T. and Maerz, N. 1989. Blast overbreak measurements by light sectioning. *Int. J. Min. Geol. Eng*. 7: pp 323-331.

Grady, D. E. and Hollenbach, R. E. 1978. *Dynamic Tensile Fracture in Rock.* Sand 78-0531.

Grady, D. E. and Kipp, M. E. 1979a. The micromechanics of impact fracture of rock. *Int. J. Rock Mech. Min. Sci. and Geomech. Abstr.* 16: pp 293-302.

Grady, D. E. and Kipp, M. E. 1979b. Dynamic rock fragmentation. *Fracture Mechanics of Rock.* B.K. Atkinson (ed.). Academic Press, London: pp 429-475.

Grant, C. H. 1964. Simplified explanation of the crater method. *E and M J.* 165(11): pp 86-89.

Green, S. J. and Perkins, R. D. 1972. Uniaxial compression tests at varying strain rates on three geologic materials. *Basic and Applied Rock Mechanics-Proc.10th Symposium on Rock Mechanics.* Edited by Gray K. E., AIME, New York: pp 35-53.

Griffith, A.A. 1921. Phenomena of rupture and flow in solids. *Phil. Transc.* Roy. Soc. London, Series A, 221: pp 163-198.

Griggs, D. T., Turner, F. J. and Heard, H. C. 1960. Deformation of rocks at 500^{o} C to 800^{o} C. *Geol. Soc. Am. Mem,* pp 79: 39.

Harry, R., Nicholls, H. R. and Hooker, V. E. 1964. *Comparative Study of Explosives in Granite.* USBM RI 6693.

Henrych, J. 1979. *The Dynamics of Explosions and Its Use.* Elsevier Scientific Publishing Company, New York.

Hino, 1956. Fragmentation of rock through blasting andshock wave, Theory of blasting. *Quarterly of the Colorado School of Mines,* (51).

Hirata, A., Yoshinaga, T., Horiba, N., Matsunaga, H. and Knaeko, K. 1999. Inspection of damaged zone in tunnel walls by compact vertical seismic prospecting system. *Fragblast* 3: pp 79-94.

Hoagland, R.G., Hahn, G.T. and Rosenfield, A.R. 1973. Influence of micro-structure on fracture propagation in rock. *Rock Mech.* 5: pp 77-106.

Hoek, E. and Brown, E. T. 1997. Practical estimates of rock mass strength. *Int. J. Rock Mech. Min. Sci. and Geomech. Abstr.* 34: pp1165-1186.

Hoek, E. and Brown, E. T. 1980. *Underground Excavations in Rock*. London. Institution of Mining Metallurgy, London, United Kindom.

Holmberg, R. and Persson, P.-A. 1978. The Swedish approach to contour blasting. *Proc. IVth Conf. on Exp. and Blasting Tech.* ISEE, New Orleans, LA: pp113-127.

Holmberg, R. and Persson, P.-A. 1980. Design of tunnel perimeter blasthole patterns to prevent rock damage. *Transc.* Inst. Min. Metall: pp A37-A40.

Holmberg, R. and Hustrulid, W. 1981. Swedish cautious blast excavation at the CSM/ONWI test site in Colorado. *7th Conf. Soc. Explosive Eng.* Phoenix, Arizona: pp 232-252.

Holmberg, R. 1982. Charge calculation for tunnelling. In: W.A. Hustrulid (ed.), *Underground Mining Methods Handbook,* Soc. Min. Metall. Explosives: pp 1580-1589.

Holmberg, R. 1993. Recent developments to control rock damage. *Rock Fragmentation by Blasting,* Rossmanith, A.A. Balkema, Rotterdam: pp 197-198.

Hustrulid, W., Bennett, R., Ashland, F. and Lenjani, M. 1992. A new method for predicting the extent of blast damage zone. *Proc Blasting Conference paper No 3* Gyttorp: Nitro Nobel.

Hustrulid, W. 1999a. *Blasting Principles for Open Pit Mining-Vol. 1, General Design Concepts.* A.A. Balkema, Rotterdam.

Hustrulid, W. 1999b. *Blasting Principles for Open Pit Mining-Vol. 2, Theoretical Foundation.* A.A. Balkema, Rotterdam.

Hustrulid, W. and Lu, W. 2002. Some general concepts regarding the control of blast-induced damage during rock slope excavation. *Fragblast-7:* pp 595-604.

Hustrulid, W. and Johnson, J. 2008. A gas pressure-based drift round blast design methodology. In Hankan Schunnesson and Erling Norrdlund (eds.), *Proceedings, MassMin 2008,* Lulea, June 9-11: pp 567-669.

Hustrulid, W. 2010. Some comments regarding development drifting practices with special emphasis on caving applications. *Proc. Caving 2010 Symp.On Block and Sublevel Caving.* Perth Australia. Editor Yves Potvin ACG: pp 3-44.

Itasca Consulting Group. 1999. FLAC: *Fast Lagrangian Analysis of Continua, Users Manual.* Minneapolis, MN, 1999a.

Itasca Consulting Group. 1999. FLAC: *Fast Lagrangian Analysis of Continua, Theory and Background.* Minneapolis, MN, 1999b.

Ito, I. and Terada, M. 1967. Stress wave and dynamic characteristics of rocks under detonator's attack. Behavior of dense media under high dynamic pressures. *Symposium H. D. P. I. U. T. A. Paris,* Gordon and Breach, New York, 1968: pp 233-243.

Iverson, S., Kerkering, C. and Hustrulid, W. 2008.Application of the HIOSH-Modified Holmberg-Persson Approach to Perimeter Blast Design. *Preceedings of the 34th Annual Conference on Explosives and Blasting Technique,* New Orleans, Louisiana, January pp 27-31

Jaeger, J. C. and Cook, N. G. W. 1976. *Fundamentals of Rock Mechanics.* Chapman and Hill Ltd, London UK.

Järnvägs, A. M. A. 1996. *Swedish National Railway Authorities Complement to AMA 83. Rock Technique Rpt.* TM-95-060 1996-09-01. Banverket, Borlänge.

Jaroslav, M. 2002. Material and geometrical nonlinearities FEM and BEM analyses. A bibliography (1998-2000). *Finite Elements in Analysis and Design* 38(3) (2002): pp 307-317.

Johnson, J. C. 2010. *The Hustrulid Bar – A Dynamic Strength Test and Its Application to the Cautious Blasting of Rock.* PhD dissertation, Unversity of Utah, Department of Mining Engineering, Salt Lake City, Utah.

Kachanov, L.M. 1986. *Introduction to Continuum Damage Mechanics.* Martinus Nijhoff Publishers.

Kanchibolta S. S., Valery, W. and Morrell, S. 1999. Modeling fines in blast fragmentation and its impact on crushing and grinding. *Proc. of Explo. '99-A Conference on Rock Breaking.* The Australasian Institute of Mining and Metallurgy, Brisbane, Australia: pp 137-144.

Kumar, A. 1968. The effect of stress rate and temperature on the strength of basalt and granite. *Geophysics* 33: 501.

Kutter, H. and Fairhurst, C. 1971. On the fracture process in blasting. *Int. J. Rock Mech. Min. Sci.*8: pp 181-202.

Ladegaard-Pedersen, A. and Daly, J. W. 1975. *A Review of Factors Affecting Damage in Blasting.* Report Nat. Sci. Found., Mechanical Engineering Department, University of Maryland, College Park, Maryland.

Lama R. D. and Vutukuri, V. S. 1978. *Handbook on Mechanical Properties of Rocks, Testing Techniques and Results,* 2. Trans Tech Publications.

Langefors, U. and Kihlstrom, B. 1973. *The Modern Techniques of Rock Blasting.* John Wiley and Sons, New York.

Lankford, J. 1981. The role of tensile microfracture in the strain rate dependence of compressive strength of fine-grained limestone-analogy with strong ceramics. *Int. J. Rock Mech. Min. Sci. Geomech. Abstr.* 18: pp 173-175.

Laubscher, D. H. and Taylor, H. W. 1990. A geomechnics classification system for the rating of rock mass in mine design. *J. S. Afr. Inst. Min. Metall.* 90(10): pp 257-273.

Li, Q. M. and Meng, H. 2003. About the dynamic strength enhancement of concrete-like materials in a split Hopkinson pressure bar test. *Int. J. of Solids and Struct.,* 40: 343-360
Lindholm, U. S., Yeakley, L. M. And Nagy A. 1974. The dynamic strength and fracture properties of Dresser Basalt. *Int. J. Rock Mech. Min. Sci. Geomech. Abstr*. 11: 181.

Liu, Q. 1987. *The Channel Effect Exhibited by Commercial Explosives.* M. S. thesis. Department of Mining Engineering, Queens University, Kingston, Ontario, Canada.

Liu, Q. 1991. *Investigation of the Explosibility of Sulphide Dusts.* PhD dissertation, Department of Mining Engineering, Queens University, Kingston, Ontario, Canada.

Liu, Q. and Proulx, R. 1995. The mechanism of rock damage in blasthole open stoping: blast induced versus stress induced. *6th Sem. Blasting Tech., Instrumentation and Explosive Applications,* Boston, Blasting Analysis Intl. Inc.: pp 22.

Liu, Q. 2002. Estimation of dynamic pressure around of fully loaded basthole in rock. *Fragblast-7:* pp 267-272.

Livingston, C. W. 1956. Fundamental concepts of rock failure. Proceedings, First US symposium on rock mechanics. *Quarterly of the Colorado School of Mines.* 51(3): pp 1-11.

Logan, J. M. and Handin, J. 1971. Triaxial compression testing at intermediate strain rates. *Dynamic Rock Mechanics-Proc. 12th Symposium on Rock Mechanics* (Edited by Clark G. B.) AIME. New York: pp 167.

Lorig, L.1997. Fundamentals of Mining Geodynamics. *SIMIN '97 (Proceedings of the Conference,* August 1997), Universidad de Santiago de Chile, Departamento de Ingener de Minas, Santiago, Chile 1997: pp 161-174.

MacKown, A. F. 1986. Perimeter controlled blasting for underground excavations in fractured and weathered rocks. *Bull. Assoc. Eng. Geol.*XXIII (4): pp 461-478.

Marsh, S. R. 1980. *LASL Shock Hugoniot Data.* University of California, Berkeley, California.

Martynyuk, P. A. and Sher, E. N. 1984. Estimating the dimensions of the radial crack zone formed in a contained explosion of a line charge in a brittle medium. *Journal of Applied Mechanics and Technical Physics,* 25(4): pp 619-625.

McHugh, S. 1983. Crack extension caused by internal gas pressure compared with extension caused by tensile stress. *Int. J. Fracture* 21: pp 163-176.

Mckenzie, C.K., Scherpenisse, C.R., Arriagada, J. and Jones, J.P. 1995. Application of computer assisted modelling to final wall blast design. *Explo'95,* Brisbane: pp 285-292.

Meng, X. 2004. *Theoretical and Experimental Study of Decoupled Charge Blasting.* Master thesis, Depatment of Mining Engineering, University of Utah, Salt Lake City, Utah.

Micro-Measurements. 2005. General Purpose Strain Gages - Linear Pattern. Gage pattern data.

Minchinton, A. and Lynch, P. M. 1997. Fragmentation and heave modelling using a coupled discrete element gas flow code. *International Journal of Blasting and Fragmentation* 1: pp 41-57.

Mojitabai, N and Beatie, S. G. 1996. Empirical approach to prediction of damage in bench blasting. *Trans. Inst. Min. and Metall.* Sect. 105: pp75-80.

Mosinets, V. N. and Gorbacheva, N. P. 1972. A seismological method of determining the parameters of the zones of deformation of rock by blasting. *Soviet Mining Science:* pp 640-647.

Nicholls, H. R., Johnson, C. F. and Duvall, W. I. 1971. *Blasting Vibrations and Their Effects on Structures.*USBM RI 656.

Nieman, I. B. 1979. Determination of the zone of crushing of rock in place by blasting. *Soviet Mining Science,* 15(5): pp 480-499.

Olson, J., Willard, R., Folgelson, D. and Hjelmstad, K. 1973. *Rock Damage from Small Charge Blasting in Granite.* USBM RI-7751.

Olsson, M. and Bergqvist, I. 1993. Crack lengths from explosives in small diameter holes. *Fragblast 4,* Rossmanith (ed.), Balkema, Rotterdam: pp 193-196.

Olsson, M. and Bergqvist, I. 1996. Crack lengths from explosives in multiple hole blasting. *Fragblast 5,* B. Mohanty (ed.), Balkema, Rotterdam: pp 187-196.

Olsson, M., Nie, S., Bergqvist, I. and Ouchterlony, F. 2002. What causes cracks in rock blasting? *Fragblast* 6(2): pp 221-233.

Oriad, L. L. 1982. Blasting effect and their control. *Underground Mining Methods Handbook.* Ed: W.A. Hustrulid (ed.), Soc. Mining Eng.: pp 1590-1603. AIME, New York.

Orica. 2008. Technical Data Sheet of Orica Products, Amex K.

Ouchterlony, F., Olsson, M. and Bergqvist, I. 2002. Towards new Swedish recommendations for cautious perimeter blasting. *Fragblast* 6(2): pp 235-261.

Ouchterlony, F. 1997. Prediction of crack lengths in rock after cautious blasting with zero inter-hole delay. *Int. J. for Blasting and Fragmentation* 1: pp 417-444.

Perkins, R. D., Green, S. J. and Friedman, M. 1970. Uniaxial stress behavior of porphyritic tonalite at strain rates to 10^3/sec. *Int. J. Rock Mech. and Geomech. Abstr.* 7: pp 527.

Persson, P.-A., Holmberg, R. and Lee, J. 1993. *Rock Blasting and Explosive Engineering.* CRC Press, London, United Kindom.

Persson, P.-A. 1997. The relationship between strain energy, rock damage, fragmentation, and throw in rock blasting. *Fragblast-International Journal of Blasting and Fragmentation,* 1: pp 99-110.

Prasad, U. 2000. *Dynamic Fracture Characteristics of Selected Rocks.* PhD dissertation, Department of Mining and Metallurgical Engineering, McGill University Montreal, Canada.

Pusch, R. and Stanfors, R. 1992. The zone of disturbance around blasted tunnels at depth. *Int. J. Rock Mech. and Geomech. Abstr.* 29(5): pp 447-456.

Pusch, R. and Stanfors, R. 1993. Disturbance of rock around blasted tunnels. In: H.P. Rossmanith (ed.), *Rock Fragmentation by Blasting.* A.A. Balkema, Rotterdam: pp 53-159.

Ricketts, T. E. 1988. Estimating underground mine damage produced by blasting. *4th Mini Symp. on Explosive and Blasting Res.,* Soc. Explosive Engg., Anaheim, California: pp 1-15.

Rinehart, J. S. 1965. Dynamic fracture strength of rocks. *VII Symposium on Rock Mechanics.* 1, The Pennsylvania University: pp 205-208.

Rossmanith, H. P. 1988. Elastic wave propagation. Ed: H.P. Rossmanith (ed.), *Rock Fracture Mechanics*1: Technical University of Vienna: pp 229-251.

Rossmanith, H. P. and Knasmiller, R. E. 1990. The role of Rayleigh waves in rock fragmentation. *3rd Int. Symp. Rock Frag. Blasting* Brisbane, Australia: pp 109-116.

Rustan, A. 1998. *Rock Blasting Terms and Symbols: 49.* Rotterdam: A.A. Balkema.

Rustan, A., Naarttijarvi, T. and Ludvig, B. 1985. Controlled blasting in hard intense jointed rocks in tunnels. *CIM Bull.* Dec.: pp 63-68.

Savely, J. P. 1986. Designing a final blast to improve stability. Preprint No 86-50. Presented at the *SME Annual Meeting* in New Orleans, Louisiana Mar pp 2-6.

Senuk, V. M. 1979. The impulse from an explosion and conditions for its greater utilization in crushing hard rock masses in blasting. *Soviet Mining Science:* pp 22-27.

Shan R., Jiang Y. and Li, B. 2000. Obtaining dynamic complete stress-strain curves for rock using the Split Hopkinson Pressure Bar technique. *Int. J. Rock Mech. Min. Sci*. 37: pp 983-991.

Sher, E. N. and Aleksandrova, N. I. 1997. Dynamics of development of crushing zone in Elasto plastic medium in camouflet explosion of string charge. *Journal of Mining Science,* 33(6): pp 529-535.

Sher, E. N. and Aleksandrova, N. I. 2007. Effect of borehole charge structure on the parameters of failure zone in rocks under blasting. *Journal of Mining Science,* 43(4): pp 409-417.

Singh, S. P. 1992. *Investigation of Blast Damage Mechanism in Underground Mines.* MRD report. Rotterdam: A.A. Balkema. Sudbury.

Singh, S. P. 1993. Prediction and determination of explosive induced damage. *4th Int. Symp. On Rock Fragmentation by Blasting, Fragblast:* pp 183-192.

Siskind, D., Steckley, R. and Olson, J. 1973. *Fracturing in the Zone Around Blasthole, White Pine, Michigan,* USBM RI-7753.

Siskind, D. E. and Fumanti, R. R. 1974. *Blast Produced Fractures in Lithonia Granite.* USBM RI7901.

Smith, A. A. 2002. *A Modified Holmeberg-Persson Approach to Predict Blast Damage.* Master thesis, University of Utah, Salt Lake City, Utah.

Song, Q., Yang, C. and Jing, S. 1997. *Explosive Theory*. Military Industry Press, Beijing, China (in Chinese).

Starfield, A. M. and Pugliese, J. M. 1968. Compression waves generated in rock by cylindrical explosive charges: a comparison between a computer model and field measurements. *Int. J. Rock Mech. Min. Sci.* 5: pp 65-77

Starzec, P. 1999. Dynamic elastic properties of crystalline rocks from south-west Sweden. *Int. J. Rock Mech. Min. Sci.* 36: pp 265-272

Stowe, R. L. and Ainsworth, D. L. 1972. Effect of rate loading on strength and Young's modulus of elasticity of rock. *Basic and Applied Rock Mechanics-Proc. 10th Symposium on Rock Mechanics* (Edited by Gray K. E.) AIME New York: 3.

Sun, C. Douglas, L. Chen G. 2002. Characteristics of shock wave in rock mass surround blastholes. *Fragblast-7*: pp 279-283

Sutherland, M. 1989. Improving mine safety through perimeter blasting at Inco Limited's Thompson T-3 Mine. *9th Underground Operators Conference,* Canadian Inst. Min. Metall., 102, Jan-April: pp A31-A36.

Thomas, C., Atchison, T. C. and Pugliese, J. M. 1963. *Comparative Studies of Explosives in Granite.* USBM RI 6701.

Tunstall, A. M., Djordjevic, N. and Villalobos, H. A. 1977. Assessment of rock mass damage from smooth wall blasting at El Soldado mine, Chile. *Trans. Inst. Min. Metall.* 106(A1-50): pp 42-46.

Vovk, A. A., Mikhalyuk, A. V. and Belinskii, I V. 1973. Development of fracture zones in rock during camouflet blasting. *Soviet Mining Science.* 9(4): pp 383-387.

Wang, Z. Q. and Hui, L. 1997. A fractal and damage model for rock-breaking by blasting. *Gen. Proc.* (Complete Explosive Reference Data Base, ISEE, 1997).

Wilbur, I., Duvall, W. I. and Petkof, B. 1958. *Spherical Propagation of Explosion-Generated Strain Pulses in Rock.* USBM RI 5483.

Worsey, P. 1985. Measurement of blast induced damage in wall rock for a selection of perimeter blasting technique. *11th Conf. Explosive and Blasting Technique,* Soc. Explosive Eng., San Diego, California: pp 175-189.

Yang, R. L., Rocque, P., Katsabanis, P. and Bawden, W. F. 1993. Blast damage study by measurement if blast vibration and damage in the area adjacent to blasthole. In: Rossmanith (ed.), *Rock Fragmentation by Blasting.* A.A. Balkema, Rotterdam*:* pp 137-144.

Yu, T. R. and Vongpaisal, S. 1996. New blast damage criteria for underground blasting. *CIM Bull.* 89(998): pp 139-145.

Zhang, S. 1993. *Explosion and Shock Dynamic.* Military Industry Press, Beijing, China (in Chinese).

Zhang, Z. 1994. *Rock Breakage Principle and Applications.* Metallurgical Industry Press, China (in Chinese).

Zhao, J. and Li, H. 2000. Experimental determination of dynamic tensile properties of a granite. *Int. J. Rock Mech. Min. Sci.* 37: pp 861-866.